2012

Probing nanoscale properties of organic conducting polymer interfaces using atomic force microscopy

Amy Alexis Gelmi
University of Wollongong

Probing Nanoscale Properties of Organic Conducting Polymer Interfaces using Atomic Force Microscopy

A thesis submitted in (partial) fulfilment of the requirements for the

award of the degree

Doctor of Philosophy

from

The University of Wollongong

by

Amy Alexis Gelmi

B. Science (Nanotechnology) (Honours 1st Class)

Department of Chemistry

2012

Certification

I, Amy A. Gelmi, declare that this thesis, submitted in partial fulfillment of the requirements for the award of Doctor of Philosophy in the Department of Chemistry, University of Wollongong, is wholly my own work unless otherwise referenced or acknowledged. The document has not been submitted for qualifications at any other academic institution.

Amy A. Gelmi

10th August 2012

Acknowledgements

To Dr. Michael Higgins, my supportive supervisor, thank you for your eye for detail and motivating enthusiasm that enabled me to be a better researcher.

To Professor Gordon Wallace for the opportunity to work in a prestigious research environment and help and support throughout, thank you.

I would like to thank the group at Dublin City University, namely Prof. Dermot Diamond and Mr. Michael Zanoni in cooperation with Dr. Klaudia Wagner at the University of Wollongong, for their collaboration with photosensitive conducting polymers.

A special acknowledgement and gratitude to Lexi Wheeler and the Bill Wheeler Award which enabled me to visit Ulm University and further my work with Dr. Christine Kranz.

A personal thankyou to Dr. Elise Stewart, Dr. Paul Molino, Miss Flora Binbin Zhang, and Eng. Stephen Beirne for being supportive friends.

To Dr. Peter Sherrell, who is my seal of affection.

Finally, thank you to my Mum and Dad who understand and support my desire for a career in science, no matter where in the world it takes me.

Publications

1. M. Higgins , G. G. Wallace, **A. Gelmi**, and S. McGovern, *Electrochemical AFM-Understanding the Electromaterial-Cellular Interface*, Imaging & Microscopy 11 (2), 2009

   Contribution: Electrochemical AFM data and images, and related experimental work.

2. K.J. Gilmore, M. Kita, Y. Han**, A. Gelmi**, M.J. Higgins, S.E. Moulton, G.M. Clark, R. Kapsa and G.G. Wallace, *Skeletal muscle cell proliferation and differentiation on polypyrrole substrates doped with extracellular matrix components*, Biomaterials 30(29), 2009

   Contribution: All AFM scans and AFM data analysis presented.

3. **A. Gelmi**, M. Higgins, G.G. Wallace, *Physical surface and electromechanical properties of doped polypyrrole biomaterials*, Biomaterials 31(8), 2010

   Contribution: All experimental work and wrote the first draft, worked the manuscript to final editing in coordination with the co-authors

4. V. Bax, Roxana S. Tipa, Alexey Kondyurin, Michael J Higgins, Kostadinos Tsoutas, **Amy Gelmi**, Gordon G. Wallace, David R. McKenzie, Anthony S. Weiss, Marcela M. M. Bilek*, Cell patterning via linker-free protein functionalization of an organic conducting polymer (polypyrrole) electrode*, Acta Biomaterialia 8(7), 2012

   Contribution: Experimental work involving the synthesis of the conductive polymer films.

5. **A. Gelmi**, M. Higgins, G. G. Wallace, *Attractive and repulsive interactions originating from hyaluronic acid and chondroitin sulfate doped conducting polymers observed using atomic force microscopy*, Journal of Physical Chemistry B 116(45), 2012

   Contribution: All experimental work and wrote the first draft, worked the manuscript to final editing in coordination with the co-authors.

6. **A. Gelmi**, M. Higgins, G.G. Wallace, *Resolving sub-molecular binding and switching mechanisms of fibronectin at electroactive conducting polymer*, Small 9(3), 2013

   Contribution: All experimental work and wrote the first draft, worked the manuscript to final editing in coordination with the co-authors.

7. A. F. Quigley, J. M. Razal, M. Kita, R. Jalili, **A. Gelmi**, A. Penington, R. Ovalle-Robles, R. H. Baughman, G. M. Clark, G. G. Wallace, and R. M. I. Kapsa, *Electrical stimulation of primary murine myoblasts on aligned nanostructured conductive polymer platforms*, Advanced Health Materials 1(6), 2012

   Contribution: All AFM scans and AFM data analysis presented

Abstract

The development of new biomaterials for the field of bionics- the fusion of electronic devices with biological tissue- is an exciting area of research. The ability to control the interaction between the electronic and biological interface in devices, such as the cochlear implant, are crucial for enhancing and improving their biocompatibility and performance.

Organic conducting polymers are widely studied for use as biomaterials to replace the conventional metallic materials currently used as electrodes and coatings in medical devices. These polymers are highly interesting due to fine level of control over material properties and the ability to incorporate biological components into the composition of the polymer itself. Thorough characterisation is needed to fully understand how these biological components influence the properties of the polymer itself and how they influence the interaction with living cells. Within this thesis I have used Atomic Force Microscopy to characterise an organic conducting polymer doped with various biological and non-biological molecules. This technique was applied so that the biomaterial could be studied on the nanoscale and on scales relevant to single cell interactions.

Characterisation of the physical properties of the biomaterial demonstrated that irrespective of whether the dopant was biologically derived, the physical properties tended to group together with films having either a low roughness, low modulus and high strain, or vice versa. When compared to previous work, which investigated these polymers as potential biomaterials for supporting the growth and differentiation of

skeletal muscle cells, these two groupings of the parameters correlated with the differing ability of the polymer substrates to support the cells.

Using AFM surface characterisation techniques, namely phase imaging, current sensing and Kelvin force probe scanning, it was deduced that the polymer displays variable dopant distribution depending on the dopant. This dopant distribution created regions of attractive and repulsive interactions across the surface, which is dependent on the redox state and degree of dopant loading of the polymer.

I developed a single protein force spectroscopy technique to measure the interfacial forces and interactions between a cell adhesion protein, fibronectin, and the biomaterial depending on dopant. This technique was able to resolve sub-molecular binding specificity between the dopants and binding domains of fibronectin. The interaction exploits a form of biological 'charge complementarity' to enable specificity. This specificity and the adhesion force were demonstrated to be influenced spatially by the distribution of dopant throughout the polymer using single protein force volume spectroscopy.

In addition, the effect of stimulus on the organic conducting polymers – protein interface was investigated. When an electrical stimulus was applied to the biomaterial, the specific interaction was switched to a non-specific, high affinity binding state that was shown to be reversibly controlled using electrochemical processes. Both the specific and non-specific interactions are integral for controlling protein conformation and dynamics – the details of which give new molecular insight into controlling cellular interactions on these polymer surfaces. A different organic polymer was stimulated

using an optical signal. The change in the surface charge was demonstrated to influence the level of adhesion of a non-specific interaction between the protein and polymer in a reversible manner.

This work provides insight into the nature of biologically doped organic conducting polymers down to the nanoscale and how their properties influence the response of living cells and tissues. The conclusions drawn here support the impetus for new biocompatible materials for use in bionic devices.

List of Abbreviations

3-EDSPA	-	3-ethoxydimethylsilylamine propyl
AC	-	Alternating current
AFM	-	Atomic force microscope
bHABP	-	Biotinylated hyaluronic acid binding protein
BNDF	-	Brain derived neurotrophic factor
BSA	-	Bovine serum albumin
C-AFM	-	Conductive atomic force microscopy
CBD	-	Corrected binding distance
CD	-	Circular dichroism
CS	-	Chondroitin sulfate A
DBS	-	Dodecyl benzene sulfonate
DC	-	Direct current
DS	-	Dextran sulfate
DMT	-	Derjaguin-Muller-Toporov
EC-AFM	-	Electrochemical atomic force microscopy

ECM	-	Extra cellular matrix
FCS	-	Foetal calf serum
FN	-	Fibronectin
GAG	-	Glycoaminosglycan
HEMA	-	Hydroxyethyl methacrylate
JKR	-	Johnson-Kendall-Roberts
KPFM	-	Kelvin probe force microscopy
MC	-	Merocyanine
MMA	-	Methyl methacrylate
NGF	-	Nerve growth factor
NHS	-	N-hydroxysuccinimide
NT	-	Neurotrophin
NT-3	-	Neurotrophin 3
OCP	-	Organic conducting polymer
PA	-	Polyaniline
PAAM	-	Polyacrylamide
PBS	-	Phosphate buffered solution
PDMS	-	Polydimethylsiloxane

PEDOT	-	Poly(3,4-ethylenedioxythiophene)
PEG	-	Polyethylene glycol
PLA	-	Poly(DL-lactic acid)
PMAS	-	Poly(2-methoxyaniline-5-sulfonic acid)
pNIPAM	-	Poly(N-isopropyl acrylamide)
PPy	-	Polypyrrole
PSA	-	Poly(sebacic anhydride)
PSS	-	Poly(styrene sulfonate)
PT	-	Polythiophene
pTS	-	Para(toluene sulfonic acid)
pTThMA	-	poly(4,4"-didecyloxy-2,2':5',2"-terthiophene-3-acetate)
pTThSP1	-	poly(2-(3,3"-dimethylindoline-6'-nitrobenzospiropyranyl)ethyl 4,4"-didecyloxy-2,2':5',2"-terthiophene-3-acetate)
QCM	-	Quartz crystal microbalance
RAIR	-	Reflectance absorbance infrared
RGD	-	Arginine-glycine-aspartic acid
RMS	-	Root mean squared
SEM	-	Scanning electron microscope

SP	-	Spirobenzopyran
SPM	-	Scanning probe microscope
VSMC	-	Vascular smooth muscle cells
XPS	-	X-ray photoelectron spectroscopy

Table of Contents

List of Figures

List of Tables

1 Introduction

1.1 Bionic Devices: New Electrode Materials

The combination of biological and electronic systems is described as 'bionic', and is applicable for the control of electrically excitable tissues such as nerve or muscle tissue within the body [1]. Bionic devices such as the cochlear implant and bionic eye require biocompatible electrode interfaces that connect the electronics of the devices to living tissue. This connection is vital for interfacing and communication between the device and living tissue.

The cochlear implant is a device that uses electrical stimulation to communicate sound to auditory nerve fibres. A microphone and processor system convert incoming sound into electrical signals, which are then delivered to the nerves via an electrode placed inside the cochlear [2]. Similarly, the bionic eye uses electrical stimulation of the nerves along the visual pathway (i.e. site of action can be at the cortical, optic nerve, or a retinal prostheses) to stimulate a visual signal where there is profound visual loss [3]. These bionic devices work to replace the damaged or faulty biological systems to provide vital electrical signals to the brain that are then perceived as sounds (e.g. speech) or vision.

The electrodes in these devices must be capable of supplying high-density electrical charge to the targeted living tissue [4], should not provoke an inflammatory response from the surrounding tissue, and the electrode-tissue interface must have a low impedance [5]. A

low impedance is vital to ensure an applied electrical stimulation is applied at thresholds that avoid cell damage in the stimulated tissue [6]; safe stimulation levels for neural prostheses vary between 0.5 to 4000 μC cm^{-2} depending on the placement and application of the electrode [7]. Low impedance is also important for efficient charge transfer between the polymer electrode and living tissue. In addition, low impedance decreases the energy required for stimulation (ideal for bionic devices that require a battery). A high charge storage capacity is desirable as the electrode is then able to store a relatively large charge without undergoing irreversible, and possibly cytotoxic, Faradaic reactions [8].

Bionic device electrodes currently use conventional metallic materials such as gold, platinum, platinum alloys, and iridium oxide to deliver stimulation [5, 9]. These metals have excellent conductivity, are stable and functional for long-term implants, and they do not react chemically with the surrounding tissue [5]. For example, platinum is used in cochlear implant electrodes as it is chemically inert, non-toxic, and has low impedance and long-term stability during electrical stimulation [10]. However, the physical properties of metallic surfaces, particularly the Young's Modulus, can have negative effects on surrounding tissues. For example, hard metals can provoke an inflammatory response from the surrounding tissue during insertion of the electrode, or after surgery due to chronic movement of the electrode [11-12].

Organic Conducting Polymers (OCP) as electrodes and electrode coatings are an alternative to metallic electrodes in bionic devices [13]. OCPs are comprised of organic aromatic cycle backbones and conduct electricity due to delocalised electrons along this backbone. OCPs act as semiconductors and exhibit both electronic and ionic conductivity and, as such, have been investigated as conductive materials in many bionic applications [14]. For example, poly(3,4-

ethylenedioxythiophene) (PEDOT), has a high charge injection limit (15 mC cm-2) and wide potential limit window compared to metallic materials (see Table 1-1) and has been explored as coatings for neural microelectrodes [7].

Table 1-1: Charge-injection limits of electrode materials for stimulation in the central nervous system. Adapted from [7]

Material	**Mechanism**	**Maximum Q_{inj} (mC cm^{-2})**	**Potential Limits vs Ag|AgCl (V)**
Pt and PtIr alloys	Faradaic/capacitive	0.05 – 0.15	-0.6-0.8
Iridium oxide	Faradaic	1 – 5	-0.6-0.8
Titanium nitride	Capacitive	~1	-0.9 to 0.9
(PEDOT)	Faradaic	15	-0.9 to 0.6

It is the electrical properties of OCPs that make them an extremely interesting area for applications in bionic devices. The conductivity of these materials is within the semi-conductor range (0.1-1000 S/cm), which is acceptable for electrode applications [15]. Due to 3-D microtopography and porosity the surface area of OCPs is much greater than conventional metal electrodes and thus leads to a higher charge density and lower impedance [16]. The charge injection mechanism for OCP electrode materials is more advantageous for biological applications compared to metals; reduction/oxidation reactions occurring within the OCP results in the electronic current being converted to an ionic current [17]. This electronic-to-ionic conversion of current is seemingly more compatible with living cells that also utilize ionic currents.

This reduces the charge transfer resistance between electrode and tissue, which reduces impedance and improves the communication across the interface [16]. The physical

properties of OCPs are more advantageous than their metallic counterparts; they are pliable, flexible and lightweight compared to these materials, in addition to being inexpensive [18]. The softer surface of these polymers provides inherent compatibility with biological systems, thus affording them superior biocompatibility compared to conventional metallic electrode materials.

A supplementary advantage of OCPs in bionic applications is the incorporation of dopants into the polymer structure. A dopant is a molecule that has been incorporated into the polymer during synthesis to balance the polymer backbone charge. The nature of the dopant molecule (such as size, charge and chemical structure) will modify the physical properties of the polymers, specifically physical properties [19-21], surface chemistry [22-23], and electrical conductivity [24-28]. The biocompatibility of OCPs can be further enhanced through the incorporation of biological dopants [29-30] without compromising, the conductive nature of the polymers. These dopants (e.g. growth factors) can also be released controllably from the polymer to improve the surrounding tissue environment [31-34]. This release of cell growth factors is controlled through electrical stimulation of the polymer and allows an OCP electrode to provide therapeutic drugs to the site of stimulation. This is of particular importance for the cochlear implant where secondary degeneration of auditory neural cells can occur due to the lack of hair cells (which is the original cause of hearing loss) within the cochlea [35]. These hair cells usually provide neurotrophic support of the surrounding neurons and without this support the effectiveness of the auditory nerves and cochlear implant may be reduced [36]. Auditory nerves have been successfully grown and stimulated using an OCP substrate with an aim to improve the nerve-electrode interface for cochlear implants [32], or used to coat metallic electrodes to improve biocompatibility with neural

cells [19]. The drug neutrophin-3 has been incorporated into an OCP coated on a cochlear implant electrode array and implanted in guinea pigs. This allowed direct delivery of the drug to the stimulated area, with auditory nerve cell density observed to greatly increase. The impedance of the OCP coated electrode was observed to not be significantly different to plain platinum electrodes [33]. The above research indicates that OCP electrode materials are not only comparable to metallic materials in electrical properties, but also add a therapeutic advantage through the inclusion of biologically active molecules directly into the electrode structure.

1.2 Organic Conducting Polymers

OCPs were initially developed by MacDiarmid, Shirakawa and Heeger [37], who were later awarded the 2000 Nobel Prize in Chemistry for this work. OCPs contain a carbonaceous backbone and conduct electricity, either as a metallic conductor or as a semiconductor (Figure 1-1). OCPs such as polypyrrole (PPy), polyaniline (PA) and polythiophene (PT) are frequently used in bionic applications, as they have demonstrated good biocompatibility and can be synthesised in an aqueous electrolyte for easy fabrication [13, 18, 38]. The structure of these OCPs is illustrated in Figure 1-1.

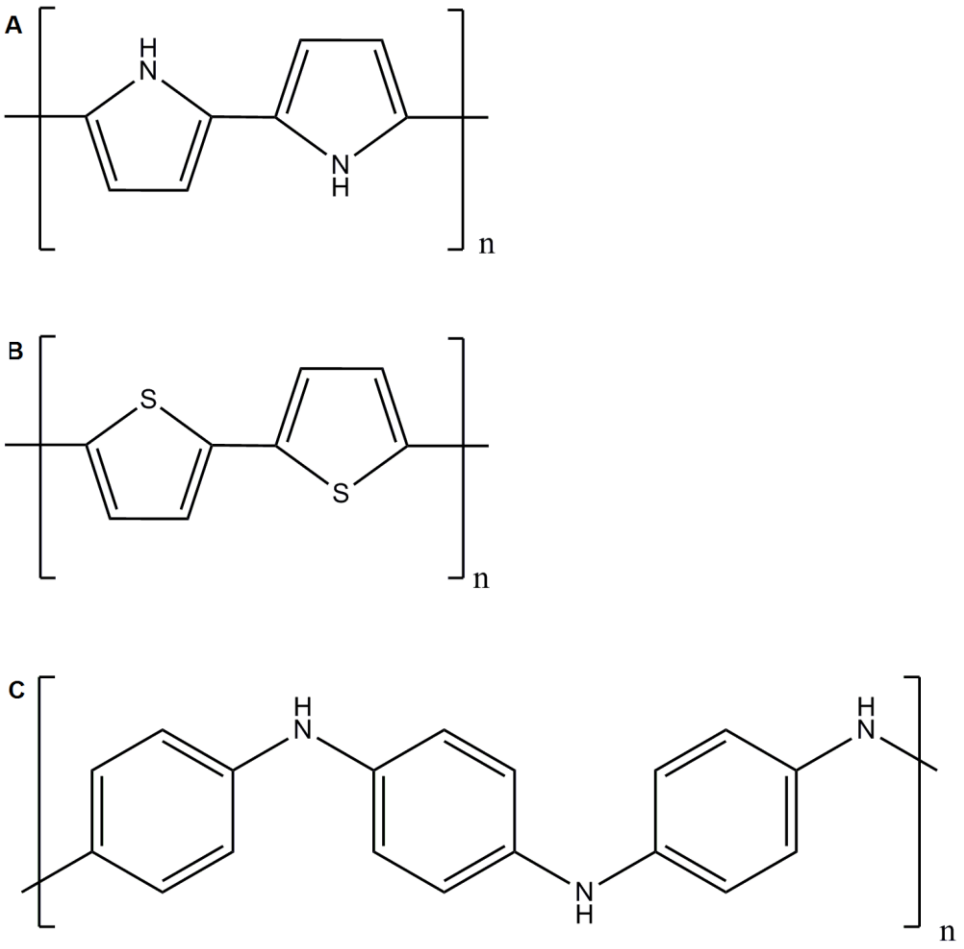

Figure 1-1: Molecular structure of (A) polypyrrole, (B) polythiophene and (C) polyaniline

1.2.1 *Synthesis of OCPs*

These polymers can be prepared through vapour phase deposition, chemical or electrochemical polymerisation process.

Vapour phase deposition uses a vapour of the monomer and exposes it to a surface pre-treated with an initiator to cause a polymerisation reaction on the surface. The polymer can be deposited onto a non-conductive substrate [13] or onto a polymer containing initiators and electron acceptors [39].

Chemical polymerisation can occur through either condensation or addition polymerisation [40]. Condensation polymerisation involves the loss of small molecules (such as water) as the molecules join together in a step-growth fashion. Addition polymerisation involves the step-growth of the polymer with the radical, cation or anion being the reactive end of the chain propagation. The advantage of chemical polymerisation is that it can be used for large-scale processing and creates a polymer that is easy to modify after synthesis.

Electrochemical polymerisation uses a three-electrode cell configuration in a solution of the monomer and electrolyte. As a current is applied to the cell the monomer undergoes oxidation on the working electrode surface to produce a radical cation, which reacts with other radical monomers in the solution to create oligimers. The anions present in the electrolyte are incorporated to ensure the charge balance of the polymer and polymer chains are formed on the working electrode [41]. This method generally creates thin films of polymer. The films can be created free-standing or left on the electrode; the polymer can be grown onto any conductive material acting as a counter-electrode, for example, carbon nanotube films [42] or electrospun fibres [43].

Electropolymerisation parameters such as growth time and polymerisation charge will influence roughness and thickness (which in turn affects ionic conductivity, Young's modulus, and nano-structure of the film) [44-45]. Many factors define the final polymer properties in this method, such as electrolyte, dopant, electrode material, monomer concentration, solvent, applied potential, and current density [41, 46-50]. This approach is less complex than the chemical method and is used more often in bionics applications as it enables greater flexibility for incorporating dopants [18].

1.2.2 *Electrochemical Doping of OCPs*

The doping of the OCPs occurs during oxidation of the polymer; for PPy and PT doping is carried out during the electrochemical synthesis of the polymer (Figure 1-2A and B, respectively). Doping of PA is carried out once the polymer has been synthesised via oxidation of the polymer in the presence of the dopant in acid form (Figure 1-2C). For PPy the dopant is incorporated into the polymer approximately at the rate of one dopant per three pyrrole rings (~0.3 doping level) [51-52], however depending on the nature of the dopant and synthesis parameters this doping level can vary from 0.1 to 0.5 [53]. The dopant content can be greater than 50% w/w and is generally incorporated between the PPy planes that are predominantly α-α bonded [40]. Similarly to PPy, PT polymers incorporate one dopant molecule per two to four thiophene rings [40]. PA requires an acidic environment to solubilize the monomer, hence the dopant needs to be an acid to ensure the pH of the electrolyte is not raised during polymerization [40]. The presence of the dopant introduces polymer chain entanglement, planar disruption of the aromatic rings and alternative charge conduction routes for the polymer [49].

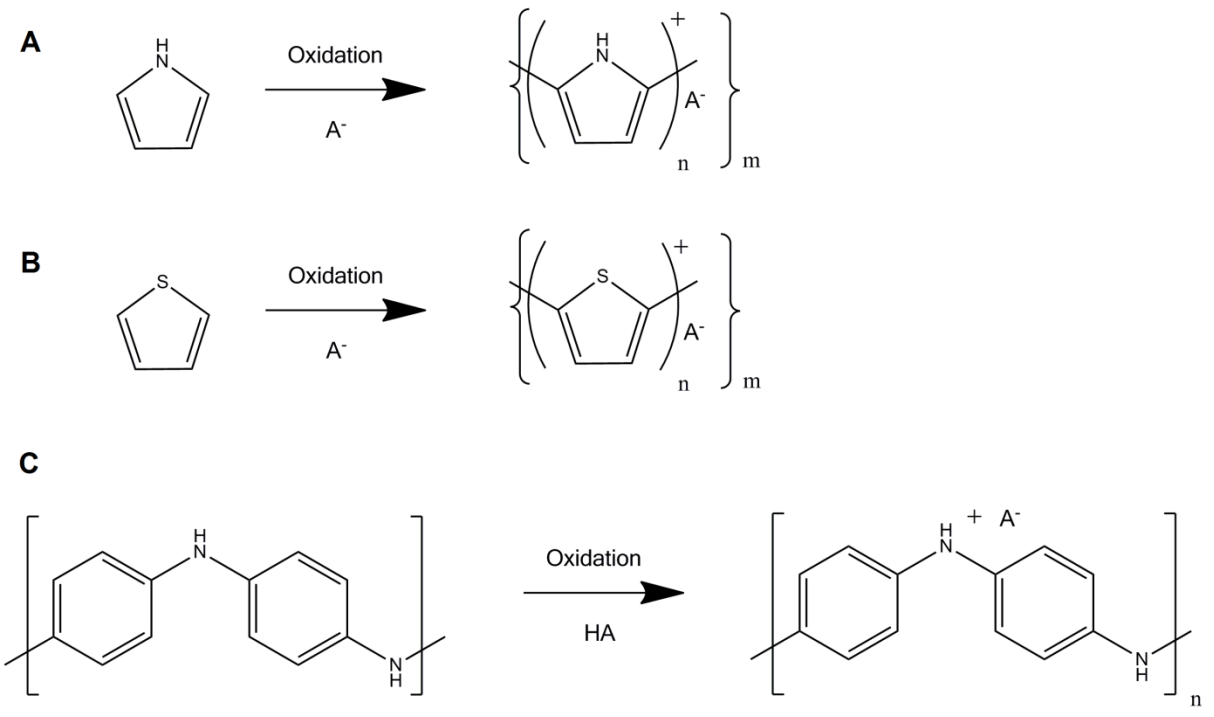

Figure 1-2: Electrochemical doping for (A) PPy, (B) PT and (C) PA with anionic dopant A^-. HA represents the acidic dopant, n and m are degrees of polymerisation.

The range of possible dopants used in OCP electropolymerisation is large, spanning a range of polarities and molecular weights. Table 1-2 lists a sample of the range of dopants presented in the literature, encompassing the small ion Cl^- to the very large polyelectrolyte polystyrene sulfonate (PSS). The size and shape of the dopant will influence the molecular organisation of the polymers, which in turn affects the morphology, conductivity, and physical properties of the material [54].

Table 1-2: Examples of a variety of dopants used in electrochemically prepared PPy, PA and PT polymers

Dopant (anionic form)	Molar Mass	OCP	Reference
Cl^-	35.453 g/mol	PPy, PA	[49]
BF_4^-	86.803 g/mol	PPy, PA, PT	[49, 55] [56]
$ClO_4^=$	99.453 g/mol	PPy, PA, PT	[56-57]
PF_6^-	144.974 g/mol	PT	[40]
$CF_3SO_3^-$	149.075 g/mol	PPy, PA, PT	[56]
$CH_3C_6H_4SO_3^-$ (*p*-toluenesulfonic acid)	172.20 g/mol (anhydrous)	PPy, PT, PA	[40, 49, 58]
$FeCl_4^-$	197.657 g/mol	PT	[49]
$C_7H_5O_6S^-$ (5-sulfosalicylic acid)	217.177 g/mol	PA	[58]
$C_{10}H_{15}O_4S^-$ (camphorsulfonic acid)	231.292 g/mol	PA	[58]
$C_{18}H_{29}O_3S^-$ (dodecylbenzenesulfonate)	325.476 g/mol	PPy, PA	[58-59]
$[C_8H_8SO_3]_n$ (polystyrene sulfonate)	10^{17}-10^{19} Daltons	PPy, PA	[44, 60]

1.2.3 *Material Properties of OCPs*

1.2.3.1 Morphology

Electropolymerised PPy and PT are known to predominantly have 'cauliflower'-like or nodular morphology, whereas PA is fibrillar and porous in nature. All of these OCPs exhibit morphological changes depending on the dopant [40]. For example, the morphology of the PPy has been shown to vary greatly with different types of dopants (Figure 1-3). The dopants used were p-toluene sulfonic acid (pTS), dodecyl benzene sulfonate (DBS), PSS and poly(2-methoxyaniline-5-sulfonic acid) (PMAS) [34].

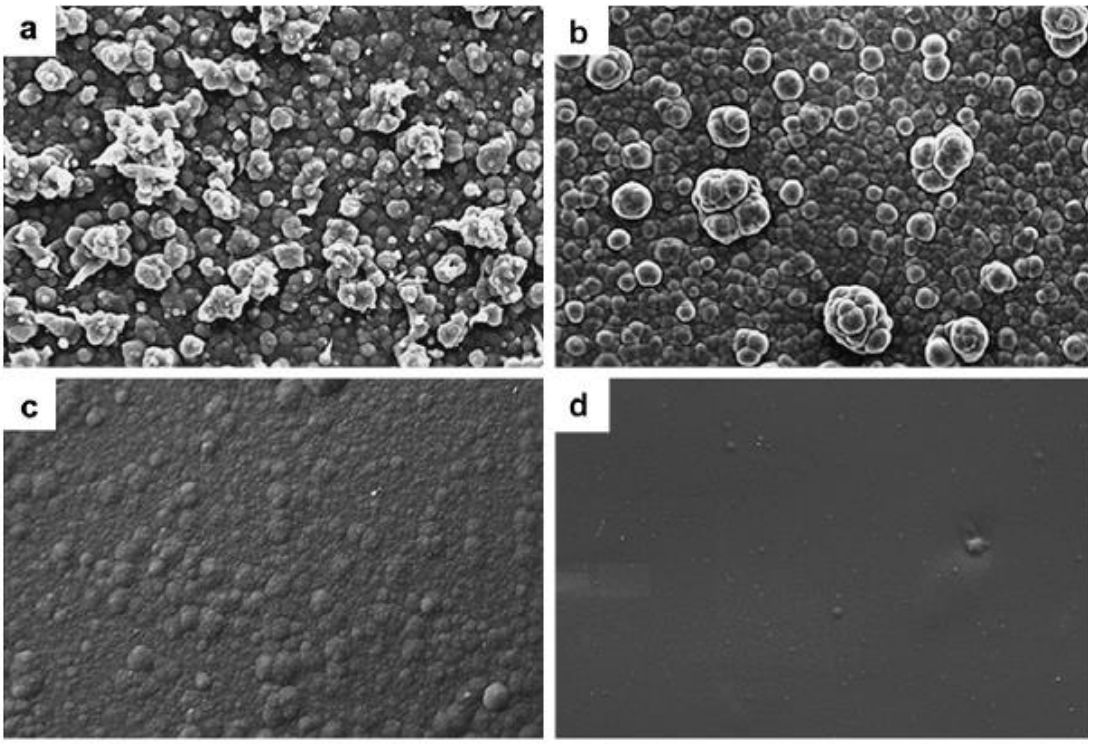

Figure 1-3: Scanning electron micrographs of polypyrrole synthesised with different dopants. (A) PPy/pTS, (B) PPy/DBS, (C) PPy/PSS, (D) PPy/PMAS. All polymers were grown using the same amount of charge (7.2 C/cm^2). The scale bar represents 40 µm [34].

The morphology and roughness of the PPy films is clearly influenced by each dopant, with the roughness across these dopants observed to increase in the order of pTS>DBS>PSS> PMAS. The roughness of the polymer can be increased by increasing the growth time [20, 44, 61] and current density [44], or by decreasing the dopant concentration [61]. For example, a PPy/dextran sulphate (DS) film showed an RMS roughness change from 8.4 ± 0.06 to 30.9 ± 3.8 nm with an increase in growth time from 1 to 10 minutes [61], while an increase of dopant concentration from 0.2 to 2 mg/mL showed an RMS roughness change of 40.2 ± 3.7 to 30.9 ± 3.8nm. The thickness of PPy films has been shown to increase with growth time and increasing current density [44]. Silk et al. found that chloride and sulphate doped PPy has increased surface roughness with thickness [62].

1.2.3.2 Conductivity

The aromatic rings of the OCPs provide the main path for charge mobility through overlapping p-orbitals due to the delocalization of π-electrons along the conjugated polymer backbone. The charge moves both along the polymer backbone and between adjacent chains, hence the disorder of the polymer will affect conductivity. The conductivity of OCPs is varied and dependent on many factors, including the dopant, oxidation level, synthesis method and temperature [18, 63]. Table 1-3 shows the large range of conductivities for OCPs and some selected dopants.

Table 1-3: Conductivities of OCPs with selected dopants. Values reproduced from [18, 49, 56]

Polymer	Dopant	Conductivity (S/cm)
PPy	$CF_3SO_3^-$, ClO_4^-	150 (film), 100 (film)
	BF_4^-, ClO_4^-, pTS	500 - 7500
PT	$SO_3CF_3^-$, BF_4^- or PF_6^-	10-20 (pp)
	BF_4^-, ClO_4^-, pTS, $FeCl_4^-$	1000
PA	HCl	200

The polarity of the dopant has a strong influence on the conductivity of the polymer. The dopant tosylate (anionic form of para-toluenesulfonic acid) produces a PPy polymer with much higher conductivity than the ClO_4^- dopant, a difference which is attributed to the higher polarizability and basicity of the tosylate [64]. The high basicity allows the radical cation monomers to more strongly associate with the dopant during growth, resulting in more stable conductive states.

1.2.3.3 Surface Energy

The surface energy of OCPs can be greatly altered with dopants of different charge densities. PT films were made with a range of hydrophobicity (75 ± 2.14° to 133.3 ±4.03° contact angle in water) using dopants with different alkyl chain lengths. Longer chain lengths resulted in more hydrophobic polymers [65]. Gilmore et al. observed that a large range of wettability could be induced for PPy films with both biological and non-biological dopants. Contact angles ranged from 13.4 ±2.6° for a biological dopant, chondroitin sulphate (CS), to 88.4 ± 1.1° for a non-biological dopant (DBS) [20]. The large biological dopant, heparin, was also observed to produce a more hydrophilic polymer than the non-biological dopant NO_3^- [66].

1.2.3.4 Modulus

The dopant can influence the modulus and porosity of the polymer [52, 58]. The inclusion of dopants reduces the polymer backbone flexibility, creating a stiffer polymer [52]. Dopants may create electrostatic cross-linking to replace van der Waals interactions within the polymer and increase stiffness [67]. The variation in Young's modulus for PPy with different dopants has been shown to vary from 0.4 to 4 GPa, with smaller inorganic dopants resulting in brittle films compared to larger organic dopants [53]. Through the use of naphthalene ring dopants with increasing numbers of sulfonate groups; a higher degree of electrostatic cross-linking and microporosity was linked to an increase in the number of sulfonate groups on the dopant [68]. The size of the dopant has been directly correlated with Young's modulus changes in a PPy film using DBS dopants with increasing anionic alkyl groups [69].

Figure 1-4 shows that the larger dopants decrease the Young's modulus of the polymer films and that the Young's modulus of the oxidised films is greater than the reduced films. This modulus change was due to the distance between PPy backbone chains increasing and the lower interchain interaction, resulting in a softer polymer [69].

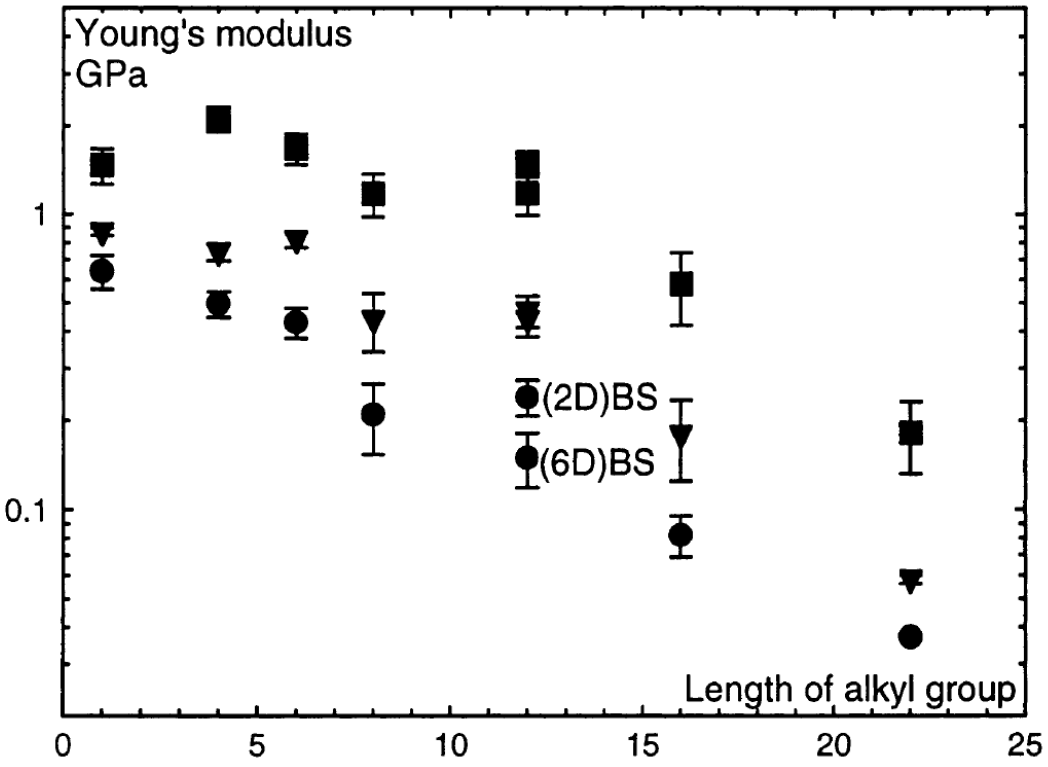

Figure 1-4: Young's moduli (stiffness) of PPy films. The modulus was measured using a mechanical method via a force-displacement set-up. The number of carbon atoms in the alkyl group of doping anion is on the *x*-axis. (■) Dry oxidized films. (▼) Oxidized films (0.0 V vs SCE) in 0.1 M NaCl. (●) Reduced films (-0.9 V vs SCE) in 0.1 M NaCl. Error bars from 3 to 5 samples [69].

1.2.3.5 Mechanical Actuation

The Faradaic electrical properties of the OCPs mean that during electrical stimulation the polymers can undergo mechanical actuation through volume changes induced by the oxidative state. The volume changes of the PPy film are due to the movement of ions and molecules in and out of the film to balance the charge of the film when it is in a reduced or oxidised state. This process is described by eq. (1) and (2);

$$P^+(A^-) + C^+ + e^- \leftrightarrow P^0 + A^- + C^+ \quad (1)$$

$$P^+(A^-) + C^+ + e^- \leftrightarrow P^0(AC) \quad (2)$$

where P+ is the oxidised polymer, Po is the reduced polymer, A- is the dopant anion, and C+ is the electrolytic cation.

Eq. (1) represents the reduction of the polymer where the ejection of anions from the polymer causes it to contract. If the anion is immobile however (i.e. a large dopant), the polymer will balance charge by up-taking cations from the electrolyte which causes it to expand (Eq. 2)[44]. Both are reversible processes that enable cyclic expansion and contraction of the polymer, a property conducive for mechanical actuators (e.g. artificial muscles)[70-71].

1.3 Cell-Material Interactions

1.3.1 Biological Cues from Physical Properties

Preceding the biological impact from ECM dopants in OCPs, it is known that the physical properties of a polymer substrate in general can have a strong influence on cellular response. The physical properties, including topography, roughness, Young's modulus and surface charge, of a biomaterial act as stimulating cues for controlling cell behaviour. Topographical features have been used to guide cell growth. C6 glioma cells were shown to align along nanoscale ridges (210 nm in periodicity, 30-40 nm deep) lasered into a polystyrene surface [72]. Surface morphology will affect cell adhesion as shown by Park et al. [73], where it was found that the adhesion of mesenchymal stem cells had a critical dependency on the diameter of vertically orientated TiO2 nanotubes. Surface structures with a diameter greater than 50 nm resulted in very poor cellular adhesion compared to a diameter of 30 nm that strongly enhanced cellular adhesion and spreading; more so than a completely smooth TiO2 surface. The lateral spacing of a cell's focal (contact) adhesion sites is hypothesised to control the cell's fate; the cell needs to create these focal adhesion sites to enable actin assembly into filaments to give the cell mechanical support and intra-cellular signalling. If the distance between surface features spreads focal points too far, the cell will fail to adhere to the surface and will undergo programmed cell death [73].

Surface roughness and specific geometry can dictate the success of cellular adhesion and has been shown to be highly dependent on cell type. Endothelial cells were found to prefer polyurethane/PEG surfaces with nanoscale roughness (Ra of ~40 nm) [74]. Osteoblasts were

tested on titanium surfaces subjected to various treatments to induce different roughness's. The cells adhered and proliferated better on the rougher surface (coarse grit-blasted Ti)[75]. The surface geometry of TiO_2 substrates has also played a role in osteoblast differentiation, with more regular surface geometry improving differentiation [76]. Neurons grown on Si substrates of varying roughness showed an optimal range for adhesion between an R_a of 10-70 nm, with the highest cell density at ~ 30 nm [77]. The influence of roughness on the success of cellular adhesion and proliferation is believed to be due to the changes in surface area. When cells are exposed to the substrates in media, the surface is conditioned by both media and serum which aids cellular adhesion [76]. Surfaces which have a roughness that increases surface area without becoming too rough for cells to form consistent focal contacts appear to enhance overall cell viability. The preference for an optimal surface roughness by cells has been used to induce guidance cues by patterning a Si substrate with varying degrees of nanoscale roughness [77].

Different types of cells will show a preference for specific ranges of Young's modulus. Materials that have similar mechanical properties to the target tissue generally induce better cell adhesion and growth [78-79]. The stiffness of a substrate can dictate the differentiation of cells. For example, substrates with a specific modulus have been used to control mesenchymal stem cell lineage[80]. Softer collagen substrates that mimicked brain tissue resulted in a neurogenic response, while softer polyacrylamide gels created a myogenic response. Softer substrate modulus have also been shown to trigger the down regulation of fibronectin (FN) expression in MCF-10A mammary epithelial cells [81]. The substrate was composed of polyacrylamide with moduli ranging between 0.3 to 3.5 kPa and cross-linked with either laminin or FN to distinguish the effects of the cell-mediating molecules from the modulus

variation. The table below, adapted from Wong et al. [78], summarises several studies that have systematically study the influence of modulus on cell behaviour.

Table 1-4: Investigation of substrate stiffness on cell behavior.

Substrate/Modification	Modulus/Method	Cell Type	Main finding	Reference
PAAM/collagen I (covalent)	*E*: 15-70 Pa/ microindentation	Fibroblasts	Reduced cell spreading and increased motility on softer substrata; Increased growth and decreased apoptosis on stiffer substrata	[82-83]
PAAM (gradient)/collagen I (covalent)	*E*~14 and 30 kPa/ microindentation	Fibroblast	Preferential migration towards stiff substrata	[84]
PAAM/polylysine (covalent) and Matrigel (physisorption)	*G**: 50–500 Pa/ rheometry	Spinal cord neurons	More neurite branching on softer substrata	[85]
PAAM/collagen I (covalent)	-	Endothelial cells	Tubulogenesis increased for softer substrata	[86]
PAAM/collagen I (covalent or physisorption)	*E*~2.5–40 kPa/ uniaxial tension and atomic force microscopy	VSMCs	Reduced cell spreading on softer substrata	[79]
PAAM (radial gradient)/ collagen I (covalent)	*E*~2.5–11 kPa/ microindentation	VSMCs	Preferential migration and accumulation of cells onto stiffer regions of substrata	[87]
Silicone rubber/no pretreatment	–/wrinkle method	Glioblastoma	Reduced cell spreading and greater motility on softer substrata	[88]
PDMS (mechanically patterned substrata)/ fibronectin (physisorption)	*E*: 12 kPa–2.5 MPa/ uniaxial tension	Fibroblasts and endothelial cells	Preferential migration and accumulation of cells onto stiffer regions of substrata	[89]
Alginate/RGD (covalent)	E_c: ~12–127 kPa (Ca2+); ~16–147 kPa (Ba2+)/ dynamic uniaxial confined compression	Chondrocytes	Reduced cell spreading on softer substrata	[90]
Alginate/RGD (covalent)	*E*~ 2–10 kPa	Skeletal myoblasts	Rate of growth and differentiation higher on stiffer substrata	[91]
Agarose/no modification	*G**: 2–13 Pa/ rheometry	Dorsal root ganglia neurons	Rate of neurite extension greater on softer substrata	[92]

*G**: shear modulus, E_c: compressive modulus, *E*: Young's modulus, RGD: Arg-Gly-Asp, LbL: Layer-by-layer, PAAM: Polyacrylamide, PDMS: Polydimethylsiloxane, VSMCs: Vascular smooth muscle cells.

The cellular preference for a particular modulus opens the use of modulus as a way to control and direct cell growth on the nanoscale [87]. The influence of substrate modulus on neural cells is believed to be dependent on the tension of neurite extensions. The growth cones of the cells pull on the neurites and maintain an external tension and this effect is suggested to control neurite extension [92]. Muscle differentiation is hypothesised to be dependent on surface elasticity due to the effect of the substrate's modulus on fibrillogenesis. The striation of muscle cells requires more than just cell adhesion, but also a surface that allows the premyofibrils to optimise contractile forces with the substrate. These contractile forces control the development of the premyofibrils into mature myofibrils and subsequent muscle differentiation and fibrillogenesis [79].

Hydrophobicity and surface charge have a strong influence on cellular adhesion and proliferation. Hydrophobic surfaces generally promote better cell adhesion and spreading compared to hydrophilic surfaces [93]. The adhesion of endothelial cells can be controlled through varying surface wettability and charge. Wettability of a substrate was controlled through decreasing the hydroxyethyl methacrylates (HEMA) content in HEMA/methyl methacrylates (MMA) copolymers. The highest concentration of endothelial cells was observed on the moderately wettable 25 HEMA/75 MMA (contact angle of 39°) and cell adhesion was greatly reduced on the more hydrophilic copolymers [94]. Surface charge was controlled in the same study using additives, with the most pronounced cell spreading observed on the positively charged copolymers. The influence of surface charge and wettability has been directly related to the ability of cell adhesion proteins to bind to the surface [65, 94-95]. The presence of these proteins aids the cellular adhesion and spreading,

and the interaction between the protein and the surface charge of a surface has been subject to several studies [96-101]

1.3.2 *Biological Properties of OCPs*

The properties of OCPs, physical, chemical, and electrical, have a direct influence on the proliferation, growth and differentiation of living cells. Cells respond to surface properties through several mechanisms and hence the surface properties of OCPs need to be carefully considered. The presence of a dopant changes the surface chemistry of the OCP surface, a feature that can be used to enhance cell growth or control cell differentiation. Finally, their electrical properties play a very important role in the bionic application of these materials; the conductive properties dictate the charge that is delivered to the cells, or even controlled release of dopant (e.g. drug molecules), and it is vital that the electrical stimulation does not cause damage to the surrounding tissue.

Therefore, OCP electrodes have the unique ability to control cell interaction through various mechanisms, including:

- Nanoscale physical properties;
- Incorporation of biomolecular dopants;
- Electrical stimulation;
- Controlled drug release; and
- Mechanical (actuation) stimulation.

1.3.3 *Physical Properties*

Compared to the extensive literature covering the physical properties of metals (i.e. TiO2) and conventional polymers (i.e. PAAMs), there has been a fraction of the work performed on conductive polymers. Physical properties such as surface topography and wettability have been studied in relevance to cellular response. Topography was used to control cellular growth direction using 1 and 2 µm wide channels of PPy/PSS polymerized on poly(methyl methacrylates [102]. Hippocampal axons were found to align along the PPy channels. PT films prepared with a set of dopants showed a dependency of neural PC12 cellular proliferation on the wettability of the polymer [65]. The wettability was changed using dopants with increasing alkyl side chains of SDBS and the hydrophobic polymers were a better support for proliferation.

1.3.4 *Biomolecular Dopants*

The inclusion of biological dopants (biodopants) is at the forefront of creating biocompatible OCPs. Biological dopants have included proteins [36], peptides [103-104] and extracellular matrix (ECM) components [20, 105-108]. The inclusion of biomolecular dopants into the polymers is focused on improving biocompatibility. The structure of these biomolecules can modify the surface energy of the polymer and may also directly interact with the cell membrane to influence cellular functions. Stauffer and Cui [104] incorporated laminin peptides into PPy in order to invoke specific cell adhesion to the polymer. The peptides, DCDPGYIGSR and DRNIAEIIKDIC, were combined with aspartic acid to increase the overall negative charge of the molecules for more efficient doping. The research showed that the peptides enhanced the density of rat neurons adhered to the PPy surface compared to the non-bioactive PSS dopant.

1.3.4.1 Glycosaminoglycan Biodopants

The class of glycosaminoglycans (GAG) biological molecules produced by the ECM are growing in recognition as suitable OCP biodopants. GAGs make good candidates for OCP doping, as they are negatively charged and soluble in aqueous solutions. They are a major component of the ECM and cellular structure within the central nervous system and other tissues, and are also found on the surface of cells. These molecules play important roles in cellular functions such as growth factor signalling, cell division, wound healing, haemostasis and tissue morphogenesis [109]. GAGs also interact with specific receptors on both the cell membrane surface and cell mediation proteins [110]. Cell adhesion to surrounding tissue is mediated by the presence of integrin receptors in the cell membrane. These integrins bind to ECM components such as fibronectin, vitronectin, laminin and collagen [111]. In turn, these ECM components bind to GAGs [112], which is critical for mediating cell adhesion.

1.3.4.2 GAG Biodopant Structure

Chondroitin sulphate (CS) is a proteoglycan that consists of GAG chains made up of repeating disaccharide units [113]. CS, as shown in Figure 1-5A, is comprised of repeating units of D-gluronic acid and N-acetyl-D-galactosamine monosaccharides. The chains can be of variable length and sulfonation of the N-acetyl-D-galactosamine usually occurs at the hydroxyls on the 4 or 6 positions. In this study, we have used a CS molecule sulfonated at the 4 position. CS is an important molecule in the central nervous system, plays a role in neural development and axon regeneration [113], and aids interactions between cells and axons [29]. The biological functions of CS are mainly due to the presence of the sulfonate groups and the degree of sulfonation that modulates the interaction with extracellular matrix (ECM) molecules such as FN [114].

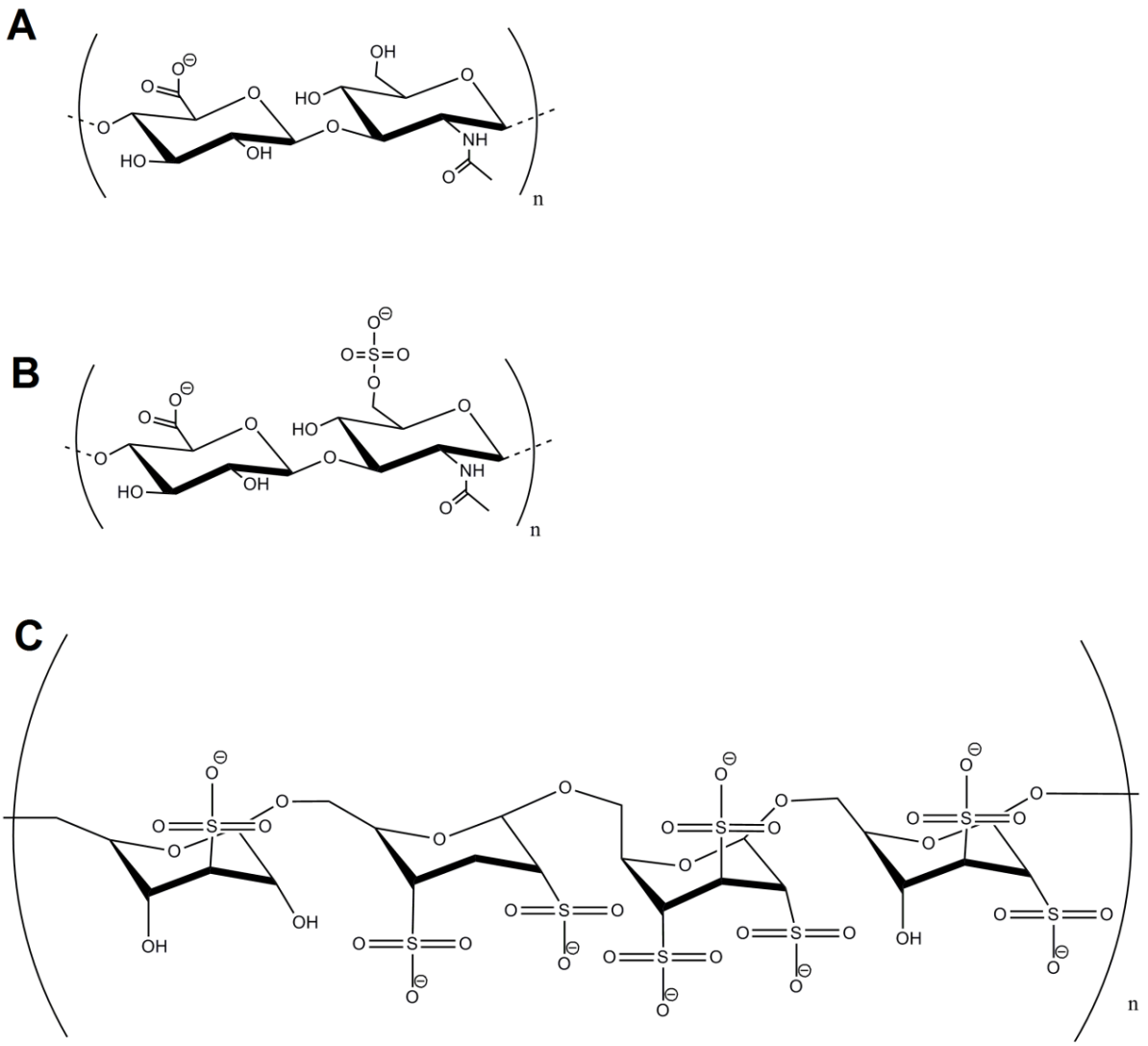

Figure 1-5: Molecular structure of anionic (A) chondroitin sulfate,(B) hyaluronic acid,and (C) dextran sulfate.

Hyaluronic acid (HA) is a similar polysaccharide to CS but unique in that it is an extremely high molecular weight, non-sulfonated GAG [115]. The structure of HA is comprised of the same repeating monosaccharides as CS but does not contain sulphate groups (Figure 1-5B). HA has many functions in the body, including a major role in cell proliferation and migration [115]. The molecule is extremely hydrophilic and makes an excellent lubricant, and is beneficial in wound healing processes and tissue regeneration [116].

Dextran sulfate (DS) has a linear polysaccharide structure (Figure 1-5C) containing α-1,6-linked D-glucopyranose units with three sulphate groups per one D-glucose unit [117]. DS is semi-synthetic, synthesised from sucrose by lactic-acid bacteria, but similar in structure to the GAGs. This molecule is primarily an anti-coagulant and acts to reduce erythrocyte aggregation and platelet adhesiveness. Compared to CS and HA, DS is the most highly sulfonated. The incorporation of DS as a dopant has been shown to produce a polymer with a high water content, due to the presence of the hydrophilic sulfonate groups [118]. DS contrasts with the two ECM dopants in that it has a similar polysaccharide structure, but carries many more negatively charged groups.

1.3.4.3 Influence of GAGs on OCP Physical properties

The influence of these GAG dopants on PPy physical properties have been the focus of several studies. Moreno et al showed that the PPy/HA films exhibited a rougher surface compared to a smooth PPy/CS prepared with the same parameters, indicating a different morphological effect from each dopant. A difference in wettability was observed between the two dopants, with PPy/HA being more hydrophilic (contact angle of 30°) compared to PPy/CS (53°). The different polar groups (presence/lack of sulfonate group) of the dopants are believed to cause this difference in wettability [29]. A difference in roughness between the two dopant/polymer combinations was also observed by Gilmore et al. PPy/HA was reported to have an Ra roughness of 21.85 nm (10µm x 10µm area) compared to 8.17 nm for PPy/CS, indicating a change in the nanoscale properties of the polymer [20]. Collier et al. synthesised PPy/HA materials, but used a bilayer composition (PPy/PSS bottom layer with a thin PPy/HA top layer) citing difficulties in handling and poor electrical properties (very low conductivity of 3.08 ± 1.39 × 10-3 S/cm), of single layer PPy/HA films [105]. As previously discussed,

physical properties such as roughness and surface energy can be influential on cellular response. The capability of these dopants to induce different physical properties is an important factor to note along with the possible chemical interactions of the molecules.

1.3.4.4 GAG Biodopant Influence on Cellular Response

The GAG, heparin, has been used in several studies for improving PPy biocompatibility. Heparin is an anticoagulant produced by cells and is highly negatively charged due to a high degree of sulfonation. Heparin was first incorporated into PPy by Zhou et al., who demonstrated that the polymer displayed specific binding with thrombin [108]. Human endothelial cells have been successfully adhered and grown on PPy/heparin polymers [30, 119], however it was demonstrated that this interaction is indirect and requires the presence of cell adhesion molecule vitronectin to aid cellular adhesion [66]. PPy has been doped with varying ratios of heparin and then added to poly(L,L-lactide) in order to produce a conductive membrane. The adhesion and growth of human fibroblast cells were greatly improved on these membranes compared to those without heparin [120]. PPy/heparin has inhibited the proliferation of the smooth muscle cells due to binding between dopant and cell membrane receptors, while allowing the growth of endothelial cells to proceed unhindered, indicating a possible application for selective cell growth on these surfaces [119]. Heparin is just one of several GAG molecules that are of interest for doping of OCP.

Other GAG ECM molecules include HA and CS. CS was first used as a dopant by Moreno et al., who found that the polymer supported the growth of fibroblast cells without the presence of foetal calf serum to aid cell adhesion [106]. Moreno et al. also compared the physical and chemical properties of PPy polymer doped with all three biological components (heparin, CS and HA). The polymer surface properties were controlled through growth parameters and it

was found that the smoother films showed good cell adhesion and proliferation compared to rougher, more irregular films. All of the GAG doped films exhibited good osteoblast adhesion and proliferation when prepared as smooth films, indicating that the physical properties of the polymer, not necessarily the surface chemistry imparted by the dopant, was an underlying factor for the cell interaction [29]. Gilmore et al. used both HA and CS as dopants in PPy and found that the polymers supported skeletal muscle (myoblast) cell adhesion. However, HA performed significantly worse than CS at supporting myoblast cell differentiation into muscle fibers [20]. As mentioned above, Collier et al. [105] synthesised PPy/HA as a bilayer material. The bilayer films supported PC-12 cell cultures and when implanted into rats over short periods of time (2 weeks) an increase in vascularisation was observed in the tissue. Lee et al. [121] discuss the use of PPy/HA as an electrode coating for discouraging fibroblast and astrocyte adhesion. By coating the electrode with a PPy/HA polymer, the adhesion of cells was minimized for up to 3 months. PPy/HA has been cited as resistant to cell adhesion [122]. HA appears to induce rough, irregular PPy films which are not conducive to cellular adhesion [20, 29]. However, PPy/HA has also been successfully used for cell adhesion through controlling synthesis parameters, as discussed above, and enhancing neural PC12 cell attachment when immobilized on a PPy surface [123]. Thus, while the chemical presence of HA does have a positive influence on cellular adhesion and growth, the physical properties it induces in PPy appear to be detrimental in some cases.

1.4 Electrical Stimulation

The electrical conductivity of PPy provides another important means to control cellular function for biological applications. Electrical stimulation plays an important role in tissue regeneration applications [124-126], improving cell growth and affinity [24, 107,127], and also through the release of incorporated drugs to aid cellular growth [32,128-129].

The influence of electrical stimulation on excitable cells has been proposed to occur via several mechanisms. The increased cell proliferation may be due to induced membrane depolarisation from the electrical stimulation [127]. This depolarisation opens voltage gated ion channels within the cellular membrane, thus allowing ionic transport (i.e. Ca2+) across the membrane into the cell. This causes an upregulation of gene pathways that control proliferation and differentiation of the cells. There may be changes in the cell membrane or ECM proteins to more favourable conformations [130], or electrophoretic redistribution within the cell of membrane growth factors and adhesion receptors [131]. It has also been proposed that pulsed electromagnetic fields may enhance protein synthesis within the cell [132].

To deliver charge from an electrode to an electrolyte (for example cell media or extracellular fluid) there are two primary charge injection methods, Faradaic and non- Faradaic (double layer capacitance).

Faradaic charge injection occurs when electrons are transferred between the electrode and electrolyte due to oxidation (electron loss) and reduction (electron gain) reactions of the electrode. This occurs at a particular charge density which is dependent on the

system [8]. This is illustrated in Figure 1-6, where the Faradaic process involves transfer of electrons from the metal electrode (green layer) to the solution. The redox reaction at the interface (purple layer) will reduce the cations (C+) and oxidise the anions (A-), and the charge diffuses through the solution with the reaction products.

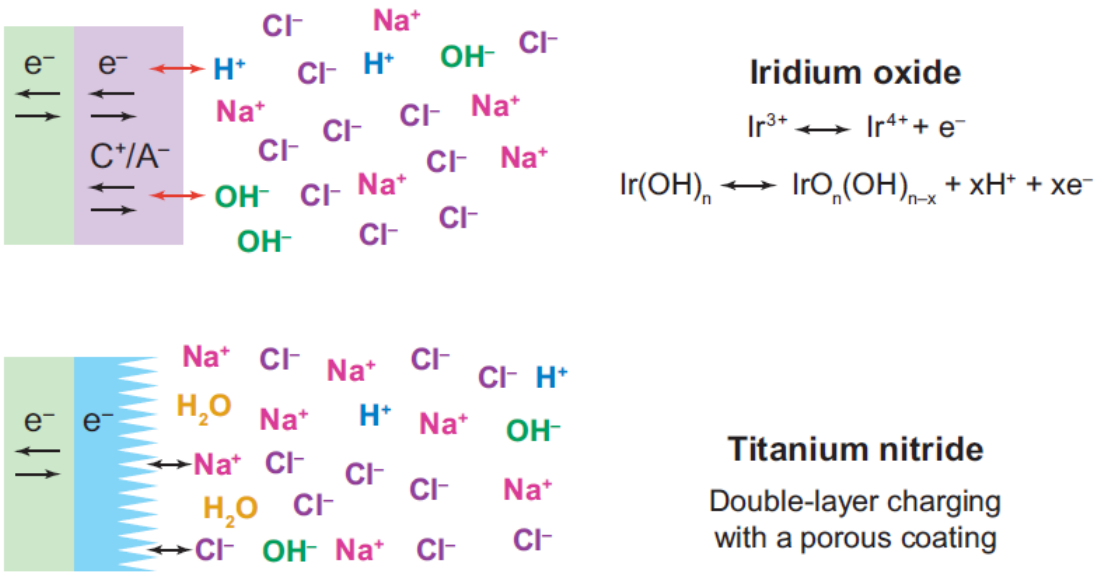

Figure 1-6: Example of electrode/electrolyte interface illustrating faradaic (top) and capacitive (bottom) materials with an aqueous NaCl electrolyte. The Faradaic charge injection results in the redox of the electrode (purple layer), creating reduced and oxidised products. The capacitive charge attracts and repels ions within the electrolyte to the electrode surface (green) which creates a charged layer on the surface (blue). Adapted from [7].

A double layer will be formed on the surface of an electrode in an electrolyte, as shown in Figure 1-6. When the charge is applied on the electrode surface (green layer), charges within the electrolyte will redistribute as anions (i.e. Cl-) and are repelled from the negatively charged electrode (blue layer) and cations are attracted to the surface (i.e. Na+). When the charge is reversed the anions are attracted to the surface and the cations repelled.

Charge injection from the electrode occurs through this redistribution of charge in the electrolyte. This is the principal mechanism for small amounts of charge injection [8].

PPy undergoes a Faradaic response when an appropriate electrical stimulation is applied and this reaction is reversible (Figure. 1-7). The direction of charge movement is dependent on the dopant size. When the anionic dopant (A-) is small, it can readily move out of the polymer to balance the charge of the oxidised polymer. If the dopant is large and immobile, cations from the surrounding electrolye can move into the polymer to balance the charge. Hence the charge injection mechanism for PPy is primarily driven through oxidation and reduction of the polymer via the movement of ions in and out of the polymer.

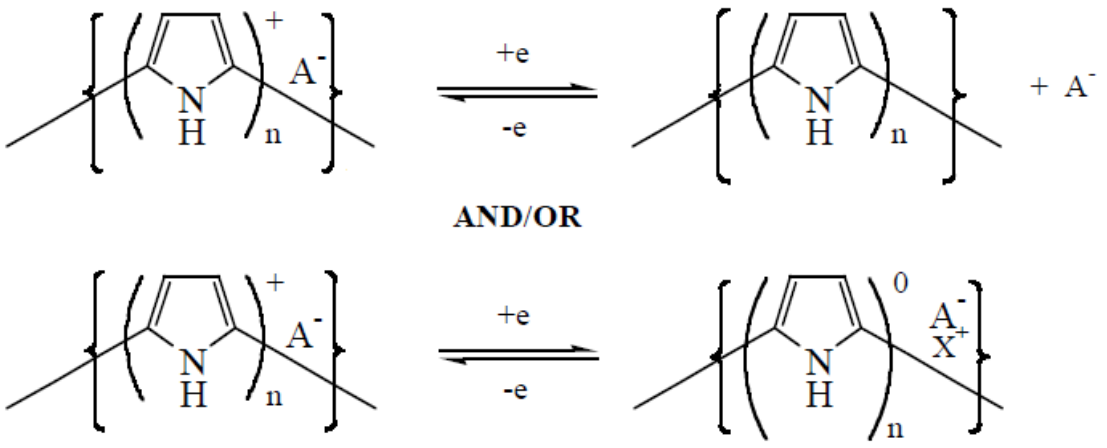

Figure 1-7: Oxidation and reduction reactions for PPy, with either a small (top) or large (bottom) anion dopant A^-, and cation in solution X^+.

Charge injection can be controlled through either the applied current or voltage. Current-controlled (galvanostatic) is the most common form of electrical stimulation applied to excitable cells. The important parameter for electrical stimulation is the current density; this

must not exceed the charge injection limit in order to avoid non- reversible Faradaic reactions at the electrode surface that may cause cellular and tissue damage.

1.4.1 *Drug Release via Electrical Stimulation*

During the reduction and oxidation of PPy it is possible for ions move in and out of the polymer to balance the charge on the electrode (Figure 1-7). By taking advantage of this mechanism, drugs for cell growth and proliferation (such as neural growth factor) can be released into the surrounding electrolyte [133]. Neurotrophin (NT) proteins are associated with the growth of neural cells and can enhance neurite outgrowth and survival. NTs have been released from PPy during optimised electrical stimulation to maximize NT release whilst minimising the applied current to ensure a safe stimulation protocol [36]. Richardson et al. has shown that neural cell outgrowth greatly improves when neurotrophin-3 (NT-3) is electrically released from PPy [32-33]. Neuron axonal outgrowth could be doubled by incorporating two growth factors, NT-3 and brain-derived neurotrophic factor (BNDF) [27]. Figure 1-8 shows representative images of neural explants when using NT-3, BNDF, and electrical stimulation. Without electrical stimulation the neuronal growth is still enhanced by the presence of the NTs (Figure 1-8 left column PPy/pTS/NT-3, PPy/pTS/BNDF, LowBNDF/NT-3, HighBNDF/NT-3), however when electrical stimulation was applied the neuronal outgrowth was increased even further (Figure 1-8 right column PPy/pTS/NT-3, PPy/pTS/BNDF, LowBNDF/NT-3, HighBNDF/NT-3).

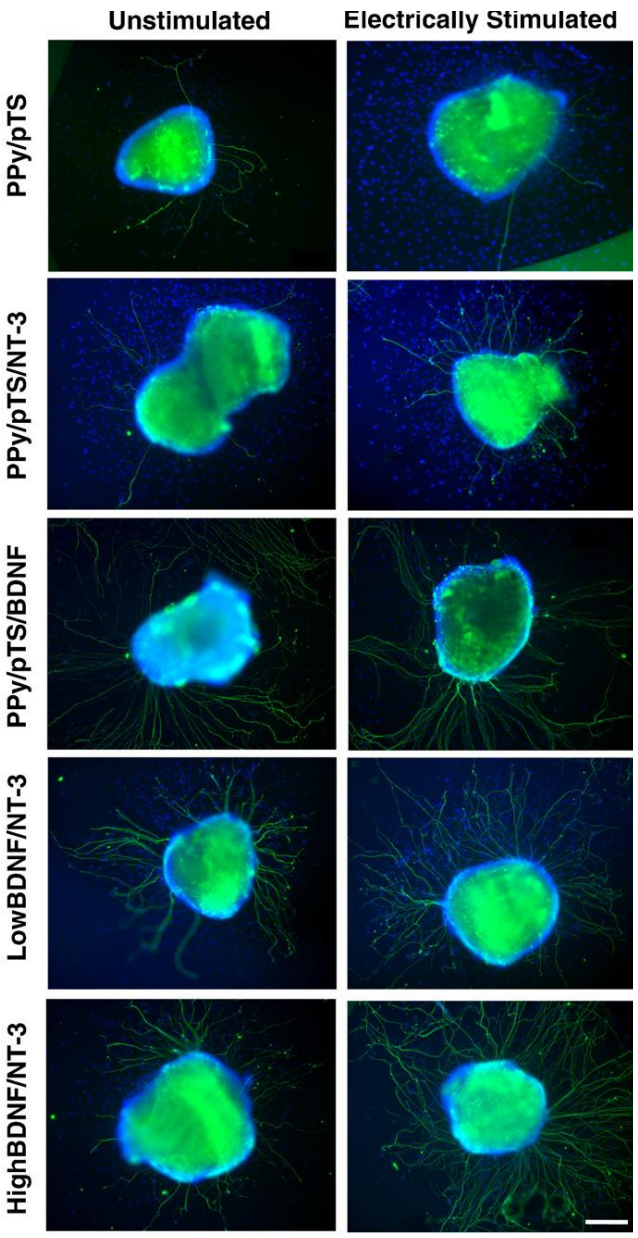

Figure 1-8: Representative images of cochlear neural explants grown on PPy/pTS polymers with and without neurotrophin. Neurites were visualised by immunocytochemistry with a neurofilament-200 primary antibody and a fluorescent secondary antibody (green). Cell nuclei are labelled with DAPI (blue) [27].

The incorporation of two growth factors means the electrode does not saturate the receptors of the cells with high concentrations as each drug has their major binding activity on separate receptors, resulting in greater activation of growth signals within the cells due to the presence of different receptors in the drug. The effect of electrical stimulation alone on the cells is not completely understood, however, there is a synergistic effect between electrical stimulation

and NT delivery as electrical stimulation increases the number of receptors expressed by the cell, thus facilitating a stronger effect from the NT [134-135].

Dexamethasone, which is a drug used to reduce inflammation in the central nervous system, has been incorporated into PPy coating an electrode surface. Using cyclic voltammetry the drug was released and increased neurite formation was observed, as well as reduced reactive astrocytes and microglia (components of cellular response to inflammation) [128].

1.4.2 *Mechanical Stimulation*

Many different methods, such as compressive loading, longitudinal stretching, substrate bending, substrate distension and fluid shear, have been used for mechano-stimulation of cells [136]. A key advantage of using PPy for mechanical stimulation is the ability to perform the stimulation in vitro or in vivo without the need for external hardware or physical manipulation of the material itself. It is the movement of ions in and out of the polymer that induces mechanical actuation, as described earlier with Eq. 1 and 2 (1.2.3.5, pg.1-15). During reduction of the polymer, the ejection of anions causes contraction, while oxidation causes uptake of cations and expansion of the polymer.

Mechanical actuation can be favourable for cellular stimulation of bone and vascular cells that rely upon physical stimulation for development and maintenance of their corresponding tissues. Bone marrow cells are observed to differentiate when stimulated with mechanical stress [137-138]. Vascular cells also respond to mechanical stimulation, particularly stimulation that mimics pulse and shear fluid mechanics [139]. Renal epithelial cells responded with an intracellular Ca2+ response to mechanical stimuli delivered on a microactuator chip made with PPy [140].

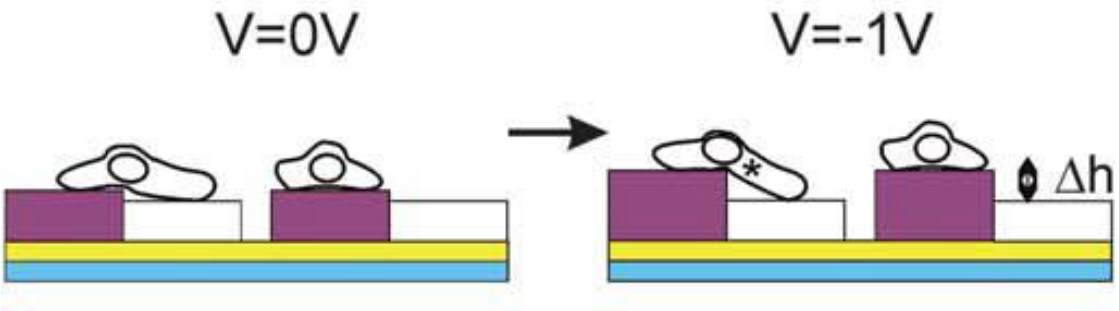

Figure 1-9: Schematic illustration of the principle of *in vitro* mechanical stimulation using PPy actuators. Upon the application of a potential the PPy lines expand vertically Δh and mechanically stimulate the cells that lie on the borders (marked with *) [140].

A microactuator chip, illustrated in Figure 1-9, delivered direct mechanical stimulation of live cells spanning a PPy electrode and a non-actuating surface. The shear stress induced on the cells with mechanical actuation may be a source for the enhanced differentiation. The mechanical stretching of cells can induce the release of adenosine-5'-triphophate within cells, which in turn causes the increased signal of Ca2+ [140].

1.4.3 *Electrical Stimulation for Cell Control*

Electrical stimulation has been shown to enhance the growth of excitable cells such as skeletal muscle and neural cells [24-25, 28, 31, 102, 131]. Using PPy to inject charge into live cells and tissues has been demonstrated in several studies. PC-12 neurite outgrowth was almost doubled when cells were electrically stimulated via PPy/PSS films using a constant potential of 100 mV for 2 h compared to the non-stimulated control films (Figure 1-10).

It was also noted that the PC-12 cells showed no directional bias of neurite outgrowth towards either electrode (Figure 1-10), indicating that the electrical stimulation enhances overall

neurite extension rather than controlling the direction of the extending neurite via electrophoretic redistribution of the cell membrane [28].

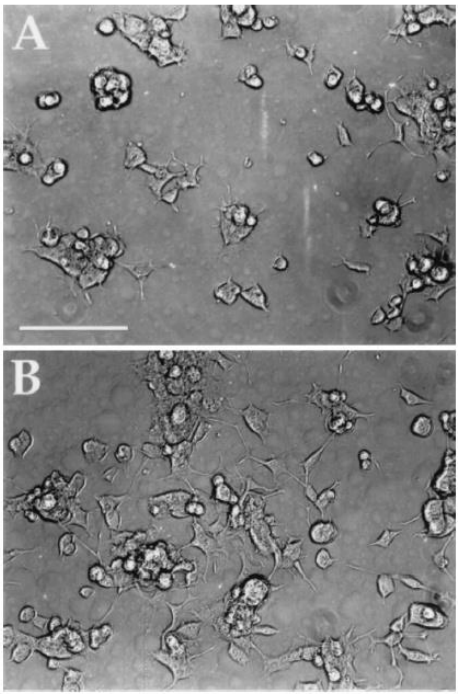

Figure 1-10: PC-12 cell differentiation on PPy/PSS without (A) and with (B) electrical stimulation. The cells were grown for 24 h prior to electrical stimulation [28].

Electrical stimulation of PC-12 cells on a PPy/PMAS composite using biphasic current pulses showed greater neurite lengths than unstimulated neurons [31]. Changes in the frequency of stimulation were shown to affect the neurite extension; 100 and 250 Hz enhanced the neurite extension, while a lower frequency of 10 Hz had no effect. PC-12 neural cells have been electrically stimulated on PPy functionalized with nerve growth factor (NGF). Greater neurite extension was observed when cells were electrically stimulated in the presence of immobilized NGF. The combination of NGF and electrical stimulation together has also been demonstrated to have a greater effect on neurite extension when compared to their

individual effects [33]. Using constant current stimulation (10 μA for 2 hours), neurite length of PC-12 cells was observed to significantly increase on PPy/PSS films. The amount of FN adsorbed onto the polymer has also been measured in conjunction with the electrical stimulation. Initial stimulation, prior to cell seeding, resulted in greater FN adsorption that corresponded with longer neurite outgrowth [25]. The adsorption of proteins such as FN from serum, or added separately, may be an important aspect of enhancing cellular response of neurites on these electrode surfaces.

Smooth muscle cells have been shown to have enhanced cellular proliferation when electrically stimulated [127]. A sinusoidal electrical signal was applied with an amplitude of 50 μA at different frequencies to a PPy/HA biomaterial coated with Matrigel® and Collagen IV. A frequency of 5 Hz was found to cause the greatest increase in cellular proliferation compared to no stimulation, 0.05 Hz and 500 Hz. The frequency of 0.05 Hz was found to be extremely detrimental to the smooth muscle cells, with less than 4% (compared to control) cells remaining after 96 hours. A possible explanation given was that the significant differences of charge for relatively long intervals (~20s) may have destroyed the coating on the polymer. The coating was comprised of a heterogeneous mix of matrix proteins, collagen, proteoglycans and growth factors; this is an indication that the surface charge of the polymer was detrimental to either the adhesion, conformation, or bioactivity of these molecules.

A difference in the oxidation state of the polymer has been used by Lundin et al. [141] to control the growth of endothelial cells. Electrical stimulation was delivered as a linear ramp of 0.02 V/sec followed by a constant potential of -0.9 V for 120 sec to stimulate foetal neural stem cells on PPy substrates with varying dopant. PPy/DBS showed a significant reduction in cell density on polymer substrates in their reduced state compared to pristine [141].

Mammalian cells have displayed behaviour dependent on the oxidation state of PPy whereby reducing the polymer led to the prevention of cell spreading and caused the cells to 'round up' [107]. In contrast, the oxidized PPy supported cell adhesion and was partially attributed to the effect of the oxidation state of PPy on the adsorption of proteins [142]. It is implicit from many of the above studies that the effect of electrical stimulation, or switching of the polymer's redox surface properties, on protein interactions is an important aspect in controlling cell adhesion and growth. This is discussed in further detail in the next section.

1.4.4 *Protein Interaction on Electroactive Surfaces*

There have recently been studies specifically addressing the effect of the oxidative state of the polymer on protein adhesion and conformation, in addition to correlating these findings with cell studies. It has been shown that proteins present in serum, or specifically added, that adsorb onto the polymer can be affected by the redox surface properties of the substrate [25]. Electrical stimulation of PEDOT:PSS films prior to cell seeding has shown that the oxidation of the polymer will affect cellular interaction [143]. Reduction of the polymer promoted cellular adhesion and proliferation (Figure 1-11A left), however oxidation of PEDOT:PSS resulted in cell detachment and death of epithelial MDCK cells (Figure 1-11A right). However, no change in cell adhesion was observed when the polymer was stimulated 24h after cells had been on the surface, indicating that once cell adhesion is established switching the redox state does not affect the cell viability. It was proposed that on the oxidized polymer (Figure 1-11A right) the FN is in an unfavourable conformation that inhibits access to the RGD binding sites by the cells. On the reduced electrode (Figure 1-11A left), the FN presents the RGD sequence for binding to cell integrins. The latter is required for the formation of actin stress fibres and macromolecular focal adhesion complexes (vinculin and

talin). This subsequently promotes the proliferation of the cell in contrast to the oxidised surface.

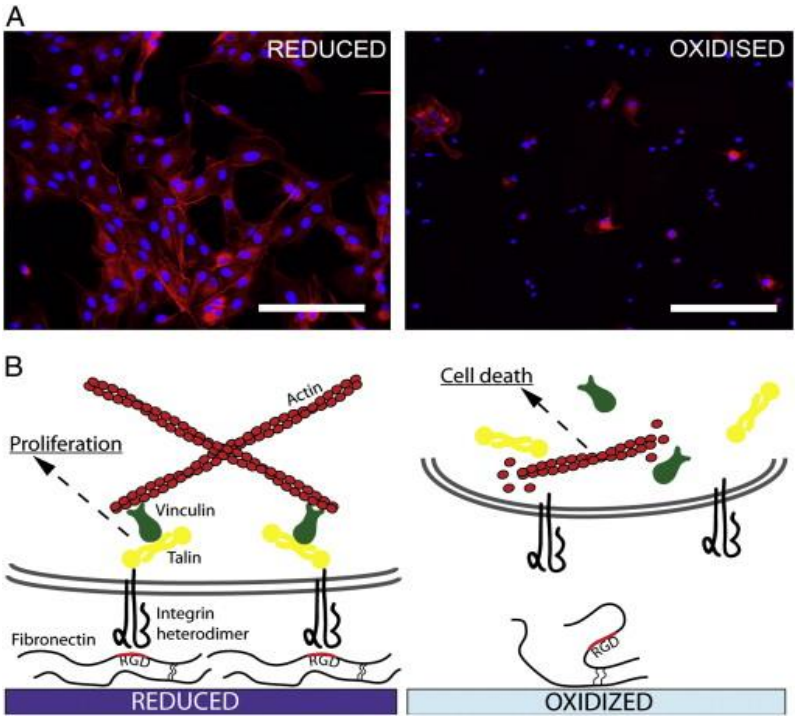

Figure 1-11: Schematic of a proposed mechanism for cell interaction with the reduced and oxidised PEDOT:PSS surfaces [143].

A potential gradient along the polymer and its relationship to protein (FN) adsorption has been used to investigate the influence of polymer oxidation on cell behaviour [144]. 3T3-L1 fibroblast-adipose cells were deposited on a PEDOT:tosylate polymer that had a potential bias of -1V to +1V applied across it before seeding the cells. A stained micrograph shows the cells distributed across the oppositely biased polymer, having a distinct cell gradient that shows the cells prefer the oxidised side of the film (Figure 1-12).

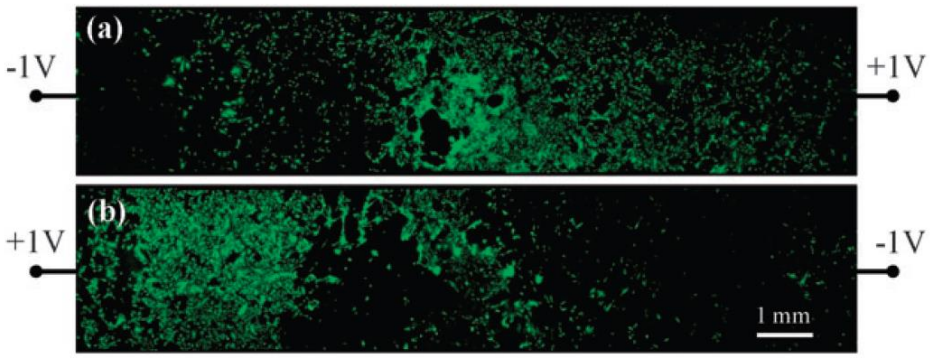

Figure 1-12: Fluorescence micrographs of calcein-green stained 3T3-L1 cells for two devices biased in opposite directions [144].

The amount of adsorbed FN from the growth medium serum was quantified on areas of different oxidation state across the polymer using an immunostaining assay. It was found that more FN was adsorbed on the reduced polymer and less FN adsorbed on the polymer compared to a control with no potential bias. This gradient of FN has been served in a separate study across a potential-biased strip using the same experimental set-up and immunostaining assay to quantify the density of FN [145].

The same effect was observed by Saltó et al. [146] with neural stem cells on a PEDOT:tosylate electrode. A labelled human serum albumin (HSA) was deposited on the polymer with different potentials (0 and ±1.5 V) and then stained to quantify adsorption. Higher protein concentration was observed on the reduced polymer compared to oxidised, however the stem cells showed a 2-fold increase in adhesion on the oxidised polymer. A proposed mechanism for this involves the conformation of the protein when it binds to the surface (Figure 1-13).

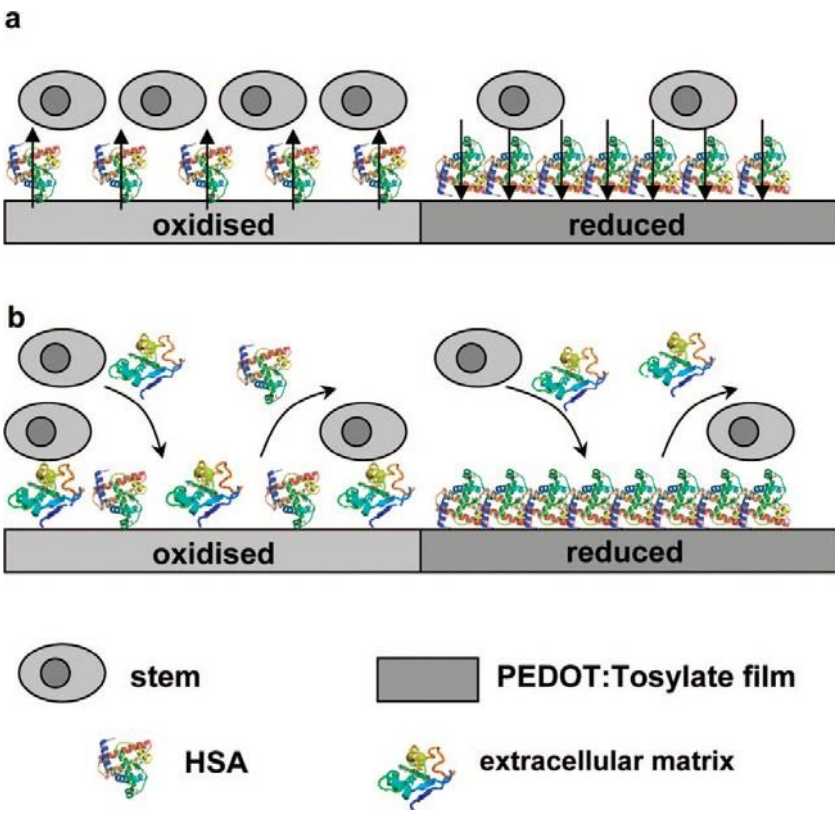

Figure 1-13: Proposed mechanisms for the difference in adhesion and density of stem cells achieved between the reduced and oxidized PEDOT:Tosylate electrode surfaces. (A) On the oxidized PEDOT surface, a less dense layer of HSA proteins is formed; however the proteins are oriented in a favourable direction that promotes good stem cell adhesion. (B) Stem cells that are approaching a potential surface launch ECM proteins to aid adhesion. A dense HSA layer prevents the formation of an optimal ECM on the surface. Adapted from [146].

Figure 1-13A illustrates that on an oxidised surface the conformation of the protein may be more conducive to cellular adhesion for the stem cells. On the reduced film the adhesion of ECM proteins produced by the stem cells are effectively 'blocked' by the dense HSA layer (Figure 1-13B). As these ECM proteins mediate cellular adhesion the adhesion of the stem cells to the surface is suppressed [146].

A study using quartz crystal microbalance (QCM) to observe changes in the conformation of bovine serum albumin (BSA) and FN showed a dependency on the oxidation state of PPy/DS films [61]. Electrical stimulation of the polymer showed that an oxidising potential resulted in greater mass of the proteins adhering to the polymer, and that the proteins became less viscoelastic, a property which is correlated with change in protein conformation from elongated to compact.

There is clearly a correlation between electrical stimulation and the behaviour of proteins such as FN on electrode surfaces. These previous studies [61, 143, 146] highlight the fact that electrical stimulation can result in opposite cellular responses (oxidised and reduced surfaces promoting/suppressing cell adhesion under different conditions). The effect is dependent on the cell type, conductive polymer, and dopants. The studies also call attention to the change in the protein conformation, an effect which can control how the protein interacts with cell. How this occurs and why there is a change of the protein interactions needs to be studied directly to determine the impact these changes have on living cells and in turn how we can control this effect to our advantage.

1.4.4.1 Implication of Fibronectin – OCP Interaction on Cell Function

FN is an important component of the ECM and responsible for many biological functions, including cell attachment, cell spreading, matrix assembly and wound healing [97, 147-148]. FN is a dimeric glycoprotein, approximately 500 kDa, which contains two subunits connected with a disulfide bridge and is comprised of three types of modules (FNI, FNII and FNIII) with N-terminals on each end (Figure 1-14). FN contains binding sites for heparin, collagen, integrins, and fibrins along both subunits [97]. The protein is often used as a

prototypical cell adhesion protein for cell-surface interactions due to its involvement in initial cell-surface interactions.

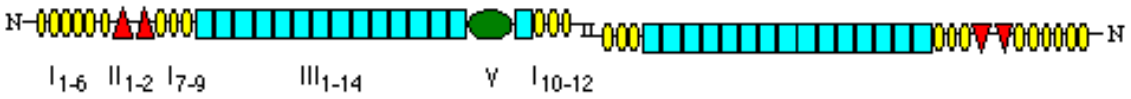

Binding site	Ligand
I_{1-5}	Fibrin
I_6-I_8	Collagens
III_{9-10}	Integrins
III_{12-14}	HSPG
III_{14}-V	Integrins

Figure 1-14: Schematic illustration of fibronectin. The modules are marked as I (yellow oval), II (red triangle) and III (teal square). Important binding regions for biomolecules are labelled [111].

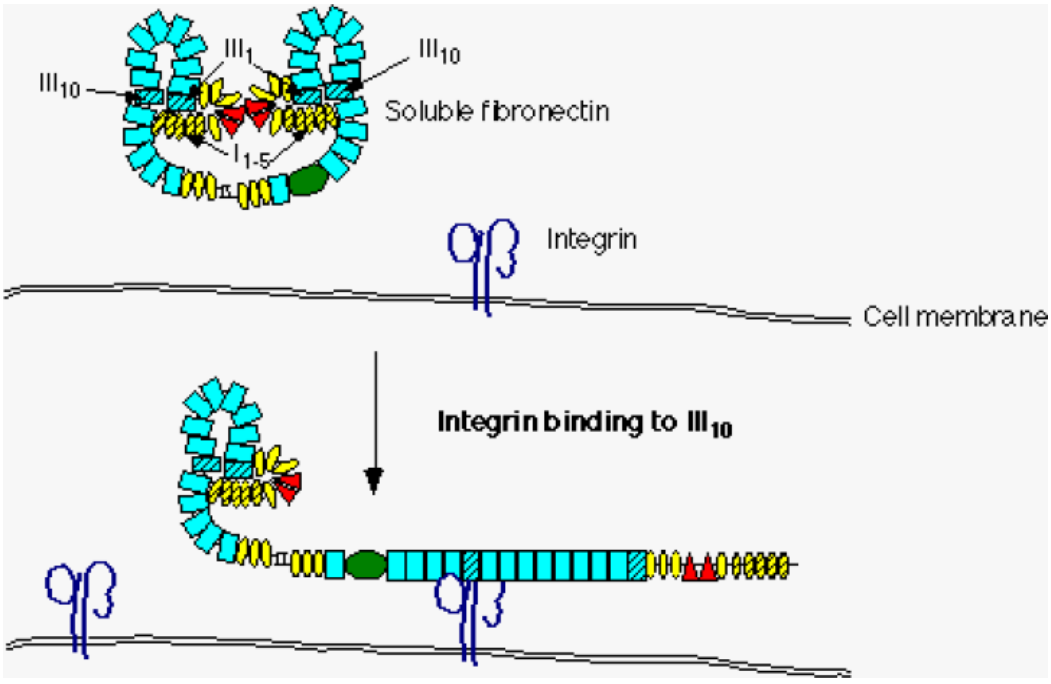

Figure 1-15: Proposed binding between FN and an integrin at the RDG region [111].

FN binds to the receptor proteins called integrins on the cell membrane surface, as well as collagen, fibrin and heparin [111]. The primary integrin receptor for FN is α5β1, with the proposed binding scheme illustrated in Figure 1-15. The RGD motif within FN, labelled in Figure 1-14, is a cell adhesion region and is the most important recognition site for half of all known integrins. This RGD region on FN is critical for mediating cell interaction such as adhesion (Figure 1-15).

When FN has mechanical force applied, cryptic sites within the FN structure are exposed [148]. It is these sites which begin the fibrillogensis process. In the fibrillogensis process the FN initially binds to the α5ß1 integrins (gold) on the cell surface membrane (Figure 1-16A). Reorganisation of the actin cytoskeleton (green) within the cell occurs and activates intracellular signalling (silver circles). Cell contractility changes the conformation of the FN, exposing the cryptic sites within the elongated protein (Figure 1-16B). Fibrils begin to form surrounding the cell membrane through FN-FN interactions (Figure 1-16C). The revealing of these cryptic sites can be forced using AFM force spectroscopy. These studies have shown how the protein intermediates are folded and provide a structural model on how cells can use mechanical forces to expose these sites [147].

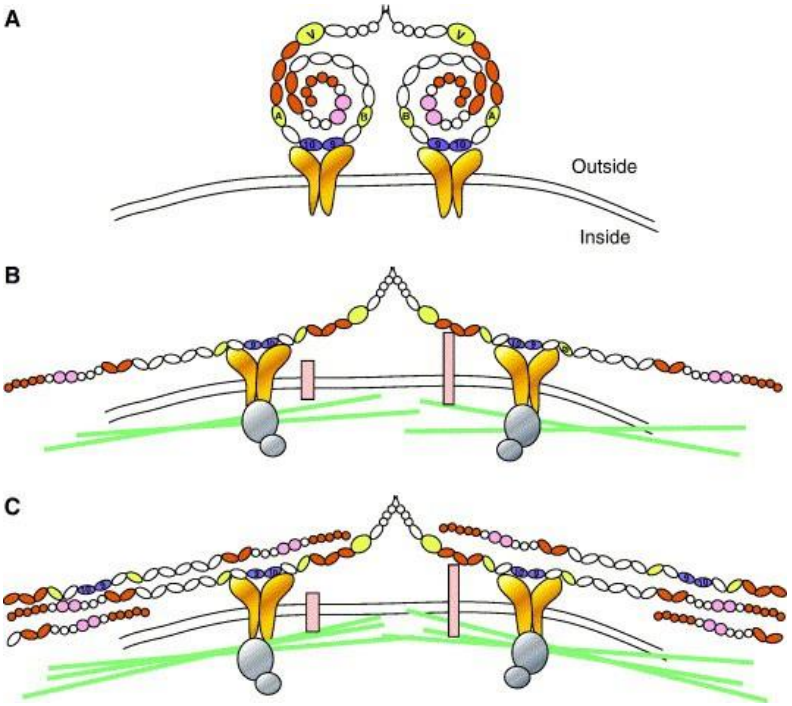

Figure 1-16: Major steps of FN fibril assembly. (A) Compact soluble FN binds to integrin α5β1 (gold) via its cell binding domain. (B) FN binding to integrins and other receptors (pink bars) induces reorganization of the actin cytoskeleton (green lines) and activates intracellular signaling complexes (silver circles). (C) Fibrils form through FN– FN interactions [148].

Integrin mediated adhesions, such as FN-RGD, between the cell and surface are intrinsically mechanosensitive [149]. As focal adhesions form and induce tensile strain across the cell, integrin signalling is triggered which in turn transmits mechanical signals to the cytoskeleton. This signalling is an important process for cell migration across a surface [150].

The binding of FN to integrins is generally governed by the conformation of the protein. FN has two distinct conformations, extended and compact (Figure 1-17). The compact form is due to electrostatic attraction between FNIII2-3 on one subunit arm and the FNIII12-14 domains on the other [151]. These conformations can be interchanged through surface properties [152].

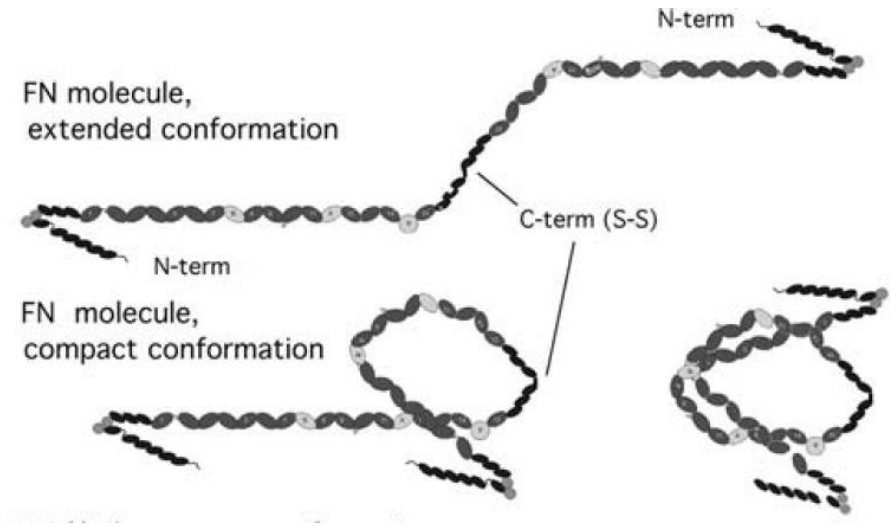

Figure 1-17: Schematic of the extended and compact conformation of FN, and the full folded conformation on the right [151].

On hydrophobic substrates, FN is typically in the compact conformation, in contrast, to extended form observed on hydrophilic substrates [97, 153-154]. The transition from the compact to extended form is most likely due to the electrostatic interactions with the surface that disrupt the stabilizing intramolecular bonds and cause unfolding of the protein. The density of FN molecules present on the surface will also influence the protein packing and hence conformation; FN adsorbed to form a monolayer will pack more tightly in an upright conformation. At low densities, the adsorption behaviour is related to single isolated proteins [153, 155]. It is believed that the bioactivity of FN is greater in the extended form due to exposure of the RGD region, as confirmed from cell studies that control the FN conformation [98, 100]. Even when FN adsorption (density) is significantly reduced on hydrophilic surfaces, the presence of the bioactive conformation of the protein (i.e. exposure RGD region) leads to a better cellular response [97, 100, 154].

1.5 Overarching Aims

At present, the underlying mechanisms of controlling cellular interactions on OCP using electrical stimulation is not well understood; though recent studies are revealing that the role of mediating ECM proteins such as fibronectin is critical. The effect of the physical and chemical properties of OCPs on ECM protein has not been well characterized beyond the bulk physical properties and interactions. In particularly, specific interactions between biological dopants, purposely incorporated into the polymer to enhance biospecificity, and ECM protein have yet to be elucidated. Furthermore, changes in the protein dynamics and interactions as function of electrical stimulation have only been recently investigated at the ensemble protein scale but not at the molecular level. Molecular level details will provide great insight and represent a significant leap forward in understanding interactions at the cellular – OCP interface.

At present, the underlying mechanisms of controlling cellular interactions on OCP using electrical stimulation is not well understood; though recent studies are revealing that the role of mediating ECM proteins such as fibronectin is critical. The effect of the physical and chemical properties of OCPs on ECM protein has not been well characterized beyond the bulk physical properties and interactions. In particularly, specific interactions between biological dopants, purposely incorporated into the polymer to enhance biospecificity, and ECM protein have yet to be elucidated. Furthermore, changes in the protein dynamics and interactions as function of electrical stimulation have only been recently investigated at the ensemble protein scale but not at the molecular level. Molecular level details will provide great insight and represent a significant leap forward in understanding interactions at the cellular – OCP interface.

To better understand the interactions of proteins and cells with OCP, the thesis therefore aims to:

- Characterise the nanoscale physical properties of PPy biomaterials with a range of dopants using AFM. The nanoscale physical properties to be characterized include roughness, topography, modulus, and strain and will be correlated cell studies undertaken on the same PPy biomaterials.

- Investigate the nanoscale spatial distribution of surface properties, such as conductivity, surface potential and surface energy, using a range of different AFM techniques. These lateral variations in surface properties will then be correlated with experiments on protein interactions at the OCP surface.

- To directly measure the interaction of single molecule protein interactions with OCP using AFM single molecule force spectroscopy. We aim to investigate the effect of incorporating biological dopants, such as GAGs, that are known to be specific for binding of ECM proteins and the effect of electrical stimulation. Such measurements will represent the first study on directly measuring specific biomolecular interactions with OCP under electrical control.

- To investigate the effect of nanoscale lateral variations in surface properties on the protein interactions using AFM Force Mapping. The latter will enable the use of functionalized probes to “map” the protein interactions (e.g. adhesion) across the surface whilst simultaneously recording the topography with nanometre resolution.

- To investigate the effect of optically stimulating an OCP incorporating light sensitive molecules (spiropyran) on surface topography and energy. AFM force spectroscopy will be used to directly measure the strength of protein adhesion as function of light switching.

2 Atomic Force Microscopy Methodology

Scanning Tunnelling Microscopy (STM) was a technique developed in the 1980's by Binning and Rohrer who received the 1986 Nobel Prize in Physics for their later work on the invention of Atomic Force Microscopy (AFM) [156]. STM uses quantum tunnelling to measure the density of states of a conductive surface. The tunnelling current between a surface and conductive tip is quantified as a function of tip position and voltage. STM has a much higher resolution (0.1nm lateral resolution and capable of atomic resolution) than optical techniques as it is not limited by an optical diffraction limit. However, one major limitation of SPM is that the surface must be conductive. Atomic force microscopy (AFM) was developed as a method for very precise, atomic scale surface imaging for both conductive and insulating surfaces [157]. AFM is a versatile tool that is capable of high resolution topographical imaging, mechanical property analysis, and measuring surface forces and interactions down to a nanometric scale.

Table 2-1: Comparison of AFM and other microscopy techniques

	Lateral Resolution	**Imaging Environment**	**Sample Requirements**
Optical	0.2 μm	Air, fluid	Dark or strongly diffracting objects best
Scanning EM	<1 nm - 20 nm (best 0.4 nm)	Vacuum	Conductive, or conductive coating, dry, fixed
Transmission EM	~0.2 nm (best 0.05 nm)	Vacuum	Thin (~100 nm), lengthy Sample Preparation
STM	0.1 nm	Vacuum, gas, liquid	Conductive, relatively flat, no loose particles
AFM	<1 nm	Vacuum, gas, liquid	Relatively flat (<20μm), no loose particles

Table 2-1 lists a comparison of the major imaging techniques with AFM. The resolution of AFM (typically 1-2 nm lateral resolution for most commercial systems) approaches the limit of EM systems and STM, surpassing optical microscopy, with the limitations of resolution dependent on the mechanical components of the system. The technique can be applied in a range of media, such as air, fluid or a gas atmosphere, compared to vacuum based systems. Samples prepared for AFM have simple preparation and fewer limitations. Unlike EM techniques, imaging can be conducted in fluid to enable biological samples (even living cells) to be imaged in near physiological conditions. A disadvantage of AFM is the limited imaging area, as most AFM systems have a maximum scanning distance of 90-150 μm in the x or y axis. The samples also cannot be overly high, as the vertical limit of the Z-scanner is typically 10-20 μm for most AFMs. Compared to optical and EM techniques, AFM imaging is slower due to raster scanning of the AFM tip. However, high-speed imaging AFMs reaching almost video- rate imaging capabilities have recently been developed and represent the systems of the future.

2.1 AFM Design and Operation

A typical AFM set-up is illustrated in Figure 2-1A. The AFM is comprised of five main elements; the piezoelectric scanner, the cantilever, the photo diode, the controller and a feedback loop. The AFM begins a scan by bringing a tip mounted on a cantilever into contact with the surface. The tip is raster scanned across the surface in the X and Y direction using a piezoelectric scanner (depending on AFM system either the cantilever or the sample may be moved).

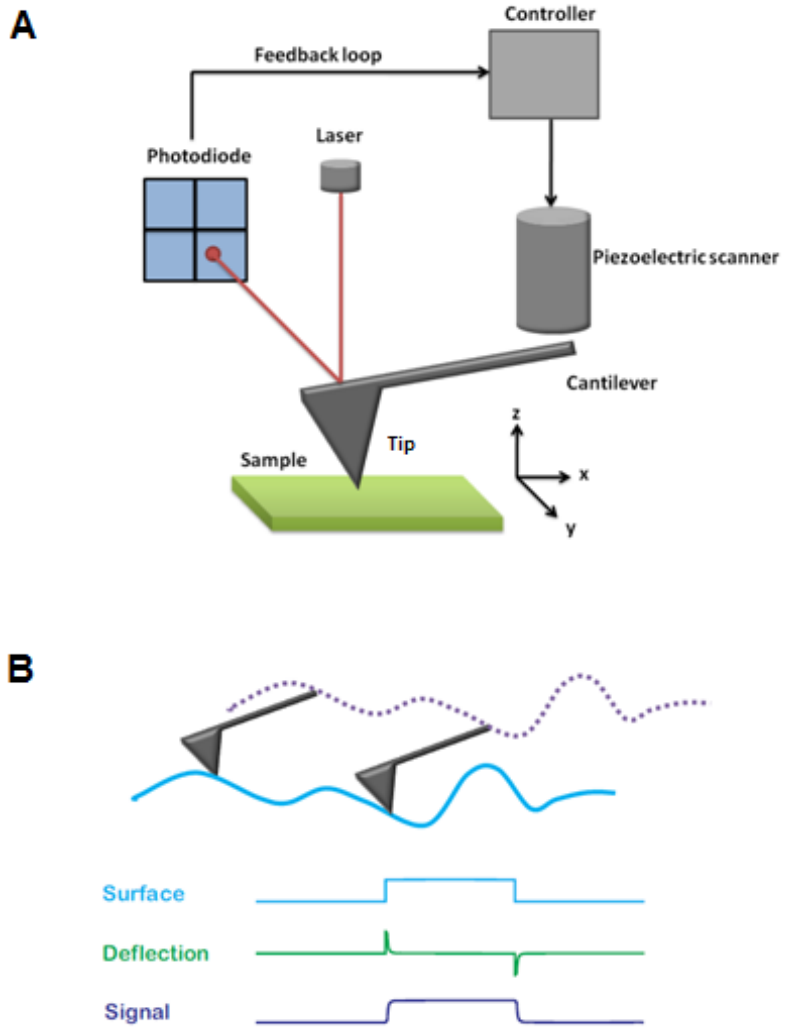

Figure 2-1: (A) AFM schematic of the major components; (B) contact mode signals, surface (blue), deflection (green) and Z piezo (purple).

The scan rate is measured as the frequency of the tip as it travels through one complete raster of a single scan line (i.e. scan rate of 1 Hz moves the tip back and forth along one scan line in 1 sec). As the tip is scanned across the surface, topographical causes deflection of the cantilever. The cantilever deflection is detected by a laser beam that is reflected off the end of the cantilever (where the tip is located) and into a photodiode. The photodiode generally has four quadrants that measures changes in the position of the laser and thus corresponding changes in the cantilever deflection. These changes in the laser position, or effective cantilever deflection, are recorded as a voltage by the photodiode.

The feedback loop monitors the deflection of the cantilever in order to control the Z- position of the tip relative to the sample surface. In contact mode imaging, the feedback loop keeps the cantilever deflection constant at a setpoint defined by the operator by adjusting the height of Z- scanner. Figure 2-1B illustrates the cantilever deflection signal (green), as the tip scans across a height change on the surface (blue). Changes in the height of the Z-piezo scanner to keep the cantilever constant (at the setpoint) correspond to height of topographic features (purple). By combining the X, Y, and Z data, a 3-D topographic image can then be collected. Small errors in the feedback can occur at the edges of surface features and cause an over- or undershoot of the setpoint. These are observed as small changes in the deflection signal (spikes in green signal) and delineate the edges of features in commonly acquired deflection or error signal images.

The two main parameters that control the tip interaction during scanning are the setpoint and gains control. The applied force between the tip and sample is controlled by the setpoint. For example, a higher the set-point voltage that results in greater cantilever deflection will increase the applied force acting on the sample. The gains control, particularly the integral

gains, is used to modulate the speed of the feedback loop. If the gains are set too high, the feedback becomes unstable and introduces noise into the image. However, very low gains results in a poorly responsive feedback, i.e. the change in the Z-piezo height cannot adjust in response to the topographic features, a greater error signal and poor tracking of the sample.

2.2 Scanning Modes

2.2.1 AC Mode

To avoid potential damage to the sample in contact mode imaging due to lateral forces, AC mode, also known as tapping or intermittent contact mode, is commonly implemented. AC mode uses an oscillatory signal to drive the cantilever at a set frequency (close to the cantilever's resonant frequency) using a piezoelectric crystal. The tip is oscillated at a free amplitude that is greater than the nominal tip-surface distance, so that when the tip comes into contact with the sample surface the amplitude is dampened (Figure 2-2).

To obtain an image in AC mode, the feedback maintains a constant amplitude (setpoint amplitude) of the AC cantilever deflection signal of the cantilever, as the tip is scanned acorss a height change on the surface (blue in Figure 2-2) The amplitude setpoint is typically set at 80% of the free amplitude. Similarly to contact mode, changes in height of the Z-piezo scanner that are required to maintain the setpoint amplitude correspond to the height of the topographic features (dark blue).

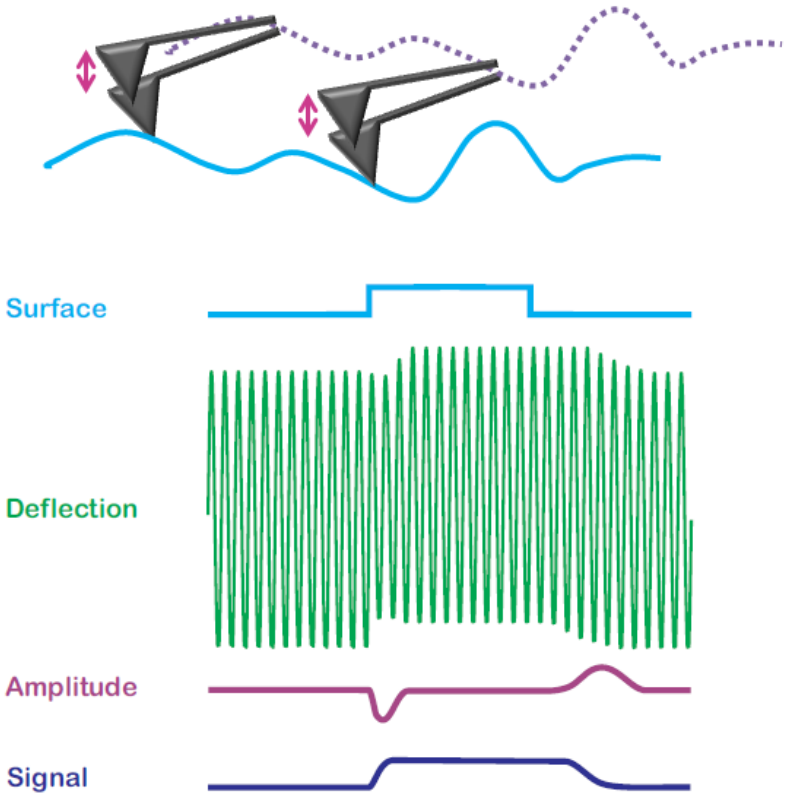

Figure 2-2: AC mode schematic, sample surface (blue), deflection signal (green), amplitude signal (maroon) and Z piezo signal (purple). Asylum research MFP-3D AFM Manual 04-08 and [160]

The setpoint amplitude of the AC deflection signal can be adjusted so to control the 'tapping force' of the tip on the sample. AC mode is preferred for delicate samples as the probe lateral forces are much lower and therefore can be used in fluid to great effect for imaging soft samples such as biological specimens or gels. Low spring constants are useful for soft or delicate samples, as they greatly reduce the amount of applied force on the sample. Conversely, high spring constant cantilevers are more suited to imaging air to overcome the strong attractive forces (i.e. meniscus forces) between the tip and sample.

2.2.2 *Cantilever Properties*

The imaging tool of the AFM is the tip located at the end of the cantilever (Figure 2-3). Cantilevers generally have either a 'diving board' or triangular design (Figure 2-4) and are designed with various dimensions, namely variations in length and width. The tip is typically pyramidal in shape coming to a sharp apex of ≈ 5-20 nm in diameter for high resolution imaging (Figure 2-5). Tips can be produced with various aspect ratios (high resolution tips can have ratios of 12:1) and tip shapes (rotated polygon, 3 and 4-sided pyramids, rounded tip, plateau tip).

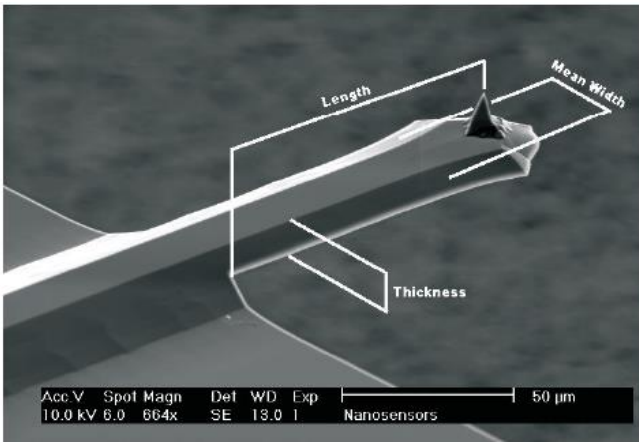

Figure 2-3: SEM image of a tip and cantilever (Nanosensors TM, Neuchátel Switzerland)

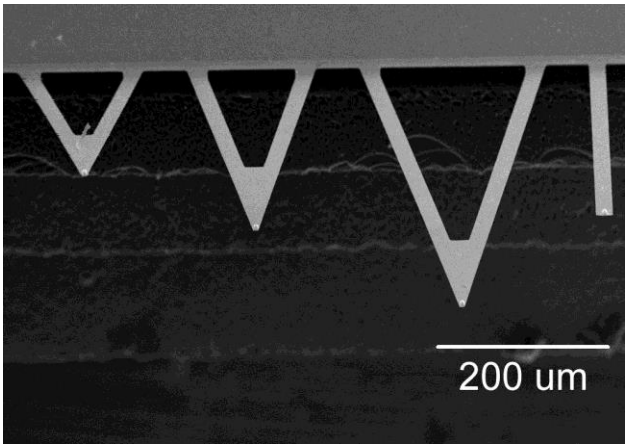

Figure 2-4: SEM image of four AFM cantilevers with both triangular and diving board geometries on the same chip

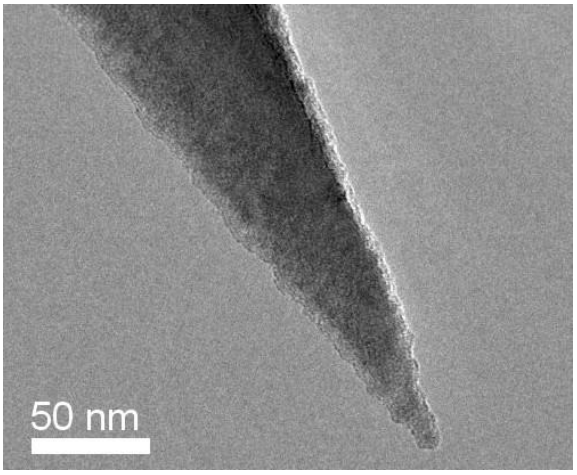

Figure 2-5: TEM image of a PointProbe® Plus tip (Nanosensors TM, Neuchátel Switzerland)

The cantilever can be made of various materials, commonly silicon nitride, but also silicon or silicon oxide. The cantilever and tip are generally produced through batch chemical etching of silicon nitride wafers. The tips can be altered post-production to produce specialized tips, such as depositing high density carbon for extremely hard tips, or attaching carbon nanotubes for very high aspect ratios tips. The tip may be coated with gold, platinum or platinum/iridium for AFM applications that require a conductive tip. Most cantilevers also have coatings on the backside to enhance laser signal reflectivity, usually a chromium or aluminium alloy.

The spring constant and resonant frequency of a cantilever are important parameters for AFM measurements. Cantilevers are made with spring constants ranging from very soft cantilevers (0.06 N/m) to very stiff (40 N/m). Stiffer cantilevers may cause damage to softer samples through sheer and indentation forces, while a soft cantilever is more suited to operation in fluids for high sensitivity measurements.

The cantilever is essentially a beam with a fixed end, which makes calculation of the spring constant reasonably simple using geometric models. The spring constant of a cantilever, as an end-loaded thin beam, is given as;

$$k = \frac{Et^3w}{4L^3} \qquad (1)$$

where *E* is the Young's modulus of the cantilever. The spring constant is dependent on the geometry of the cantilever (width *w*, length *L* and thickness *t*,

Figure 2-3), and has a strong inverse relationship with the cantilever length. The resonant frequency (ω) of the cantilever has a simple relationship with the spring constant as

$$\omega = \sqrt{\frac{k}{m}} \qquad (2)$$

where m is the mass of the cantilever. Cantilevers with a higher resonant frequency are preferable as they allow faster scanning rates due to the increased response time of the cantilever. Both spring constant and resonant frequency are chosen depending on the AFM mode used, which is discussed below.

2.2.3 *Topographical Imaging*

To produce a topographical image of a sample the Z-piezo signal is converted from volts to metres using the calibrated piezo sensitivity. Changes in the Z-piezo height during scanning are then plotted relative to the X Y position of the tip to produce true 3-dimensional

topographic image. Figure 2-6 shows a topographical height image of a polypyrrole film sample across a 500 x 500 nm area.

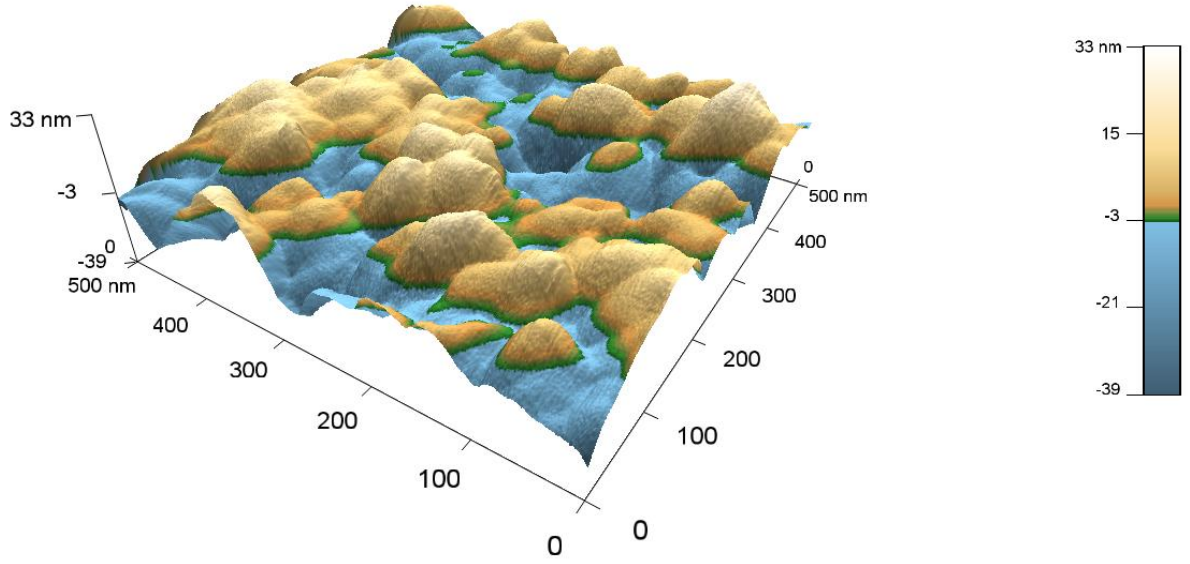

Figure 2-6: Contact mode image of polypyrrole in air, 1 Hz scan rate, 0.8 V set-point

An advantage of AFM topographical images is that they contain quantitative information on surface properties such as the roughness and surface area. Roughness values are generally calculated as an RMS (root-mean-square average) value, which is the function of height deviation from the mean surface level within a scan. This can be represented as;

$$RMS = \left[\frac{1}{N}\sum_{i=1}^{N} Z_i^2\right]^{\frac{1}{2}} \qquad (3)$$

where N is the number of data points and Zi is the distance from the mean surface level [62]. For example, the polymer surface in Figure 2-6 has an RMS roughness of 8.9 nm and a surface area of 0.294 µm2 (compared to the scan area of 0.25 µm2, an increase of 17.8%).

2.3 Phase Imaging

During AC mode imaging, it is possible to simultaneously acquire a height image and phase image that is related to changes in the materials properties across a sample such as adhesion or Young's Modulus [159-161]. The phase of the cantilever oscillation will generally shift (or lag) due to energy dissipation resulting from tip-sample interactions. More specifically, the phase signal represents the phase shift between the AC voltage applied to the cantilever (used to drive the cantilever oscillation) and outputted AC deflection (oscillatory) signal of the cantilever deflection, which is collected in the photodiode. Figure 2-7 is a schematic of an oscillating cantilever as it scans across a theoretical sample with two different materials, A and B.

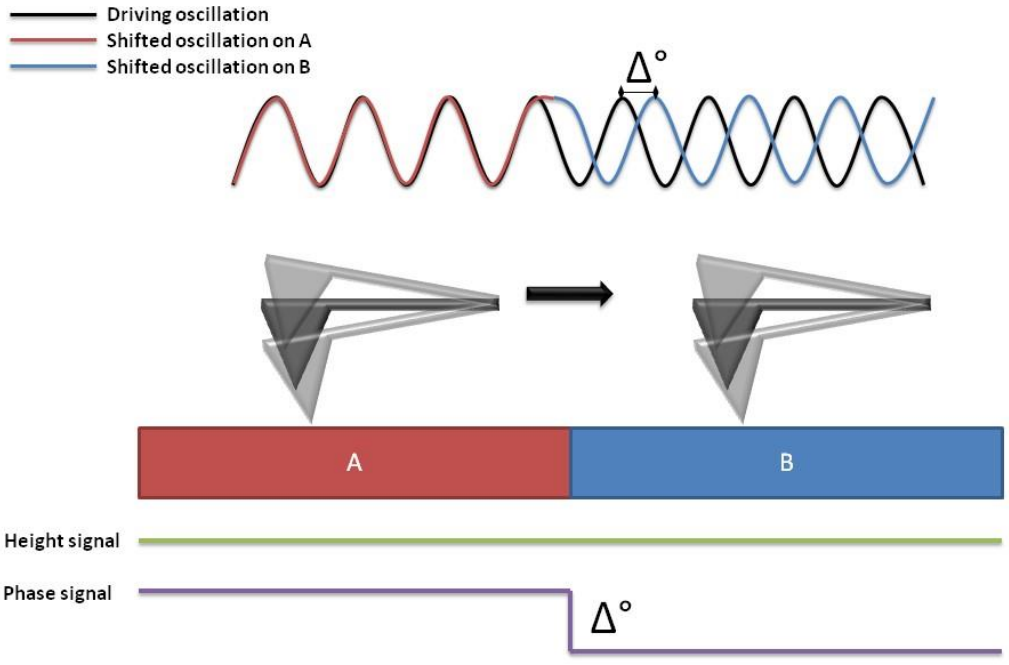

Figure 2-7: Schematic of a tip scanning across a surface with two areas of different energy dissipation. Height signal (green) shows no change while the phase signal (purple) changes with a difference of Δ°, corresponding to the change in the oscillatory signal.

The phase signal as the tip scans over Material A is not shifted relative to the cantilever deflection, while on Material B the signal is shifted 90°, indicating the latter contains different material properties. Even though the height of the sample does not change (Figure 2-7 green line), the phase imaging is sensitive to the two different regions.

The energy dissipation related to the phase signal of the cantilever can be described by a simple harmonic oscillation. In this case, the cantilever with a stiffness, k0, is freely oscillating with a frequency of ω0 and free amplitude of A0 when it is far above the surface. At the cantilever resonance (with no interaction with the surface), the phase is at 90°. When the cantilever is brought into contact with the surface, the cantilever oscillation is dampened to amplitude A.

This is described mathematically in Equation (2) [162];

$$P = \frac{k_0 A^2 \omega_0}{2Q_0}\left(\frac{A_0}{A}\sin\Phi - 1\right) \qquad (2)$$

where P is the tip-sample power dissipation and Q0 is the quality factor of the cantilever. It is important to note that there are two solutions to this equation, which are illustrated in Figure 2-8 (dashed line). When the phase shifts above 90°, the tip is operating in the attractive regime, where the tip is attracted towards the surface. When the phase shifts below 90°, the tip is operating in the repulsive regime and the tip experiences repulsive interactions at the surface.

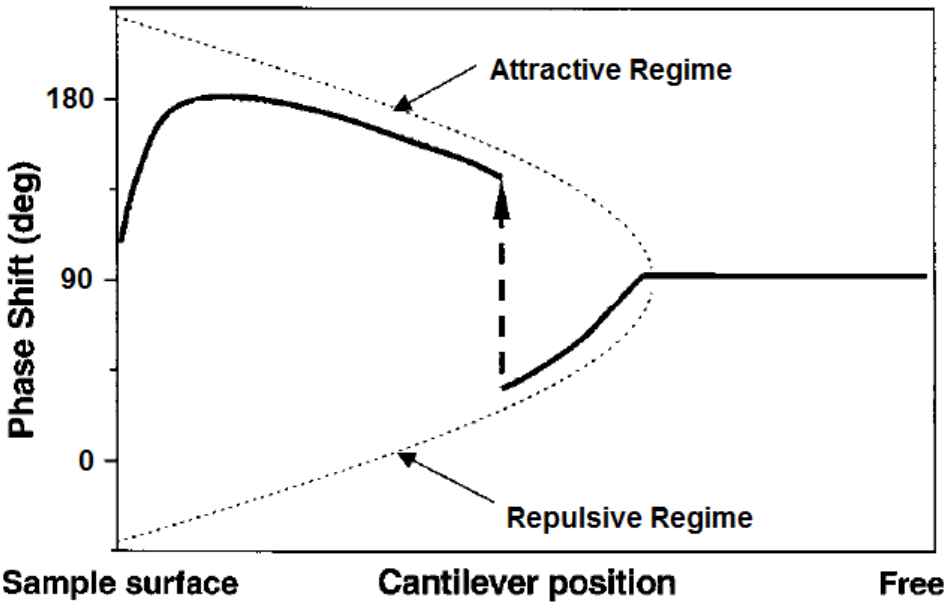

Figure 2-8: Schematic of two possible solutions to Equation (1) and the resulting phase lag signal. The dotted line represents the solutions and the solid line represents a theoretical tip approach [163].

More often in experiments, an initial attractive region followed by a 'jump-down' into a repulsive region is observed (solid line), particularly if sufficiently higher free amplitudes (A0) and lower set-points (A) are used. This jump from attractive to repulsive regions is termed bistability (arrow with dashed line) and may result in phase artefacts if the tip uncontrollably moves between the two regions. As long as the phase remains in either the attractive or repulsive regime, any shifts in the phase are directly due to changes in the energy dissipation between tip and sample [162]. Figure 2-9 shows topography and phase images of a poly (sebacic anhydride) (PSA) and poly (DL- lactic acid) (PLA) blend of two different ratios (Figure 2-9A and B 10% PLA/90% PSA, Figure 2-9C and D 40% PLA/60% PSA).

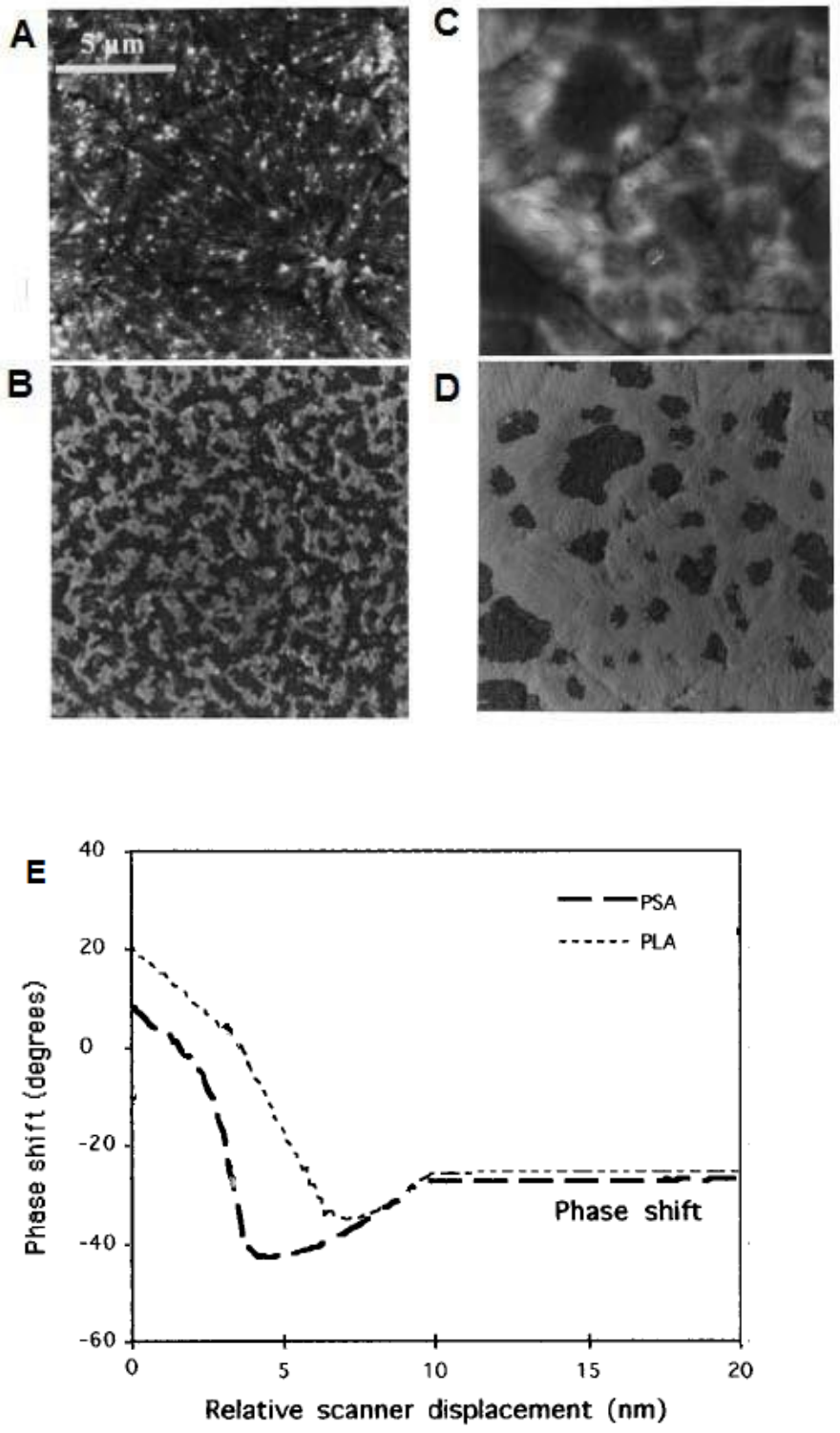

Figure 2-9: (A) Topography and (B) Phase-detection imaging of 10% PSA/90% PLA. Maximum phase shift 45°.(C) Topography and (D) Phase-detection imaging of 40% PSA/60% PLA. Maximum phase shift 52°. (E) Cantilever vibration amplitude and phase shift measured on 60% PS

The sample is a polymer blend of two materials with different physical properties, semi-crystalline PSA and amorphous PLA. The phase images of each sample (Figure 2-9B and D) clearly show that there are two phases present, a light and dark contrast, consisting of a phase shift of ~50°. An increase in the light phase correlates with an increase of PLA in the polymer blend. The phase-separation curves on each of the polymers shows a different response as the tip comes into contact (Figure 2-9E). As the tip approaches PSA (long dashed line) there is initially a repulsive force until the tip is ~4 nm from the surface and then the force becomes attractive. This correlates with a phase shift of ~ 9°. As the tip approaches PLA (dotted line) the initial repulsive force is overcome sooner and the tip feels an attractive force from a distance of ~6 nm giving a final phase shift of ~ 20°. With prior knowledge of such samples, we are able to correlate the phase change with differences in the material crystallinity (stiffness). In this case, the dark and light phases indicate the harder PSA and softer PLA, respectively [164]. This is reinforced by the higher ratio of light phase areas for the higher ratio of PLA in the polymer blend. When a sample, like PLA, is amorphous and soft the tip-sample deformation results in energy dissipation from the tip to the sample and thus shifts in the phase signal. This is in contrast to the more crystalline and hard PSA [164-165].

2.4 SPM Techniques

2.4.1 Conductive AFM

Conductive AFM (C-AFM) is a scanning probe microscopy (SPM) method that measures the conductivity of a sample using a conductive probe in contact mode. The conductive probe is generally a silicon or silicon nitride probe with a metallic or metallic alloy coating. The C-AFM tip and sample interaction is illustrated in Figure 2-10.

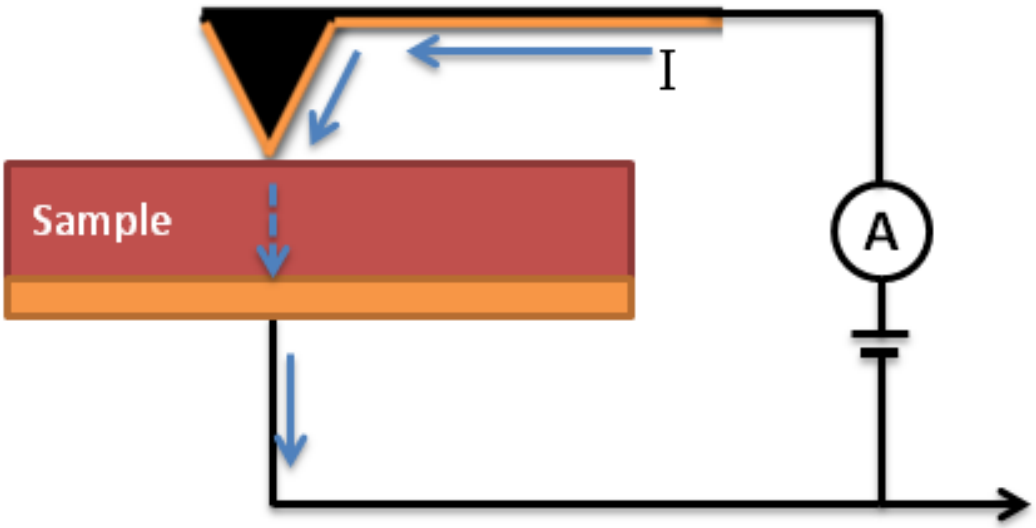

Figure 2-10: Schematic of C-AFM tip and sample. A DC voltage bias is applied to the conductive tip or sample. The current (blue arrow) passing through the tip to the sample is measured.

A DC voltage bias is applied to the tip while the sample is held at a ground potential. When the tip is in contact with the surface a current flows from the tip through the sample and into the conductive sample holder. Alternatively a bias can be applied to the sample and the flow of

current from sample to tip is measured. This flow of current between tip and sample is simultaneously measured with topography as the tip scans across the surface. A conductive image is created using the current signal versus the X- Y location of the tip on the sample. Contrast in the conductive image is gained from differences in conductivity across the surface. As this technique is conducted in contact mode damage to softer materials may occur due to lateral forces of the tip and it is often the case that the conductive coating of the tip is damaged.

2.4.2 *Kelvin Probe Force*

The surface potential of a sample can be measured using Kelvin probe force microscopy (KPFM). KPFM is a non-contact scanning method which uses a potential offset between tip and sample to measure electrostatic forces, and requires a conductive tip. Figure 2-11A illustrates how we measure a change in surface potential with KFPM. The tip and surface have different work functions (the difference being ΔΦ) which results in a flow of electrons from the tip to the surface (Figure 2-11A.i), assuming the tip has the smaller work function which is typical. A second feedback loop is used to apply a DC voltage (V_{DC}) to the tip (Figure 2-11A.ii). In addition, a sinusoidal AC signal ($V_{AC}sin(\omega t)$) is applied to the cantilever to oscillate it at its resonant frequency (Figure 2-11A.iii). The total voltage applied to the tip contains both DC and AC components ($V = V_{DC} + V_{AC}sin(\omega t)$).

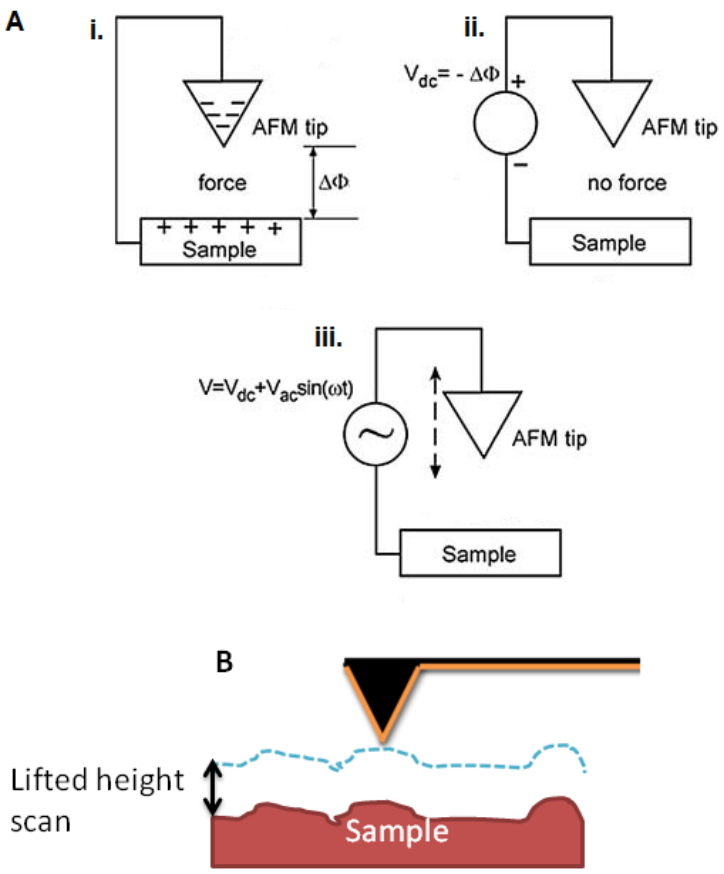

Figure 2-11: Schematic of (A) tip-sample forces during KFPM; (i) differences in work function, (ii) applied DC voltage bias to tip which is equal to work function difference and (iii) AC voltage results in electrical oscillation of AFM tip [173]. (B) Schematic of KFPM tip and sample interaction.

The application of AC voltage applied directly to the conductive tip, and constant potential difference between tip and sample, produces an oscillating electrostatic force. Importantly, the feedback adjusts V_{DC} to nullify this electrostatic force and the changes in V_{DC}, otherwise known as the contact potential difference, reflects the surface potential of the surface [166].

When scanning an image, the tip first scans a single pass across the sample in AC mode to acquire topographical data and uses this height data to repeat the pass with the tip at a

constant height (blue dashed line) above the surface (Figure 2-11B). An image is produced by plotting the surface potential voltage with the X-Y position of the tip on the sample. If the tip has been calibrated on a surface with a known work function (to determine the tip work function), this method can be used to calculate the work function across a sample.

2.4.2.1 C-AFM and KPFM on OCPs

C-AFM and KPFM has been used extensively to analyse changes in conductivity across OCP surfaces. Previous studies on PT [160] and PPy films [64] using C-AFM and KPFM have shown a higher conductivity and changes in surface potential correlating with changes in topography, indicating the heterogeneous conductive nature of OCPs.

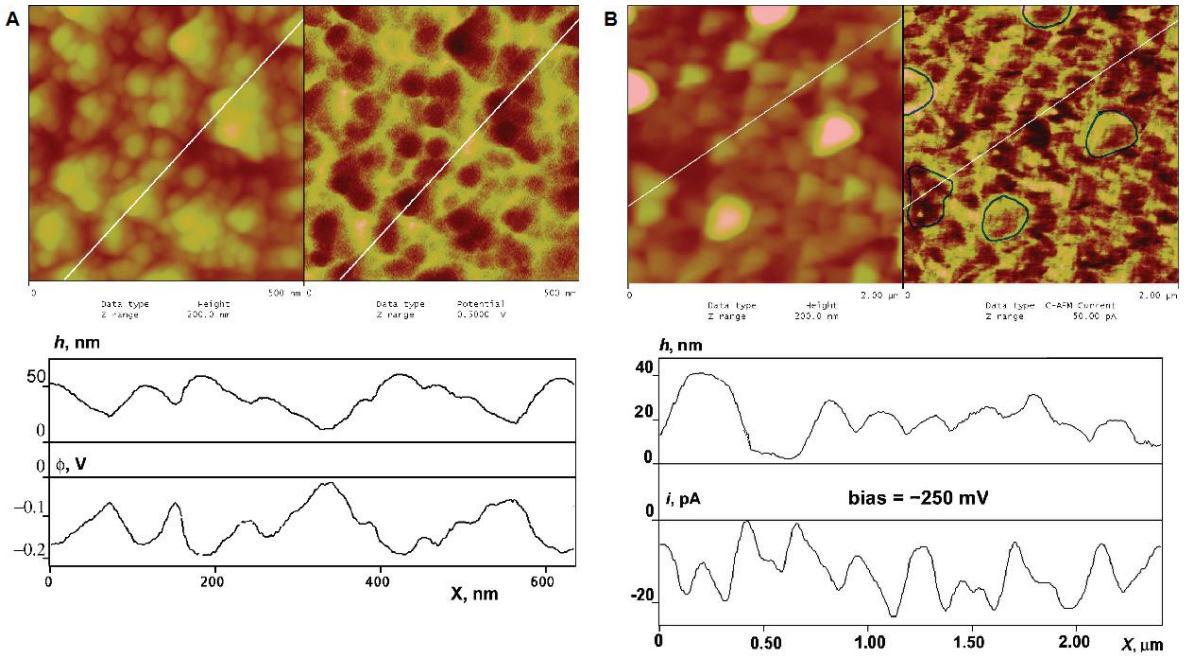

Figure 2-12: Simultaneous topography and surface potential scan (top), topography and current (bottom) for polybithiophene film with cross-sections below respectively [160]

Figure 2-12 shows both KPFM and C-AFM scans of a polybithiophene conducting polymer with simultaneous topography [160]. The darker areas in the KPFM scan (Figure 2-12A) correspond to nodular features in the topography scan. The cross- sections in Figure 2-12A shows that for the higher, nodular regions of the film there is a lower voltage (~-0.2 V), and hence, work function. Figure 2-12B shows the current sensing with a negatively applied bias (meaning a negative current correlates to higher conductivity). Darker areas in the C-AFM scan also correspond to nodular features in the topography scan. The cross-section in Figure 2-12B shows that the higher regions of nodules correspond to areas of negative current (~ -20 pA) and hence areas of higher conductivity. For conducting polymers prepared as films, electrical AFM techniques are ideal for analysing electrical surface properties and provide high resolution lateral information [167]; imaging these polymers can be difficult however, due to the softness of the material (as C-AFM must be conducted in contact mode) and effects from variable contact resistance between the tip and sample.

2.5 Electrochemical AFM

Electroactive properties of conducting polymers are best studied *in situ* in order to elucidate the dynamic, electrochemical properties of the polymers and their interactions. This has been achieved by applying Electrochemical AFM (EC-AFM) to conducting polymers that allows the dynamic redox surface properties of the polymers to be probed in electrolytes during electrical stimulation [44, 168-171].

EC-AFM involves using the sample as a working electrode, with a counter and reference electrode incorporated into a 3-electrode electrochemical cell underneath the AFM scanning head. The tip scans or probes the surface whilst an electrical potential is applied to the polymer. This technique has been used to study morphological changes on the surface of PPy as the polymer is reduced and oxidised [170] and the degradation of PPy as it is placed under oxidative stress [171].

EC-AFM is not limited to topographical scans as the tip can be used to measure various signals such as real-time z-displacement of the surface. Changes in the material volume with an applied voltage can be directly measured by keeping the tip in contact with the surface with the feedback on. For example, as the surface swells and shrinks, the height of the Z-piezo will move up and down accordingly and recorded to quantify the displacement of the surface.

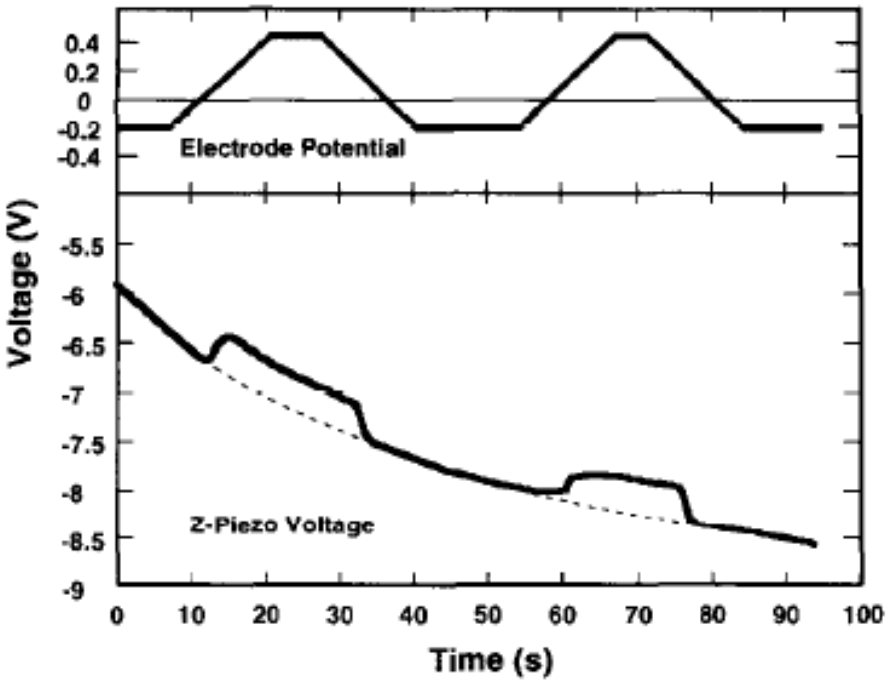

Figure 2-13: Typical result of two subsequent oxidation reduction cycles. Potential of the substrate (above). Signal of the z-piezo (below). The signal to noise ratio is rather low leading to a readout error of up to 10% [169].

Figure 2-13 displays an applied potential to a PA polymer (top) and the height change measured in volts by the Z-piezo (bottom). An oxidation/reduction cycle between -0.2V and 0.45V was applied to the PA film and a height change of 26.9 nm was observed (converted from piezo voltage). The slope of the Z piezo signal is due to long-term drift in the system that can be corrected to measure an accurate change height of the Z- piezo [169]. Thus, EC-AFM is able to measure in real-time the swelling and shrinking of the PA with an applied potential. The actuation of a surface can also be measured using a 'slow-scan disabled' image. In this case, the tip scans for a specified distance over the same line repeatedly along the X-axis and the Y-axis is quantified as time.

This type of measurement is shown in Figure 2-14A for the mechanical actuation of a PPy film during the application of cyclic voltammogram (CV). The AFM scan is shown as a function of time and allows for direct observation of the actuation of the film across a distance of 1

micron. Figure 2-14B displays the cross-section of the height measured in Figure 2-14A with an overlay of the voltage and current signal. The film reversibly swells in response to reduction and shrinks with oxidation [44]. Providing that the electrical and physical behaviour of the film does not interfere with the measurements, the use of EC-AFM allows full characterization of these electroactive materials, as they are electrically stimulated.

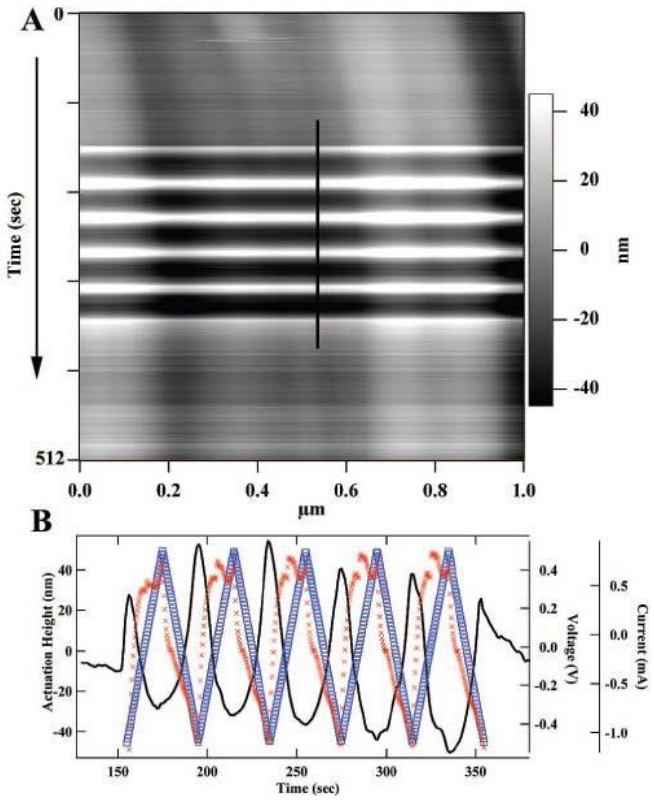

Figure 2-14: (A) AFM height image of the 10 min grown PPy/PSS- film in 0.05 M NaPSS during a cyclic voltammogram (CV) measurement initiated at ~150 s into the AFM scan. CV was performed with an applied,potential moving from -500 to +500 mV at 50 mV/s for five cycles. (B) Cross-sectional height profile (black line) taken through the vertical line shown in (A) as a function of the CV time (s). The height profile shows a cyclic increase and decrease in height, and out-of-phase response with the corresponding applied voltage (blue square) and current (red hatch) signals[44].

2.5.1 *Design of EC-AFM*

A 3-electrode electrochemical cell was developed for use with the Asylum AFM system used in this project. The experimental schematic is illustrated in Figure 2-15. The counter electrode surrounds the working electrode (conductive sample), essentially creating a virtual 2-dimensional electrochemical cell. The electrolyte covers both electrodes and forms a meniscus with the AFM cantilever holder as it approaches the surface to fully immerse the system in electrolyte. The cell is connected to a potentiostat for external electrical stimulation. The electrical stimulation does not affect the deflection of the laser through the fluid [172] and the electrochemical cell is completely isolated and does not interfere with the electronics of the AFM. A small Ag wire pseudo-reference is inserted from the side and is preferable to an Ag/AgCl reference electrode as it easily fits into the e-cell without interfering with the AFM head (Appendix I). The reference electrode was also calibrated and showed no difference to the use of a conventional reference electrode.

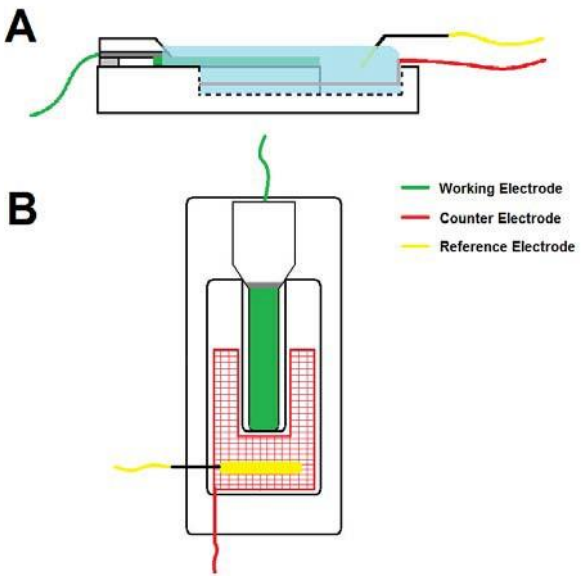

Figure 2-15: (A) Cross-section and (B) top view of EC-AFM three point electrochemical cell schematic. The working electrode is coloured in green, the counter electrode in red and the reference electrode (yellow).

2.6 Force Spectroscopy

A unique method of AFM is force spectroscopy; a technique that enables the direct measurement of tip-surface interaction forces with very high resolution. This technique can be performed in air or in fluid.

2.6.1 *Principles of Force Spectroscopy*

Force is measured with an AFM by performing a force curve. A force curve is a plot of cantilever deflection as a function of Z-piezo position and can be conducted as a function of the X-Y position.

A force spectroscopy curve is comprised of four main regions, as displayed in Figure 2-16, which provides information about the tip-sample interaction. At point (i) in Figure 2-16, the approaching tip is far above the surface and there is no recorded cantilever deflection or interaction between tip and surface. At point (ii), the tip feels long-range repulsive forces and then makes contact with the surface. The Z-piezo position continues towards the surface, causing the tip to deflect (linear slope in contact region) until it reaches a maximum deflection (point iii).

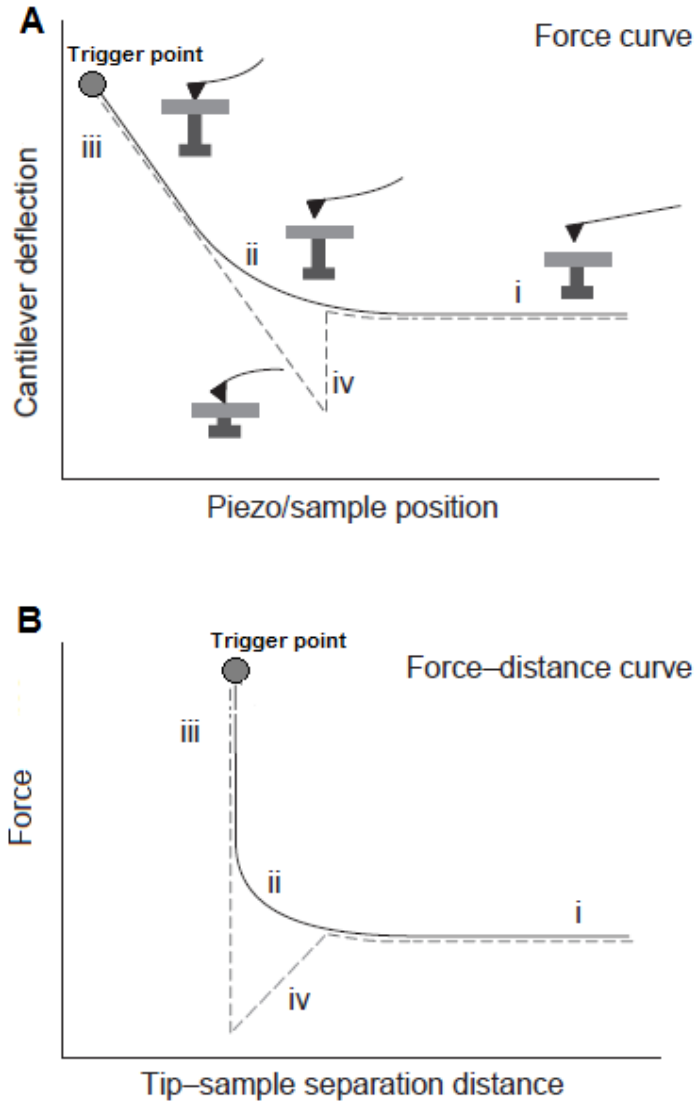

Figure 2-16: Illustration of a typical cantilever deflection/force vs. (A)piezo/sample (or tip) position, and (B) tip-sample separation. Approach curve is solid, retract curve is dashed. Adapted from [175].

The Z-piezo then retracts away from the surface and the cantilever deflection reaches zero. If there are adhesion forces between tip and sample, the cantilever may continue to deflect downward (point iv) until the adhesion forces are overcome and the cantilever "snaps" back to its unperturbed position (zero deflection) as it continues to move away from the surface.

The conversion of the deflection (typically in volts)-piezo position curve into a force- distance curve (illustrated in Figure 2-16B) is necessary for quantification of forces.

Firstly, the inverse optical sensitivity (inVOLS) of the cantilever obtained from the inverse of the slope in the contact region (point iii), is used to convert the deflection voltage into metres. By knowing the spring constant of the cantilever, the cantilever deflection can be converted into a force using simple Hooke's Law;

$$F = -kx \qquad (1)$$

where *k* is the spring constant of the cantilever and *x* is the deflection of the cantilever in metres. The tip-sample distance is calculated by adding the cantilever deflection and Z piezo distance. Hence for an infinitely hard surface the curve is vertical once it makes contact with the surface (as demonstrated in **Error! Reference source not found.**B).

2.6.2 *Cantilever Calibration*

The cantilever must be calibrated when performing quantitative AFM force spectroscopy measurements. Cantilevers are sold with a manufacturer's spring constant, however variation throughout batches of cantilevers occurs and for accurate measurements each cantilever should be individually calibrated. The relationship between tip-sample forces and spring constant is described using Hooke's Law (1).

In order to quantitatively determine the force we must know the spring constant. The spring constant can be calculated using the thermal noise method, or with the geometry of the tip [176]. The cantilever is modelled as a simple harmonic oscillator, and when a harmonic oscillator is in equilibrium it will fluctuate in response to thermal noise [177]. In order to isolate the thermal oscillations from ambient noise a thermal spectrum of the cantilever

deflection is measured. As the ambient noise is very unlikely to have the same frequency as the cantilever's resonant frequency, the noise can be subtracted from the resonant frequency peak. The area under the resonant frequency peak is a measure of the power of the cantilever thermal fluctuations; hence the spring constant can be estimated:

$$k = \frac{k_B T}{P} \qquad (2)\ [177]$$

Where kB is the Boltzmann constant, T is temperature and P is the area of the power spectrum of the thermal fluctuations. This method is calculated using the AFM software once the resonant frequency and optical sensitivity of the cantilever has been obtained. For a more detailed description see Hutter and Bechhoefer [175].

The Sader method requires the cantilever geometry and a measurement of the cantilever resonant frequency and quality factor. The spring constant is calculated using the geometric measurements of the tip (width w and length L) and the density of the surrounding fluid:

$$k = 0.1906 \rho_f w^2 L Q \Gamma_i(Re) \omega_0^2 \qquad (3)$$

Where ρ_f is the density of the fluid surrounding the cantilever (i.e. air, water), Q is the quality factor of the resonant frequency peak, ω^2_0 is the resonance frequency of the cantilever, Γ_i is the imaginary part of the 'hydrodynamic function', which takes into account the viscosity of surrounding fluid (η) and is dependent on Re.

$$Re = \frac{\rho_f \omega_0 w^2}{4\eta} \qquad (4)$$

Re is the Reynolds number which contains the resonant frequency of the AFM tip. As the Sader method uses the geometry of the tip and resonant frequency, but no physical manipulation of the tip (i.e. performing a force curve) this method is more advantageous

when keeping the tip pristine before beginning experiments. This method is available online to quickly calculate the spring constant of a cantilever (http://www.ampc.ms.unimelb.edu.au/afm/calibration.html), and is also available in the App Store for iPhones (http://itunes.apple.com/gb/app/sader-method/id402544930?mt=8) for easy calibration of cantilevers on the go.

2.6.3 *Force Curve Interactions*

There are many different tip-sample interactions that can occur as the tip approaches and retracts from a surface and display characteristic force curves. Figure 2-17 presents several typical forces curves to highlight different interactions.

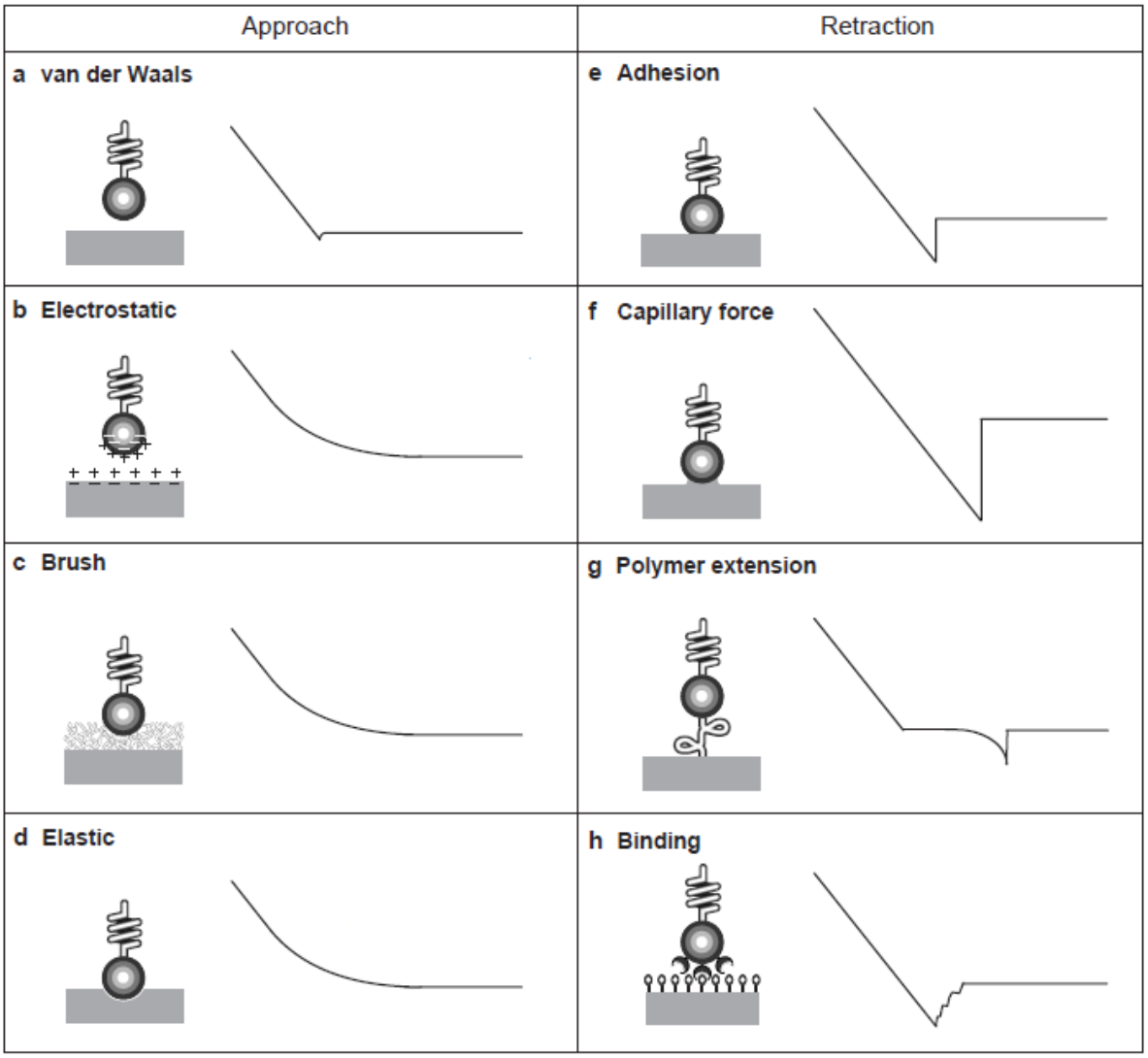

Figure 2-17: Examples of force curves. The AFM tip is presented as a ball on a spring. Notice that the curves are shown as force versus sample-position curves, which is the most common way they are displayed in the literature. (A-D) are approach curves, (E-H) are retraction curves. Adapted from [175]

Figure 2-17A is an ideal, attractive van der Waals force, Figure 2-17B is a repulsive electrostatic double layer in fluid, Figure 2-17C is polymer-brushing forces resulting from thermally driven motion of polymers grafted onto a solid surface in solution and Figure 2-17D is an indentation into an elastic sample. In the case of Figure 2-17D, the point of contact is where the cantilever begins to deflect. Figure 2-17E is adhesion between the tip and a surface

in the absence of any contaminants. Figure 2-17F shows capillary (meniscus) adhesion between the tip and surface with adsorbed water (very typical in ambient conditions). Figure 2-17G is polymer-extension curves where there is a negative deflection far from the surface (as the polymer stretches at a constant force) until the polymer breaks or detaches from the surface and then jumps back to zero deflection. Figure 2-17H is the unbinding of specific receptor-ligand pairs. The stepwise return to zero deflection from an adhesion point can be attributed to the sequential unbinding of multiple receptor-ligand pairs [173].

These different tip-sample interactions can be very useful for characterising materials. For example, elastic indentation curves (Figure 2-17D) are used to determine the Young's modulus of a material. Using force spectroscopy, specific biomolecular forces between molecules on the tip and surface can be quantified, as in Figure 2-17H.

2.6.4 *Young's Modulus*

The Young's Modulus of a material can be quantified using AFM. This type of measurement utilizes the approach and indentation areas of a force curve. Typical force-distance curves can qualitatively reveal information about the stiffness of a material. Figure 2-18A shows a schematic of an approach curve as a tip pushes into two materials of differing stiffness that undergo linear compression. The slope of the force-distance curve can be used to qualitatively compare the stiffness. The first material (solid line) is stiffer than the second material (dashed line) as it has a higher slope; i.e. a force of 20 nN corresponds to the tip pushing 20 nm into the first material compared to a distance of 40 nm for the second material - hence the first material is stiffer. This is not a quantitative method and is only useful for pseudo-quantitative comparisons. To fully quantify the Young's modulus, force curves must initially be obtained on an infinitely hard surface followed by the sample. For hard surfaces, the force-distance curve

typically has a linear response as the tip does not indent the material under an applied load. However, indentation of soft materials will occur and typically displays a non-linear increase in the force in the contact region. Figure 2-18B illustrates a linear force curve on a hard surface (dotted line) compared to a non-linear response on a soft material. The indentation (I) is calculated as the Z-height between any two points on the hard on soft sample curves at a given force, i.e. at 5 nN the indentation is ~220 nm (Figure 2-18B). By knowing the indentation as a function of force, several different models can be used to calculate the Young's modulus, including the Hertz, the JKR, and the DMT model [174].

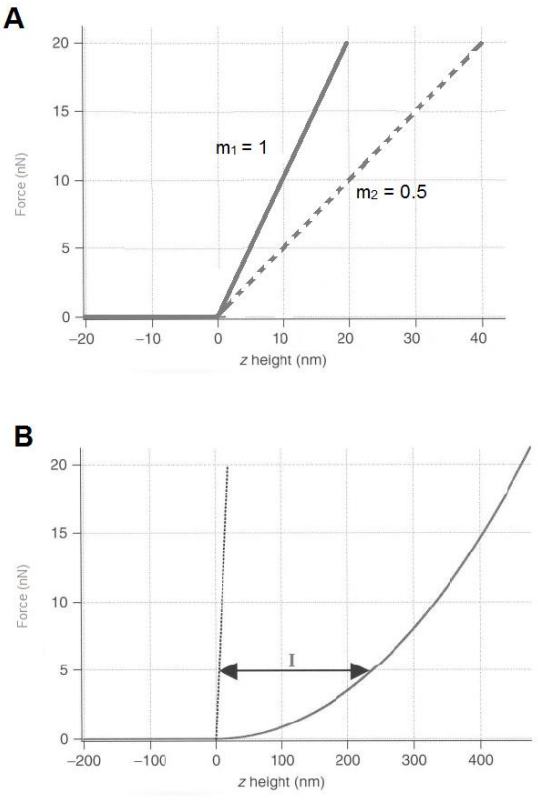

Figure 2-18: (A) Simulated force curves of materials of different stiffness, *m* being the slope of the linear response. (B) Simulated force curve of a soft material, showing a non-linear indentation response (solid) compared to the linear behaviour on a stiff material (dotted). Indentation (I) is annotated with the arrow. Adapted from [176]

The JKR and DMT models take into account adhesion to the sample, outside or inside the contact area, respectively [174]. However, in this work we have applied the Hertz model to our data to fit for Young's modulus, as the adhesion force between sample and tip is much lower than the maximum load.

This model is best applied when the sample is much softer than the indenting material (AFM probe). For a spherical indenter indenting an elastic, homogenous material the Hertz model is described as;

$$F = \frac{4E_{tot}\sqrt{R}}{3(1-v^2)} I^{\frac{3}{2}} \qquad (4)$$

Where *F* is the applied force by the indenter (the tip), *I* is the indentation depth, *R* is the radius of the spherical indenter (generally 10-20 nm), *v* is the Poisson's ratio and E_{tot} is the complex Young's modulus [177]. A spherical model is applicable as the interaction area between the tip and sample is assumed to remain spherical due to the indentation forces used; the shape of the indenter dictates the exponent in Equation (4) which for a sphere is $\frac{3}{2}$. Punch and cone indenters can be applied to the Hertz model, which have exponents of 1 and 2 respectively. The complex Young's modulus is a function of the Young's modulus of both the tip (indenter) and the sample (indented material), given as

$$\frac{1}{E_{tot}} = \frac{3}{4}\left(\frac{1-v_s^2}{E_s} + \frac{1-v_t^2}{E_t}\right) \qquad (5)$$

where v_t is the Poisson's ratio of the tip, E_t is Young's modulus of the tip, v_s is the Poisson's ratio of the sample and E_s is the Young's modulus sample. Using a Si_3N_4 tip we assume the Young's modulus is 290 GPa and the Poisson's ratio is set to 0.25 using the manufacturer's

data of the tip. As the E_t is known, we are able to obtain E_{tot} from a fit of the force versus indentation curves and thus the Young's modulus of the sample can be calculated.

Figure 2-19 displays a Hertz model fit applied to two deflection-indentation curves performed on a fibroblast cell [176]. Deflection is given here as the Y-axis as it has not been converted to force, however the Hertz model can still be applied. The dotted black line is an example force curve on a hard surface, used to provide a zero-point for the indentation. The distance between the dotted line and sample force curves gives the sample indentation (I).

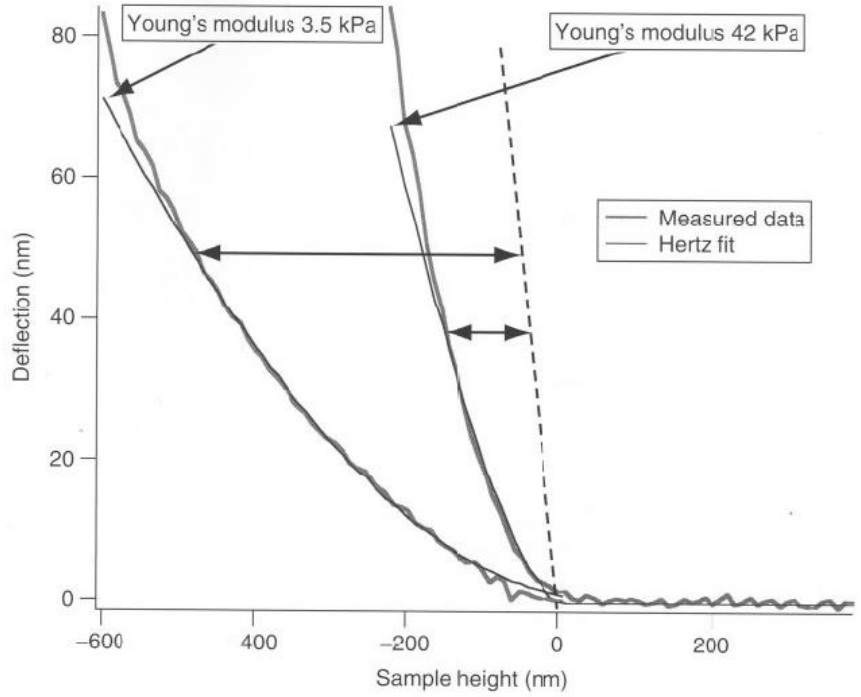

Figure 2-19: Two sample force curves performed on different regions of a fibroblast cell (thick). A Hertz model has been fitted to each curve (thin), with the calculated Young's modulus for each fit annotated next to the appropriate curve. The left curve was taken on a thick region on the cell, the right taken on a lamellipodial region. Adapted from [176]

The curve with the larger indentation is fitted to give a Young's modulus of 3.5 kPa, while the curve measuring a smaller indentation gives a Young's modulus of 42 kPa. The softer curve

was performed on a thick part of the fibroblast, while the stiffer curve was performed on the thinner lamellipodial region. The fit follows the data well at low loading forces, however begins to deviate as the indentation approaches the known thickness of the two sample regions (at higher loading forces). Thus, while the Hertz model is well applied to calculating the Young's modulus from force-distance curves, care must be taken that as a general rule the indentation distance should not exceed 10% of the material's thickness, so as to minimize the influence from any underlying substrate [178].

2.6.5 *Force Volume Mapping*

The force spectroscopy methods described above operate at a single point X-Y on the sample surface. Using the same methods, we can measure forces across a surface in a grid array to provide lateral resolution to the force spectroscopy. This method, termed 'Force Mapping', is widely used to sample interaction forces (e.g. adhesion) across a material.

Figure 2-20 is an illustration of a force-volume map. The resolution of the scan area (i.e. 5µm x 5µm area) is defined by the number of 'pixels' (typically 32 x 32 or 64 x64). Each pixel represents a single force curve from which the height and other parameters (i.e. modulus and adhesion) can be extracted and displayed as an image.

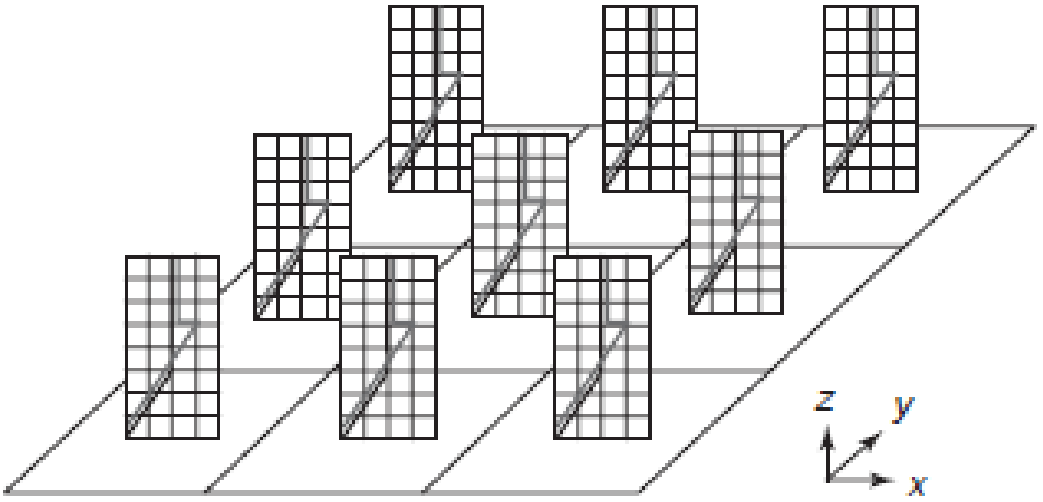

Figure 2-20: Force-volume imaging illustration. Each pixel within the image is a force distance curve.[175]

An image can be created by plotting the force values versus the X-Y position of the tip. Topographical data is also measured during a force curve to produce a corresponding height map. During a force-volume map, the tip has a set starting height above the surface (for example, 500 nm). The topographical height is determined by the point where the tip comes into contact with the surface relative to the starting height.

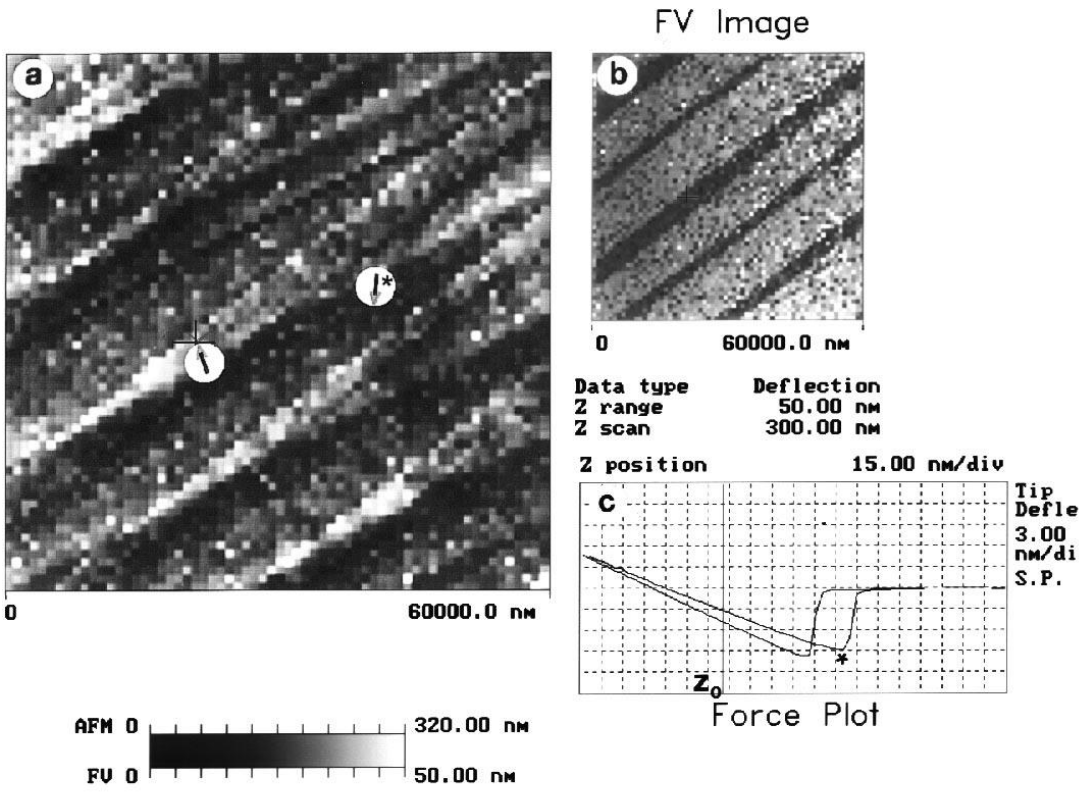

Figure 2-21: Force volume maps of (A) topography and (B) modulus of a PE sample. (C) Force plot illustrating force-distance curved obtained on soft layer(*) and hard layer in the places indicated with arrows in the height image (A).[179]

Figure 2-21 shows a force volume map of simultaneous topography (A) and stiffness (B) across a material using approach curves. The topographical map in Figure 2-21A shows there are fibre-like features on the surface. Figure 2-21B is a map of differences in the deflection of the cantilever at Z0 (Figure 2-21C) and shows hard and soft regions across the sample corresponding the topography. Two force curves from Figure 2-21B are graphed in Figure 2-21C, with their topographical position marked in Figure 2-21A. The difference in the slope of the contact region of the force curves indicate that the marked (*) curve is pushing into a softer surface compared to the unmarked curve.

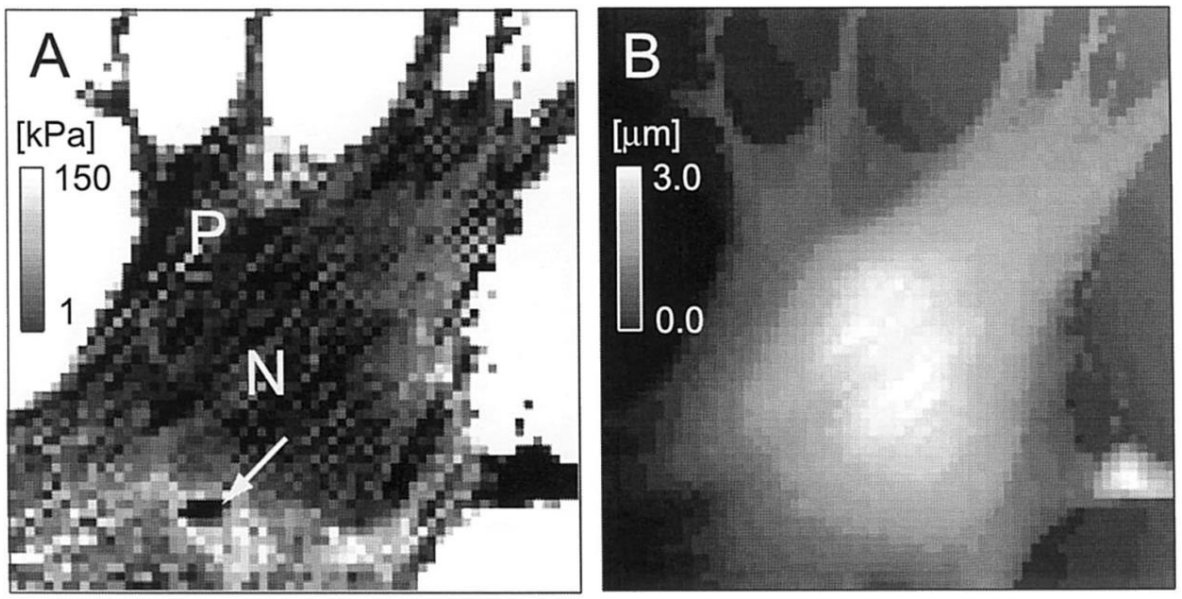

Figure 2-22: Elasticity map (A) and corresponding topography (B) of a living "broblast (NIH3T3) calculated from 64 pixel]64 line force curves. Data acquisition time was 40 min. The nuclear portion (marked N) is the softest (about 4 kPa). A small softer portion was observed in the perinuclear region (marked by arrow). P represents a region with a high concentration of microtubules. [180]

A quantitative force-volume map can be produced by using the indentation data of each approach force curve and applying a Young's modulus fit. A living fibroblast was mapped by applying the Hertz model to the indentation data to reveal regions of variable stiffness [180]. Figure 2-22A shows the variation in Young's modulus across the cell, ranging from ~4 kPa to 150 kPa. The height image of the fibroblast is mapped in Figure 2-22B and the nucleus area of the cell (marked N) is observed to be softer. The stiffer areas are attributed to microtubules within the cellular structure (further confirmed by immunofluorescence data not shown here) [180].

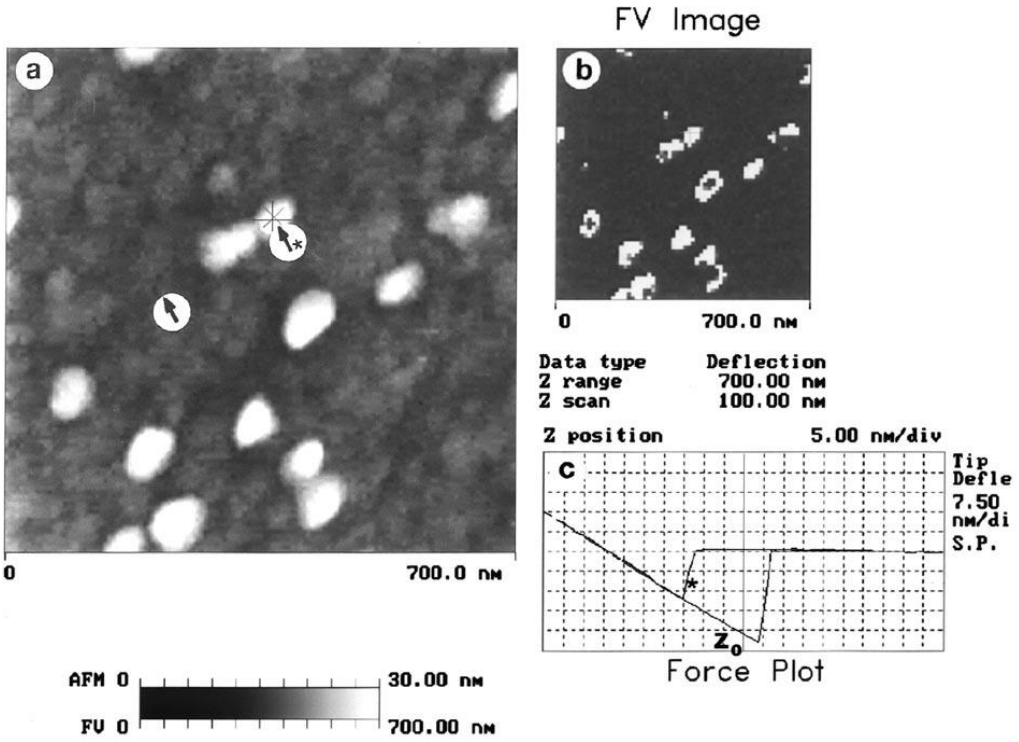

Figure 2-23: (A) AFM height scan (height contrast of 0-72 nm), and (B) force-volume map of thin lube sputter textured surface of a hard disk. (C) Force plot illustrating force-distance curves obtained at places indicated with arrows on elevated (*) and flat regions of the disk. Force variations are measured as the difference between cantilever deflections in the force curve at the Z_0 position in (C). [179]

Force volume mapping can also be applied to adhesion forces with retract curves. The AFM height image in Figure 2-23A is of a computer hard disk surface sputtered with lubricant. The force- volume map (Figure 2-23B) displays the difference in cantilever deflection across the same area as the height image. The force curves in Figure 2-23C were performed on the flat disk surface and on an elevated feature (*) and show a difference in adhesion as the tip pulls away from the surface. As the force-volume map uses the cantilever deflection value at the Z0 point (marked in Figure 2-23C), the dark areas indicate a lower adhesion than the bright areas, thus the elevated regions are more ‘sticky’ than the flat regions.

2.6.6 *Single Molecule Force Spectroscopy*

The functionalization of AFM tips with molecules allows specific interactions to measured using force spectroscopy.

2.6.6.1 Functionalization Methods

A wide variety of chemical functional groups and biomolecules can be attached to the tip either through physisorption or chemical bonding. Importantly, the forces binding the molecule to the tip must be stronger than the interaction forces with the surface to ensure they remain immobilized on the tip. The functionalized molecules should also have enough mobility to interact freely with complementary molecules or ligands[181].

There various strategies to chemically functionalize an AFM tip. AFM tips are generally made of Si or SiN3 and often require an initial functionalization layer to facilitate attachment of other molecules. Gold coatings on AFM tips enable thiols and disulfides to bind strongly through their mercapto group and form self-assembled monolayers (SAMs) on the tip surface. From this basic chemical bonding, hydrocarbons can be chosen for specific interactions and forces between the surface and defined chemical groups can be measured. As schematised in Figure 2-24A, the tip can have many different hydrocarbon groups attached through this method, for example carboxyl, hydroxyl, methyl, amide and amine molecules [182-183]. The tip can be used to study many different interactions such as those with other hydrocarbon groups (Figure 2-24A). Silanization is another method used to modify the Si or SiN3 tip surface where the reaction is with the silanol group. The silane layer can then be used to covalently bind the desired molecule to the surface [174].

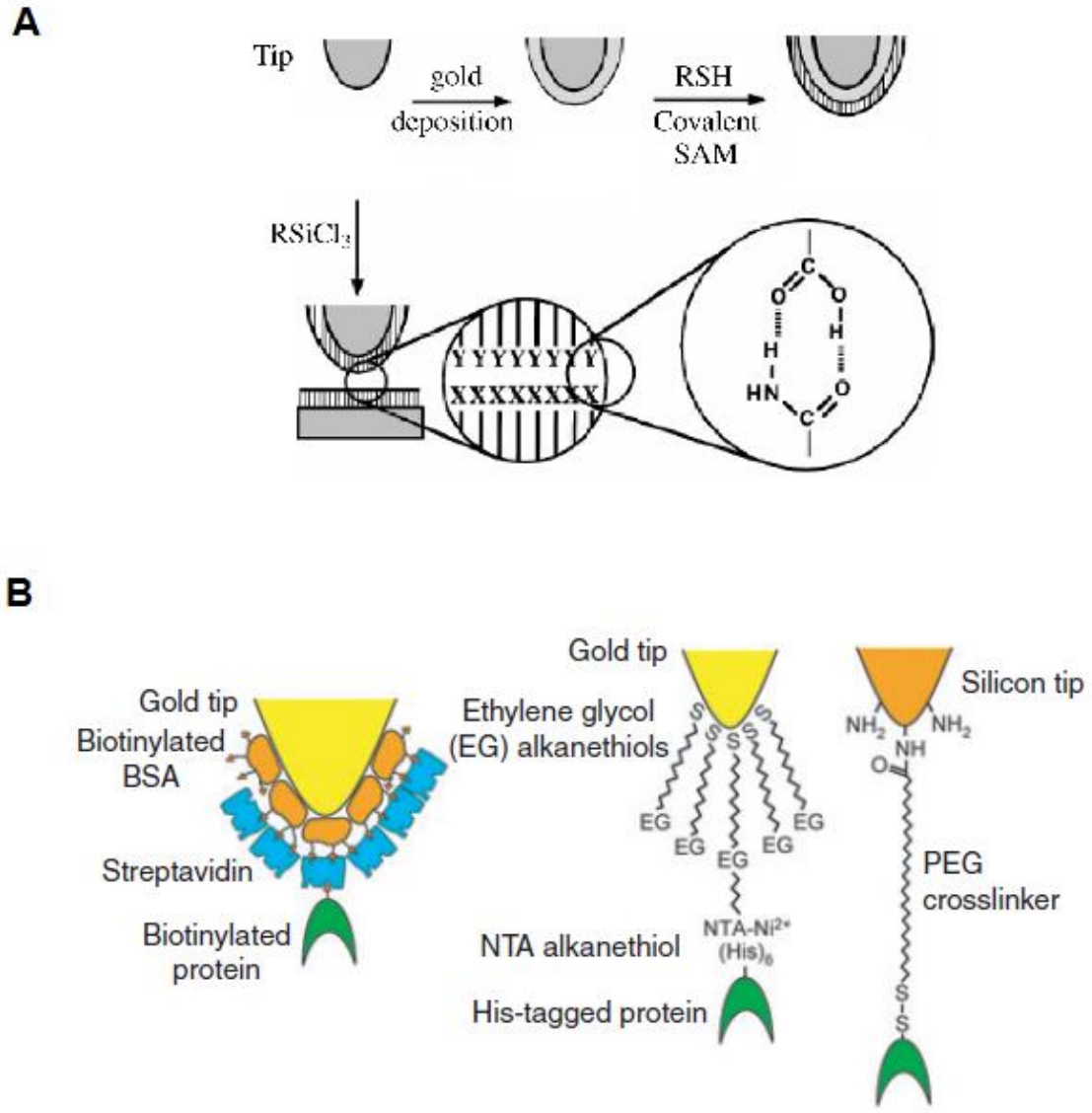

Figure 2-24: (A) Tip coated with a thin gold layer, then immersed in a thiol solution (RSH) to form a layer of hydrocarbon groups. Similarly, a cleaned Si or Si_3N_4 tip functionalized with a reactive silane $RSiCl_3$. R represents an organic alkyl chain that ends with a functional group X (X = CH_3, COOH, CH_2OH, NH_2, etc) [184]. (B) Common strategies used for modifying AFM tips for single molecular recognition studies: physisorption of proteins such as biotinylated BSA, chemisorpotion of alkanethiols on gold and covalent coupling of silanes on silicon oxides [185].

When studying biological systems, immobilization of biomolecules such as proteins can be achieved through several methods, as illustrated in Figure 2-24B. Non-specific physisorption

of biotinylated bovine serum albumin (BBSA) can be used to attach avadin/streptavidin to the tip and can even then be further reacted to attach biotinylated molecules. The gold-thiol approach can also be used to bind biomolecules. For example, the use of SAMs has been applied to the binding of alkanethiols on a gold-coated tip to bind N-hydroxysuccinimide as cross-linker for the subsequent attachment of His-tagged protein (Figure 2-24B). Silanization is often used to covalently bind proteins to an AFM tip. The silane is bound to a cross linking agent, such as gluteraldehyde or polyethylene glycol (PEG) (as used in Figure 2-24B), that tethers the protein to the probe [186]. The cross-linkers generally have two different functional ends, an amine-reactive and a thiol-reactive end, to direct the binding [181].

2.6.6.2 Single Molecule Spectroscopy using Biomolecules

Single Molecule Force Spectroscopy is a method that directly measures the interaction between single molecules on the AFM tip and/or surface. In addition to measuring binding forces, we can also observe the confirmation and behaviour of the protein under tensile forces. Some approaches to measuring biomolecular forces have in fact involved placing an entire living cell on an AFM tip and measuring the interaction with a specific surface. For example, A K562 cell was attached to the AFM probe and the forces between the cell and a substrate coated with FN measured. The $\alpha_5\beta_1$ integrin interaction with the RGD sites in FN was observed; the interaction of the $\alpha_5\beta_1$/FN domains 7-10 was shown to be stable but the dissociation was very sensitive to a pulling force [187]. AFM tips functionalized with single molecules, such as antibodies used to bind to antigens on a surface, can be applied to determine the specific unbinding force [188].

Receptor-ligand interactions mediate a variety of cellular interactions and processes. Performing single molecule force spectroscopy using a receptor-ligand pair can assist in the understanding of these interactions [189]. The ligand-receptor pair in Figure 2-25A is present in plants and the lectin concanavalin A has interesting aggregating properties when binding to certain glucose groups. The tip was functionalized with oligoglucose hexasaccharides and the subsequent interaction with concavalin-A analysed. Figure 2-25 shows an unbinding force of 100 pN along with non-linear elongation forces. This force profile is indicative of single lectin-carbohydrate complex rupturing, indicating a specific interaction [189]. AFM has also been used to measure single protein-surface interactions on surfaces with well-defined surface chemistries to study the behaviour of FN to help elucidate subsequent cellular behaviour [96, 190].

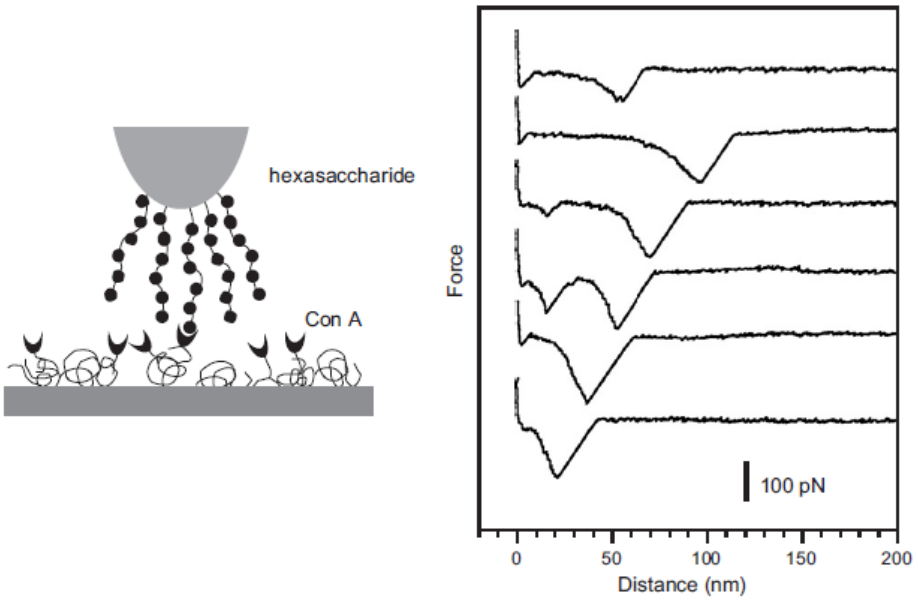

Figure 2-25: Interaction illustration between hexasaccharide-terminated tips and concanavalin A-functionalized substrate. Force-distance curves measured show adhesion forces of ~ 100 pN [189].

Proteins have been used primarily for studying many protein-material, protein-cell and protein-protein interactions [191]. There has been a major research effort on the unfolding of proteins and their domains, and the forces required for this.

Table 2-2: Stretching of multi-domain proteins, adapted from [191]. Extension is the stretching length of a subunit or domain.

Native protein, recombinant fragment, or polyhomodomain	**Extension per sub-unit/domain (ΔL_c)**	**Average force (pN)**	**Reference**
α_2-macroglobulin	150nm for each of four identical sub-units;	>250	[192]
Titin (native protein or recombinant fragments containing 8 or 4 immuno-globulin)	25±28nm	150±300	[193]
Nine identical repeats of the C2A domain of synaptotagmin I[$(C2A)_9$]	38nm (106 amino acids)	~60	[194]
Tenascin (native protein or recombinant fragment containing 15 Fn-III-like domains)	28.5nm	~140	[195]
Spectrin (native protein or recombinant fragment) containing repeats 13±18; α-actinin (four spectrin-like domains α1±α4)	31.7nm	~25±35	[196]
Four identical repeats of a rat calmodulin domain CaM_4	The protein extends in one step; 225nm	~600	[194]

Table 2-2 lists just some of the work done in the area of protein stretching and unfolding, and the lengths and forces measured. Using the extension lengths it is possible to identify the domain and the intermolecular forces occurring as it is stretched. Biological binding forces typically lie with the range of 50-400 pN [181], forces which are very small but easily measured using AFM.

The unfolding events of the protein occur when a protein undergoes a stretching force and also reveal information on the interaction of the protein with the surface [197].

If the molecule functionalized on the AFM tip is a biomolecule consisting of individual folded domains, such as a FN, unfolding of these proteins occurs when a tensile force is applied during extension of the protein (Figure 2-26A).

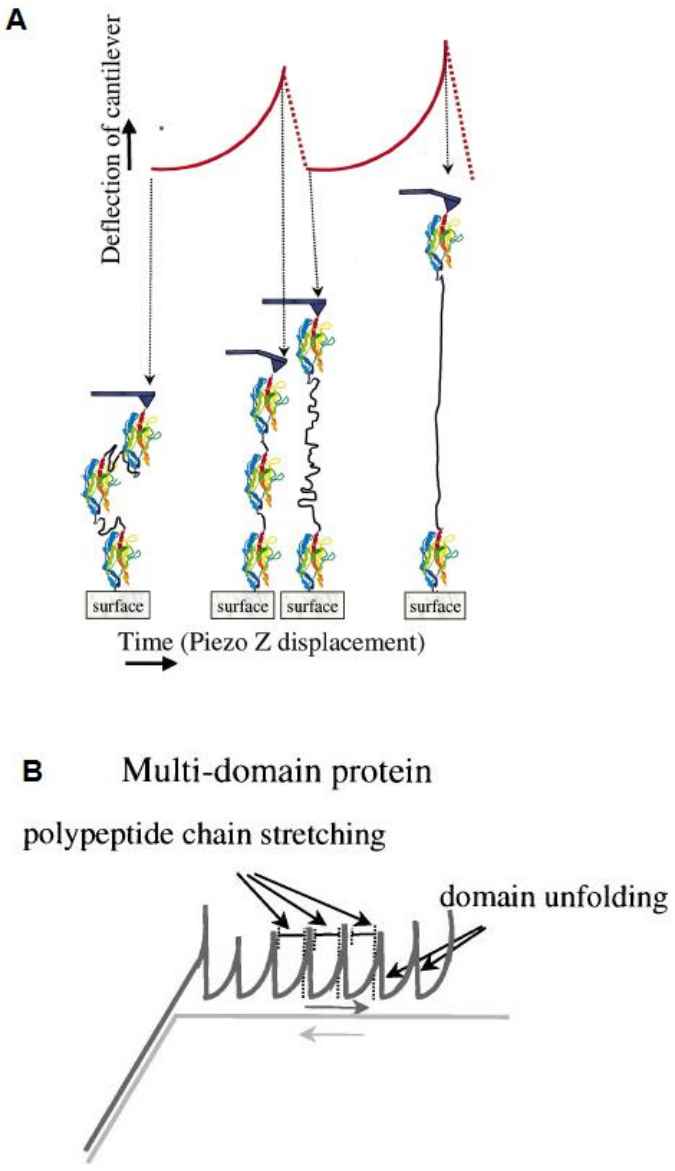

Figure 2-26: (A) Schematic showing the structural transitions in multi-domain proteins giving rise to multi-peak force curves. (B) Typical force curve obtained on stretching multi-domain proteins [191].

Initially the protein is extended and gives rise to a non-linear increase in the force profile (non-linear region of peak). When there is sufficient force, one of the domains within the protein unfolds and causes the cantilever to relax (deflection return to zero). The cantilever continues to pull the protein until the unfolded region reaches its fully extended length (e.g. contour length) and force is again sufficient to cause unfolding of another domain. This cyclic stretching and unfolding is typically observed as multiple “saw-tooth” peaks where the spacing between each corresponds to the full unfolded length of a single domain (Figure 2-26B). The specific force required to unfold the domains has previously been related the thermodynamic stability of the protein [191].

These single protein AFM measurements can be prepared through either 'picking' the protein off a surface whilst measuring the interactions with the AFM cantilever [195]. Alternatively, the protein can be attached to the AFM cantilever through functionalization and brought down to the surface to measure the interactions [174, 198-199]. By directly functionalizing the probe there is more freedom and repeatability in the measurements.

The forces generated when the AFM pulls on modular proteins such as FN is an important in the context of cell matrix interactions that usually occur involve either internal or external forces that act on, or are applied by, the cell [187]. These mechanical force and subsequent protein unfolding play a role in the polymerization of FN to its fibrillar form (i.e. fibrillogenesis), which helps to assemble the ECM around the cell [147].

2.6.6.3 Functionalized Tip Force Volume Mapping

More specific detail about surface characteristics can be gained using force-volume maps in conjunction with a specially functionalized tip. Interactions across a surface can be mapped to reveal areas on a sample that influence, or bind directly to the molecule attached to the tip. By simultaneously acquiring a topographical map, it is possible to correlate the specificity of interactions with topographical features.

Figure 2-27 shows a force volume map calculated from the rupture forces between a AFM tip functionalized with lectin and two different types of blood cells, group A and O. The lectin used (helix pomatia) has a high specificity for N-aetylgalactosamine-terminated glycolipids that are present in group A red blood cell membranes. The force volume map, using the adhesion values of the force curves (Figure 2-27A), shows higher adhesion only on some of the cells. In the topographical image (Figure 2-27B), the cells are indistinguishable from each other. As the lectin binds specifically to group A blood cells, the two different blood cell types can be identified by comparing the force volume adhesion map to the topographical map [200].

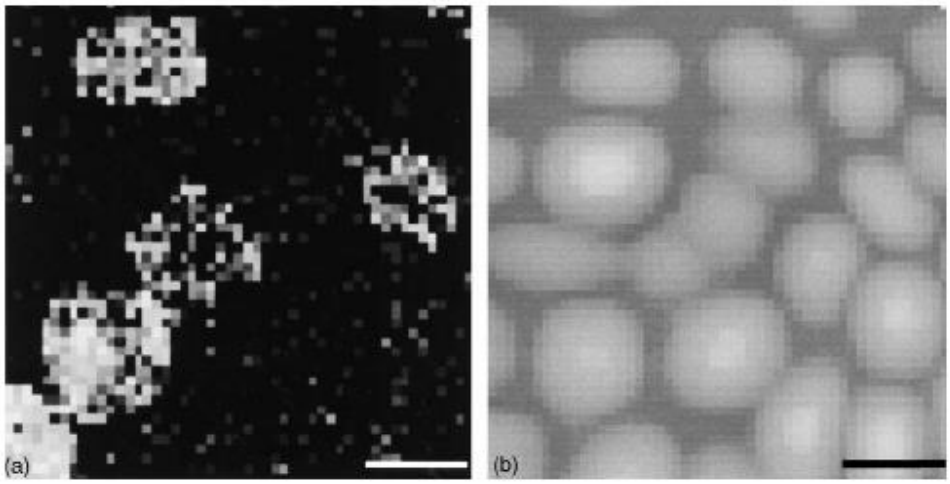

Figure 2-27: (A) Adhesion image of a mixed group of A and B blood cells. (B) Topographical image of the blood cells. Scale bars are 5 µm. [200]

This example highlights that force volume mapping using functionalized probes provides high resolution lateral information on the tip-surface interactions. This is particularly important for materials that are inhomogeneous, or contain bioactive components, that may support biological interactions with lateral dependency across a surface.

2.6.6.4 Importance of Studying Single Molecule

Interactions In order to determine how a material is influencing cellular response, the molecular basis of cell-material interactions must be understood. Using bulk methods such as immunofluorence staining and radioactive labelling will reveal information on essential protein interactions (adsorption and conformation). Methods that operate on the scale of a single cell, and smaller, offer far more information than bulk or visual techniques. This information is hugely relevant to the molecular mechanisms that trigger cell interactions. Using a cell adhesion molecule, such as the protein FN,

offers a much more specific and unprecedented control over studying cell-material interactions. The conformation of a protein can be visualised using microscopy methods [97, 152] or measured through time-of-flight secondary ion mass spectrometry [201] and circular dichromism [202-203]. However, actively measuring interactions occurring in real-time as a single protein binds to a surface is beyond these techniques. The previously described section on single molecule AFM (2.6.6.2, pg. 2-92) is able to address the ability to undertake real-time, direct measurements at the single molecular level.

3 Physical Properties of Polypyrrole Biomaterials

3.1 Introduction

Biomaterials that have multiple functions, or are bioactive, are the focus of intense interest in the tissue engineering sciences. This type of biomaterial provides a scaffold for physical support, as well as making use of additional properties to augment the function of the surrounding biological environment [15]. OCPs mmare relatively new to the tissue engineering field and appear to be excellent candidates for use as bioactive materials due to their biocompatibility [204] and ability to perform multiple bio-related functions, including topographical cell guidance [205-206], controlled drug release [32], mechanical stimulation and electrical stimulation [28, 207-208]. In particular, the inherent conductive properties of OCP are ideally suited for stimulating cells that respond to electrical signals such as muscle and nerve [209]. Their efficacy for nerve and muscle tissue regeneration [210] has been shown by the ability of OCP implants to promote in vivo cell growth through electrical stimulation [28]. Their ability to function in vivo has also benefited from incorporating biomolecules (biodopants) into the polymer, a process termed doping [211]. Optimising this process to introduce specific biomolecular interactions at the polymer interface, has seen the use of ECM

molecules [29, 106, 212]. By increasing the inventory of suitable biodopants, OCPs have potential to become more widely applicable to different cell and tissue types.

3.1.1 *Biomolecular Doping of Polypyrrole*

The process of doping is well characterised and generally occurs during the synthesis of the polymer [40]. Oxidation of the monomer results in polymerisation to produce a conjugated polymer chain with positive charges along its length. Anionic molecules in the growth electrolyte (dopants) are then incorporated to balance the charge on the polymer [106, 212].

When incorporated into the polymer, exposed chemistries of the biodopants are attributed to increasing biocompatibility by promoting favourable cell interactions at the polymer surface. ECM molecules such as HA and CS have previously been incorporated in the commonly used OCP, PPy [106, 212]. Biodoped PPy has been subject to several in vitro studies on the efficacy of the material as a cellular substrate. No difference was observed between single PPy/HA bilayers and PPy films doped with the non-biological molecule, poly(sodium 4-styrenesulfonate) (PSS), when assessing their cytotoxicity and ability to support pheochromocytoma rat cell(PC-12) growth [105]. However, the PPy/HA bilayers performed better when implanted into subcutaneous rat tissue for in vivo experiments. PPy/HA surfaces in a different study were observed have active HA groups available on the polymer surface, but had poor PC-12 rat cell adhesion when not in the presence of NGF [123]. PPy/HA and PPy/CS films have also been reported as biocompatible substrates for supporting osteoblast cell growth [29]. PPy/CS has been assessed for biocompatibility using human fibroblast cells, which showed good spreading and adhesion on the polymer substrates with and

without the use of foetal calf serum (FCS)[106]. Cell adhesion on the PPy/CS substrates without FCS was explained by the polymer surface interacting with the cell adhesion molecules via RGD sequences in the cell proteins, suggesting a role for the chemical specificity of the biodopant in enhancing the material biocompatibility.

3.1.2 *Dopant Influence on Physical Properties*

At present, ECM molecules are mainly chosen as biodopants under the premise that the polymer will have a higher binding affinity for cell adhesion molecules (e.g. integrins). However, the incorporation of a biodopant into the polymer, irrespective of its biological activity, will inevitability give rise to characteristic physical properties specific to the dopant-polymer combination. Variations in morphologies of PPy have been observed for different dopants, which are evident in many studies of PPy across a range of dopants [20, 30, 62, 105, 108, 161, 167, 170, 213-214]. For example, the incorporation of HA into PPy was qualitatively shown to result in rougher and more brittle films when compared to PPy/PSS films [105]. For PPy/CS films, the surface roughness was observed to increase as a function of the CS dopant concentration[106]. Hence, in an effort to improve the biocompatibility through chemical specificity of the dopant, ensuing changes in the physical properties of the polymer can also occur. Beneficial or detrimental changes to the properties in terms of influencing cell growth may account for the observed variations in the dopant performance.

3.1.3 *Selected Biodopants*

To gain a better understanding of the effect of different biodopants on the physical properties of OCP, we studied PPy films doped with ECM components using AFM. We specifically investigated PPy films that were assessed in our recent study on the growth and differentiation of primary skeletal muscle cells[20]. More specifically, HA and CS were the chosen biodopants in both these studies, as they can be found in the ECM and provide specific growth, cell regeneration and adhesion factors[106, 215]. DS was chosen as another biodopant and acts primarily as an anti-coagulant, though also plays a role in the immune system. Of the non-biological dopants for comparison, the anion para-toluenesulfonic acid is a relatively small and simple molecule compared to the biodopants and has been studied extensively for its electroactive properties [208]. The polyelectrolyte poly(2-methoxyaniline-5-sulfonic acid) was also included as a non-biological dopant. PMAS as a large counter-ion is less likely to leach out of the polymer regardless of electrochemical state. Both PPy and PMAS are also redox active as well, which gives rise to multiple switching abilities of a PPy/PMAS composite [216].

3.1.4 *Characterising Physical Properties*

The quantification of nanoscale physical properties of the PPy biomaterials is an important foundation in understanding how the biomolecular dopants change polymer properties. AFM was used to measure the physical properties commonly recognised as stimulus cues for influencing cell behaviour, including topography [73], roughness [74-75] and Young's modulus [79]. In contrast to studies assessing the bulk properties of free-standing OCP films[217], AFM allowed probing of the nanoscale properties, which

is relevant considering that cellular interactions with the polymer films vary over similar length-scales.

3.2 Materials and Methods

3.2.1 Reagents

The pyrrole monomer was obtained from Merck and distilled prior to use. The chemicals used as the dopants were the sodium salts of pTS, HA, DS, CS and PMAS. CS and DS were obtained from Sigma, pTS from Merck and HA from Fluka. All solutions were prepared with deionised Milli-Q water (18.2MΩ).

3.2.2 Preparation of Biodoped Polypyrrole

Gold coated mylar was firstly prepared by cutting into strips of 0.5 cm by 2 cm area and then cleaned with methanol and Milli-Q water. Gold coated Mylar (18 Ω/square) was purchased from CPFilms Inc (USA). An aqueous monomer solution of 0.2 M pyrrole and 2 mg/mL of the dopant was degassed in N_2 for 10 min prior to polymerisation of the polymers. PPy films were grown galvanostatically at a current density of 0.25 mA/cm^2 for 10 min in the aqueous monomer solution using an eDAQ EA161 potentiastat. Polymer growth was performed in a standard 3-electrode electrochemical cell with the gold coated mylar as the working electrode, a platinum mesh counter electrode and Ag/AgCl reference electrode. After growth, the films were washed with Milli-Q water, gently dried with N_2 gas and placed in petri dishes until use.

3.2.3 Profilometry

A Veeco Dektak Profilometry system (Veeco Instruments Inc., NY) was used to measure the thickness of the films in air. A stylus force of 3.0 mg was used and three line

profiles were recorded on each film. For each doped film, three film samples were analyzed.

3.2.4 *Topography*

The polymer films were imaged in 0.1 M NaCl using a MikroMash CSC21 cantilever (spring constant of ≈2 N/m) in AC mode with an MFP-3D AFM (Asylum Research, CA). Scans of 10 µm and 2 µm were performed at a scan rate of 1 Hz. The RMS roughness (R_{RMS}) values of the scans were calculated using the Asylum Research analysis program in Igor Pro software (WaveMetrics, OR).

3.2.5 *Force Measurements*

Force measurements were conducted using a MikroMash cantilever with thermally calibrated spring constant of 37 N/m. The polymer films were pre-soaked in 0.1 M NaCl for 24 h to ensure full hydration and then the measurements performed in fresh NaCl solution. Each film was firstly imaged over a 20 µm square area in AC mode, with five points within the image selected as the X–Y positions of the force measurements. The AFM tip could be accurately moved to these positions using the closed-loop feedback system controlling the X–Y piezos. At each point, a minimum of five force curves were performed using a scan rate of 0.5 Hz and maximum load of 200 nN. The force versus distance curves were converted to force versus indentation (F–I) curves and then fitted by the Hertz model to quantify the Young's Modulus, as described in Chapter 2-2.5.1 By using the same cantilever tip for the measurements, we could also further eliminate variations in the tip radius and shape to give a relative comparison of the modulus between the differently doped films.

3.2.6 *Electrochemical AFM*

EC-AFM was implemented by positioning a 2-dimensional electrochemical cell on the AFM sample stage. The electrochemical cell was made out of a Teflon block that consisted of a u-shaped fluid well etched around a platform. A PPy/dopant coated gold Mylar strip was glued onto the platform and acted as the working electrode. A platinum mesh counter electrode was positioned in the fluid well and a silver wire reference electrode was placed alongside the polymer film. Measurements were carried out in0.1M NaCl solution, which was injected into the fluid well to immerse the three electrodes. Five points were selected on the film using the top-view optics of the AFM. The cantilever tip was then brought into contact with the polymer surface, with the Z-piezo feedback keeping the deflection of the cantilever constant (i.e. at the deflection set-point value). A biphasic pulse voltage with a ±100 mV potential range was applied to the polymer film at different frequencies of 0.1, 1 and 10 Hz using an eDAQ EA161 potentiostat. A minimum of 20 pulses were performed for each frequency at the five positions on the polymer film. During the applied potential, the displacement due to expansion and contraction of the film (i.e. electromechanical actuation) was measured by recording the Z-piezo voltage output. For these recordings, the displacement of the film caused a deflection of the cantilever, which was maintained at the set-point by adjusting the height of the Z-piezo. The latter could be calculated from the Z-piezo voltage output using the sensitivity of the piezo and corresponded to the actual height change of the sample. The Z-piezo height was recorded simultaneously with the applied potential and current signals using an eDaq recorder and e-Chart software

3.3 Results

3.3.1 Morphology

AFM imaging revealed that each dopant-polymer film displayed a nodular morphology common for PPy films [6][7][8] (Figure 3-1), with the exception of PPy/PMAS. The morphology of PPy/CS (Figure 3-1C), PPy/DS (Figure 3-1D) and PPy/pTS (Figure 3-1F) were very similar, each with uniformly sized nodules, while PPy/HA had larger irregularly sized nodules (Figure 3-1E). PPy/PMAS had a smoother morphology comprised of particulate surface features that were significantly smaller than the nodules of the other films (Figure 3-1A). In some cases for PPy/PMAS, the images showed a 'smeared' appearance, indicating that the surface consisted of a softer material that was easily displaced/damaged by the AFM tip during scanning (Figure 3-1B). The surface morphologies in Figure 3-1 were consistently observed for each dopant-polymer combination in many AFM scans and on different film samples.

3.3.2 Roughness

A direct comparison of the film roughness for each polymer-dopant is shown in 3-dimensional height images (Figure 3-2). Each image has a comparable z-height scale (500 nm maximum) and was taken over a 10 µm scan area. The RMS roughness (R_{RMS}) values calculated for each type of film are shown in Figure 3-2F.

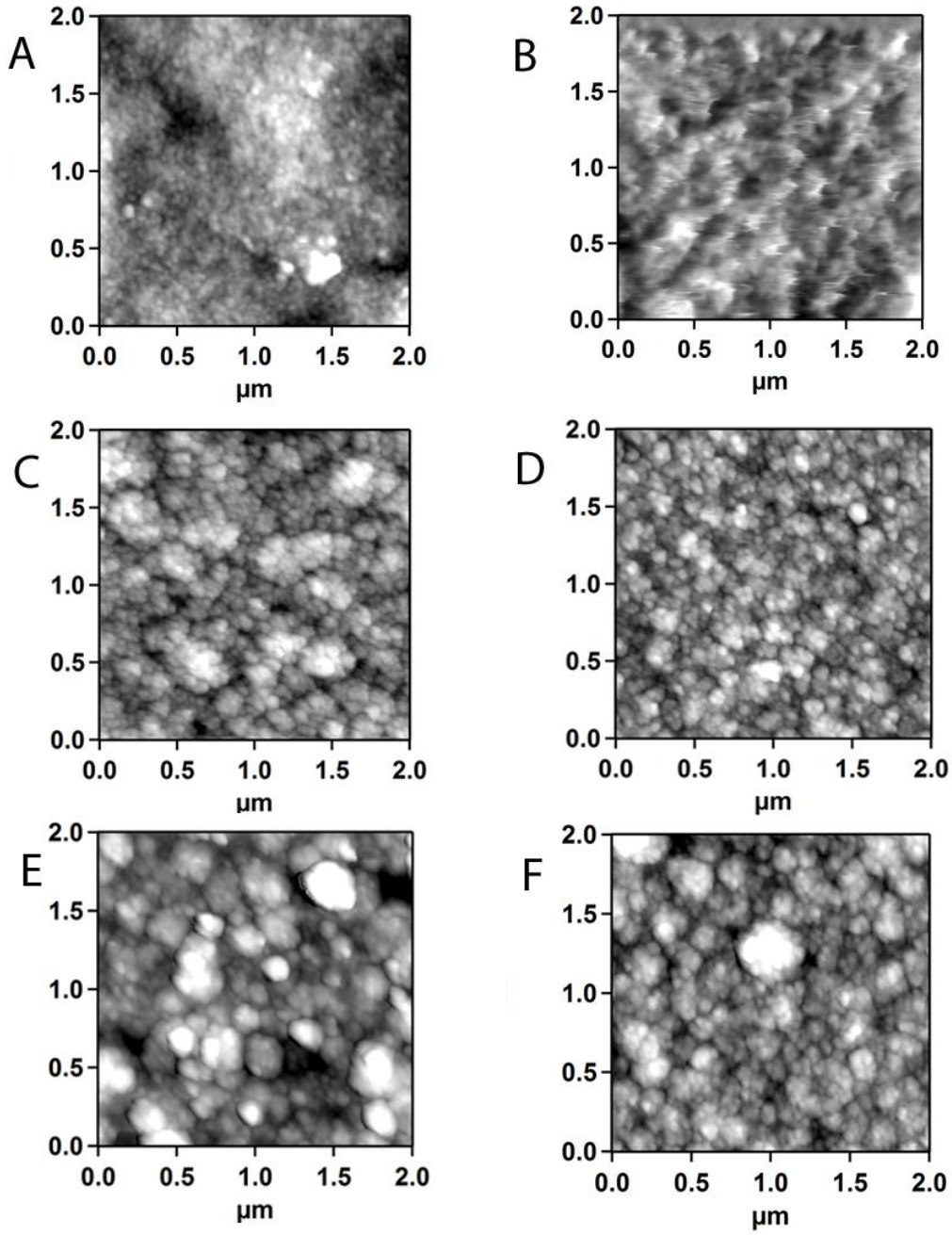

Figure 3-1: AFM 2 µm scans. (A) PPy/PMAS, (B) PPy/PMAS, (C) PPy/CS, (D) PPy/DS, (E) Ppy/HA, and (F) PPy/pTS. Z range of 200 nm.

Differences in the roughness for PPy/CS, PPy/DS, PPy/pTS and PPy/HA were reflected by differences in the dimensions of their nodular structures. In particular, PPy/HA and PPy/pTS were the roughest films for 10 µm scans with R_{RMS} values of 32.3 nm and 30.1 nm, respectively. The next roughest film over 10 µm scans was PPy/DS (25.2 nm), while PPy/CS and PPy/PMAS were significantly smoother with values of 12.1 nm and 5.8 nm, respectively. R_{RMS} values were also calculated for the 2 µm scans in Figure 3-1 and compared in Figure 3-2F.

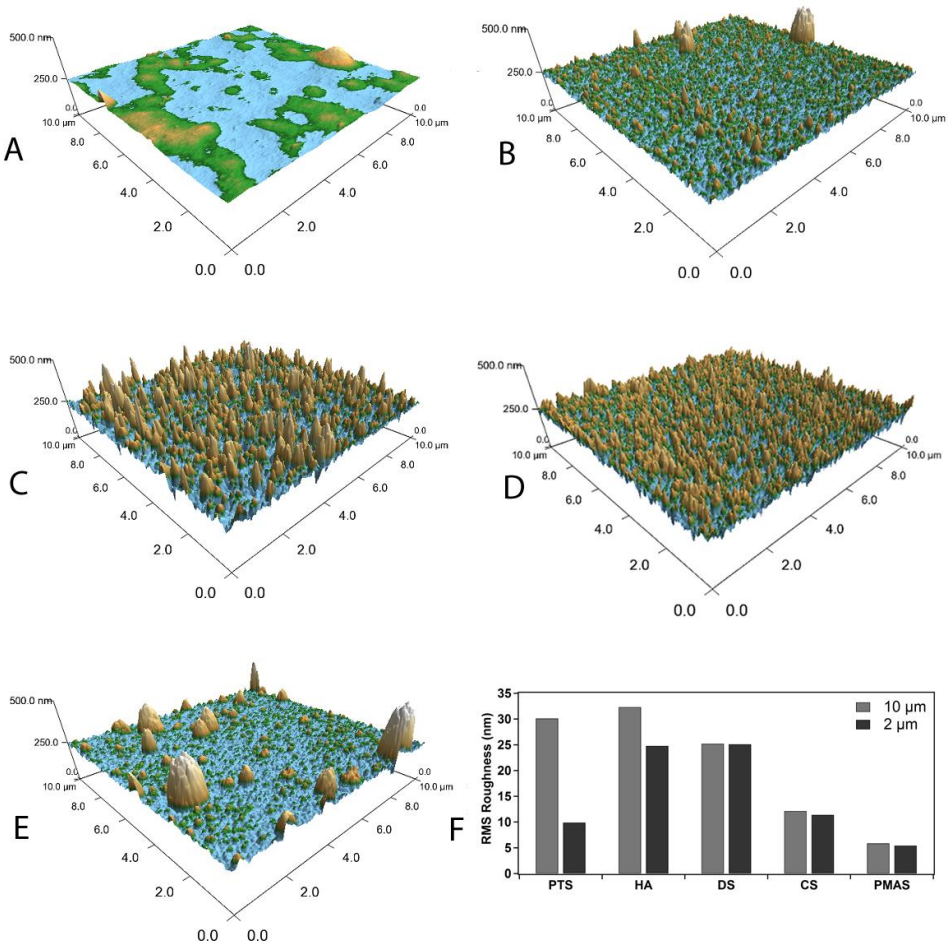

Figure 3-2: 3-dimensional height images of 10 µm AFM scans. (A) PPy/PMAS, (B) PPy/CS, (C) PPy/HA, (D) PPy/DS, (E) PPy/pTS, and (F) Histogram showing the R¬RMS values for each film and scan areas of 2 µm and 10 µm.

For these 2 µm scans, PPy/HA had a lower value of 24.8 nm and PPy/pTS had a significantly lower value of 9.9 nm. This decrease in the roughness for the smaller scans was due to PPy/HA and PPy/pTS having a non-uniform surface morphology consisting of larger nodules structures with smoother intervening areas (i.e. smaller nodules). The larger nodules, particularly in the case of PPy/pTS, were increasingly observed in the larger scans. In contrast, the R_{RMS} values for 2 µm scans of PPy/DS (25.1 nm), PPy/Cs (11.4 nm), and PPy/PMAS (5.4 nm) were not significantly different to the larger scans, indicating that these dopant-polymers had a more uniform nodular morphology across the surface.

3.3.3 *Thickness*

Height profiles of each polymer-dopant film obtained from the profilometry measurements are shown in Figure 3-3A, with their mean thickness values given in Figure 3-3B. The thickest film was PPy/DS with a mean value of 342 ± 11 nm and the thinnest film being PPy/PMAS with a value of 150 ± 19 nm. PPy/pTS and PPy/HA had similar thicknesses of 276 ± 25 nm and 264 ± 24 nm, respectively, and PPy/CS was measured to have a thickness of 228 ± 19 nm.

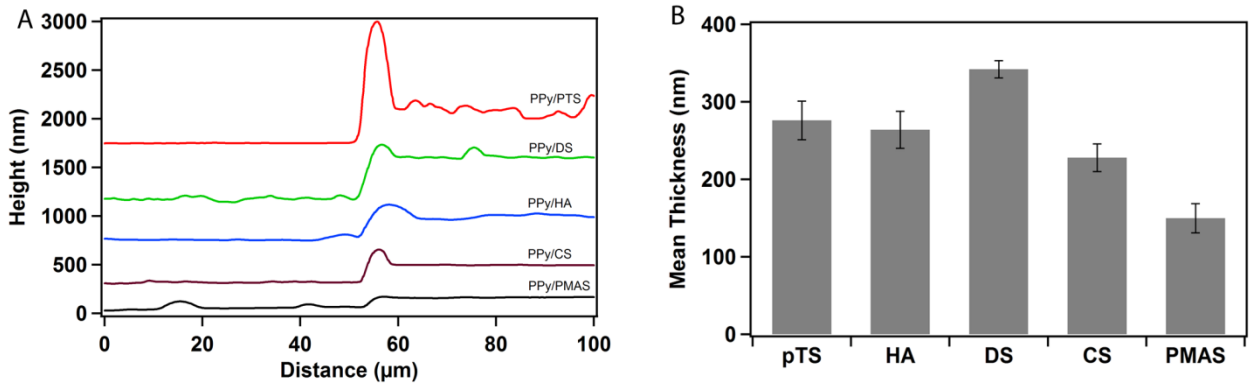

Figure 3-3: (A) Representative profiles of each film (B) Histogram of mean film thickness. Error bars are standard error

3.3.4 *Young's Modulus*

Force versus indentation curves indicated that PPy/PMAS was the softest film due to the larger indentation distances being measured at applied forces equivalent to the other films (i.e. the gradient of the curve is lower for softer films) (Figure 3-4A). A relative comparison showed that PPy/CS was stiffer than PPy/PMAS, followed by the order of PPy/DS, PPy/HA and PPy/pTS. The latter three were significantly stiffer than PPy/PMAS and PPy/CS. Hertzian fits to the curves provided a quantitative comparison of the Young's modulus for each of the polymer-dopant combinations (Figure 3-4B). PPy/PMAS had a significantly lower mean modulus value of 30 ± 2.0 MPa compared to PPy/CS, which recorded the next highest value of 293 ± 31 MPa. Similar values for PPy/DS (706 ± 44 MPa) and PPy/HA (660 ± 49 MPa) were significantly higher than PPy/CS and PPy/PMAS. PPy/pTS recorded the significantly highest value of 1000 ± 87 MPa compared to all other films.

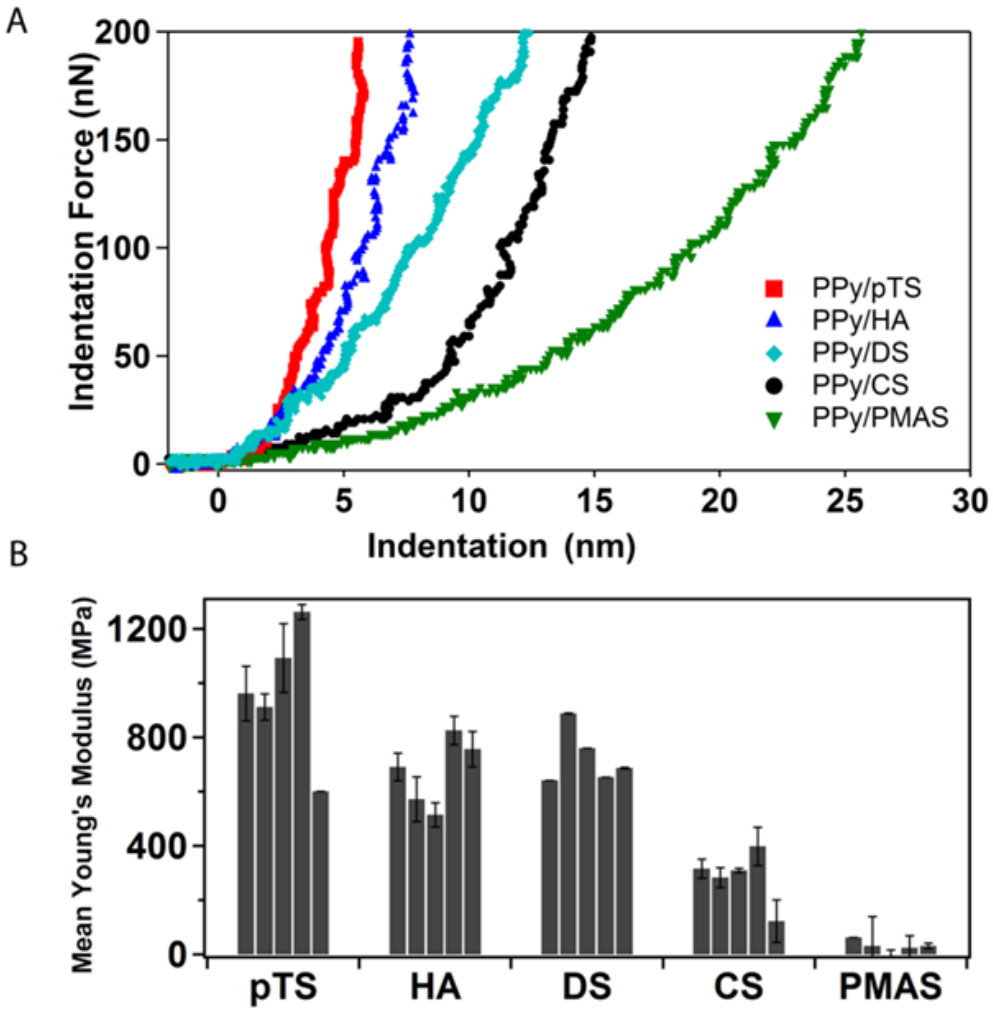

Figure 3-4: (A) Representative force-indentation curves for each film. (B) Histogram of mean Young's modulus, each column represents the average value on one spot on the surface. Error bars are standard error.

Significant variation in the modulus values was also observed across the five different positions within each film sample (Figure 3-4B), indicating that the modulus of the films was not uniform across the surface. For instance, PPy/pTS recorded a high modulus value of 1250 MPa in one position, but also recorded a 50% modulus decrease of 600 MPa in another position. Similar variations of between 10-50% within the samples were also observed for the other films.

3.3.5 *Mechanical Actuation*

During the application of the biphasic voltage pulse, the polymer films undergo expansion and contraction (electromechanical actuation) due to the diffusion of electrolyte ions in and out of the polymer to compensate for a charge imbalance on the polymer backbone. Figure 3-5A shows an example of the applied biphasic potential (dashed red), current signal (thin black) and converted Z-piezo height signal (thick green) for the mechanical actuation of PPy/CS when electrically stimulated at 0.1 Hz (i),1 Hz (ii), and 10 Hz (iii).

During the application of a positive voltage (oxidation) pulse, an increase in the Z-piezo signal indicated that the height of the sample increased, or the film had expanded. The Z-piezo signal then decreased, indicating the film contracted during the negative voltage (reduction) pulse. Figure 3-5A (i) shows that the Z-piezo signal plateaued during the constant potential region of the pulse at the slowest stimulation of 0.1 Hz, indicating that the film had reached maximum expansion/contraction during the stimulation cycle. At 1 Hz (Figure 3-5A,i), the actuation decreased and showed a triangular profile, while no actuation was discernable at 10 Hz (Figure 3-5A, iii). Differences in the polarity of actuation were observed for the polymer films. PPy/CS, PPy/DS, PPy/HA and PPy/PMAS were all observed to expand during reduction of the films, while PPy/pTS expanded during oxidation. The observed decrease in actuation with an increase in the electrical stimulation frequency was expected due to the time-limited diffusion processes of the dopant ions moving in and out of the polymer (i.e. larger actuation is achieved at lower frequencies because the ions have more time to diffuse into the polymer.

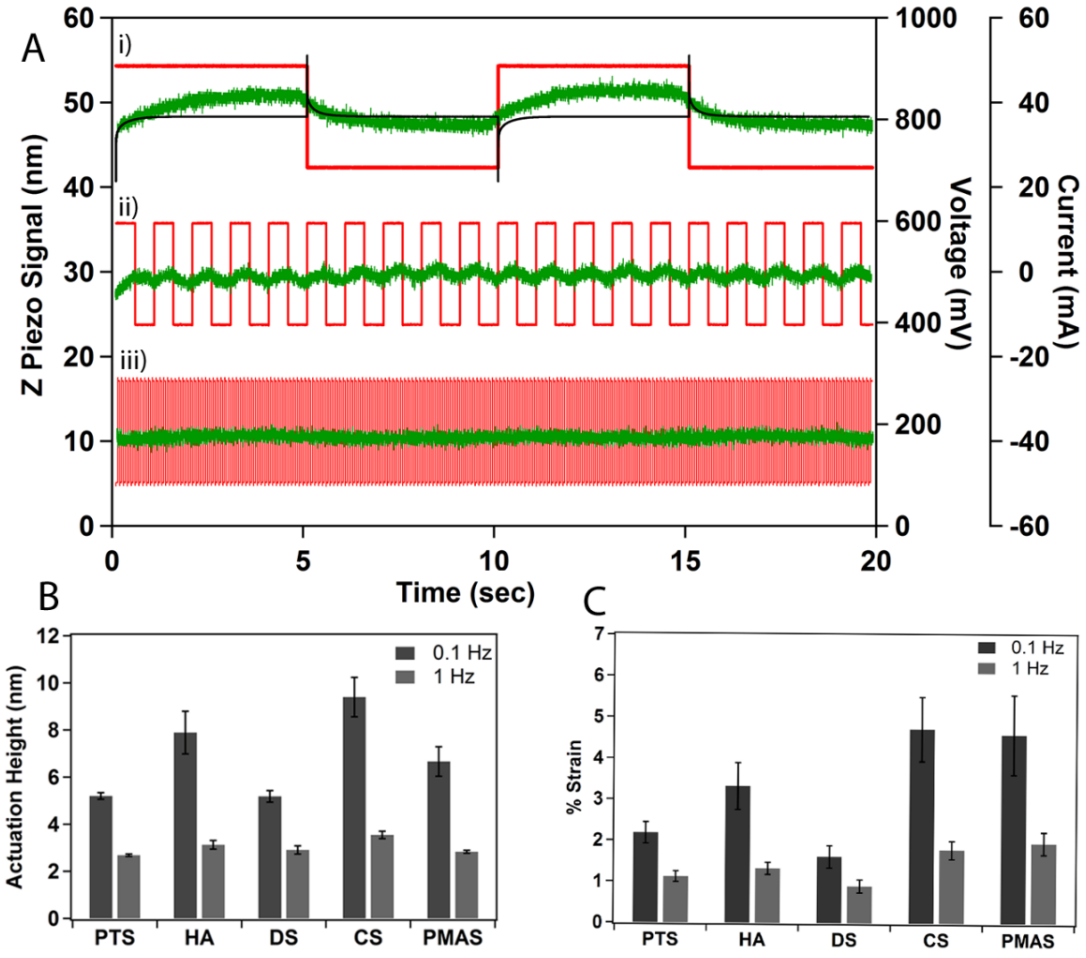

Figure 3-5: (A) Example PPy/CS data for biphasic waveform stimulation and actuation with frequencies. Red represents the voltage signal, green represents the Z piezo signal and black represents the current signal; (i) 0.01 Hz (ii) 0.1 Hz (iii) 1 Hz. (B) Histogram of mean actuation height for 0.1 and 1 Hz stimulation. (C) Histogram of mean % strain for 0.1 and 1 Hz stimulation. All error bars are standard error.

At 0.1 Hz, PPy/CS (9.4 nm) showed the greatest actuation height followed by HA (7.9 nm)> PMAS (6.7 nm)> DS (5.2 nm) and pTS (5.2 nm) (Figure 3-5B). At 1 Hz, the actuation height consistently ranged from 2 to 4 nm, with no significant differences observed between the dopant–polymer films (Figure 3-5B). Figure 3-5C shows the maximum strain calculated using the mean thickness value of each film. PPy/CS (4.7%)

and PPy/PMAS (4.6%) showed significantly higher strains at 0.1 Hz compared to PPy/HA (3.3%), PPy/pTS (2.2%) and PPy/DS (1.6%). A similar trend in the strain was observed for the films at 1 Hz.

3.3.6 *Correlation of Physical Properties*

Table 3-1 shows a summary of the quantified values for the different physical properties, including morphology, roughness, modulus, actuation and strain. In particular, when the polymer films were arranged in order of modulus, the modulus values appeared to show a correlation with the roughness and strain. For example, a modulus increase correlated with an increase in roughness, while films with the lowest modulus (CS and PMAS) also had significantly higher strain values when compared to the other films.

Table 3-1: Summary of physical properties for each dopant–polymer. Errors are standard error.

Dopant	Morphology	Roughness (nm)		Thickness (nm)	Young's Modulus (MPa)	Actuation (nm)		% Strain	
		2 µm	10 µm			0.1 Hz	1 Hz	0.1 Hz	1 Hz
pTs	Nodular	9.88	30.10	276 ± 25	1000 ± 87	5.2 ± 0.1	2.68 ± 0.05	2.2	1.1
HA	Nodular	24.76	32.30	264 ± 24	706 ± 44	7.9 ± 0.9	3.1 ± 0.2	3.3	1.3
DS	Nodular	25.08	25.20	342 ± 11	660 ± 49	5.2 ± 0.2	2.9 ± 0.2	1.6	0.9
CS	Nodular	11.38	12.13	228 ± 18	290 ± 31	9.4 ± 0.8	3.54 ± 0.2	4.7	1.8
PMAS	Smooth	5.43	5.84	150 ± 19	30 ± 2	6.7 ± 0.6	2.83 ± 0.06	4.6	1.9

To observe these correlations more clearly, Figure 3-6A and Figure 3-6B shows plots of the roughness and strain versus the modulus. The roughness and strain were confirmed to have a positive and negative correlation with the modulus, respectively. As a consequence of these correlations, a 3-dimensional plot in Figure 3-6C shows that the physical property signatures of the different films tended to group together according to having either a: 1) low modulus, low roughness and high strain (PMAS and CS), or 2) high modulus, high roughness and low strain (DS, pTS and HA).

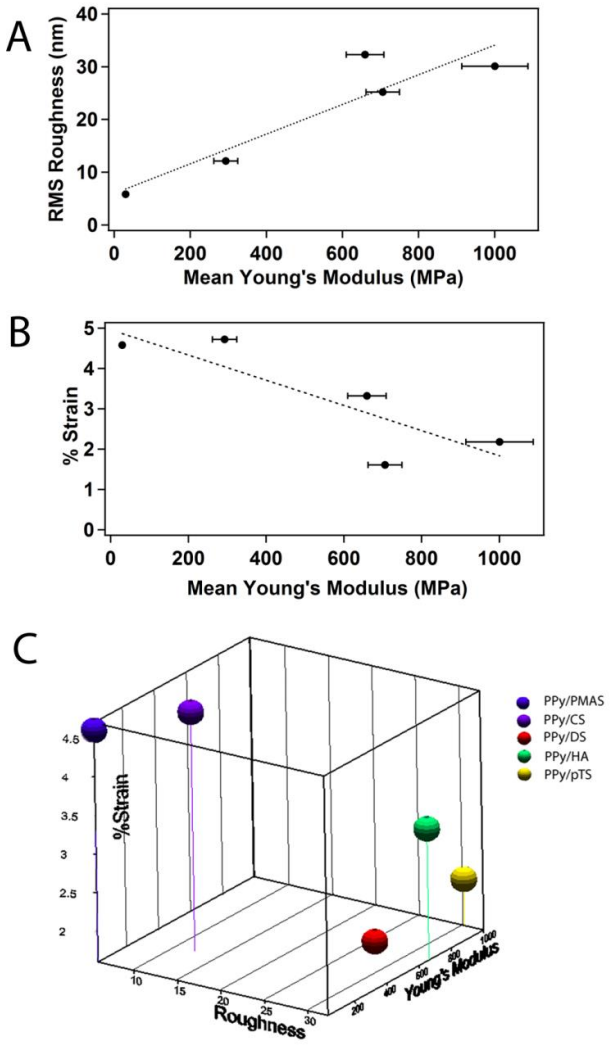

Figure 3-6: A. RMS roughness vs. mean Young's modulus for each dopant-polymer film. B. Strain vs. mean Young's modulus for each dopant-polymer film. C. 3-dimensional plot for each polymer-dopant film using strain, roughness and Young's modulus to define the positions.

3.4 Discussion

3.4.1 *Material Properties of Biodoped Films*

3.4.1.1 Topography

The incorporation of four of the dopants (CS, DS, HA, pTS) resulted in subtle variations in the commonly observed “nodular” Ppy morphology[57]. These variations were due to differences in the size and frequency of the nodule structures and quantitatively represented by differences in their roughness values. PPy/PMAS films lacked the distinct nodular morphology and were significantly smoother, as confirmed in our recent studies on the use of PPy films for mammalian cell growth [20]. Since the PMAS dopant ion is itself a conducting polymer, the significant difference in its film morphology can occur during polymerisation through not only electron transfer in the PPy network but also the PMAS chains[216]. Oxidation of the PMAS may also provide additional electrocatalytic sites for pyrrole oxidation during the film growth[216].

3.4.1.2 Roughness

Although these film morphologies were similar to those in our related study [20], there were differences in the absolute roughness and thickness values. This related study was done in tandem with the work presented here, correlating the PPy films with skeletal muscle cell adhesion and differentiation. Ppy/pTS roughness values (100 nm) for our previous study were significantly higher than the values obtained here. Conversely, roughness values for DS (7.5 nm) were significantly lower. Differences in these roughness values coincided with differences in their film thicknesses, where PPy/pTS (1850 nm) and DS (31.8 nm) in our previous study were significantly thicker

and thinner, respectively, when compared to this study. As PPy films generally become thicker and rougher with longer polymerisation times [20], this suggests that the extent of PPy/pTS and PPy/DS film growth differed between the two studies, even though the same polymerisation solution and growth times were used. It is noted that different electrochemical cells were used, thus any variations between the experimental setups (e.g. cell volume, distance between electrodes, cell resistances) may cause differences in the deposition efficiencies of the films. Despite these differences, the relative trends in both studies were similar in that pTS and HA were significantly rougher, followed by DS, while CS and PMAS were the smoothest films.

3.4.1.3 Young's Modulus

The Young's modulus of the different films after 24 hr in electrolyte ranged from 0.030-1.000 GPa, indicating a significant effect of the dopant on the modulus of the Ppy material. For comparison, a modulus of 1.5 GPa has been reported for free-standing, 32 µm thick benzenesulfate doped PPy films in air[218]. The elasticity of these films reduces to ≈ 0.7 GPa after immersion in electrolyte for 60 for 1 hour. Other conducting polymers such as PEDOT/PSS have a modulus ranging from 1.5–3 GPa for free standing films in air, where the value decreases with an increasing humidity range of 25-65% [219-220]. For modulus values determined directly in electrolyte, PPy free-standing films have typical values of 0.1 – 0.8 GPa[70-71, 221], which depend on the voltage applied to the polymer during the tensile test measurement. Our modulus values obtained from the AFM measurements are comparable to the above values and also recent studies using AFM to directly measure the modulus of supported PEDOT/PSS (1.3 GPa)[222] and PPy/PSS (0.6 – 1GPa)[44, 218] films in air and

electrolyte, respectively. The former study confirmed the reliability of their AFM measurements by calibrating the technique using a set of reference samples of known modulus (independently measured using DSI testing). Modulus values for our samples may also equate with higher than expected values when considering the differences between supported nanometer thick films and the majority of measurements done on free-standing micron thick films. Polythiophene films that reach < 500 nm thickness have shown a 3-fold increase in modulus[223]. Nanometer thick conducting polymer films are also generally considered to be denser and less porous, thus the uptake of solvent and associated increase in plasticization of the polymer may be less pronounced for these films.

By using the same cantilever tip for the measurements, a direct relative comparison of the modulus could be made between the different films. In particular, the PPy/PMAS films not surprisingly had the lowest modulus (30 MPa), which was also qualitatively indicated by damage to the film's surface caused by lateral forces imposed by the AFM tip during imaging. PPy/PMAS has hydrogel-like properties and its high water content of > 90%[216] is expected to contribute to the observed low modulus. The significant increase of modulus for the other four doped films (pTS, HA, DS, CS) may be associated with their reduced water content, though the exact reason for the differences requires further investigation. Attempts were made to measure the cross-sectional height profile of the films when dried and hydrated, yet no significant height change in any of the films due to swelling was observed.

The significant variations of up to 10-50% in the modulus observed across the surface of the films are likely to depend on variations in the local polymer structure and

properties such as porosity, density and/or degree of crystallinity. Such observations highlight that the bulk modulus values commonly obtained from tensile testing of free-standing films[218] represent the average of significant variations in the elastic properties occurring at the micro- and nanoscale domains. Quantifying the magnitude of these lateral variations is expected to be just as important for understanding how living cells respond to the modulus of these polymer substrates. Further measurements mapping the modulus with higher spatial resolution are required to give a comprehensive statistical correlation between the modulus and polymer surface structures.

3.4.1.4 Mechanical Actuation

EC-AFM measurements revealed that all the films showed an actuation response within the small potential window (± 100 mV) of the biphasic pulse waveform, indicating the possibility of using analogous clinical stimulation protocol to generate a mechanical stimulus through the films. Calculated strain values indicated that films with both the lowest modulus and thickness values, PPy/PMAS and PPy/CS, had the highest strain. Assuming the PPy films obey Hooke's law [221] and by neglecting the effect of the external force of the AFM tip, these observations suggest that the mechanical actuation follows the relationship that films with lower modulus will achieve greater strain. In this case, the strain induced in the polymer is caused by the applied potential and the intercalation of ions that provide the driving force to move the polymer chains apart (i.e. film expansion). The lower thickness values of PPy/PMAS and PPy/CS are also expected to contribute to an increase in strain due to the reduced path length for ion diffusion into the polymer [44].

3.4.1.5 Correlation of Physical Properties

The significant partitioning of the physical properties, particularly for PPy/HA and PPy/CS, in Figure 3-6 is interesting given they are both ECM molecules and have similar chemical structures based on the GAGs. The only difference between these two molecules is that HA is non-sulfated, while CS carries a sulfate group on the 4 position of the N-acetyl-galactosamine monosaccharide. A higher degree of electrostatic cross-linking and increased microporosity has been linked to an increase in the number of sulfonate groups on the dopant[68]. This has shown to improve solvent uptake and ion diffusion through the polymer, and may account for differences in their physical properties.

As described above, the correlation between the Young's modulus and the electrochemically induced strain can be used to plausibly explain the observed correlation between these two parameters. The correlation may also be influenced by other factors including ion diffusion coefficient and porosity, though the clear differences between the films suggests that the modulus to some extent is having a dominant causative effect on the strain. The reason for the correlation between modulus and surface roughness is however less clear. An increase in roughness of PPy films is typically associated with the formation of larger nodules or "cauliflower-like" structures[213], suggesting that these structures may underlie the observed increase in modulus. However, as mentioned above, such correlations were not observed when the position of the force measurements were cross-referenced with the film morphologies

from the AFM images. Whether the observed correlation is due to a direct causative effect or other influencing factors, the overall picture emerging from quantifying the different physical properties in this study is that each parameter is inextricably linked and perhaps better addressed as a consortium of properties. This characteristic of conducting polymers has also been made apparent from extensive work done on free-standing polymer actuators [224].

3.4.2 *Implications of Dopant-Related Properties on Muscle Cell Differentation*

To evaluate the performance of the different biodopants for muscle regeneration, we recently investigated the proliferation, adhesion and differentiation of primary muscle cells on PPy films doped with the same ECM and non-biological molecules [20]. The study characterised the electroactivity, wettability, film thickness, topography and roughness of the differently doped PPy films and attempted to correlate these properties with the ability to support muscle cell growth. While all the substrates supported cell adhesion and proliferation to varying degrees, it was found that the dopants, HA and pTS, were significantly worse in supporting cell differentiation (i.e. muscle fibre formation) compared to the other dopants. PMAS and CS, along with DS, performed well in supporting cell differentiation, which was associated with increased cell adhesion to their surfaces. Increased cell adhesion and hence a greater capacity for muscle fibre formation was shown to correlate with polymers of low surface roughness, though the effect of the dopant chemistries could not be ruled out, particularly in the case of HA. With the aim of this study being to further correlate the

physical properties of the same films used in the above study, the observed clustering of the properties in Figure 3-6C conveys a deeper intricacy to the influence of the physical properties on muscle cell differentiation. In particular, the results open up the possibility of exploring the additional effect of modulus, which may exert a greater influence on the muscle cells as the films become rougher. The modulus of a material is an important parameter that when tuned to match the modulus of the tissue from which the cells are derived can significantly improve the biocompatibility. Skeletal muscle tissue has a modulus of 12–15 kPa, an order of magnitude less than the conducting polymers. These cell types prefer to differentiate on gel substrates of similar stiffness (~12 kPa), rather than on glass or much softer gels [79, 225]. Furthering our ability to lessen the modulus of PPy by introducing the dopants such as PMAS is an encouraging step towards controlling the modulus whilst maintaining the conductive properties of the polymer.

3.5 Concluding Remarks

The study highlights that both PPy/PMAS and PPy/CS films, which have previously been shown to support the differentiation of skeletal muscle cells [20], have a low surface roughness and modulus in comparison to the other dopants. PPy/HA and PPy/pTS films on the other hand have significantly higher surface roughness/modulus and conversely found to be poor substrates for supporting muscle cell differentiation. These results indicate a correlation between the physical properties of the films and efficacy for supporting muscle cell differentiation.

The study also reveals a relationship between the magnitudes of the different physical parameters and as a result the effect of the modulus on the cell growth may come into play as the surface roughness of the films increases. These findings are important as they emphasize the importance of considering both the biological activity of the dopant and the effect it has on the material properties of the substrate being fabricated.

4 Phase Shift Imaging of Polypyrrole Biomaterials

4.1 Introduction

4.1.1 *Surface Property Influence on Cellular Response*

The distribution of surface properties is important as it affects cell adhesion molecules and cellular attachment [94, 97, 100, 226]. Using a range of polymeric and metallic biomaterials, Hallab *et al.* [214] found a complex relationship between surface energy and roughness, with materials of lower surface energy having an increase in cellular adhesion with increased surface roughness. Materials with high surface energy however demonstrated negligible change in cellular adhesion with increasing roughness. Protein adhesion can also be influenced by surface charge and in turn the nature of the dopant will influence surface energy. The adsorption of three different proteins, lysozyme, myoglobin and α-lactalbumin, was measured on PEG surfaces with varying surface energy [99]. Lysozyme, a small stable protein, responded in a manner similar to a hard colloid particle when interacting with the varying surfaces. The two large, more flexible proteins however had a far more complex relationship with surface energy as the proteins changed conformation when adsorbing to the surfaces. Hence

studying the surface properties of our polymers will aid the understanding of protein and cellular interaction with these biomaterials.

4.1.2 *Revealing Heterogeneity of OCPs*

The dopant chemistry influences cell-surface interactions either through direct interactions with the cell membrane or via ECM components (e.g. HA, CS, FN, collagen) that bind cell surface receptors (e.g. integrins) to mediate cell adhesion and form part of the continuum with the cytoskeleton for cell signalling. However, little is known about the effect of doping biomolecules on the nanoscale surface chemistry of conducting polymers, particularly possible heterogeneity in surface charge/energies or specific distribution of exposed regions of the doped biomolecule at the interface. Fundamental forces such as hydrogen bonding, electrostatic, and hydrophobic forces can influence the interaction of cell mediation proteins in the ECM.

Using dynamic mode (AC mode) AFM we can further elucidate variations in surface properties of PPy/CS and PPy/HA substrates on a lateral nanometric scale, which is relevant to the length scale of cellular interactions. This mode of AFM is used to acquire topographical information but is also sensitive to local variations in surface properties (e.g. surface stiffness) that cause changes in the frequency, amplitude and phase signal of the cantilever as it is oscillated during scanning across the sample. In particular, changes in the phase signal can be attributed to non-dissipative and dissipative interactions between the tip and sample [227-228] and recorded simultaneously with the topography image during scanning.

4.1.3 *Phase Imaging of OCPs*

In the few studies using AFM phase imaging to study OCPs, phase separated regions in PA and cellulose acetate blends were attributed to differences in the stiffness of the two components [229]. For electrochemically polymerized polybithiophene films, AFM phase imaging has been used to study stiffness changes associated with variations in crystallinity [160]. Variations in the phase signal correlated with topography and were attributed to the presence of crystalline and amorphous areas. The nodules of the polymer films were described as being composed of higher molecular weight components with more crystallinity and higher conductivity [159, 161, 230]. However, determining the origin of phase separated regions is often ambiguous, particularly for heterogeneous materials with unknown properties. Typically a phase shift is defined through *a priori* knowledge of the sample (e.g. block copolymer of known constituents) [231] or through further analysis to verify the interpretation of the phase separation [163]. For example, the latter can be achieved by acquiring force measurements in the different regions to directly quantify the Young's modulus or viscoelasticity of the material [232]. In this work we use AFM phase imaging to understand phase separated regions in PPy films doped with HA and CS (chemical structures shown in Figure 1). The previous research in Chapter 3 show that these dopants produce polymers with very different physical properties and both have been used previously in biocompatibility and adhesion studies for nerve, bone and muscle cells [105-106, 123, 233-234], hence the two dopants are suitable to be compared and contrasted. By correlating the topographical and phase images with a more in depth analysis of monitoring the phase signal as a function of the tip-sample separation distance phase-

separation curves), we show that phase separated regions arise due variations in the propensity of the tip to sample attractive and repulsive forces in different regions of the polymer. This appears to be a general phenomenon in conducting polymers, irrespective of the dopant, and holds important information for further work using these materials in fluid environments to study protein and cellular interactions.

4.2 Materials and Methods

4.2.1 Reagents

The pyrrole monomer was obtained from Merck and distilled prior to use. The chemicals used as the dopants were the sodium salts of HA and CS. CS was obtained from Sigma and HA from Fluka. All solutions were prepared with deionised Milli-Q water (18.2 MΩ).

4.2.2 Preparation of PPy/HA and PPy/CS films

Gold coated mylar was firstly prepared by cutting 1 cm^2 areas and then cleaning with ethanol and Milli-Q water. Gold coated Mylar (18 Ω/square) was purchased from CPFilms Inc (USA). Aqueous monomer solutions were prepared for the two dopants, HA and CS. The monomer solutions of 0.2 M pyrrole and dopant were degassed in N_2 for 10 min prior to polymerisation of the polymers. Three different dopant concentrations of 0.1 mg/mL, 2 mg/mL and 10 mg/mL were used. PPy films were grown galvanostatically at a current density of 0.25 mA/cm2 for 10 min in the aqueous monomer solution using an eDAQ EA161 potentiostat. Polymer growth was performed in a standard 3-electrode electrochemical cell with the gold coated mylar as the working electrode, a platinum mesh counter electrode and Ag/AgCl reference electrode. After growth, the films were washed with Milli-Q water, gently dried with N_2 gas and fixed onto glass slides until use.

4.2.3 *Topographical and Phase Imaging*

The polymer films were scanned using MikroMasch NCS15/AlBS cantilevers (spring constant of ~35 N/m) in AC mode with an MFP-3D AFM (Asylum Research, CA) to simultaneously produce topographical and phase images. The scanning was conducted in air in ambient conditions with a scan-rate of 0.5 Hz and scan area of 500 nm. Imaging was compared using two different set-points, a higher value of 750 mV and a lower value of 600 mV. An initial free amplitude of 800 - 900 mV was used for both set-point values. For imaging of the films prepared using different dopant concentration films (both PPy/HA and PPy/CS), five images were obtained from different regions of the films using a set-point of 600 mV for a statistical analysis of the phase signal.

4.2.4 *Conductive Force Microscopy*

Mikromasch EFM-20 Pt/Ir coated cantilevers were used for conductive tip AFM, using ORCA mode in the Asylum Research software. A 20 mV samples bias was applied to the polymer films. 1 µm by 1µm scans were taken in contact mode at a set point of 200 mV.

4.2.5 *Kelvin Probe Force Microscopy*

KPFM was performed using Nanoworld EFM-20 cantilevers (spring constant of ~2.8 N/m) with a $PtIr_5$ coating. The scanning was conducted in air in ambient conditions with a scan-rate of 0.5 Hz over a scan area of 1 µm x 1 µm with a set-point of 700 mV and an applied bias of 3 V on the tip.

4.2.6 *Phase-Separation Curves and Mapping*

The phase-separation curves were performed using a z-distance of 500 nm, with an absolute trigger point of 600 mV amplitude volts at a scan rate of 1 Hz. Phase curve mapping was performed over a scan area of 500 nm with a resolution of 32 x 32 pixels. The phase value (contrast) of each pixel represented the final phase value measured at the amplitude set-point of 600 mV.

4.2.7 *Electrochemically Stimulated Films*

Phase-separation maps were performed on oxidised and reduced PPy/HA and PPy/CS polymers. Phase-separation maps were performed on the film after oxidation and then on the same film after reduction. The films were oxidised and reduced with an applied voltage of 500 mV and -500 mV, respectively, in an electrolytic solution of 0.1 M NaCl for 10 minutes and then washed with milli-q water and dried with N_2 prior to the measurements.

4.2.8 *Raman Spectroscopy*

A Jobin Yvon Horiba Raman spectrometer was utilized for acquisition of the Raman spectral data. A 632.8nm laser line filtered through a D2 density filter allowed for examination of the polymer surface without heat damage during prolonged exposure.

4.3 Results

4.3.1 *Phase Imaging*

Figure 4-1A and B show a 500nm topographical and phase image of a PPy/HA film, respectively, measured using the higher set-point of 750 mV. The typical nodular or "cauliflower", topography is observed (Figure 4-1A), while the phase image (Figure 4-1B) displays a similar appearance. For the phase image, the delineation of the nodular topography arises from positive (lighter areas on the right edge of features) or negative (darker areas on the left edge of features) phase shifts representing very small changes of ±2 °.

These small phase changes are due to error in the feedback that attempts to maintain a constant tip-sample separation during imaging and are only indicative (i.e. artefact) of variations in surface topography. Figure 4-1C shows the same region of the film imaged with the lower set-point of 600 mV. Phase separated regions are clearly defined by the nodules displaying a more negative phase shift (darker regions), while the periphery of the nodules show a more positive phase shift (lighter areas). Imaging with this lower set-point also produces significantly larger phase shifts of ≈ 30°.

To understand how changes in the phase can occur, different solutions for the phase as a function of tip-sample separation are shown in a schematic diagram (Figure 4-1D). The corresponding amplitude signal is shown as a solid red line. When off the surface the cantilever oscillation is unperturbed and the phase is 90° at the cantilever resonance frequency.

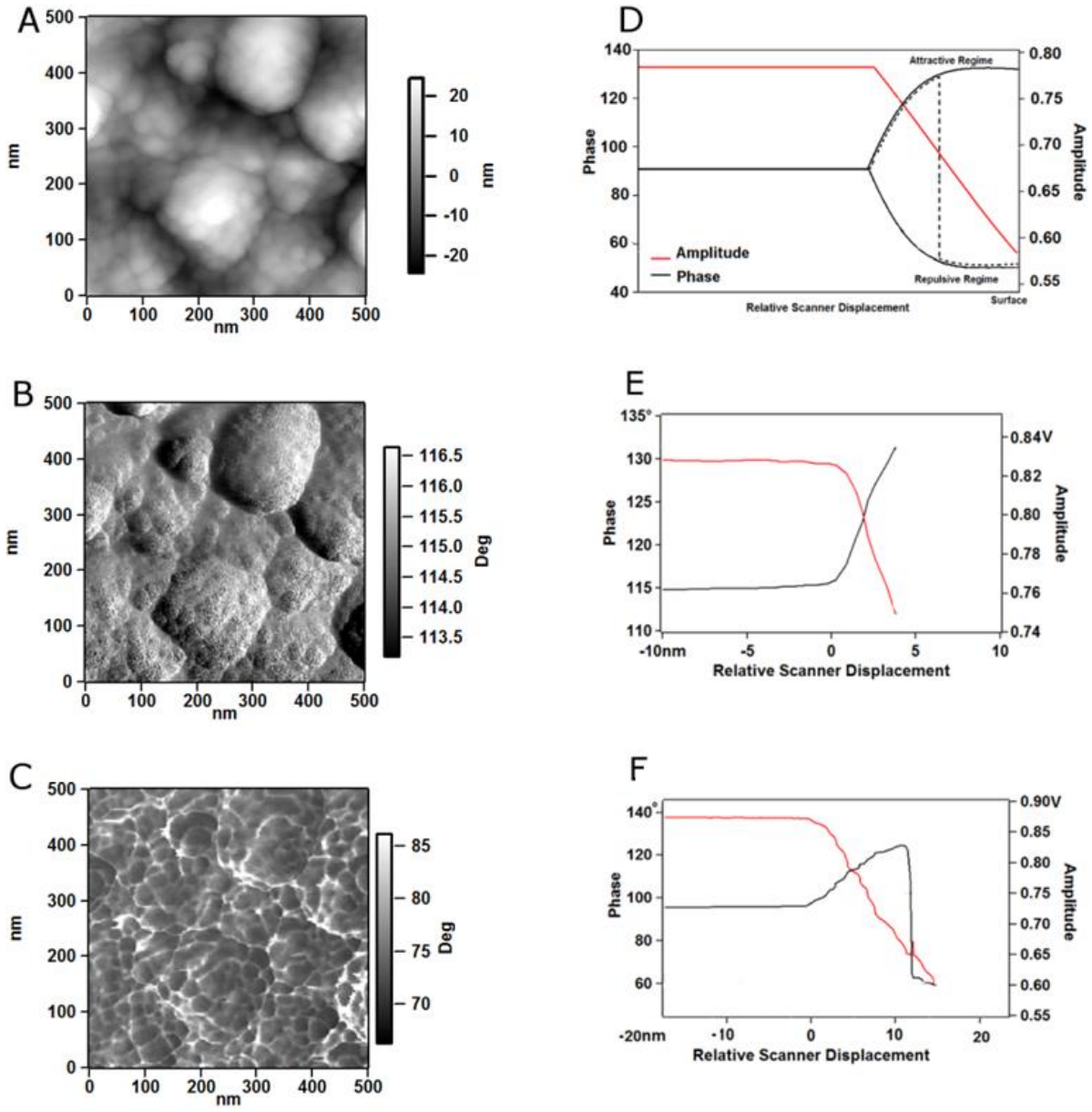

Figure 4-1: (A) Topography scan of PPy/HA; phase scans over same area, (B) 750 mV set point, (C) 600 mV set point. (D) Phase-separation curve schematic, (E) phase-separation curve performed on PPy/HA surface with a 750 mV trigger, and (F) phase-separation curve performed on PPy/HA surface with a 600 mV trigger.

As the tip starts to interact with the surface and causes damping of the amplitude, there are two possible solutions for the phase in conservative interactions (e.g. where the net energy dissipated from the tip is zero). For purely attractive interactions, there

is a positive phase branch to 180° (attractive region). Conversely, for purely repulsive interactions, there is a negative phase branch to 0° (repulsive region). More often in experiments an initial attractive region followed by a jump down into a repulsive region is observed (dashed line), particularly if sufficiently higher free amplitudes and lower set-points are used. The jump from attractive to repulsive regions is termed bistability and may result in phase artefacts if the tip uncontrollably moves between the two regions. This is particularly the case if one is intent on observing dissipative/phase changes associated with material stiffness. The issue can be avoided by choosing a suitable set-point, as determined by the phase-separation curves. Maintaining the tip in the attractive region is generally referred to being in "non-contact", while for the repulsive region the tip intermittently contacts the sample (standard AC mode). A more detailed theoretical and experimental analysis of dynamic AFM modes, including details on the phase signal, has been undertaken by others [229,

Figure 4-1E shows an actual phase-separation curve performed on the PPy/HA surface with a set-point of 750 mV. The tip remains in the attractive region, as only a positive phase shift is observed, and generally represents the condition for the "non-contact" image in Figure 4-1B. In contrast, the lower set-point of 600 mV produces an initial positive phase shift followed by a negative shift into the repulsive region (Figure 4-1G), as schematised in Figure 4-1D and is the condition for Figure 4-1C. To avoid the bistability region and operate in the repulsive region, a lower set-point of 600 mV was used throughout the remainder of the study to undertake a more in depth analysis of the phase contrast. The phase separation when operating at the lower set-point was measured for these polymers, as shown in Figure 4-1C. This was done using phase

mapping by performing an array of phase-separation curves to simultaneously provide information on the topography and corresponding spatial distribution of phase signal (Figure 4-2).

4.3.2 *Phase Volume Mapping*

Of interest to this study was elucidating the phase separations when operating at the lower set-point, as shown in Figure 4-1C. This was done using phase volume mapping by performing an array of phase-separation curves to simultaneously provide information on the topography and corresponding spatial distribution of the phase signal (Figure 4-2).

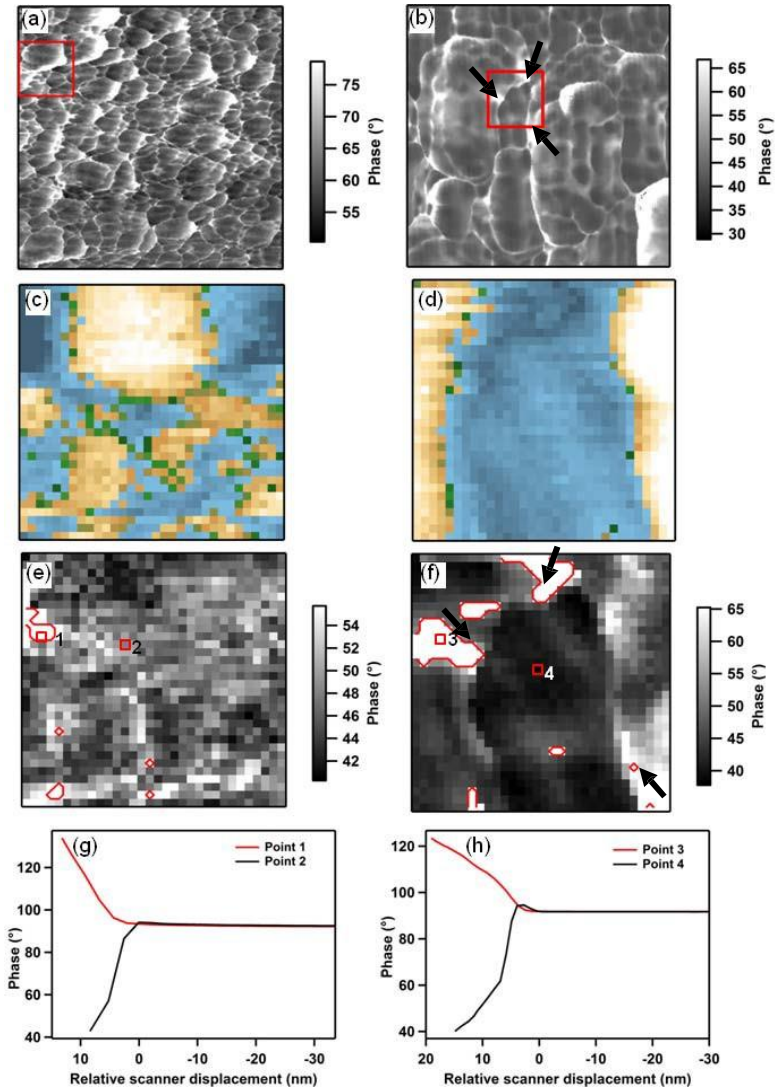

Figure 4-2: 500 nm phase scan of (A) 2 mg/mL PPy/CS, and (B) 2 mg/mL PPy/HA. Phase-separation volume map of 100 nm area marked in red. 100 nm phase-separation volume maps of topography, (C) PPy/CS and (D) PPy/HA, and phase (E) PPy/CS and (F) PPy/HA. Phase curves of (G) Points 1 and 2, and (H) Points 3 and 4 as annotated in (E) and (F). Attractive regions are outlined in red in (E) and (F).

A standard AC mode phase scan (Figure 4-2A and B) of the polymer surface shows the typical phase response, and the phase volume map area is outlined in red. The phase maps (Figure 4-2E and F) were performed over an area of 100 x 100 nm, and the corresponding topographical map is also displayed (Figure 4-2E and F). The phase separation (i.e. light and dark regions) in the phase maps did not always correlate with their expected distribution at the nodules and nodule peripheries in the topographic

image and nor did they always correlate with the phase separated regions in the standard AC mode phase images. This appeared to be due to a number of reasons; firstly, the phase maps and corresponding topographic image have lower lateral resolution compared to the standard AC mode imaging. This means that the phase map may not have been able to discern the same phase separated regions, particularly those of smaller nodules that reside within larger nodules. This was particularly evident for PPy/CS whose structure was comprised of nodules with smaller diameters. For example, in PPy/CS, the lighter areas of the phase map (Figure 4-2E; red outline) occurred more at the peripheries (blue regions) in the corresponding topographic image (Figure 4-2C), however the same phase regions did not correlate strongly with the phase separation in the AC mode phase image (Figure 4-2A). Secondly, the lighter phase areas at the peripheries of smaller nodules tended to extend onto regions of surrounding higher nodules. This observation was more noticeable in smaller scan areas of the phase maps and corresponding topographic image and thus the correlation between the phase and topography was not always clear. This is evident for PPy/HA in Figure 4-2F where the lighter phase regions (red outline) do not correlate clearly with the peripheries (blue regions) in the corresponding topographical map (Figure 4-2D) but in this case they still identified at their equivalent positions (3 black arrows) in the AC mode phase image. It is also noted in that in Figure 4-2F where lighter regions were expected in the peripheries (blue region), the latter were in fact lower lying nodules; this highlighted the difficulty in visually recapitulating the AC mode phase image in the phase maps.

As each pixel in the phase maps represents a single phase-separation curve, representative curves from light and dark areas, marked point 1 and 2, for both PPy/HA and PPy/CS are displayed in Figure 4-2G and F. For the lighter areas, the curves displayed only a positive shift indicating the tip remained in the attractive region. Therefore, the tip is no making contact with the surface in these regions and phase signal does not measure dissipative interactions associated with, for example, material stiffness. For the darker areas, the curves showed an initial small positive phase shift followed by negative phase shift into the repulsive region. This was observed for both PPy/CS (Figure 4-2G) and PPy/HA (Figure 4-2H).

Collectively, the above observations indicate the phase separation in both PPy/HA and PPy/CS occurs at the nodules versus the periphery of the nodules and that this is qualitatively well-defined in the AC mode phase images. Importantly, the phase maps and their phase-separation curves indicate that phase separated regions with a significant 'jump' in the phase shift (e.g. 100-120° down to 40-60°) are due to the tip differentially sampling attractive or repulsive interactions. A stronger, longer-range attractive interaction prevents the tip from entering the repulsive region over the nodule peripheries, while a weaker, shorter-range attractive interaction results in a shift to the repulsive region on the nodules.

4.3.3 *Dopant Variation*

Further phase imaging was performed to assess the effect of varying dopant concentration in the monomer electrolyte on the phase separated regions. Figure 4-3 shows representative phase images of each dopant concentration for PPy/CS (Figure

4-3A; 0.1 mg/ml, B; 2mg/ml, C; 10 mg/ml) and PPy/HA (Figure 4-3D; 0.1 mg/ml, E; 2mg/ml, F; 10 mg/ml). The magnitude of the phase difference between the phase separated regions was observed to decrease with increasing dopant concentration, as indicated by the decreasing phase range of the scale bars (to the right of each image).

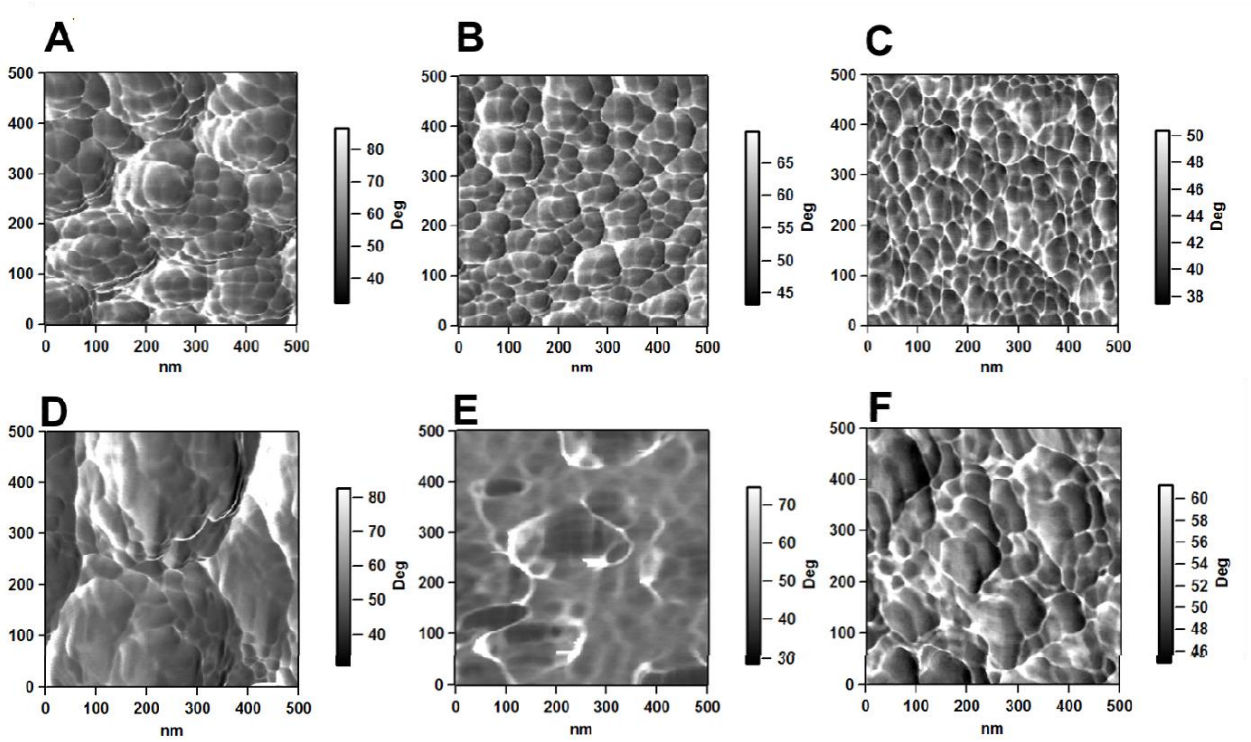

Figure 4-3: Phase images scanned using a set-point of 600 mV. PPy/CS: (A) 0.1 mg/mL, (B) 2 mg/mL, (C) 10 mg/mL . PPy/HA: (D) 0.1 mg/mL, (E) 2 mg/mL, (F) 10 mg/mL.

The phase range for the scans of the samples was averaged and correlated with dopant concentration. A dopant concentration of 0.1 mg/mL had the highest difference with 56.7 ± 4.7° and 52.4 ± 0.9° for PPy/HA and PPy/CS, respectively. This decreased to 36.4 ± 3.2° and 23.3 ± 1.2° for a dopant concentration of 2 mg/mL and further reduced at the highest concentration of 10 mg/mL with 19.8 ± 2.3° and 12.8 ± 0.1° for PPy/HA and PPy/CS respectively. The decrease in the phase difference was primarily due to a decrease in the positive phase shift, as phase values for the

repulsive region remained constant around ≈ 40°, indicating that the attractive interactions become weaker as dopant concentration increases. One important consideration was that there were also changes in the surface roughness of the films as function of the dopant concentration, which could possibly influence the extent of the phase shifts. The average of the RMS roughness values from several images for PPy/CS with increasing dopant concentration was 22 ± 1 nm, 6.3 ± 0.7 nm, and 5.8 ±0.2 nm. The RMS roughness for PPy/HA with increasing dopant concentration was 57 ±13 nm, 6.1 ± 1.8 nm, and 13 ± 5 nm. No significant change in roughness was observed as the dopant concentration increased from 2 mg/ml to 10 mg/ml; however the magnitude of the phase shift decreased significantly for both films, indicating that roughness was not causative factor at these higher dopant concentrations.

4.3.4 *Raman Spectroscopy*

The Raman spectra of the polymer films can be interpreted for comparative dopant loading levels, and conductivity of the films [226]. Table 4-1 displays the C=C bond stretching peak positions for the dopants at each concentration.

Table 4-1: Raman peak positions of PPy/CS and PPy/HA at 0.1, 2 and 10 mg/mL

Dopant	Dopant Concentration in electrolyte (mg/mL)	C=C Stretching Peak Position (cm^{-1})
CS	0.1	1604.3
	2.0	1600.0
	10	1593.6
HA	0.1	1602.1
	2.0	1583.0
	10	1604.3

The Raman peak position of the C=C bond stretching of PPy will shift to a higher wave number if the conjugation length of PPy is shortened, and can also shift to a higher wave number when PPy has a lower loading level. The C-H in plane deformation and ring stretching Raman peaks are also indicative of a change in loading levels; higher intensities of these peaks correspond to higher loading levels. While the relative intensities do not give a loading level ratio, the trend is consistent with loading levels. Hence the spectrum tells us that the PPy/CS polymers do in fact incorporate more dopant when increasing dopant concentration in the monomer solution. PPy/HA however shows the highest loading levels for the 2 mg/mL film, with loading levels dropping for the 10 mg/mL film. This is most likely due to poor dopant loading for this polymer, as the 10 mg/mL monomer solution is extremely viscous. This may hinder the reactants during polymerization, thus creating a polymer with less incorporated dopant.

4.3.5 *Electrochemical Stimulation of Polymers*

To exclude other possible causes, primarily topography, of the differential sampling of attractive and repulsive forces, phase maps of PPy/CS and PPy/HA films were performed after oxidation and reduction (Figure 4-4).

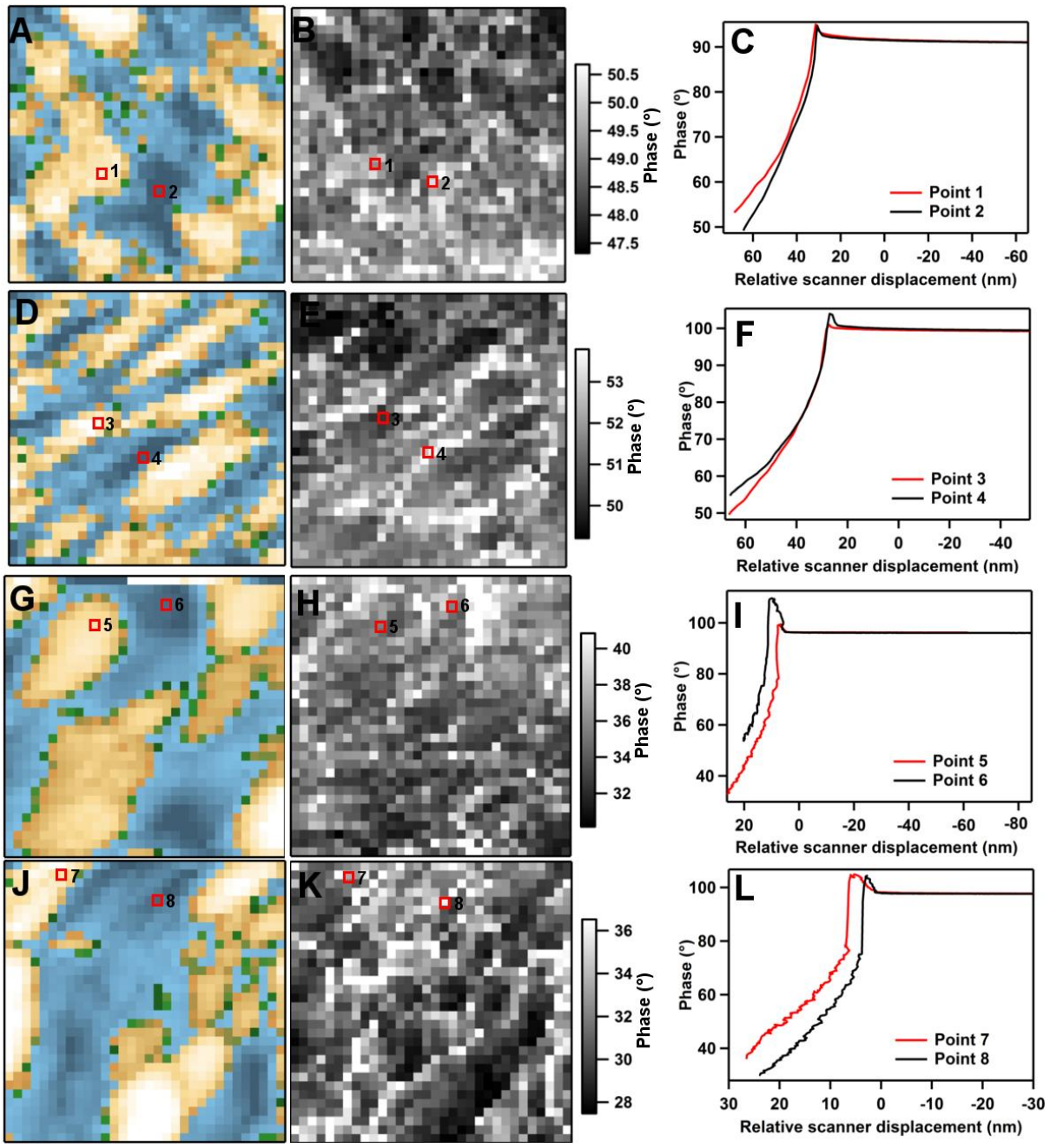

Figure 4-4: Phase-separation volume maps. (A) Oxidised 2 mg/mL PPy/CS topography, (B) reduced 2 mg/mL PPy/CS phase, (C) phase curves of Points 1 and 2, (D) reduced 2 mg/mL PPy/CS topography, (E) reduced 2 mg/mL PPy/CS phase, (F) phases of Points 3 and 4, (G) oxidised 2 mg/mL PPy/HA topography, (H) reduced 2 mg/mL PPy/HA phase, (I) phase curves of Points 5 and 6, (J) reduced 2 mg/mL PPy/HA topography, (K) reduced 2 mg/mL PPy/HA phase, and (L) phase curves of Points 7 and 8.

For PPy/CS, the topography image in the oxidised state showed clear nodules that were unchanged from the as-grown films (Figure 4-4A). The corresponding phase map (Figure 4-4B) showed some differences in the phase signal however the magnitude of the shift (as indicated by the scale bar) was significantly smaller in comparison to the non-electrically stimulated films. These smaller phase shifts were confirmed in the corresponding phase separation curves, which showed a similar profile for both the nodules (point 1) and nodule peripheries (point 2) (Figure 4-4C). Both phase curves showed a small positive shift before an overall negative shift (Figure 4-4C), indicating a significant reduction in the extent of the attractive branch on the nodule peripheries. Furthermore, we did not observe any phase separation curves consisting of only purely attractive (branches) forces in all phase separation maps for both PPy/CS and PPy/HA irrespective of oxidation or reduction. No purely attractive regions, or phase values above 90°, were observed in any of these phase maps. Therefore, the phase separated regions were effectively removed by the oxidation and reduction even though the topography of the films did not significantly change, indicating that the latter is not the underlying cause of the phase separation observed in the non-electrically stimulated films. The phase value of each pixel in the maps is taken at the maximum point of the relative scanner displacement (i.e. minimum of tip-sample separation) and thus the phase contrast that still exists (Figure 4-4B, E, H, K) is due to shifts of the phase only in the repulsive branch, as shown by the phase separation curves (Figure 4-4C, F, I, L). This represents the situation where sampling of the phase (i.e. a deviation from the purely repulsive branch) can be related to the material stiffness. Based on the phase maps in Figure 4-4, the lighter (lower dissipation) and darker areas appeared to

correlate with nodules and nodule peripheries, respectively, suggesting that the nodules are stiffer.

4.3.6 *Current Sensing Imaging*

C-AFM scans were performed on PPy/HA and PPy/CS. The 1 µm by 1 µm topographical and current scans are shown in Figure 4-5. PPy/HA shows an obvious correlation of the nodular features (Figure 4-5A) of the films having higher conductivity than the area around the nodules in Figure 4-5C.

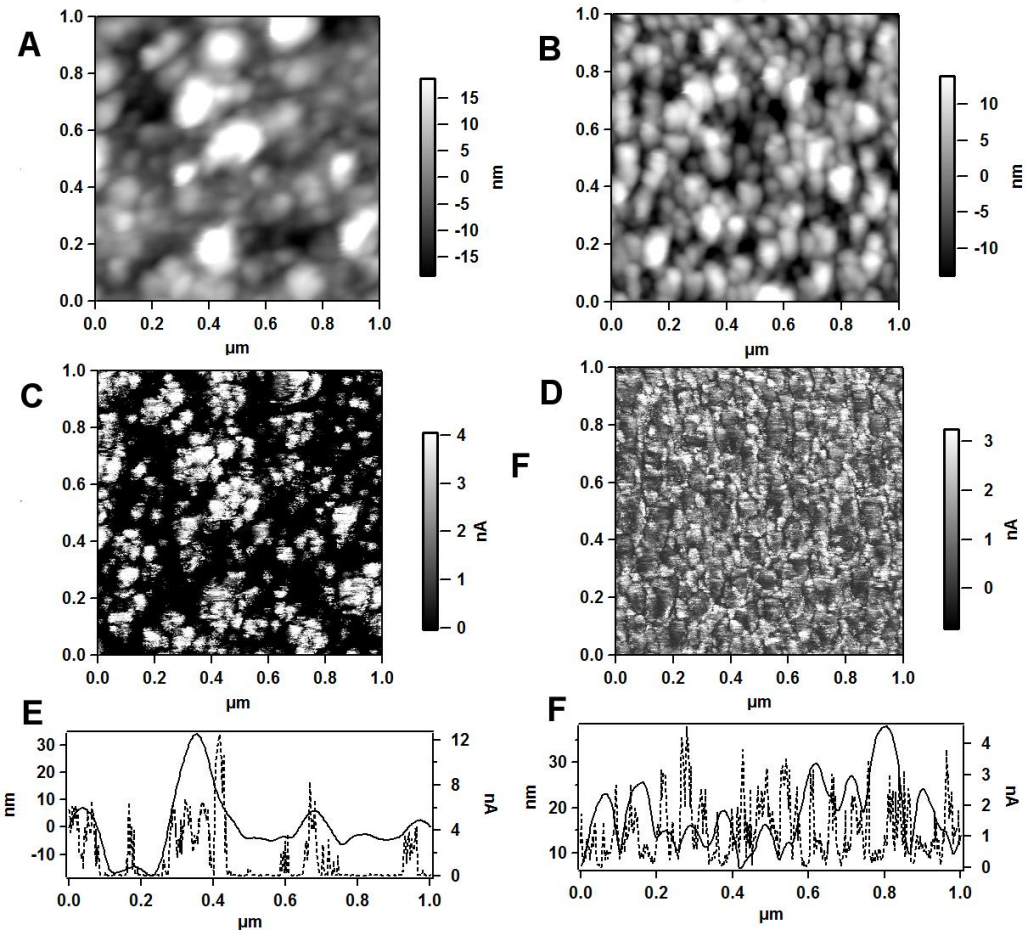

Figure 4-5: 2 mg/mL PPy/HA (A) height scan, (C) current sensing scan. (E) Cross-section showing topography (solid) and current (dashed). 2 mg/mL PPy/CS (B) height scan, (D) current sensing scan and (F) cross-section showing topography (solid) and current (dashed).

A cross-section across this scan (Figure 4-5E) clearly shows the increase in conductivity across the nodules and negligible conductivity in the periphery regions. PPy/CS shows a more homogenous conductivity (Figure 4-5D) and topography (Figure 4-5B) than PPy/HA, with an RMS current of 1.57 ± 0.001 nA (RMS ± s.d.) compared to PPy/HA with an RMS current of 2.51 ± 2.16 nA (RMS ± s.d.). The cross-section of the PPy/CS scan shows that the increases in conductivity appear to occur on the inside periphery but not always on top of the nodular features. The areas of lower conductivity across the scan have distinct borders that do not necessarily correlate with the borders of nodular features, indicating some order within the polymer that is controlling the conductivity. Conductivity of PPy films is directly related to the presence of dopant; if the PPy backbone is undoped the polymer cannot transfer an electric charge. The presence of the dopant molecule allows delocalization of the π-electrons, which in turn allows charge carrier mobility along the polymer chain [13]. Therefore, the areas of higher conductivity indicate areas with higher doping levels, or oppositely lower conductivity areas devoid of dopant [35].

4.3.7 *Surface Potential Imaging*

The surface potential of a sample can be measured using Kelvin probe force microscopy (KPFM), a technique which measures the electrostatic forces between the tip and sample using a potential bias applied to the tip. Figure 4-6 shows the topographical and corresponding KPFM scan of PPy/CS and PPy/HA films. Both polymers show a clear correlation between areas of high surface potential and the nodular features. The peripheries around the nodules are areas of low surface

potential. This correlation has been reported before for PPy polymers, and the high surface potential has been attributed to dopant rich areas [167].

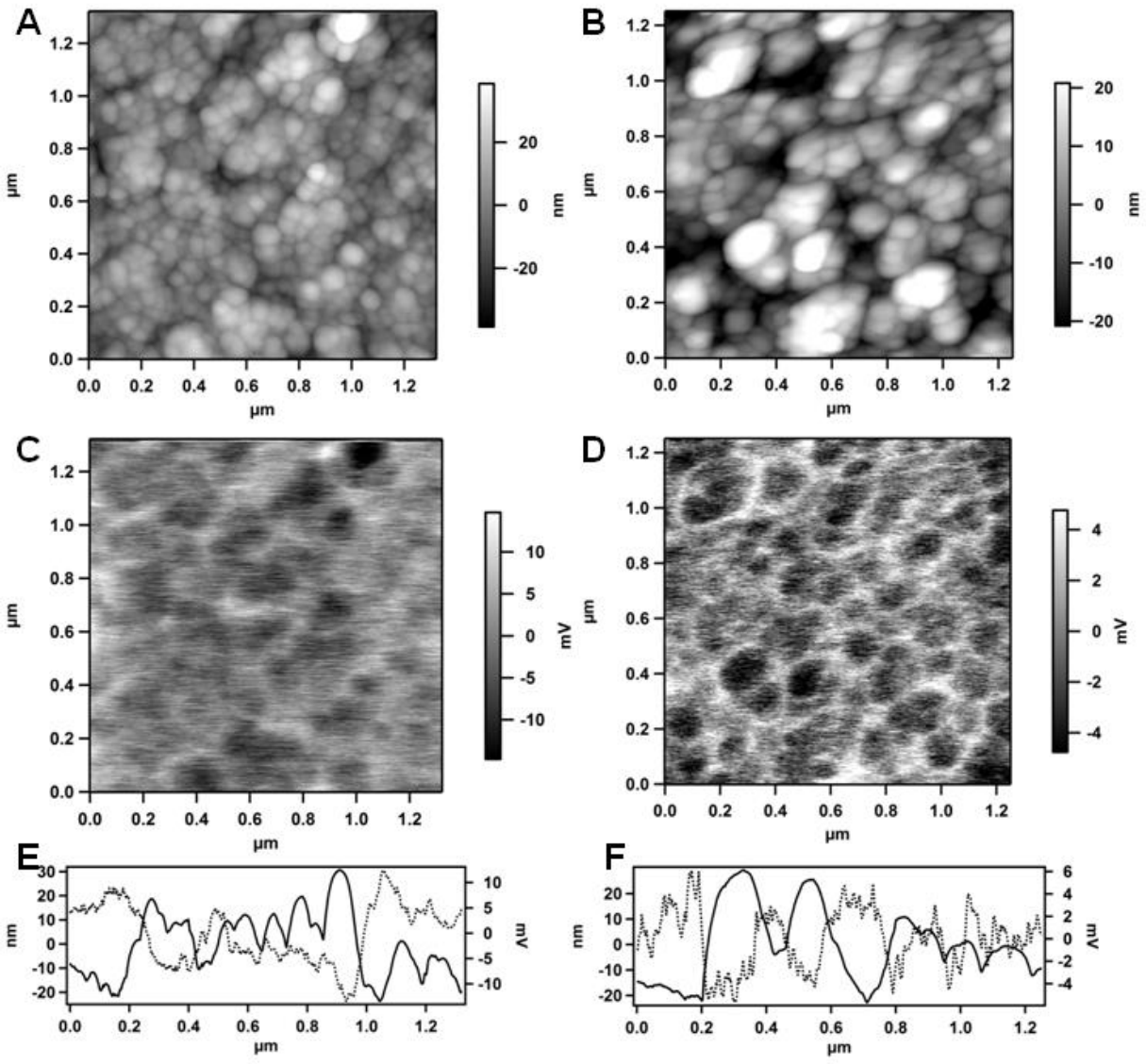

Figure 4-6: 2 mg/mL PPy/HA (A) height scan, (C) surface potential scan. (E) Cross-section showing topography (solid) and potential (dashed). 2 mg/mL PPy/CS (B) height scan, (D) surface potential scan and (F) cross-section showing topography (solid) and potential (dashed).

4.4 Discussion

4.4.1 Origin of Phase Shift on OCPs

AFM phase imaging has been used to shed light on the evolution of the polymerization process and heterogeneity of conductivity in OCP's. O'Neil et al. attributed phase separation in polybithiophene films to surface variations in the polymer stiffness, which further reflected amorphous or crystalline areas of the polymer [159-160]. The phase separated regions were described as being due to crystalline polymer forming the nodules in contrast to more amorphous polymer located at their periphery. For this to occur during electrochemical polymerization, higher molecular weight components were said to initially deposit to form the primary nuclei and proceed to eventually be the cores of the nodules. Smaller molecular weight components are then deposited later and become the nodule peripheries. The model described from this work suggests that because the higher molecular weight components are more likely to form crystalline polymer, then it is expected that the nodules have a higher stiffness [227, 237-238].

The nomenclature for the phase signal in the above study is different to ours (i.e. our attractive branch $180^{o} = -90^{o}$; our repulsive branch $0^{o} = +90^{o}$) thus one must not rely on directly comparing light and dark phase contrasts. For changes in modulus or viscoelasticity an increase in energy dissipated from the tip is observed as a shift from the purely repulsive branch of the phase (where the tip is intermittently contacting the sample). For example, a greater positive shift from 0^{o} when the tip is in the repulsive region corresponds to areas of lower modulus. In the above study, this would

correspond to a negative shift from +90° resulting in darker phase areas, as was observed at the nodule peripheries. We could arrive at the same conclusion if our images of the as-grown PPy/CS and PPy/HA were interpreted based only on the direction of the phase shift, i.e. a shift towards brighter phase regions at the nodule peripheries. However, by undertaking additional phase-separation curves further information reveals that the observed phase separation arises from variations in attractive and repulsive interactions between the tip and polymer. This origin of the phase separation also has a correlation with the topography of the polymer. Our study closely follows previous work aimed at attempting to understand phase contrast by investigating Nafion membranes [163]. In this study, phase-volume images of the Nafion consisted of two main types of phase-distance curves. One type of phase-separation curve required considerably more force (a greater attractive interaction) to enter the repulsive region and was attributed to the C+ and H+ ion-rich regions that would damp the cantilever oscillation with an attractive electrostatic force at longer distances. A second type of curve moved quickly from the attractive to repulsive region with final phase values indicating little energy dissipation. These regions were attributed to the hydrophobic backbone of the polymer.

4.4.2 *Effect of Dopant Distribution on Phase Shift*

Similarly, our results show that the phase separation in the as-grown films arises from differences in the strength of attractive interactions across the polymer surface. These are most likely due to variations in Coulombic forces, however contributions from capillary forces (i.e. due to the presence of adsorbed water) cannot be completely ruled out. Previous studies on polybithiophene films using C-AFM have shown a higher

conductivity in the nodules compared to the nodular periphery [160]. This was also observed for our polymers, however the degree of homogeneity was vastly different for PPy/HA and PPy/CS. These observations are further supported by surface potential AFM imaging of as-grown PPy/pTS films showing a more negative potential at the nodules [167], indicating that these regions have a higher work function, or are more highly doped, than their peripheries. This result is also evident in our KPFM scans, with the nodules clearly showing a more negative potential. These scans confirm the hypothesis drawn from the phase signal data for dopant distribution throughout the conductive polymers. In terms of electrostatic force contributions to the phase signal, stronger attractive forces could arise from interactions between the silicon nitride tip which carries a net negative charge [239] and less doped polymer with excess positive charge at the nodule peripheries. A greater negative charge at the nodules would conversely diminish the electrostatic attractive forces.

Related to the increased negative charge at the nodules is an increase in doping that would minimize the magnitude of the attraction force through screening of the backbone cationic charge. This effect is actually confirmed in Figure 4-3, as an increase in dopant loading causes a decrease in the positive phase shift of the attractive branch. By making more dopant available during electrochemical polymerization and concomitantly increasing the polymer loading levels (as confirmed by Raman spectroscopy), a greater screening of positive charge and/or distribution of charge neutrality therefore reduces electrostatic attractive forces. Interestingly, oxidation and reduction of the polymers was shown to eliminate the phase separated regions, a finding that may also relate to increased charge neutrality through doping in the

oxidised state, or particularly as the polymer adopts more hydrophobic, neutral characteristics in the reduced state. Once the electrostatic forces are nullified, it is possible to observe changes in the energy dissipation across the sample which may be attributed to changes in modulus. The darker areas of the phase map indicate an area where there is higher energy dissipation, indicating a stiffer material. As the dark phase areas correspond to the nodules of the film, this agrees with the literature discussing the nodular features of PPy being more crystalline than the surrounding areas [160, 229].

The influence of capillary forces is also a possibility [239]. Due to the preferential adsorption of water at hydrophilic regions, capillary neck formation and rupture between the tip and surface can lead to phase contrasts mechanisms. Simulated and experimental AFM observations show that the phase transition from the attractive to repulsive region is suppressed with an increase in relative humidity % [228, 232]. However, we suggest that the contributions of these forces on the phase separation are less likely. This is because increasing the dopant loading normally associates with an increase in surface hydrophilicity, as shown by contact angle measurements, and would be expected to have more adsorbed water and thus suppress the transition from attractive-to-repulsive branches. This was not the case however, as Figure 4-3 showed that an increase in dopant concentration actually displayed the opposite by promoting a shift to repulsive interaction. If the surface had increased hydrophilicity with an increase in dopant concentration this strong shift to a repulsive interaction would not be observed.

4.4.3 *Implication of Dopant Distribution*

The two dopants show differences between the films in the phase, conductivity and surface potential scans. The use of HA as a dopant results in a polymer with very distinct phase separated regions and areas of highly contrasting conductivity, suggesting that the dopant is poorly distributed throughout the polymer and has a detrimental effect on the conductive properties of the PPy. This effect is consistent with earlier work by Collier et al. [195] who reported a lower conductivity of a PPy/HA film compared to a PPy/PSS film. In contrast, the PPy/CS polymer displayed less distinctly phase separated regions and more homogenous conductivity indicating that the dopant is more uniformly distributed throughout the polymer.

The inhomogeneous distribution of both dopants gives rise to nanometer spatial variations in surface chemistry and related nanoscale forces under the control of these regions. The observed variations in the strength of attractive forces represent differences in surface charge and/or surface energy that have implications for these materials when under investigation in a fluid, or biological environment. For example, such surface variations may play a role in double-layer formation, which in turn can influence protein and cellular interactions. Further work is required to indeed understand the extent to which these variations in surface charge/energy will exert their influence over such biointeractions. Already, studies have shown that surface charge can affect protein conformation that is critical for enabling cell adhesion [100], while the nanometer length scales over which the phase separation occurs can have an effect on cell interactions operating on the same nano-(molecular)scale [240].

4.5 Concluding Remarks

Rather than the phase separation solely being indicative of a change in the Young's modulus, the imaging parameters and approach used in this study has found a relationship between the phase signal's relationship to variations in the surface charge of the films. A number of conclusions can be drawn from this study:

When investigating heterogeneous polymers, such as the OCP studied here, AFM phase imaging is more clearly defined when operating in one regime (i.e. attractive or repulsive) or another. This should follow the intent of which surface properties are under investigation. The correlation between the nanoscale topography and variations in the spatial distribution of surface properties, including conductivity, degree of doping and surface charge, also extends to surface forces. Electrochemical oxidation and reduction can produce a more homogenous surface chemistry, as evidenced by a reduction in the phase separation. These lateral nanometer variations in surface property – related forces may manifest in fluid and biological environments and have an influence on biointeractions such as protein and cell adhesion.

5 Resolving Single Protein Interactions with Organic Conducting Polymers

5.1 Introduction

5.1.1 *Protein Interaction and Mediation*

When cells adhere to synthetic surfaces, they utilize ECM proteins such as fibronectin and laminin to create structural support and scaffolds to aid adhesion. The adsorption of the proteins forms an initial step in the process of cellular adhesion to a substrate and as such is a vital part of the cell-substrate interaction. The schematic (Figure 5-1) envisages possible various interactions that occur as the cell adheres to a PPy surface doped with biological molecules such as glycoaminoglycans (GAGs) and depicts the important role played by ECM proteins like FN for mediating the cell-polymer interactions.

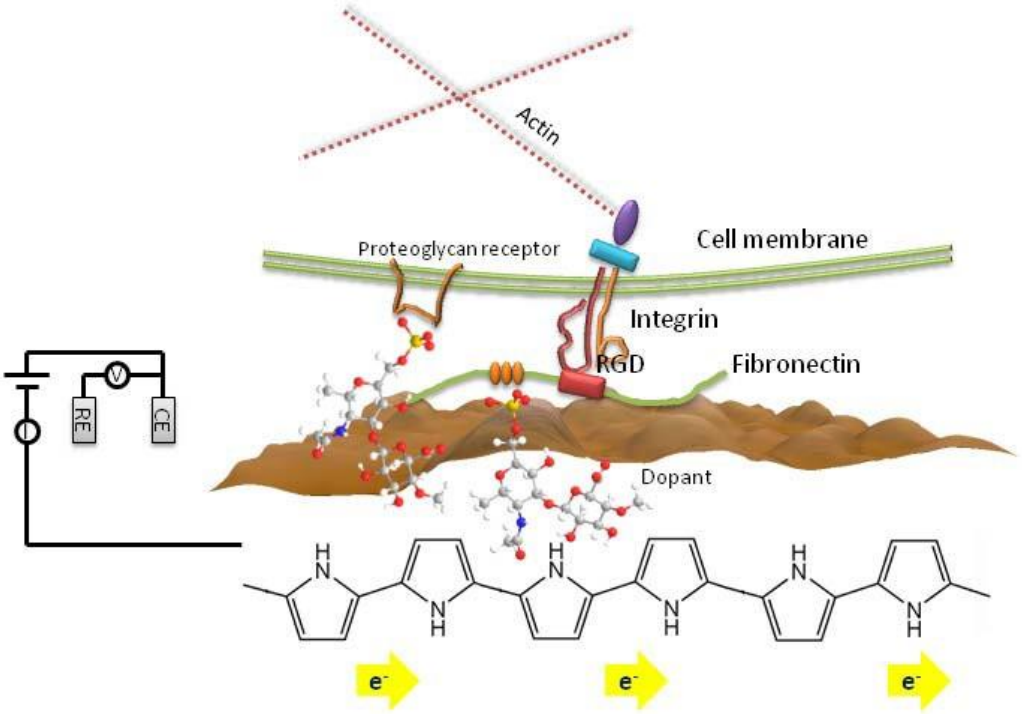

Figure 5-1: Schematic of processes occurring as FN mediates cell-polymer adhesion. The biological dopant (CS) may interact with a site within FN (orange ovals), or with a proteoglycan receptor on the cell surface. The $\alpha_5ß_1$ integrin binds through the RGD site within FN (red rectangle) to anchor the cell to the substrate and to support the formation of actin stress fibres and focal adhesion complexes vinculin (purple oval) and talin (teal rectangle). All of these processes can be manipulated once an electrical stimulation is applied to the PPy backbone.

The presence of the biological dopant (CS, see chemical structure in 1.4.2.2, pg. 1-23) can support the binding of FN to the surface, in addition to direct binding to proteoglycan receptors available on the cell surface. Furthermore, direct electrical stimulation through the polymer present exciting possibilities for controlling these interactions.

The FNIII domains of the protein are responsible for the process of cell binding, as described earlier in Chapter 1 (1.4.4.1, Page 1-40). Cells bind to FN via the RGD sequence which is located at the 10th FNIII domain. Another binding domain of FN that is important to note is the heparin binding domain near the disulfide bridge. It is

believed to be the dominant interactive site for heparin [241] and other GAGs of very similar in structure such as the dopants CS and HA investigated in this study. Excess anionic groups, for example freely available sulfonate groups, are often exposed at the surface and therefore we expect involvement in surface interactions defined by classical GAG-protein (e.g. FN) binding recognition [242] which localizes, stabilizes, activates or inactivates incoming proteins [243]. This GAG-FN interaction further supports the binding of integrins, which in turn trigger the formation of actin stress fibres that promote the adhesion and proliferation of cells. Hence, the FN protein is a critical mediator of the cell-material interface. Understanding the molecular level interactions at this interface will be important for the ongoing development of OCP in their biological applications, including cell culture coatings (e.g. electronic Petri dish), biosensors, organic bioelectronics, implantable electrodes and tissue regeneration devices.

5.1.2 *Analysis Method of Protein Binding*

The adsorption, adhesion and conformation of ECM proteins are factors that determine their interactions with living cells, including their spreading, migration, proliferation and differentiation [98, 100, 244]. These factors are heavily influenced by the physical and chemical surface properties of the substrate [97, 152-154] and as such the dependencies of these two entities on each other have commonly been studied in material science. Specifically for OCP, there has been growing interest in understanding protein-OCP interactions, as it is believed that they form an underlying mechanism for controlling cell interactions using these materials. While earlier studies speculated on the involvement of protein (i.e. fibronectin) interactions through their

cell observations, recent studied have turned to various techniques such as Quartz Crystal Microbalance (QCM) and Fluorescence Microscopy to focus on measuring the adsorption and conformation of FN on different OCP surfaces, including PPy and PEDOT.

QCM measures changes in the mass and viscoelasticity of absorbed proteins on substrates. The kinetics of adsorption for FN were modelled using QCM in a recent study [61]. Increasing the dopant loading of DS in PPy resulted in a more 'relaxed', i.e. more viscoelastic, and higher density FN layer. When electrical stimulation (± 300 mV) was applied to reduce or oxidise the polymer, the protein adsorbed with a higher density on the oxidised film and had a more viscoelastic response. Conversely less protein adsorbed on the reduced film and has a less viscoelastic, or 'rigid', response. The 'relaxed' response is attributed to the elongated conformation of FN, and the 'rigid' response the compact conformation.

The fluorescence microscopy technique, Förster resonance energy transfer (FRET), uses labeling of the protein to determine its conformation through fluorescent intensity. Malliaras et al. used this technique in combination with CD spectroscopy to observe changes in FN conformation on PEDOT:tosylate [245]. CD spectroscopy is commonly used to study the secondary structure of proteins as the chiral structure of these molecules produces differential absorption of circularly polarized light. The conformation of FN was measured using CD spectroscopy of suspended proteins; subsequent FRET analysis of these suspended proteins was used to correlate an intensity ratio with a CD confirmed conformation. The protein was labelled at various positions so that a folded conformation would produce a different intensity compared

to an elongated conformation. It was claimed that a high intensity ratio correlated to a folded conformation and a low intensity ratio correlated to an elongated conformation. Using the establishment of the FRET signals, the conformation of FN on the PEDOT:tosylate surface was found to change depending on a potential gradient (+1 V to -1V). The compact conformation (high intensity ratio) was observed on the reduced surface, and the elongated conformation (low intensity ratio) on the oxidised surface. This result is contrary to the previous QCM study [61], which highlights that this redox effect may also be dependent on the cell type, conductive polymer, and dopants. However, FRET cannot directly observe the protein conformation without previously determining the conformation using a secondary technique. FRET may also suffer from discrepancies introduced from autofluorescence, intensity quenching, and detector/optical noise during measurement [246]. This redox effect may also be dependent on the cell type, conductive polymer, and dopants. In order to fully understand the interaction of the protein a more direct method using an applied electrical stimulation may be more informative.

5.1.3 *Single Molecule Characterisation*

The analysis methods described above characterize the ensemble adsorption and/or conformation of the proteins. However, to truly understand the specific, molecular interactions that provide fine control, especially under electrical modulation, at the cell- or protein-material interface, one must probe at the single molecule level. The level of detail required is emphasized in the schematic in Figure1-1. At present, the molecular details of FN interactions with OCP are not known and as yet no direct measurement for probing single protein molecule binding or conformation on an OCP,

or any type of organic conductor (e.g. carbon nanotube, and graphene), under electrical control has been demonstrated; understanding the dynamics and physics of single protein interactions will be a major step forward in this field of organic bioelectronics.

In this chapter, we have applied the use of AFM tips functionalized with FN to directly measure the interaction of the protein with PPy at the single molecule level. Using AFM it is possible to deconvolute the complexity of interactions arising from the intrinsic spatial heterogeneity of the polymer-dopant constituents, as highlighted in previous chapters. Due to the nanoscale dimensions of the probe, any given X-Y location of the measurements can represent a single, isolated molecular interaction between a molecule on the tip and surface groups, with the bond bearing its own characteristic fingerprint; the key is to relate the interaction back to the interacting molecules. We have specifically investigated the interaction of FN with PPy doped with various GAGs, including CS, HA and dextran sulfate (DS). The GAG dopants can make up to 50% of the polymer composition and not all their anionic groups participate in charge neutralization of the polymer. For example, free sulfonate and carboxyl groups are anticipated to be involved in surface interactions defined by classical GAG-protein adhesion and recognition [242], which is important for regulating cellular activities, including cell adhesion, extracellular matrix modelling and fibrillogenesis [243].

5.2 Materials and Methods

5.2.1 Reagents

The pyrrole monomer was obtained from Merck and distilled prior to use. The chemicals used as the dopants were the sodium salts of pTS, HA, DS and CS. CS and DS were obtained from Sigma, pTS from Merck and HA from Fluka. All solutions were prepared with deionised Milli-Q water (18.2MΩ).

The functionalization chemicals 3-ethoxydimethylsilylamine propyl (3-EDSPA), gluteraldehyde (GAH) and human plasma FN were obtained from Sigma Aldrich. Phosphate buffered saline (PBS) was prepared at pH 7 in Milli-Q water (18.2MΩ). The 3-EDSPA was prepared as a 1% solution in toluene. The GAH was prepared as a 2.5% solution in pH 7 PBS buffer. The FN was prepared as a 10 µg/mL solution in pH 7 PBS buffer.

The fluorescence antibody binding chemicals used were donkey serum and Alexa488 goat anti-rabbit IgG from Invitrogen, and primary anti-FN rabbit antibody from ICN Biomedicals Inc.

5.2.2 Methods

5.2.2.1 Preparation of Biodoped Polypyrrole

Gold coated mylar was firstly prepared by cutting into strips of 0.5 cm by 2 cm area and then cleaned with methanol and Milli-Q water. Gold coated Mylar (18 Ω/square) was purchased from CPFilms Inc (USA). An aqueous monomer solution of 0.2 M pyrrole and 2 mg/mL of the counter-ion dopant was degassed in N_2 for 10 min prior to

polymerisation of the polymers. PPy films were grown galvanostatically at a current density of 0.25 mA/cm^2 for 10 min in the aqueous monomer solution using an eDAQ EA161 potentiastat. Polymer growth was performed in a standard 3-electrode electrochemical cell with the gold coated mylar as the working electrode, a platinum mesh counter electrode and Ag/AgCl reference electrode. After growth, the films were washed with Milli-Q water, gently dried with N_2 gas and placed in petri dishes until use.

5.2.2.2 Protein Functionalization of AFM Tip

The tip is functionalized using an aminosilzation method to covalently bind the FN to the tip. Silicon nitride (SiN) Nanoworld PNP-DB tips are used for this method due to the availability of silicon oxide groups on the surface. The tips were initially cleaned with a plasma cleaner to remove any impurities or functionalized groups on the surface. Once cleaned the tips were immediately functionalized to minimise any contaminants on the surface. The tips were placed into the EDSPA solution at room temperature for 1 h. The tips were then removed, washed consecutively with toluene, then PBS solution. The tips were then encapsulated with the GAH solution for 1 h, then rinsed with PBS solution. The tips were finally encapsulated in the FN solution for 1 h, then rinsed and refrigerated in PBS solution until use.

5.2.2.3 Fluorescence of Protein Functionalized Surfaces

FN functionalized silicon wafer and µMasch CSC12 colloidal probes were prepared for antibody binding. The silicon wafers were cleaned in piranha solution prior to FN functionalization method described above. Both functionalized and non-functionalized (control) wafer and probes were stained. The wafers and tips were blocked in PBS with

10% donkey serum at room temperature for 1 hr then incubated in primary anti-FN (rabbit) antibody in PBS with 10% donkey serum at 37 °C. The wafers and tips were rinsed twice in PBS, then incubated in a secondary antibody (Alexa488 goat anti-rabbit IgG) in PBS with 10% donkey serum. The wafers and tips were then rinsed twice with PBS and imaged using the Acio epifluorence microscope.

5.2.3 *Force Spectroscopy Measurements*

5.2.3.1 Step Analysis of Protein Functionalization

In order to measure the interaction between each functionalization component and the polymer surface, tips were analysed at each step of the functionalization procedure; i.e. a clean SiN tip, a tip terminating in a silane group, GAH, and FN respectively. Three tips were prepared at each step, with five force spectroscopy curves performed at three different points on a PPy surface for a total of 45 force curves for each functionalization. This was performed in PBS fluid.

5.2.3.2 Dwell Time Measurements

The force measurements were performed in PBS fluid using the experimental set-up described in Chapter 2. The AFM parameters were set for 500 nm approach, 0.5 Hz scan rate, and 1 nN trigger force. The dwell time was varied from 0, 1, 3, 5, and 10 sec. Single point force spectroscopy measurements were performed with 3 consecutive measurements at one point, with a rest of 3 seconds, across 3 different points on the polymer surface for a total of 9 force curves per dwell time.

5.2.3.3 Force Spectroscopy Measurements on Non-stimulated Polymer

The force measurements were performed in PBS fluid using the experimental set-up described in Chapter 2. The AFM parameters were set for 500 nm approach, 0.5 Hz scan rate, 1 sec dwell toward (excluding 5.3.5) and 1 nN trigger force. Single point force spectroscopy measurements were performed with 5 consecutive measurements at one point, with a rest of 3 seconds, across 5 different points on the polymer surface over three individual samples for a total of 225 force curves. Force measurements were performed on PPy films prepared with the four dopants.

5.2.3.4 EC-AFM Force Spectroscopy Measurements

EC-AFM was implemented by positioning a 2-dimensional electrochemical cell on the AFM sample stage. The electrochemical cell was made out of a Teflon block that consisted of a u-shaped fluid well etched around a platform. A PPy/dopant coated gold Mylar strip was glued onto the platform and acted as the working electrode. A platinum mesh counter electrode was positioned in the fluid well and a silver wire reference electrode was placed alongside the polymer film. Measurements were carried out in PBS buffer solution, which was injected into the fluid well to immerse the three electrodes.

When performing force measurements the output of the Z-piezo was recorded simultaneously with an electrical stimulation input while performing continuous force curves. The electrical stimulation was applied using a cyclic voltammetry. For the PPy films the applied CVs had a ±100 and ±400 mV range, and a scan rate of 50 mV/s and 4 mV/s (for the ±400 mV). The gold mylar had a CV applied with ±400 mV with a scan

rate of 50 mV/s. The force curves were conducted at the same point at a rate of 0.16Hz over 300 seconds of stimulation, each stimulation set resulting in 48 force curves. The Z-piezo output recorded the movement of the tip during the force curve corresponding to an exact time, voltage and current when the tip came into contact with the stimulated polymer.

5.3 Results

5.3.1 *Fibronectin Functionalization*

The AFM tips were functionalized in a step-wise manner to covalently bind FN to the SiN_3 tip surface. The use of amine-functionalized procedures to bind biological molecules to SiN_3 tips is a common approach [188, 247]. The amino-terminated surface can then be reacted with a cross-linking molecule which can then bind the desired biological molecule [181].

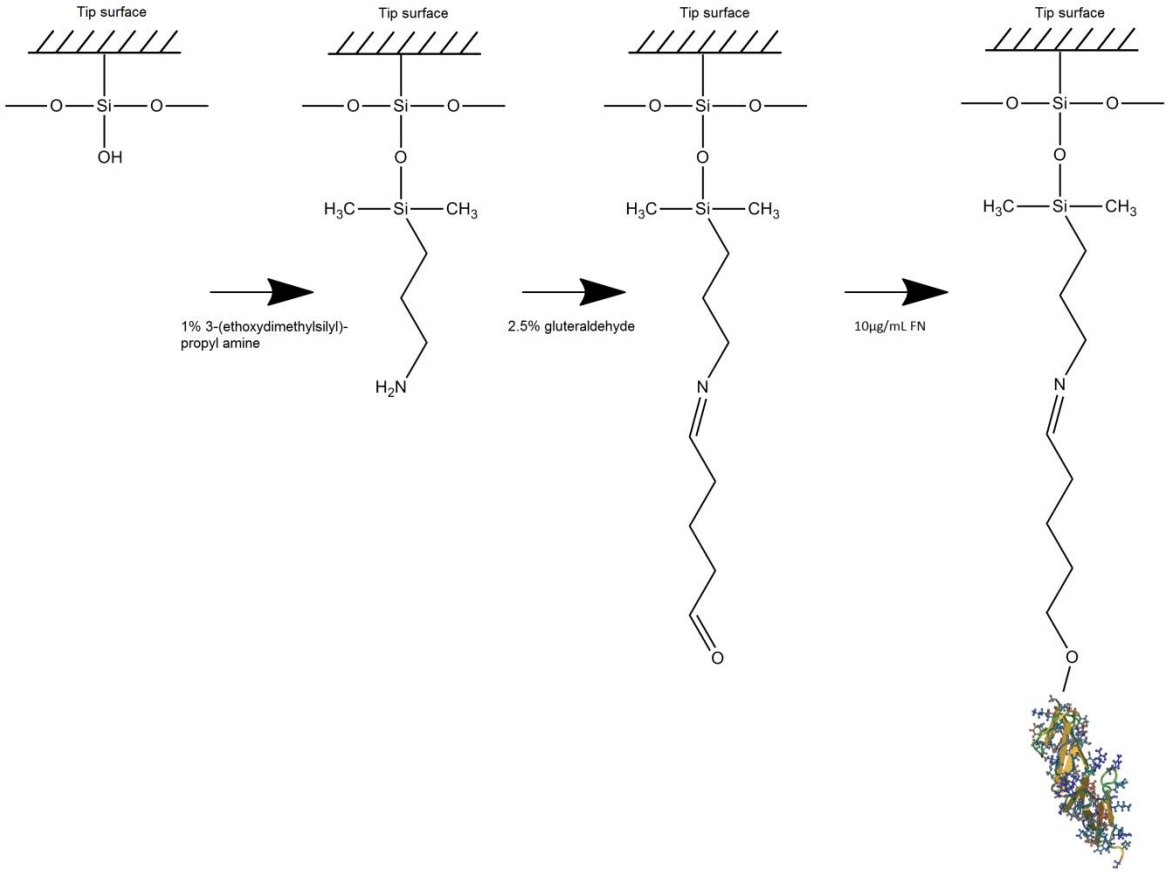

Figure 5-2: Illustration of tip FN functionalization reaction scheme. The plasma cleaned SiN surface is exposed to 3-EDSPA for one hour then washed in PBS. The tip is then placed in a GAH solution for one hour then washed in PBS, and finally placed in a solution of FN for one hour, then washed and stored in PBS.

The functionalization method uses silanization to bind the cross-linking molecule, GAH, to the tip, which in turn cross-links the protein (Figure 5-2). This method was adapted from a previous study by Vinckier et al. [248] that used a silane-GAH binding reaction to attach microtubule proteins to a silicon wafer. To confirm that the FN is present on the tip and that other functional groups introduced during to the functionalization procedure did not interfere or inhibit the FN interaction, a thorough characterization of the tips by performing fluorescent measurements and AFM force measurements prior to the experiments.

5.3.2 *Fluorescence*

The AFM tips and a control silicon wafer surface were stained with FN antibodies to determine that FN was bound to the surface. A control tip and wafer show no presence of FN across the probe and chip surface (Figure 5-3A and B). The FN functionalized surfaces (Figure 5-3C and D) show a fluorescence signal on the chip, along the cantilever and at the tip, indicating the presence of an FN coating.

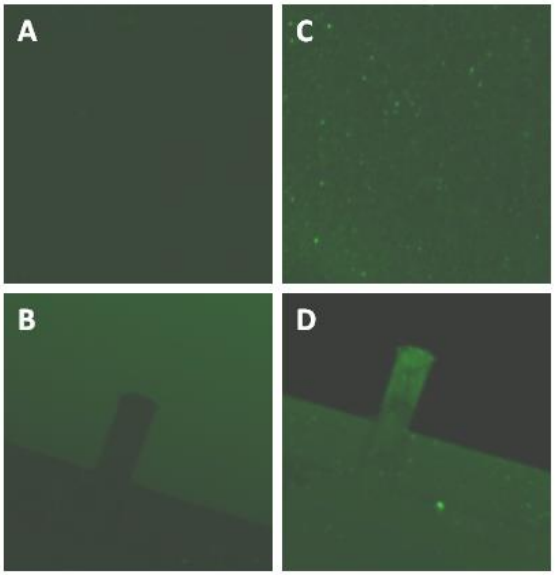

Figure 5-3: Alexa488 goat anti-rabbit IgG stained control (A) silicon wafer and (B) AFM probes, and FN functionalized (C) silicon wafer and (D) AFM probes.

5.3.3 *Functionalized Probe Characterisation*

Figure 5-4 displays representative curves of force measurements performed after each functionalization step to assess the involvement of the introduced functional groups (i.e. -OH, NH_3^+ and C=O) and final coupling of the FN on the interaction between the tip and conducting polymer. For these initial measurements, only PPy films doped with CS were assessed. Plasma treated silicon nitride tip (SiN3) bearing –OH groups, which are hydrophilic and negatively charged at neutral pH, showed no adhesion to PPy/CS (Figure 5-4A). In contrast, 3-EDSPA treated tips terminated with protonated NH + groups at neutral pH showed an electrostatic double layer force that is attractive upon approach followed by direct tip-surface adhesion of 2.0 ± 0.14 pN (mean ± s.e.m., n = 20) during retraction of the tip from the polymer surface (Figure 5-4B). This attractive interaction with the positively charged tip indicates the polymer surface is negatively

charged and further supports the presence of anionic, sulfate groups of the CS. We note that the adhesion force diminished over time, indicating contamination of the aminosilane layer. Similarly to the plasma treated tips, the gluteraldehyde (GAH) functionalized tips bearing reactive carbonyl groups are hydrophilic though showed a small adhesion of 406 ± 35 pN (mean ± s.e.m., n = 32) with the polymer surface (Figure 5-4C). The interaction of the FN functionalized tip showed longer range interactions, consisting of multiple adhesion peaks, that are characteristic for this type of protein interaction observed using AFM [197, 249] (Figure 5-4D) These initial force measurements were thus useful in providing general information on the polymer surface chemistry (e.g. surface charge) and, importantly, confirming the FN interaction with the polymer.

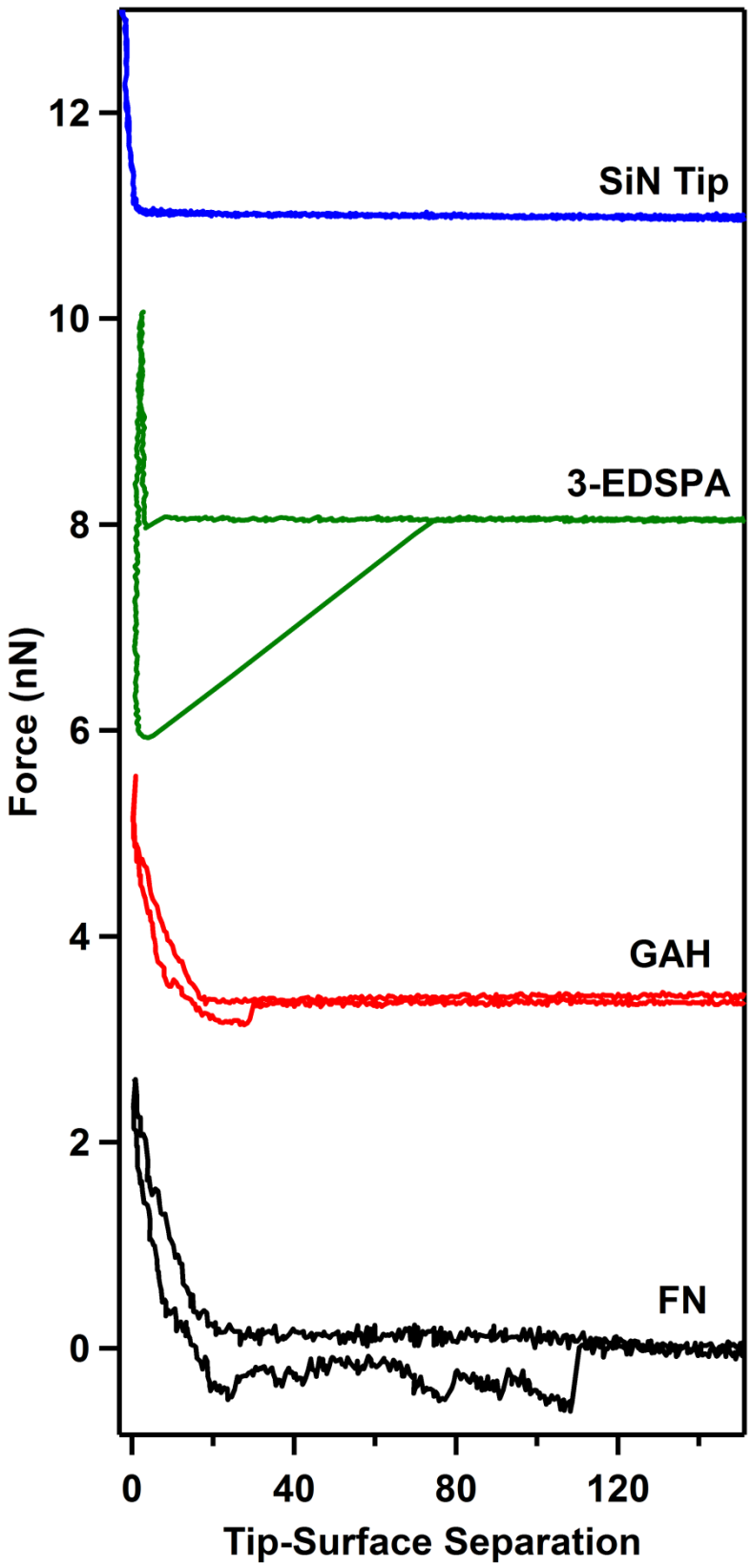

Figure 5-4: Representative force curves for interactions of each additional functionalization chemical. (A) Clean SiN tip, (B) 3-EDSPA, (C) GAH, and (D) FN. Performed on PPy/CS film.

5.3.4 *Fibronectin Force Curve Profile*

Figure 5-5 shows a typical force curve for the FN-polymer interaction; the rupture events (peaks) during retraction (blue line) indicate protein adhesion and subsequent protein extension and unfolding, as the tip retracts from the surface [96, 190].

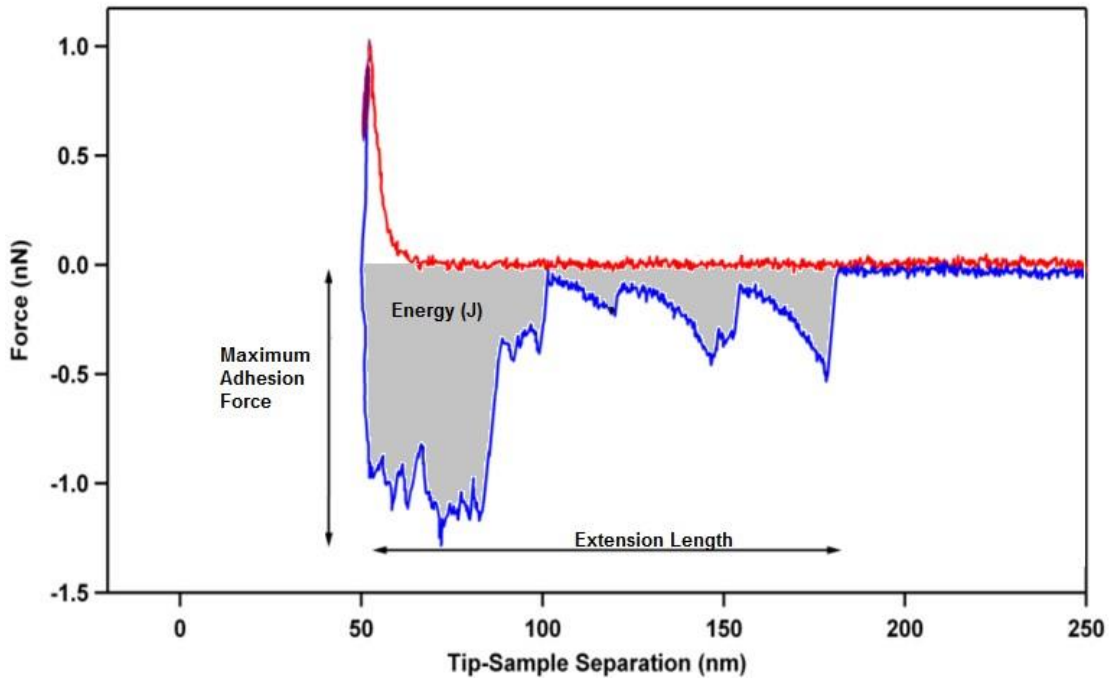

Figure 5-5: Example force curve analysis, extension (red) and retraction (blue) curves. The energy (integral of the retraction) is marked in grey. The maximum adhesion force and total extension length are annotated.

The initial adhesion (large peak), labelled as non-specific adhesion, is due to the inter- and intra-protein interactions and detachment of several proteins from the surface. The maximum adhesion force (vertical arrow), given as the maximum of the peak, if often used to quantify the general strength of protein adhesion to the surface. The subsequent smaller peaks, or rupturing events, that occur as the tip is retracted to longer separation distances provide information on the unfolding of FN. The final peak can be analysed to calculate the extension (stretched) length of a protein just prior to

detaching form the surface. The final peak force mostly reflects the force required to detach a few or even a single molecule. While forces can be assigned to the various peaks and their specific interactions, the total energy consumed for the entire interaction and to completely remove the protein from the surface is given as the integrated area of all peaks (grey shaded area). There may also be an attractive force between the protein and the polymer surface upon approach (not depicted in Figure 5-5); this is indicated by a small deflection towards the surface before contact is made (interaction described in general detail Figure 2-17, pg. 2-80).

5.3.5 *Dwell Time*

The dwell time parameter for force spectroscopy determines the length of time the tip spends in contact with the surface during the measurement (i.e. once the tip has reached the maximum applied force and prior to retracting from the surface). This will influence the protein-surface interaction due to time-dependent interactions such as the ability for protein to fully bind to the surface or undergo conformation changes. To determine the appropriate dwell time, force curves were conducted at different dwell times of 0, 1, 3, 5 and 10 seconds on a PPy/CS sample.

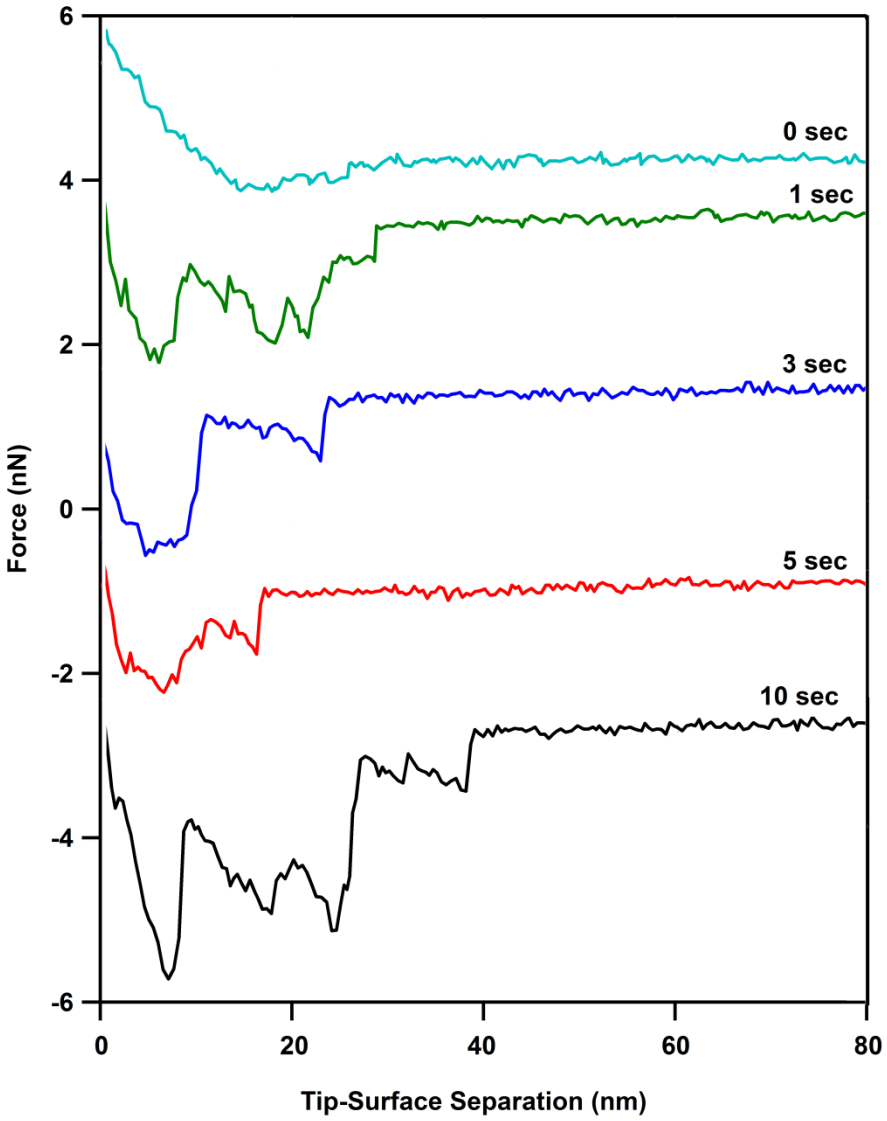

Figure 5-6: Representative force curves for dwell times; 0 sec (teal), 1 sec (green), 3 sec (blue), 5 sec (red), and 10 sec (black).

Figure 5-6 displays representative curves for each dwell time. With zero dwell time (zero sec), there was very little interaction between protein and the polymer (Figure 5-6 teal curve). Beyond a dwell time of > 1 sec, the FN interaction was observable. The mean energy and maximum adhesion force for the FN detachment as a function of the different dwell times is shown in Table 5-1.

Table 5-1: Mean adhesion force and energy for dwell times 0-10 sec (N=9)

Dwell Time (sec)	Adhesion Force (nN)	Energy (J)
0	0.61 ± 0.09	1.1 ± 0.7 e^{-17}
1	2.3 ± 0.8	2.0 ± 0.8 e^{-17}
3	0.95 ± 0.02	0.96 ± 0.25 e^{-17}
5	0.89 ± 0.13	1.6 ± 0.8 e^{-17}
10	2.3 ± 0.5	7.5 ± 3.8 e^{-17}

There was no significant difference in the adhesion force for dwell times of 1 and 10 seconds. The longest dwell time of 10 sec, while allowing the protein to develop strong binding to the surface, is not ideal. There may be drift of the cantilever position which can damage the functionalized tip and introduce errors into the measurements. Furthermore, the significantly higher interaction energy for the 10 sec dwell time suggests a possible interaction with multiple FN molecules which is not desirable for single molecule measurements. The 1 sec dwell time was sufficient to induce an FN– surface interaction and thus was chosen for the measurements. The use of this dwell time avoided the need to use longer dwell times that showed no significant difference in adhesion/detachment energy and minimised issues due to drift and long experiment times.

5.3.6 *Force Curve Profile Classification*

Four prominent force curve profiles that were indicative of different FN-PPy interactions were observed (Figure 5-7). No interaction was defined as a null force curve (Figure 5-7A).

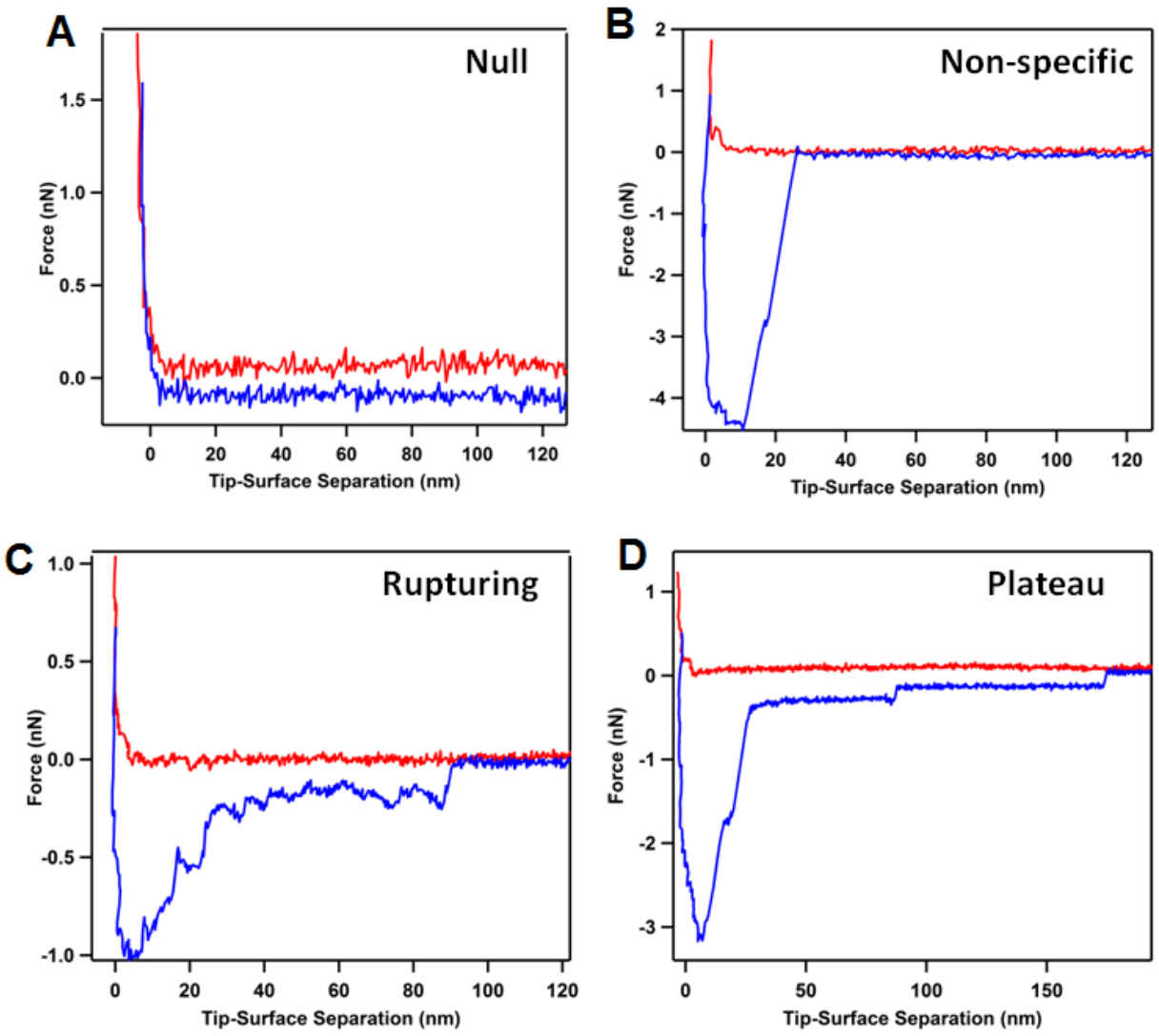

Figure 5-7:Force curve profile types; (A) Null (performed on PPy/HA), (B) non-specfic (performed on PPy/pTS), (C) rupturing (performed on PPy/pTS), and (D) plateau (performed on PPy/pTS).

5.3.6.1 Non-specific Force Curve Profile

Non-specific interaction is defined here as adhesion represented by a peak that occurs directly at the surface or effectively at the point where the tip detaches from the surface (Figure 5-7B). This type of adhesion is typically due to the interaction of several proteins on the tip, involving both intra and inter-protein interactions. Inter- protein interactions include electrostatic, hydrophobic and hydrogen bonding, while inter-protein interactions include unfolding of the protein or adhesion between the proteins, all of which may contribute to the strength or energy (integral of area under peak) of protein adhesion. Even though the peak reflects the degree of protein adhesion to the surface, this type of interaction is generally referred in AFM measurements as being 'non-specific' as the specific forces involved are not readily identified. For AFM tips functionalized with proteins, the non-specific adhesion is often always present due to the inevitable direct tip-surface interaction and as such is initially observed in the other main types of interactions.

5.3.6.2 Rupturing Force Curve Profile

Force curves that display rupturing events indicate that the protein ruptured as the tip retracted from the surface (Figure 5-7C). These rupturing events can be characteristic of domains with the protein unfolding [190], and may also be due to multiple proteins binding and/or multiple binding sites on a single protein. For the protein domains to unfold under force the FN must be tethered to the surface strongly enough to cause the rupturing events, and this process can be studied in greater detail through analysing the rupture lengths as discussed in further detail below (5.3.6.4, pg. 5-175).

5.3.6.3 Plateau Forces

The detachment of the protein can proceed via 'non-specific' desorption forces that show a constant force independent of the extension length, i.e. force plateau, as shown in Figure 5-7D. The plateau forces were observed to occur in both non-specific and rupturing profiles, as the tip finally detaches from the surface. These plateau forces are well described in studies on polyelectrolyte chain desorption from a surface and arise due to dependencies on the dissociation rate of repeating polymer chain-surface contacts relative to the extension rate and presence of a charged surface [250-251].

The probability of each of these interactions was analysed for each polymer/dopant system (Figure 5-8).

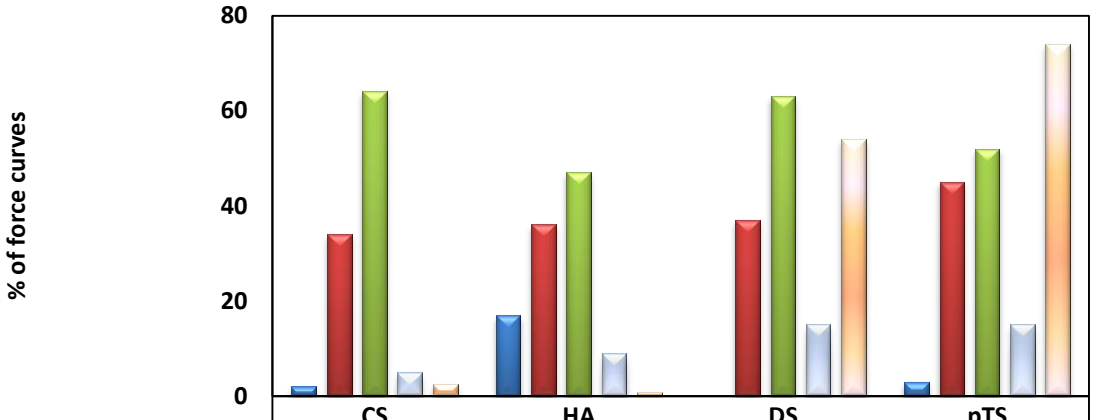

	CS	HA	DS	pTS
Null	2	17	0	3
Non-Specific	34	36	37	45
Rupturing	64	47	63	52
Plateau	5	9	15	15
Attractive Approach	2,5	0,8	54	74

Figure 5-8: Percentage of force curve profile types for each dopant, in addition to plateau events and attractive forces upon approach. n=225 for each dopant.

The probability of a null adhesion interaction was negligible for all dopants except HA. PPy/HA showed a probability of 17% of no interaction between the polymer and protein. The probability of a non-specific interaction occurring was similar for all dopants (~ 35%), although PPy/pTS had a slightly higher probability (45%). The probability of a rupturing event occurring was highest for PPy/CS and PPy/DS (64% and 63% respectively). PPy/pTS and PPy/HA had much lower probabilities (52% and 47% respectively), as this type of interaction only occurred for approximately half of the interaction.

There was a sharp division between CS and HA, and pTS and DS for the plateau events and attraction upon approach. The probability of an attractive force upon approach was significantly higher for PPy/DS and PPy/pTS (54% and 74% respectively), and also the probability of a plateau event occurring (15% for both dopants) compared to PPy/HA and PPy/CS. The attractive force upon approach suggests a Coulombic attraction between protein and polymer, indicating that the surface charge of PPy/pTS and PPy/DS facilitates a stronger attraction compared to the other dopants. Plateau events are the result of repeating protein-surface contacts due to an oppositely charged surface; pTS and DS may present a more strongly negatively-charged surface which promotes this type of interaction compared to HA and CS.

5.3.6.4 Single Molecule FN Instructions

In the rupturing curves (Figure 5-7C), there are various characteristics of the force curve that define whether a single FN molecule remains tethered between the tip and polymer after the initial non-specific adhesion. These types of curves are displayed in Figure 5-9A and are accompanied by a schematic depicting the different single FN

molecule interactions (Figure 5-9B). The peak at Figure 5-9A(i) corresponds to initial detachment of the tip and FN molecules from the surface, which is the result of a non-specific adhesion. The two subsequent peaks and peak spacing at Figure 5-9A(ii) and Figure 5-9A(iii) correspond to the sequential unfolding of domains, represented by red spheres (Figure 5-9B), of a protein that is tethered between the tip and sample.

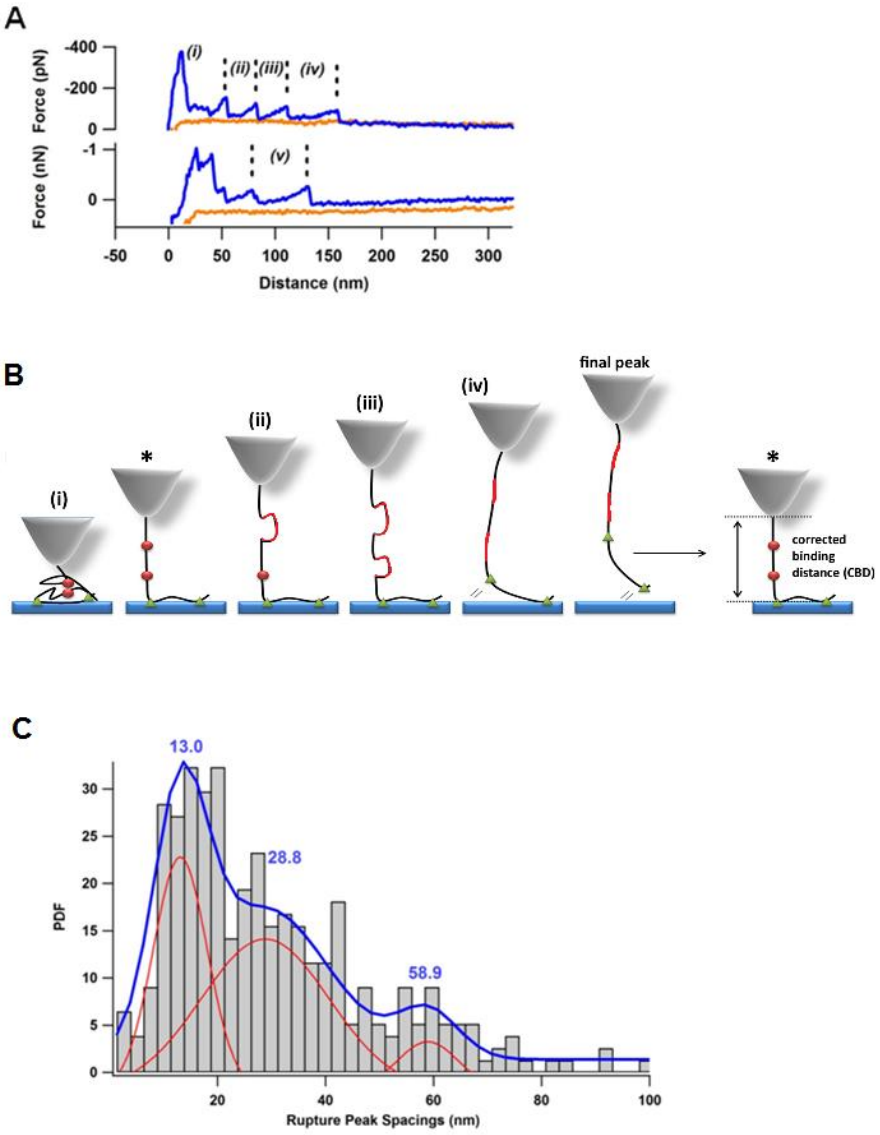

Figure 5-9: (A) Representative force curve on PPy/CS with specific binding and domain unfolding marked. (B) Corresponding schematic of the interactions in (A). Red spheres are unfolding domains, red lengths the unfolded domain lengths, and green triangles FN-polymer binding sites.(C) Probability density functions of distances between successive rupture peaks in force profiles from all polymers. Red curves are individual gaussian fits and automated multipeak fitting (blue curves) (IGOR PRO, Wavemetrics).

As the domain(s) unfold they add distance (Figure 5-9B red line) to the overall extension length of the molecule. The distance spacing of these peaks is quantified as a probability density function (Figure 5-9C), producing peak distributions at 13.1 ± 0.4 nm (mean ± s.e.m., n = 137) and 28.8 ± 0.7 nm (mean ± s.e.m., n = 107). These distances have previously been attributed to intermediate and fully unfolded lengths of FNIII domains respectively [197]. The unfolding forces (~150 pN) and peak spacing of ~ 28 nm, which is consistent with the fully unfolded length of FNIII (~ 90 amino acids), indicates the interaction of single molecule FN.

Successive rupture peaks may also occur due to the detachment of multiple protein binding sites (Figure 5-9B green triangles) from the polymer wherein the first binding site detaches at point (v) (Figure 5-9A), followed by extension of the protein, until elastic restoring forces of the protein cause detachment of the final binding site. These binding events can occur in the absence of domain unfolding and have peak spacings of 58.9 ± 3.0 nm (mean ± s.e.m., n = 67) (Figure 5-9C). This peak spacing of 58.9 ± 3.0 nm also suggests that binding is most probable at sites on the protein separated by this distance or, alternately, the existence of specific binding sites on the protein.

5.3.7 *Single Molecule Unbinding Forces*

The force required to detach a single FN molecule off the polymer surface was measured using the unbinding force of the final rupture peak (annotated in Figure 5-9B). The binding force indicates the affinity of the interaction between protein and polymer, with a higher binding force caused by a stronger affinity.

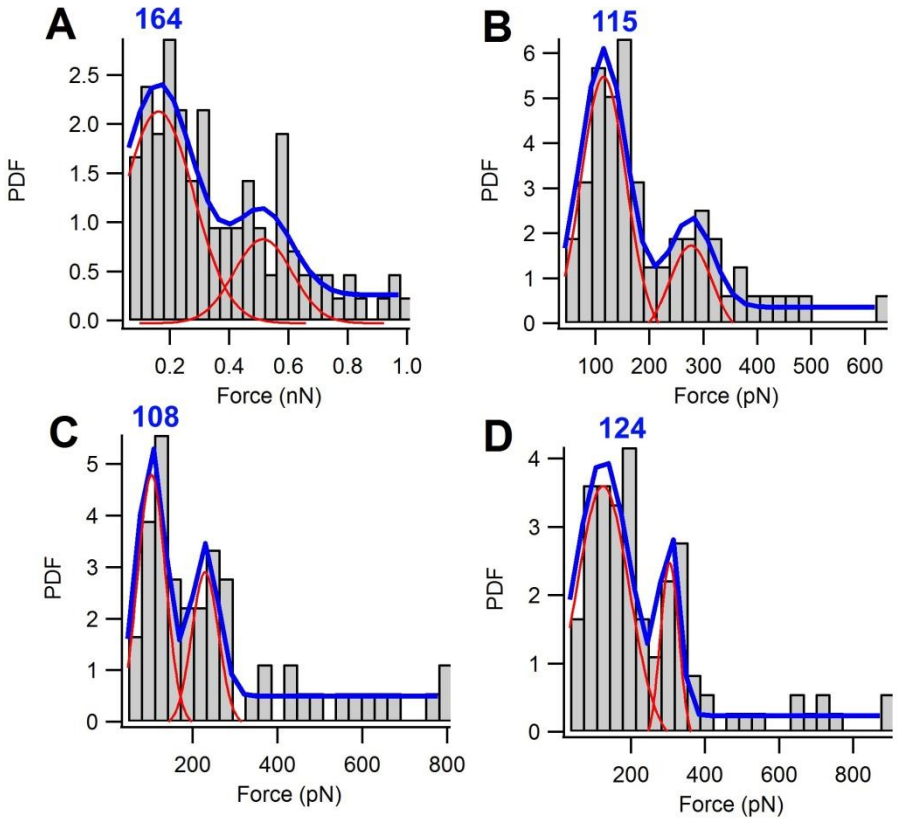

Figure 5-10: Probability density functions of unbinding forces for the final rupture peak of (A) CS (n = 109), (B) DS (n = 65), (C) HA (n = 58) and (D) pTS (n = 102). Red curves are individual gaussian fits and automated multipeak fitting (blue curves) (IGOR PRO, Wavemetrics).

The unbinding force of the final detachment of FN from the polymer was quantified as a probability density function (Figure 5-10). A higher affinity for binding was observed for CS (164 ± 10.1 pN, *n* = 61) compared to DS (115 ± 11.0 pN, *n* = 41), HA (108 ± 8.5 pN, *n* = 30) and pTS (124 ± 12.5 pN, *n* = 66).

5.3.8 *Corrected Binding Distance*

To elucidate interactions involving detachment (or effective binding) sites of the protein we focused on analysing individual force profiles representing the unfolding and/or extension of FN, as described above in Figure 5-9A. More specifically, the

analysis involved subtracting the distances of all peak spacings, including those associated with unfolding and protein–surface detachment, from the distance at the final peak. This gives what we refer to as the “corrected binding distance” (CBD), representing the extended length of the FN, tethered between the tip and surface, just prior to undergoing domain unfolding and/or surface detachment (Figure 5-11B); far right schematic). The CBD is thus governed by the distance between the two attachment positions (dashed lines) of the protein to the tip and polymer; this being firstly, the covalent attachment of the protein to the probe and secondly, the non-covalent protein-surface binding site that is either the first of multiple binding sites to detach, as shown in (Figure 5-9B), or the sole (and final point of detachment) when no other binding sites are present.

Probability density functions of the CBD show a primary peak distribution value ranging from 59 - 66 nm for all polymers, with a secondary peak distribution value ranging from 116 – 119 nm for CS and DS polymers and possibly PTS and HA (Figure 5-11A). Minor peak CBD distribution values also appear at 171 nm and 166 nm for CS and PTS, respectively (Figure 5-11A).

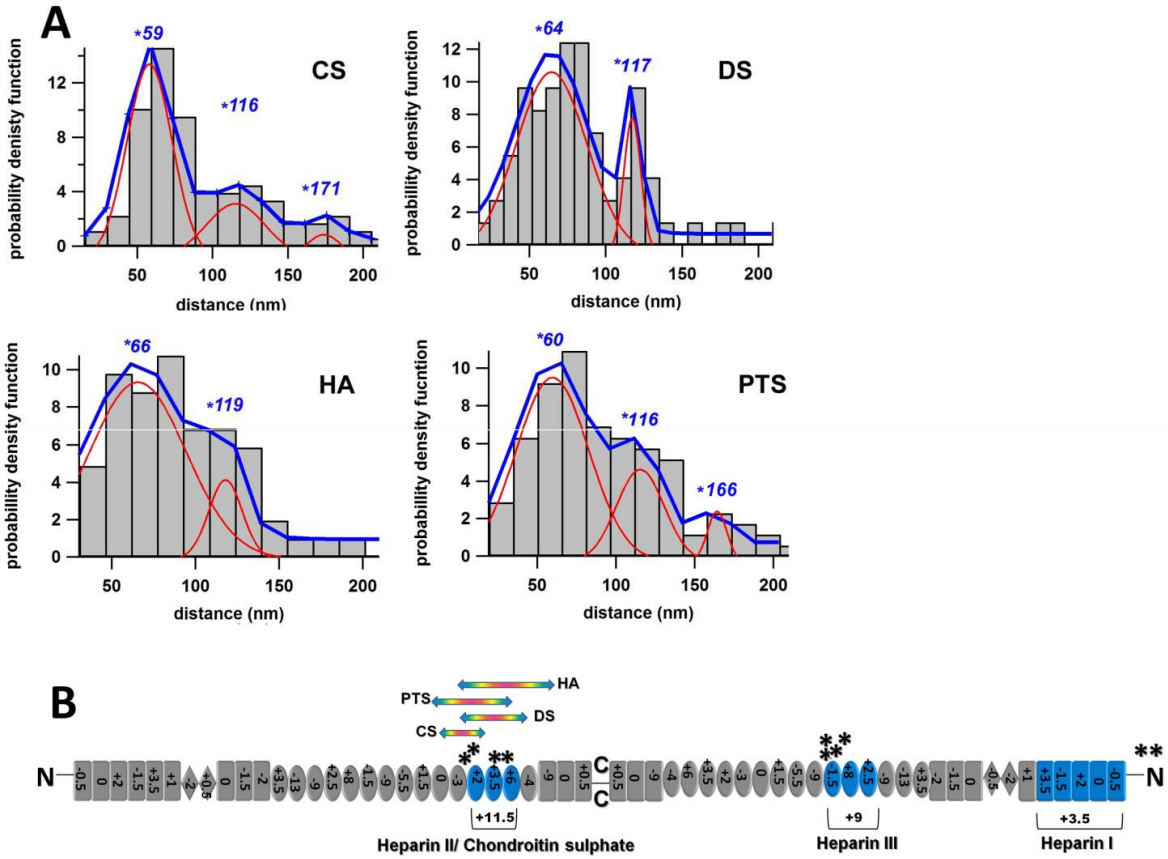

Figure 5-11: Probability density functions of corrected binding distance (CBD) values (black), Gaussian fit (red), and detachment forces (blue) corresponded with CBD values for (A) PPy/CS, (B) PPy/DS, (C) PPy/HA, and (D) PPy/pTS. (B) Model of extended FN showing calculated length (158.8 nm) of based on x-ray crystallography dimension of FNI (2.5 nm, rectangles), FNII (0.7 nm, diamonds) and FNIII (3.2 nm, ovals), where 0 nm corresponds to attachment position of FN to the AFM tip. The most probable CBD values (black asterix) are marked at their respective positions on the protein (B). The heparin binding domains, $HepII_{Fn12-14}$ (59.1 – 68.7 nm), $HepIII_{Fn4-6}$ (115.7– 125.3 nm) and $HepI_{Fn1-5}$ (143.2– 158.8 nm) are coloured in blue. Standard deviations (σ) calculated from full width half maximum (FWHM) (where FWHM = 2 √2ln2σ) of CBD distributions for the $HepII_{Fn12-14}$ (at position 59.1 – 68.7 nm) of each dopant are given by the length of the rainbow arrow.

The significance of these CBD distributions is that, even though FN binding to the tip is generally expected to be random via gluteraldehyde linkages with nucleophilic amine groups at the N-terminus and on free lysine residues, their observation indicates that both the tip and polymer must bind to specific sites on the FN. Furthermore, the presence of CBD values at 166-171 nm corresponds to the length of ≈ 160-175 nm for

fully stretched plasma FN [148, 252-253] To obtain these values, it would require that the FN be attached to an N-terminus and interact with the polymer via the opposing N-terminus. This binding configuration, which presumably allows the entirety of the extended FN molecule to freely interact, is likely to facilitate binding at additional sites separated by the distance of 58.9 ± 3.0 nm (mean ± s.e.m., n = 67) previously observed in the rupture spacings (Figure 5-9C). Repeated sampling of the 3 different peak CBD distribution values within sets of force curves (n = 25) from all individual AFM tip experiments (n = 36) further supports the detection of multiple binding sites along a single FN molecule instead of multiple FN molecules having 3 different binding configurations and each with an extended length differing by ≈ 60 nm. These observations suggest that FN preferentially has a fixed attachment to the tip in the vicinity of an N-terminus with binding occurring at specific sites along its length.

Based on the above observations, we use the known FN structure and dimensions of the FNI, FNII, FNIII domains based on X-ray crystallography studies [254] to construct coordinate map for identifying positions on the protein involved in binding to the polymer (Figure 5-11B). The map gives a calculated FN length of 158.8 nm by taking into account the size of each individual domain and absence of variable splicing regions for plasma FN. The preferred N-terminus binding position of the tip is made the zero reference point to identify the binding locations. The extent of net positive charge of each FN domain [255], which generally underlies their binding affinity to sulfate sites on GAGs [256], is also specified. When cross-referencing the peak distribution values of the CBD (black asterix) to their locations on the model, we observe that they superimpose to well-known Heparin (Hep) binding domains (Figure 5-11B; blue

highlighted domains), including a particular sequence of the HepII $FNIII_{12-14}$ near the COOH-terminus, HepIII $FNIII_{4-6}$ and HepI FNI_{1-5}. The main CBD distribution at 59-66 nm indicates most probable binding occurs at the HepII domain and accordingly this is recognized as the highest affinity GAG binding site due to the presence of discontinuous positively charged amino acids in $FNIII_{13-14}$ domains that form a cationic cradle [257]. Standard deviations of the CBD distributions associated with the HepII domain reflect the binding specificity at this position (Figure 5-11B; coloured arrows), which is highest for CS followed by DS and then HA and PTS. As shown previously in Figure 5-10, a higher affinity and/or specificity of binding for CS is also evident in single molecule FN-polymer unbinding forces that are significantly higher for CS compared to the other dopants.

5.4 Electrical Stimulation

Electrical stimulation of the polymer electrodes during force spectroscopy measurements showed a significant change in the adhesion of the protein to the polymer. FN adhesion was significantly increased by an order of magnitude (2-20 nN) at the onset of the PPy oxidation potential (≈ 400 mV) and then reversibly decreased to values of 100-200 pN with force profiles similar to those for the non-stimulated polymer. The change in the interaction between protein and polymer is displayed in Figure 5-12A, with representative force curves at different voltages with the potential window.

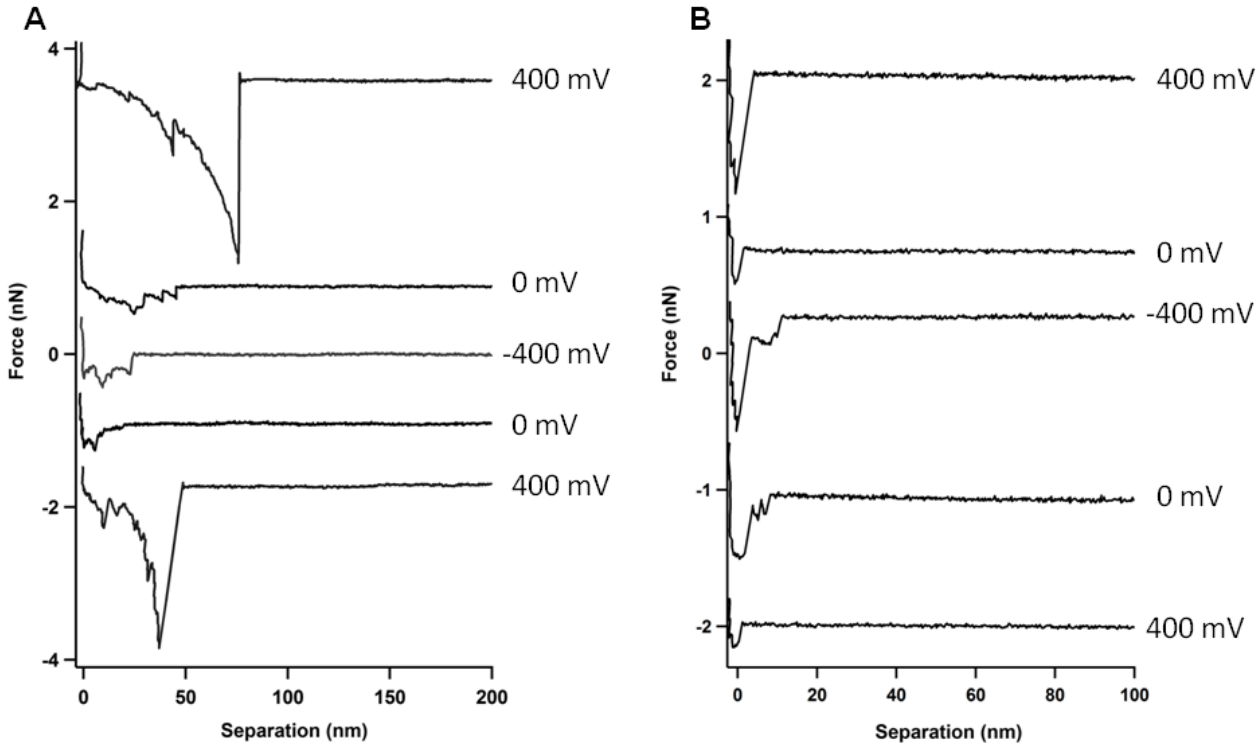

Figure 5-12: Representative force curves for 400 mV, 0 mV and -400 mV during electrical stimulation for (A) PPy/DS and (B) gold mylar

When the same electrical stimulation is applied to a gold mylar substrate, force curve profiles showed no change in FN adhesion (Figure 5-12B). Although the interaction of multiple FN molecules is likely, the magnitude of the adhesion increase does not scale with (*n)* number of possible interacting proteins given that the size of a single FN molecule (≈ 25 nm) is comparable to the interaction area of the probe. Thus, the very high forces over relatively small extension lengths indicate that it is likely that one or a few proteins are strongly bound along their length.

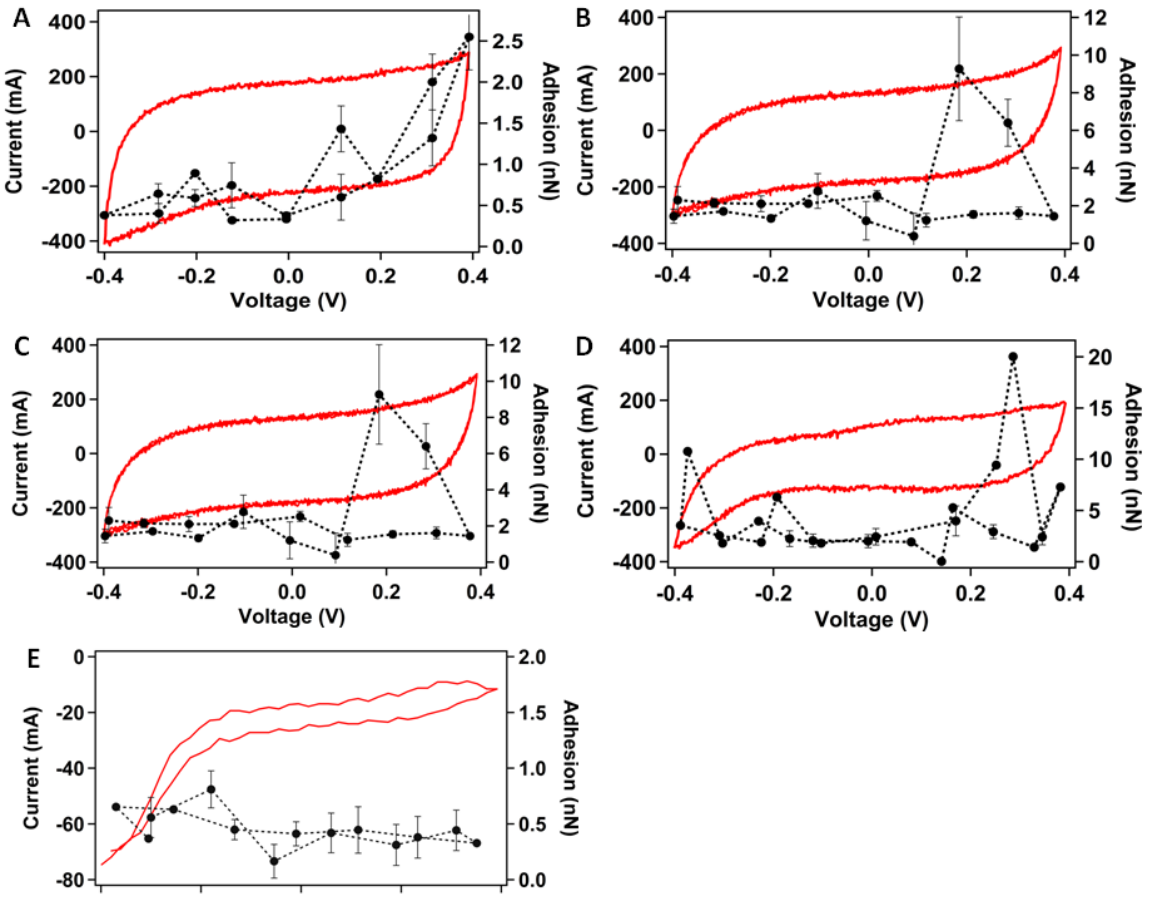

Figure 5-13: Adhesion force (black points) and CV roburograms (red) for (A) PPy/CS, (B) PPy/HA, (C) PPy/DS, (D) PPy/pTS and (E) gold mylar

All dopants showed a similar response, in particular a sharp increase in adhesion at 0.2-0.4 V (Figure 5-13). In contrast, gold electrodes do not show distinct FN adhesion, apart from that related to direct tip-sample adhesion, nor any adhesion dependence on the applied potential (Figure 5-13E). The experiments were repeated using a smaller potential window and slower scan rate for the PPy/CS polymer only (Figure 5-14). Conversely for these experiments, there was no change in the FN adhesion during the electrical stimulation of the polymer.

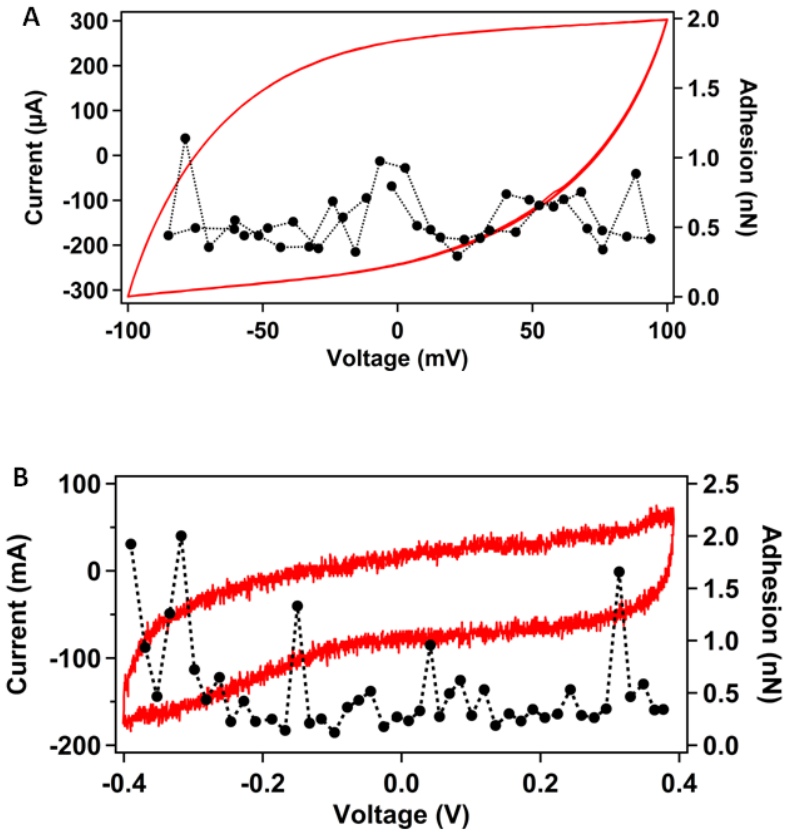

Figure 5-14: Roburograms of PPy/CS FN adhesion of (A) potential window of ±100 mV, scan rate of 50 mV/s, and (B) potential window of ±400 mV, scan rate of 4 mV/s.

5.5 Discussion

5.5.1 *Probability of Binding*

The dopant distribution within a PPy films has already been discussed (Chapter 4 , pg. 4-125) and it is known that the distribution homogeneity of the polymer can vary depending on the dopant. PPy/HA has a much more inhomogenous distribution of dopant compared to PPy/CS as shown by several AFM surface characterisation techniques (including C-AFM and KPFM). The probability of PPy/HA having no interaction with the protein (null adhesion) is greater than the other dopants (17%), which we discuss in the next chapter may be due to the availability of dopant on the surface. The higher possibility of attractive approach forces and plateau events present for PPy/pTS and PPy/DS may be due to the higher degree of sulfonation of the polymer. The structure of DS is very similar to HA and CS in that they are all polysaccharide chains, however DS carries four sulfonate groups per repeat compared to the single sulfonate group of CS and single hydroxyl group of HA. pTS is much smaller than other three dopants and consists of benzene ring with a sulfonic acid and a methyl group ($CH_3C_6H_4SO_3H$), and has a relatively strong polarity. The presence of these negatively charged groups in a higher density may promote repeating points of contact along the protein, therefore resulting in a plateau event as the protein is pulled off the surface.

5.5.2 *Binding Specificity*

When cross-referencing the CBD values to their positions on the model, we discover that they superimpose to well-known heparin binding domains, indicating binding to a

particular sequence of the HepII Fn_{12-13} domain near the COOH-terminus, HepIII Fn_{1-5} domain, and HepI domain making up the NH terminal region (depicted in Figure 5-11B). The compact form of FN supports this model as the domains collectively present themselves to presumably facilitate binding of this particular sequence of the Hep domains. Of the three domains, the most probable binding clearly occurs at the HepII domain (CBD at 60-70 nm) for all dopants and accordingly HepII is recognized as the main GAGs binding site due to the presence of eleven discontinuous positively charged amino acids clustered together by the tertiary folding of the FNIII13th and FNIII14th to form a cationic cradle [257].

Heparin has the highest negative charge density of any known biomolecule and is very similar in structure to the other GAGs, CS and HA. Heparin carries three sulfonate groups compared to the single group on CS and lack of sulfonate groups on HA. The synthetic GAG, DS, also carries many sulfonate groups and is highly negative, while pTS carries a single group. It is these density and arrangement of these sulfonate groups in GAGs that are known to facilitate binding to the Heparin I, II, and III domains on FN; though termed the Heparin domain (due to early studies on Heparin and its high affinity of binding) binding to these domains is also synonymous with CS. The heparin binding sites are all highly positive domains, with the HepII site being the area of highest positive charge along the protein.

Hence, the cationic cradle of the Hep domains will preferentially bind when encountering negatively charged surface groups such as the sulfonate groups within the dopants. The standard deviation of the CDB distribution associated with the HepII

domain reflects the specificity of binding at the position of the site, which was highest for CS, followed by DS and then HA and pTS (Figure 5-11B arrows). Along with heparin,

CS is prominent in FN binding with important determinants located to the FNIII14 and FNIII13 [114], leading to the high specificity for CS. Heparin-FN interactions have been mimicked using synthetic polysaccharides like DS [258], while for the non-sulfonated HA it is uncertain if binding on its own is possible or requires the presence of mediating proteoglycans [259]. Many of these early studies involve binding of FN fragments whereas our approach using intact FN shows that all polymers, including those with HA, are capable of specific binding. Even for small molecular weight pTS bearing a single sulfonate group per molecule, its distribution at the polymer surface is sufficient to enable specific binding of the HepII domain. The high specificity for CS is also shown through the binding forces of the protein to the polymers, as CS results in the highest affinity binding compared to the other three dopants.

5.5.3 *Electrical Stimulation Effect on Binding*

The influence of electrical stimulation on the protein adhesion is due to the polymer's inherent 3-dimensional nano- and micro-topography, and porosity, which significantly increases the charge storage capacity of the electrode. Gold mylar is not capable of the same charge storage capacity, evidenced by the much smaller area of the cyclic voltammogram compared to the polymer. The associated dramatic increase in surface charge density during oxidation is then responsible for strong Coulombic attraction that "pins-down" the protein. The latter occurs only at faster scan rates of 50 mV/sec where counter ion diffusion, but not electron charge transfer, is the limiting electrochemical process. Diffusion of charge balancing cations, e.g. sodium ions

occupying anionic sites on the dopant, out of the polymer during oxidation is rate limiting. This renders anionic sites on the dopant unavailable for charge neutralization of positive charges generated on the polymer backbone – this gives rise to a high positive surface charge density. When cycling at slower rates (5 mV/sec) that do not impose time-limiting diffusion, charge equilibrium occurs and reduces the Fn-polymer Coulombic attractive forces. With a smaller potential window the polymer does not have enough charge injection to oxidise to the point where the surface charge density will increase for noticeable adhesion changes.

5.5.4 *Binding Model*

Based on the above picture emerging of FN-binding, we describe a prospective model to provide the first insight into "molecular switching" of single FN molecules as they alter their binding affinity and related conformation in response to equilibrium and non-equilibrium redox states of the polymer during electrical stimulation.

The model translates the AFM observations to the expected binding interaction of a single FN molecule (only one FN monomer is shown) given the involvement of multiple heparin domains (blue domains). The ability of multiple binding via the different heparin domains indicates that the FN is more likely to adopt an extended conformation, which is depicted in the model based on previous representations of unfolded FN adsorbed onto negatively charged surfaces [260]. This configuration is considered to be more bioactive due to the presentation of RGD regions.

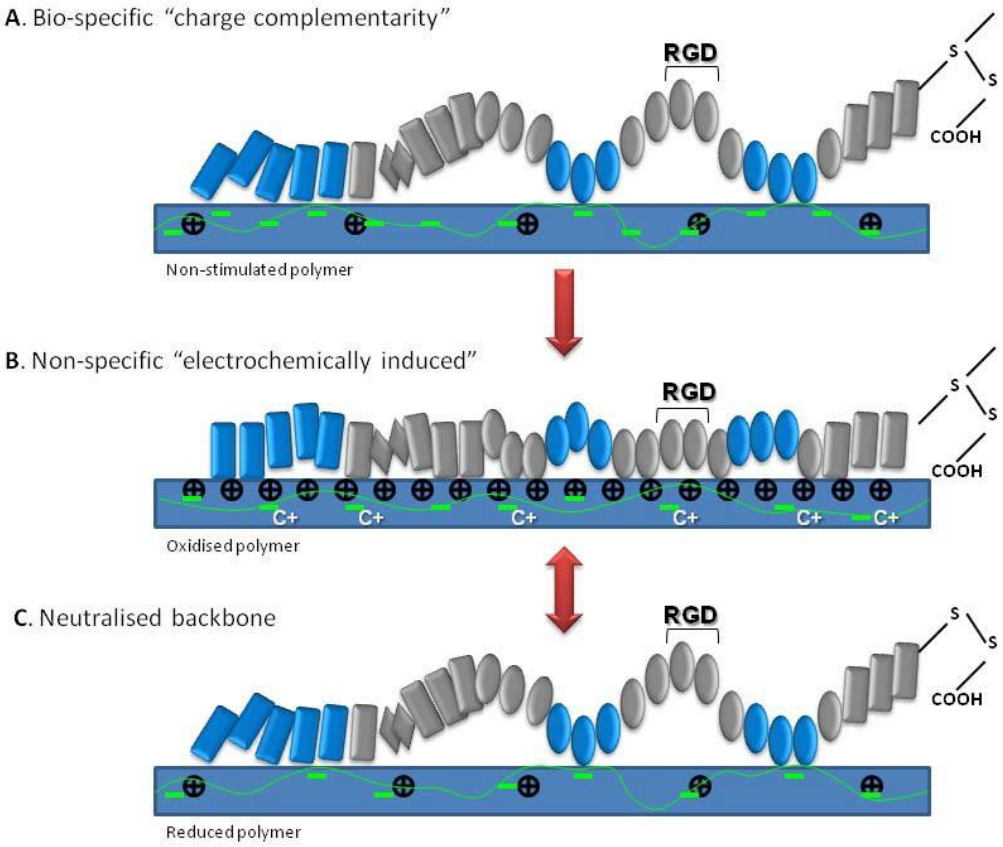

Figure 5-15: Model of FN-polymer interaction for (A) as grown, (B) oxidised, and (C) reduced polymer.

For the non-stimulated polymer in Figure 5-15A, ionic interactions stabilizing the native compact FN conformation are disrupted by interacting hydrophilic, charged surface groups of the polymer, causing the protein to adopt a more open conformation. As FN is an amphoteric protein, comprising a mixture of negative and positively charges, repulsion of the predominately negatively charged protein with anionic/sulfate groups of the GAGs can change to attractive forces due to preferential alignment of the cationic heparin domains. When the protein is at very small separation distances from the polymer, ions interact as discrete entities rather than part of an overall net charge and their subsequent Coulombic attraction as individual ion pairs governs the protein-surface binding, as opposed to the net protein interaction. This type of interaction is

referred to as “charge complementarity”. Charge complementarity is often exploited by biological macromolecules, for example docking in protein-DNA complexes, to change a non-specific interaction into a highly specific one. By applying more negative (reduction) potentials, the interaction can be reversed to resemble single molecule binding and extension interactions of FN with the conducting polymer surface. The application of a positive voltage induces charge (black positive charge) on the polymer backbone causes a strong Coulombic attraction of the negatively charged FN domains (Figure 5-15B). At higher scan rates (50 mV/sec), outward diffusion of charge balancing cations (C+) occupying anionic sites on the immobile GAGs is rate limiting. This renders anionic sites on the dopant unavailable for charge neutralization of the positive charges on the polymer and protein adhesion is present. At lower scan rates (5mV/sec), outward cation diffusion (black arrows) is not rate-limited and charge neutralization of the polymer proceeds to decrease protein adhesion. During the application of negative potentials (Figure 5-15C), the polymer backbone is uncharged and free sulfate or carboxyl groups are expected to similarly interact with the protein, as described above in Figure 5-15A. The mechanism is reversible (red arrow) between Figure 5-15B and Figure 5-15C.

The model provides molecular insight into the switching mechanisms of single molecule FN-conducting polymer interactions, particularly as the protein alters binding affinity and conformation in response to equilibrium and non-equilibrium redox states of the polymer under electrical control (Figure 5-15). The implication for the subsequent formation of discrete bonds at heparin domains, coupled to the flexibility of the protein’s extended conformation, is that local structural changes are induced to

actively present cell binding (RGD) domains [261]. This binding configuration can be electrochemically switched to induce non-specific binding (Figure 5-15B); a reversible process that is expected to significantly alter the protein conformation. Oxidation of the polymer results in a dramatic increase in binding strength; however the flexibility of the protein is diminished (Figure 5-15B). During reduction of the polymer, the polymer backbone is uncharged and the protein is presumably able to interact with free anionic groups in a similar manner to the non-stimulated polymer (Figure 5-15C). While others have focused on the FN conformation [143, 145, 245], our study uniquely quantifies the FN-polymer interfacial forces that play a critical role in force-dependent signal transduction processes such as cellular forces exerted on FN through integrins to regulate cell adhesion and migration.

5.6 Concluding Remarks

The study provides molecular details of controlling protein–conducting polymer interactions, which is currently tantalizing researchers in the field - from both a current perspective on the use of conducting polymer as “electronic switches” or implantable electrodes for spatially and temporally controlling cell interactions (e.g. electronic Petri dishes and electronic 3-D gels) but also retrospectively for better elucidating binding specificity of conducting polymer biosensors used extensively in the past.

These AFM measurements show that it is possible to deconvolute the complexity of interactions at these electrodes which are brought upon by their heterogeneous polymer structures coupled with dynamic redox properties. It opens up the possibility of assessing a range of other biomolecules such as soluble growth factors (e.g. NGF, fibroblast growth) whose redox-controlled extrinsic surface binding and subsequent release is increasingly being implicated as an important for strategy for implementing these materials to control nerve, muscle and stem cell growth and survival.

6 Spatial Resolution of Single Protein Interactions on Polypyrrole

6.1 Introduction

6.1.1 *Spatial Control of Protein Interactions*

The function of the ECM protein FN as a mediator for cell-surface interactions is vital for cellular adhesion and structural support on a surface [148, 262]. The adhesion and conformation of an FN layer on a surface can be manipulated via the protein density and surface properties.

The surface coverage density of FN can modify the conformation of FN as the amount of FN adsorbed onto a surface increases [155]. It was shown that as the amount of FN adsorbed on mica surface increased, the FN changed to a more 'upright' conformation. This was demonstrated using single molecule AFM force spectroscopy that showed there was an increase in the specific binding force between collagen peptides bound to the tip and the upright FN layer on the surface, and attributed to the upright FN presenting the collagen binding site [155]. Similarly for cell adhesion, the conformation of FN adhered to a surface should present cell binding sites (i.e. collagen, RGD) to aid adhesion via interactions with integrins.

The RGD binding site within FN is the primary site that facilitates cell adhesion. The clustering of RGD peptides has been demonstrated to influence cellular adhesion on the nanoscale via patterning of the sequence onto a substrate. Micellar nanolithography was used to create spatial arrays of immobilized RGD peptides linked to gold nanodots with spacings varying from 28 to 145 nm (Figure 6-1A and B).

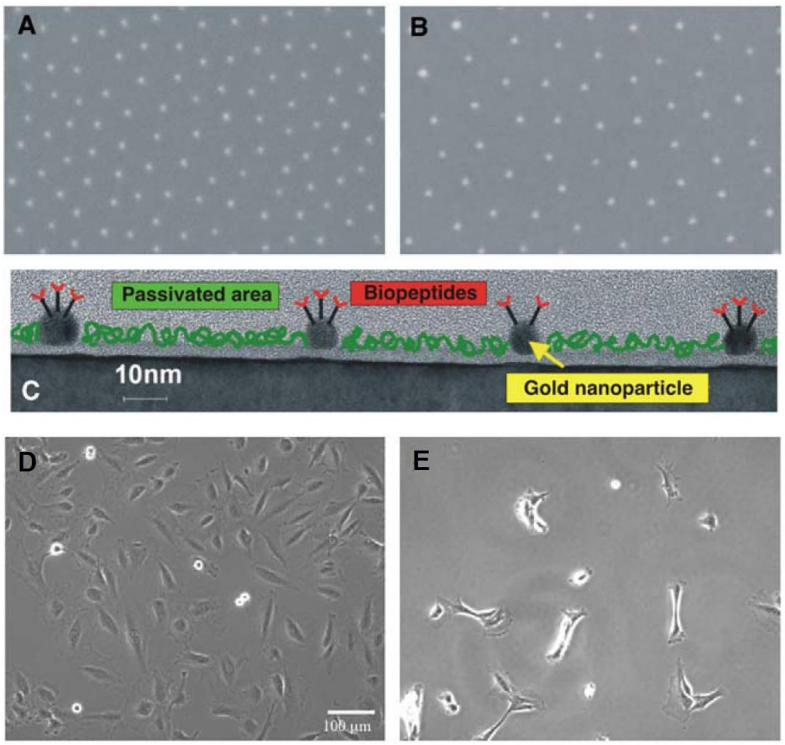

Figure 6-1: Scanning electron microscopy images of gold nanodots deposited on glass surfaces by micellar nanolithography, with average inter-dot distance (A) 58 nm, and (B) 110 nm. (C) Illustration of surface patterning; non-adhesive polyethylene glycol (green), and bioactive RGD peptides (red). Phase contrast images of fibroblasts after 24 hours adhering on nanopatterned surfaces of (D) 58 nm and (E) 110 nm [263].

The RGD peptides have a diameter of ~ 9 nm [263], hence each gold nanodot can only interact with single integrins. It was observed that the spread of the rat embryonic

fibroblasts was greatly reduced when the distance between the nanodots exceeds 58 nm, as shown by the phase contrast images in Figure 6-1D and E. The distance of 110 nm shows far fewer fibroblasts adhered to the substrate compared to 58 nm. The increasing distance between the RGD peptides reduced the ability of the fibroblasts to develop stable focal adhesion, demonstrating a dependency on the clustering of the RGD groups on the nanoscale [263].

Further studies on nanoscale RGD spacing and cluster density demonstrated an influence on cell migration [264]. Motility is a cellular response that is strongly affected by cell adhesion. A nanopatterned surface with discrete clusters of 1-9 ligands per cluster with defined spacings of 6-300 nm was produced through tethering a YGRGD ligand to a non cell-adhesive surface (polyethylene oxide hydrogel) [264]. Clustered YGRGD enhanced cell migration speed of the murine fibroblasts (WT NR6) for all of the densities prepared compared to surfaces prepared with a uniform YGRGD layer. Cell adhesion was also observed to be significantly enhanced on the substrates prepared with clustered YGRGD ligands. The variation in the YGRGD clustering was observed to affect the formation and organization of actin stress fibres within the cells, an important step of the cellular adhesion process and migration. The density of adsorbed FN has been suggested as a limiting factor for cell migration [145, 265]. Adhesion of cells to a surface is mediated by the presence of proteins such as FN, therefore integrin- ligand interactions can influence the speed of cell migration. Ligand concentration, integrin expression, and integrin affinity all contribute to changing cell migration speed, and for maximum migration the FN density is optimised with an intermediate level of integrin-ligand binding [265]. This effect was observed by

measuring the velocity of endothelial cells on a surface with a gradient of FN density (using a PEDOT:TOS electrode with a potential gradient) [145]. High density FN decreased the migration of the cells compared to the low density FN, and this was attributed to the cells being limited due to strong cellular adhesion. With a high number of integrin- ligand bonds the cells find it difficult to break these bonds, thus slowing down their migration compared to binding to areas of lower FN density. This study demonstrated the capability of using an OCP material to direct cellular migration by controlling FN adsorption using electrical stimulus.

The studies above highlight the balance required for a surface to promote both good cellular adhesion and migration, as too high a protein density will retard cell migration but too low protein density and poor adhesion will result in unsuccessful cell growth. The ideal FN concentration therefore depends on the desired cellular response, and for either situation nanoscale characterisation of local FN binding is necessary.

6.1.2 *Implications for Cell Interactions*

The structure of our OCP polymers is complex, however our nanoscale surface characterisation of surface properties shows that the surface of these polymers do have a form of innate patterning, or 'mesoscale-patterning' (mesoscale is dimensions between nano- and microscale). This pattern is growth dependent (e.g. polymerization time or dopant concentration) and defined by the repeating boundaries of the nodular structures. Furthermore, this repeating nodular structure also delineates the patterned surface distribution of surface potential, energy, dopant and conductivity, as shown in previous chapters. For example, AFM surface characterisation techniques such as phase imaging, KPFM, and C-AFM demonstrated differences in the distribution of the

dopants CS and HA throughout PPy films (4.2.4, pg. 4-130). The surface potential and current scanning (KPFM and C-AFM respectively) indicated that the dopant HA was more prevalent in nodular features of the polymer, while PPy/CS polymers had a more homogenous distribution of the dopant.

A significant finding in the previous chapter was that the GAG dopants in the polymer were shown to promote specific binding to the FN protein. The GAG dopants specifically bound to the heparin domains of the protein, with the highest affinity GAG, CS, shown to have the higher binding forces and probability of binding compared to the other dopants. Therefore, given that FN-PPy binding is likely to be mediated by the GAG dopants, we expect the mesoscale patterning of the PPy to affect the density and conformation of FN as it interacts with the surface. Implications for variations in FN binding/conformation across the surface may be changes in the density or presentation of cell binding motifs on the protein, as mentioned above.

6.1.3 *Spatially Resolving Protein Adhesion*

In order to further understand the interaction between FN and our OCP biomaterial surfaces we have applied AFM force volume mapping to spatially resolve adhesion forces. Force volume maps provide a way to simultaneously measure the protein interaction with topographical information. Measuring the adhesion force can also provide insight into the number of proteins that are binding to the surface and the probability of binding across the surface.

As we have previously revealed a relationship between surface properties and topography for these materials, we expect that the distribution variation in surface properties may influence the protein interaction.

For this study we have chosen the two GAGs CS and HA. These dopants produce polymer films that have contrary properties, while both being important ECM molecules. The variation in surface properties and the difference in their interaction with FN make these two dopants ideal for comparing and contrasting their spatial protein interactions.

6.2 Materials and Methods

6.2.1 Reagents

The pyrrole monomer was obtained from Merck and distilled prior to use. The chemicals used as the dopants were the sodium salts of pTS, HA and CS. CS was obtained from Sigma and HA from Fluka. All solutions were prepared with deionised Milli-Q water (18.2MΩ). The functionalization chemicals 3-EDSPA, GAH, and human plasma FN were obtained from Sigma Aldrich. PBS was prepared at pH 7 in Milli-Q water (18.2MΩ).

6.2.2 Methods

6.2.2.1 Biodoped Polypyrrole

Gold coated mylar was firstly prepared by cutting into strips of 0.5 cm by 2 cm area and then cleaned with methanol and Milli-Q water. Gold coated Mylar (18 Ω/square) was purchased from CPFilms Inc (USA). An aqueous monomer solution of 0.2 M pyrrole and 2 mg/mL of the counter-ion dopant was degassed in N2 for 10 min prior to polymerisation of the polymers. PPy films were grown galvanostatically at a current density of 0.25 mA/cm2 for 10 min in the aqueous monomer solution using an eDAQ EA161 potentiastat. Polymer growth was performed in a standard 3-electrode electrochemical cell with the gold coated mylar as the working electrode, a platinum mesh counter electrode and Ag/AgCl reference electrode. After growth, the films were washed with Milli-Q water, gently dried with N_2 gas and placed in Petri dishes until use.

6.2.2.2 Protein Functionalization

The tip is functionalized using an aminosilzation method to covalently bind the protein to the tip. Silicon nitride (SiN) Nanoworld PNP-DB tips are used for this method due to the availability of silicon oxide groups on the surface. The tips were initially cleaned with a plasma cleaner to remove any impurities or functionalized groups on the surface. Once cleaned the tips were immediately functionalized to minimise any contaminants on the surface. The tips were placed into the EDSPA solution at room temperature for 1 h. The tips were then removed, washed consecutively with toluene, then PBS solution. The tips were then encapsulated with the GAH solution for 1 h, then rinsed with PBS solution. The tips were finally encapsulated in the FN solution for 1 h, then rinsed and refrigerated in PBS solution until use.

6.2.2.3 Force Volume Spectroscopy Measurements

The force measurements were performed in PBS fluid using the experimental set-up described in 5.2.2.3 (pg. 5-160). The AFM parameters were set for 1 µm approach, 0.5 Hz scan rate, 1 sec dwell toward, 1 sec dwell away and 1 nN trigger force. The force volume maps were conducted over a 500 nm x 500 nm and 250 nm x 250 nm area on each of the polymer samples with a resolution of 32 x 32 force curves. The topographical map is generated simultaneously with the adhesion force map. The adhesion force is measured at the minimum of the retract curve, returning a value that is the maximum adhesion force.

6.3 Results

6.3.1 Force Volume Curve Analysis

The force volume map produces a topographical map (Figure 6-2A) and a corresponding adhesion map of a PPy/HA surface (Figure 6-2B). The maximum adhesion value of each individual force curve is assigned a colour scale and plotted versus the X-Y position of each individual force curve. The areas of low maximum adhesion are represented by the dark pixels while areas of high maximum adhesion are represented by yellow pixels.

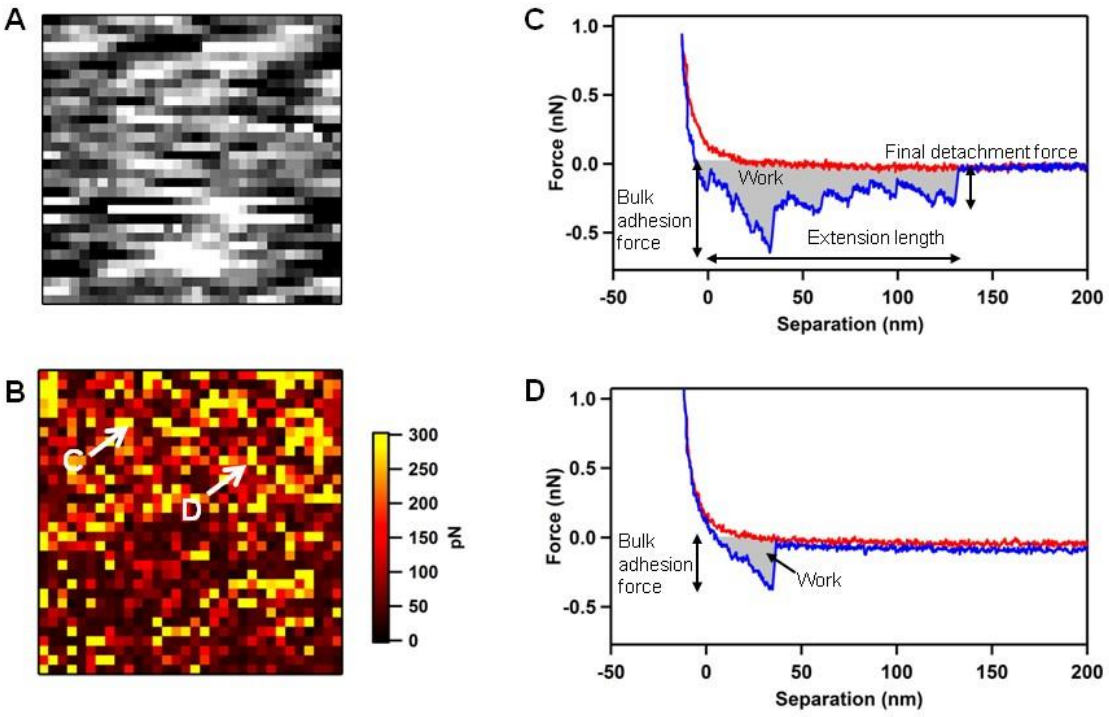

Figure 6-2: 500 x 500 nm example adhesion volume map on PPy/HA. (A) Topography (Z scale 20 nm), (B) adhesion, (C) rupturing force curve, and (D) non-specific adhesion force curve.

Individual force curves (Figure 6-2C and D) corresponding to the pixels marked in Figure 6-2B show two commonly observed interactions between the protein and polymer. Each of the force curves that comprise the force volume map can be analysed for several parameters, namely the maximum adhesion force, final detachment force and the work (energy) required to pull the protein off the surface (annotated in Figure 6-2C). Figure 6-2C is an example of a rupturing force curve as the protein detaches from the surface. As discussed in the previous chapter (5.3.6, Figure 5-7, pg. 5-169), this type of force curve is often indicative of the protein unfolding [190] but may also involve multiple proteins binding to the surface and/or multiple binding sites along a single protein. The final detachment force represents the force required to pull a single protein off the surface. The total extension length is a measure of the distance the protein extends before completely detaching from the surface.

The second force curve profile (Figure 6-2D) demonstrates an example of non-specific adhesion, as classified in the previous chapter. The observed adhesion force may be an amalgamation of several forces, such as electrostatic, hydrophobic, and/or hydrogen bonding between the protein and the polymer. This type of adhesion mostly involves multiple proteins binding from tip to surface.

6.3.2 *Laterally Resolved Protein Adhesion*

Figure 6-3 shows the topography and adhesion force volume maps of the PPy/GAG polymers. The skewed appearance of the nodular features in the topography maps is due to drift within the system, as the maps take considerable time to complete (~50 minutes). The roughness of both scans over the small scan areas are comparable, with PPy/CS and PPy/HA having an RMS roughness of 6.5 ± 6.5 nm (mean ± s.d; n=1024)

and 6.1 ± 6.1 nm (mean ± s.d; n=1024) respectively. The adhesion maps show a difference between the polymers in both distribution and magnitude of maximum adhesion; PPy/CS has a much higher average protein adhesion across the sample compared to PPy/HA (as shown by the yellow in the force volume map Figure 6-3B). Note that the colour scale for PPy/CS ranges from 0 – 1 nN, while PPy/HA ranges from 0-0.5 nN. PPy/HA also has more dark regions (i.e. low adhesion) compared to the lighter yellow/red map of PPy/CS (higher adhesion). The adhesion is quantified using the RMS of each map, revealing PPy/CS has an RMS maximum adhesion of 633 ± 350 pN (mean ± s.d; n=1024) and PPy/HA an RMS maximum adhesion of 305 ± 221 pN (mean ± s.d; n=1024).

The probability of a binding event, both non-specific and rupturing, occurring in the mapped area was also quantified for both polymers. PPy/CS had a binding probability of 97% (991 in 1024 force curves) and PPy/HA had a probability of 85% (875 in 1024 force curves). This probability matches the results from the single point adhesion study for all types of binding events (98% and 83% for PPy/CS and PPy/HA respectively, Figure 5-8, pg. 5-172).

An overlay of adhesion was placed over the topographical maps for both polymers to augment any correlation between protein adhesion and topographical features. The red pixels in the overlays represent force curves that measured over 0.3 nN maximum adhesion.

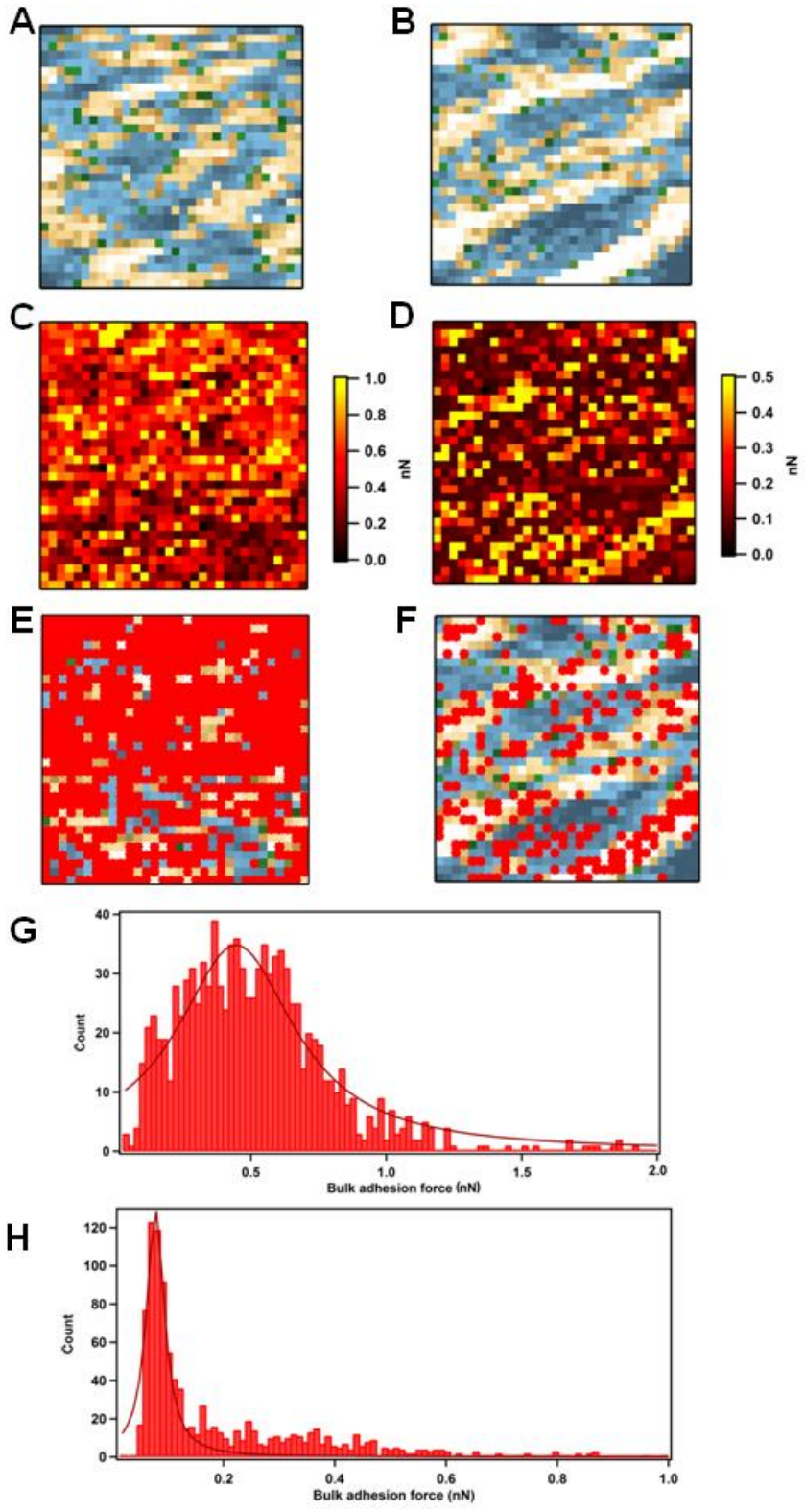

Figure 6-3: 500 nm force volume maps for topography (A) PPy/CS (Z scale 30 nm) and (B)PPy/HA (Z scale 20 nm), adhesion (C) PPy/CS and (D)PPy/HA. A mask was applied to each map, creating an overlay in red for (E) PPy/CS (threshold 0.3 nN) and (F) PPy/HA (threshold 0.3 nN). (G) and (H) are the distribution of maximum adhesion force values for (E) PPy/CS and (F)PPy/HA respectively.

The overlay for PPy/CS (Figure 6-3E) displays a high density of red pixels distributed across the surface (77% surface coverage). This indicates a uniform and high density of strong adhesion forces across the surface; however the high surface coverage makes any correlation between topography and adhesion ambiguous. In an attempt to observe if there is any correlation between strong maximum adhesion and topography the threshold was increased to 0.8 nN, however no correlation was observed. In contrast, the red pixels are distributed along the nodular features for PPy/HA (Figure 6-3F) suggesting a spatial dependency for FN affinity in regards to topography. This density for these maximum adhesion events is also lower compared to PPy/CS (24%).

The maximum adhesion force between the protein and polymer can be further displayed as a distribution of forces (Figure 6-3G and H for PPy/Cs and PPy/HA respectively). The histogram for the PPy/HA map clearly shows a much lower, narrower distribution of all maximum adhesion forces compared to the PPy/CS map. The Gaussian fit for the PPy/CS maximum adhesion force gives a peak at 0.45 ± 0.18 nN (mean ± s.d; n=1024) and the fit for PPy/HA gives a peak at 0.078 ± 0.010 nN (mean ± s.d; n=1024), thus again showing that the strength of protein adhesion is higher on PPy/CS.

The nodular features were mapped at a higher resolution across a 100 nm x 100 nm area (Figure 6-4). The overlay of adhesion, using a threshold of 0.13 nN, on the topography showed no show no clear correlation for PPy/CS maps (Figure 6-4A, C, E), i.e. more adhesion on the nodules was not observed.

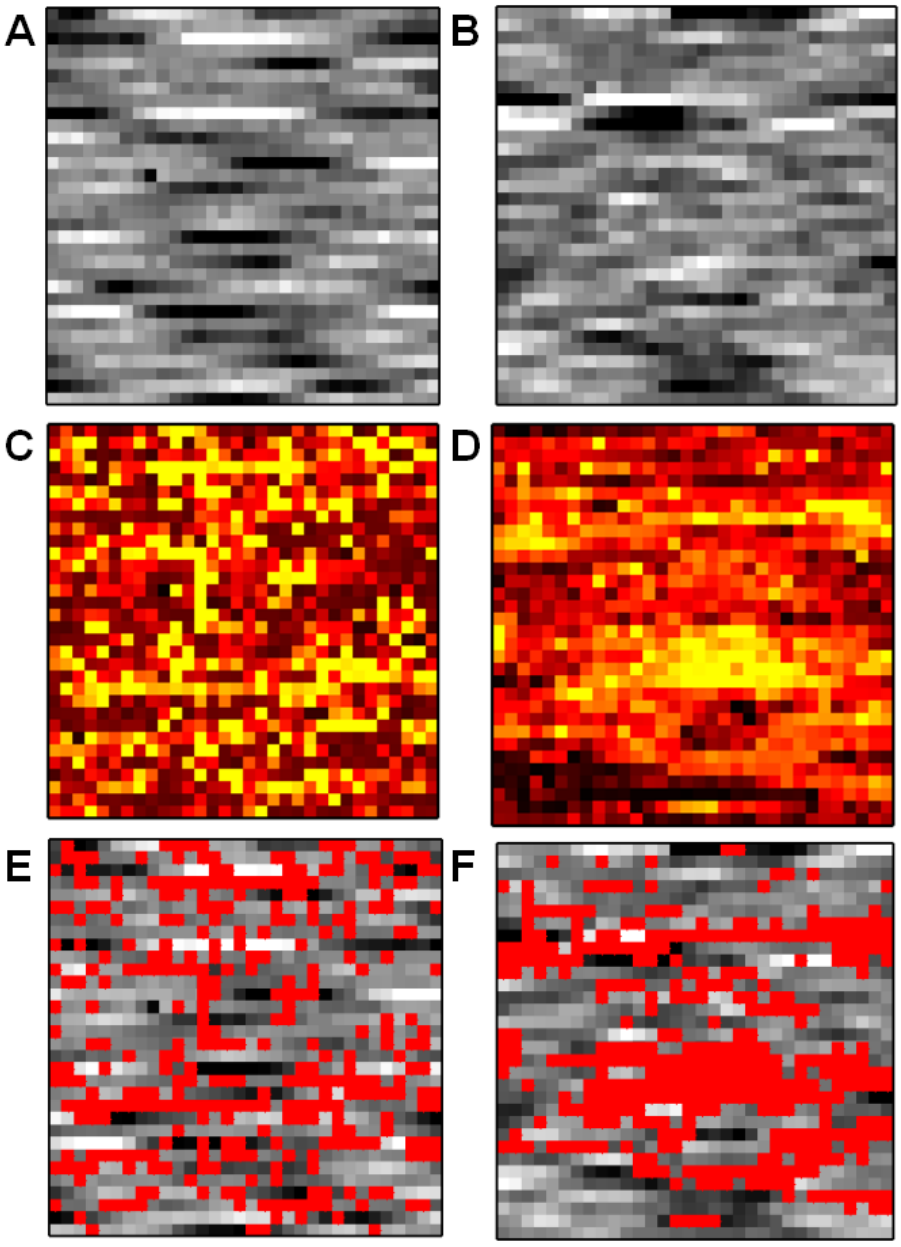

Figure 6-4: 100 nm force volume maps for topography (A) PPy/CS (Z scale 12 nm) and (B)PPy/HA (Z scale 30 nm), adhesion (C) PPy/CS (Z scale 0.2 nN) and (D) PPy/HA (Z scale 1.6 nN), and an overlay of high adhesion for (E) PPy/CS (threshold 0.13 nN) and (F) PPy/HA

PPy/HA (Figure 6-4B, D, F) displays a correlation between the nodular features and higher maximum adhesion force (threshold 1nN) that was confirmed in the adhesion-

topography overlay image (Figure 6-4 F). This was largely evident in a large nodular structure (annotated with *) in the middle of the PPy/HA adhesion map (Figure 6-5D) has a very strong correlation with high maximum adhesion values.

6.3.3 *Laterally Resolved Protein Interactions*

The position of curves displaying rupturing events, as classified earlier (6.3.1, pg. 6-200), were marked with green pixels in the overlay of the topographical maps for PPy/CS and PPy/HA (Figure 6-5A and B respectively). The overlay shows a relative abundance of the rupturing events on the PPy/CS polymer, with a probability of 33% (333 in 1024 force curves) for this type of event to occur. The rupturing events occur less often on the PPy/HA polymer with a probability of 21% (215 in 1024 force curves). The % probability effectively represents a "surface density of FN binding" given that the probability of these rupturing curves occurs within a defined scan area; PPy/CS and PPy/HA had density of binding values of 1189 and 796 per µm2 ,respectively. The surface area for each map was calculated as 0.28 and 0.27 µm2 for PPy/CS and PPy/HA respectively, both films having similar roughness over the small map area.

The final detachment peak generally represents the force required to completely detach a single protein molecule from the polymer surface and is representative of the affinity of the protein for the polymer, as analysed specifically in the previous chapter. The force curves that displayed rupturing events in the maps were analysed for this final detachment force. Gaussian fits for PPy/CS give a mean of 122 ± 23.5 pN (mean ± s.d; n=1024) (Figure 6-5C) and PPy/HA a mean of 70.3 ± 13.5 pN (mean ± s.d; n=1024) (Figure 6-5D), confirming results in the previous chapter that CS binding has higher affinity compared to HA at the single molecule level. The final detachment force peak

on the PPy/HA film is also comparable to the mean maximum adhesion force of the protein (78 pN). The dual mode probability distribution for the final detachment force was not observed as it was in the previous work, possibly due to tip variation and the much higher sampling numbers in Chapter 5 (pg. 5-152). The initial peak < 150 pN for the previous data (Figure 5-10, pg. 5-176) however is of the same magnitude as the peak distributions measured here.

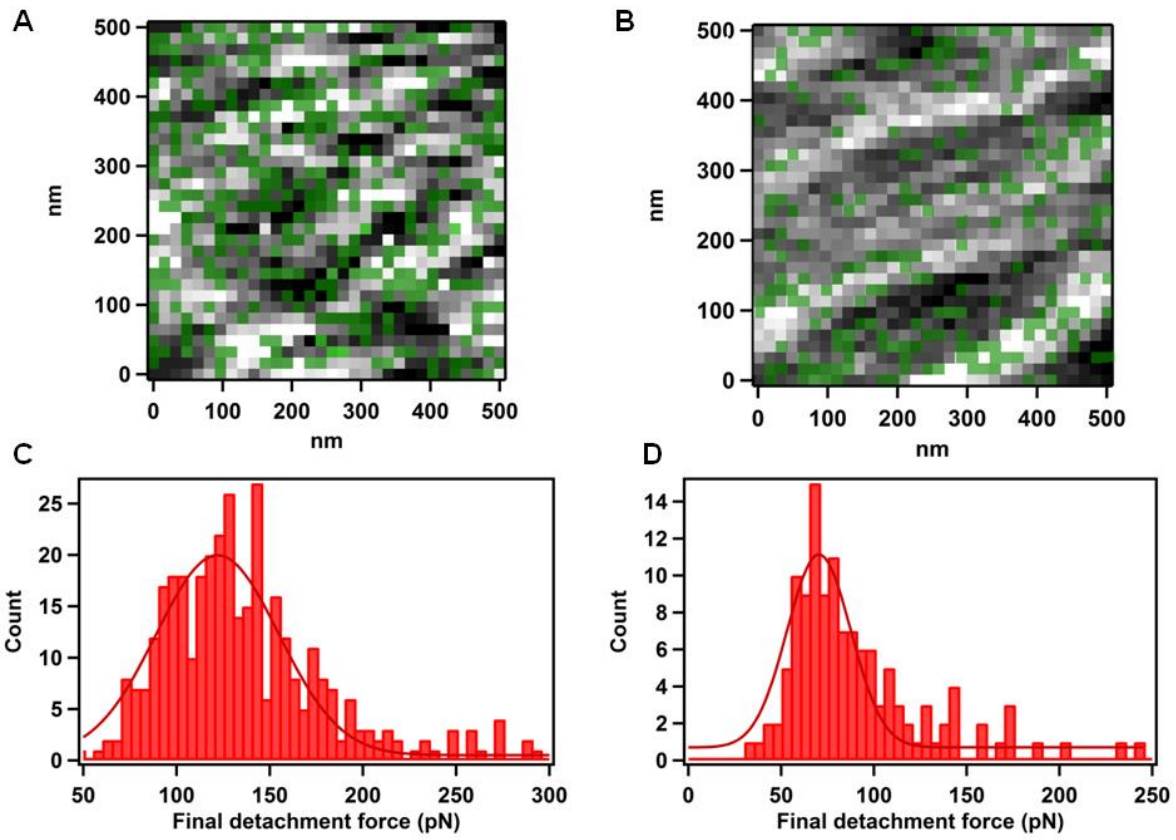

Figure 6-5: Topographical map overlayed in green for rupturing events for (A) PPy/CS and (B) PPy/HA. Distribution of final detachement force with Gaussian fit (dark red) for (C) PPy/CS and (D) PPy/HA

6.4 Discussion

6.4.1 *Spatial Variation in Protein Adhesion*

The specific binding of the GAG dopants to the FN has previously been shown in Chapter 5 (5.5.2, pg. 5-184). This evident as the binding location(s) resides at the well known Heparin I, II, and III domains that have high affinity and structural recognition for sulfated and negatively charge GAG. This interaction is facilitated by the highly localized positive charge of the Heparin domains, with the Heparin II having the highest affinity for binding. CS, which is recognized as being highly specific for the Hep II domain, was shown to have the highest binding force compared to HA that is non-sulfonated.

PPy/HA was observed to have a much more inhomogeneous distribution of dopant loading compared to PPy/CS, particularly using C-AFM scans (Figure 4-5, pg. 4-143). This is also supported by several studies using C-AFM and KPFM of OCPs [160-161, 230]. Regions of high conductivity indicate areas with high dopant loading; the polymer cannot conduct a current without the presence of the dopant hence areas of low to zero conductivity indicate areas with negligible dopant. PPy/HA was shown to have higher conductivity in the nodule regions indicating the presence of more doped regions, whereas surrounding regions showed very low conductivity (current). In contrast, PPy/CS showed conductive regions more uniformly distributed across most of the surface, indicting the greater coverage of doped regions. For example, from the conductivity scans, the calculated surface area of regions with conductivity lower than 5 pA was 0.3% and 46% for PPy/CS and PPy/HA, respectively. Therefore, given that FN

binding is facilitated by the GAG dopants, then it is expected that FN binding will be influenced by the varying distribution of conductive (doped) regions of PPy/CS and PPy/HA. This was indeed observed for PPy/HA where the most prevalent FN binding appeared to be primarily located at the nodular (more doped) regions of the polymer. In contrast, the significantly higher density of FN binding on PPy/CS was in accordance with the more uniformly doped regions across most of the surface.

The higher adhesion measured on PPy/CS has previously been attributed to the higher affinity of FN for the CS dopant compared to HA (Chapter 5). HA and CS are very similar in structure but CS has single sulfonate group compared to a single hydroxyl group of HA within the repeat chain. However based on the different surface properties of the two different films, we propose that higher adhesion forces observed for PPY/CS versus PPy/HA may also be due the influence of multiple protein interactions.

A model of the protein interaction with both PPy/GAG polymers uses topographical scans overlaid with the corresponding conductivity scan (Figure 6-6). Areas of black indicate no conductivity, while areas in green indicate conductivity.

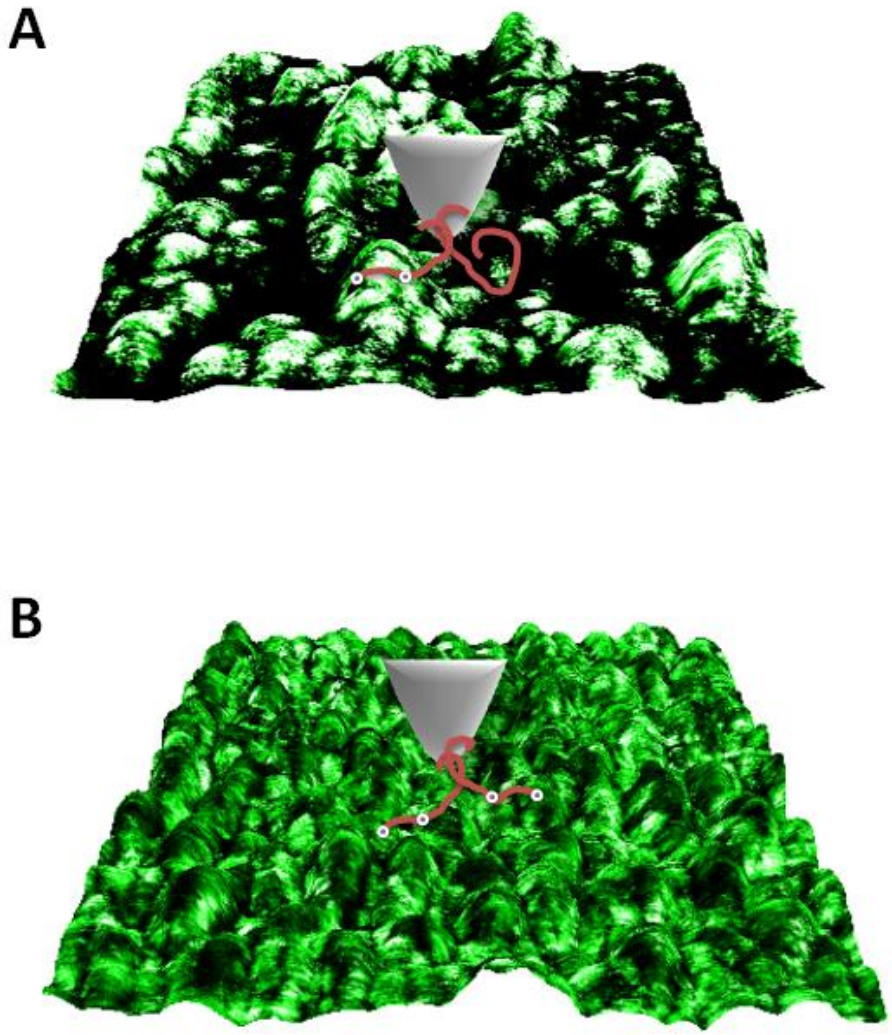

Figure 6-6: Schematic for areas of protein-dopant interaction using 3D topography scan and colour overlay of corresponding conductivity (green is conductive, black is non-conductive, Z scale 4 nA). FN is represented as red, purple circles representing binding points.(A) HA is less homogenous resulting in lower binding probability; FN binds on top of the nodule but not on the areas of no conductivity.(B) CS is more homogenous giving higher probability of interaction and multiple protein binding.

The protein interaction on PPy/HA (Figure 6-6A) shows the FN (red) interacting with the green dopant areas (binding sites represented with purple circles), but not the non-conductive black areas. For PPy/HA the strongest affinity between the protein and the polymer is confined to the nodules with a lower binding density. The

inhomogeneous dopant distribution reduces the probability of multiple proteins binding to the surface, thus resulting in the lower affinity and binding density.

Conversely, as PPy/CS has a more homogenous dopant distribution, the possibility of multiple proteins binding is increased as there are more available sites for FN to bind to (Figure 6-6B). Hence PPy/CS promotes higher FN affinity and higher binding density.

The question remains as to why the overlayed maps depicting single molecule interactions do not show a correlation with topography, as we expect specific binding between FN and the GAGs to occur in the areas of higher dopant presence. The probability for this type of interaction is clearly lower for PPy/HA, suggesting that the distribution of the dopant is playing some role as PPy/CS shows a much more evenly distributed probability of these interactions. However, the reasons for why this binding event is not restricted to high dopant loading areas for PPy/HA is unknown. In part this may be attributed to the theoretical area of interaction of the protein as it approaches the surface. Assuming that a tip with a single protein tethered at the terminal has a possible binding radius of ~ 60 nm (estimated using average CBD lengths as discussed in 5.3.8, pg. 5-176) the minimum spatial resolution the protein can achieve is only > 60 nm. The pixels in the 500 x 500 nm maps represent an area of 15 x 15 nm, therefore there may be some loss in spatial resolution if the protein is binding to points beyond the topographical pixel. Regardless, the density of these events remains an important aspect for this analysis.

6.4.2 *Implication of Inhomogeneous Doping for Cellular Response*

The importance of the spatial distribution of RGD sequences for the success of cellular adhesion and migration is known to require distances of no more than 60 nm between sequences [263]. This corresponds to a density of binding events of 278 per µm2. The density of binding events for both polymers was 1332 and 860 per µm2 for PPy/CS and PPy/HA, respectively. Our values can be extrapolated to suggest that when FN is adhered to the polymer the density should be sufficient to facilitate cellular adhesion and migration. The inhomogeneity of PPy/HA result in regions larger than 60 nm x 60 nm areas that have low dopant loading (hence no support for FN adhesion), suggesting that these regions of the film may not provide continuous lateral support for cells.

The affinity of the protein for a surface, signified by the strength of adhesion, is important as cells apply a mechanical force to FN to assemble the ECM via polymerisation of the protein to its fibrillar form [147]. Cells also require stable binding to the surface to support mechanotransduction processes such as focal adhesion and motility [150]. If the protein is not well adhered to the surface, these important processes are disrupted and can lead to call detachment and death. The increased probability of clustering of the protein, and subsequently the RGD frequency, is an important aspect for these cellular processes. Hence areas of strong affinity due to the presence of the dopant are more supportive for the cells, an advantage to the homogenous PPy/CS films as they have strong affinity uniformly across the surface. The PPy/HA films may perform poorly at supporting this cellular process due to the regions of low affinity for FN.

6.5 Concluding Remarks

The nanoscale lateral resolution of protein interactions across a complex surface such as the PPy/GAG materials enlightens us about the effect of variation in physical properties influence the protein interaction. Spatial variation of the dopant may exert some effect on cellular response due to the spatial dependency of FN affinity. This effect is clearly demonstrated for PPy/HA, a polymer known to have inhomogeneous surface properties, compared to PPy/CS which does not show this lateral dependency. The conformation and density of FN, and the cell adhesion binding sites within, will control the cellular response on the polymer. Hence, the synthesis of conducting polymers should encourage homogenous doping to increase the possibility of binding sites across the polymer.

7 Single Protein Interactions on Photosensitive Conducting Polymers

7.1 Introduction

Switchable surfaces offer control over the material interface (e.g. molecular or physicochemical changes) via an applied stimulus. There are several types of stimuli that can be applied either as a 'one-off' or a reversible change. The most commonly used stimuli are light, temperature, pH, and electrical field [266].

For cell-based applications, switchable materials offer the ability to control interactions at the cell-material. For example, the adsorption of proteins can have an advantageous affect on cellular proliferation and differentiation due to protein-cell interactions [98, 154, 266]. In other applications (e.g. biosensing), however, the surface adsorption of proteins is undesirable and decreases the efficacy of the device [122, 267-268]. A material that combines and controls both of these behaviours opens up possibilities in patterned cell growth, tissue engineering, and drug delivery [269-271].

There are two main mechanisms through which the stimulus can control the interaction between a biomolecule and the material surface. The stimulus can change the interfacial surface properties of the material, thus changing the interaction the biomolecule has with the surface (i.e. attracted or repelled). Alternatively, the stimulus

may also physically alter the biomolecule by changing its conformation, or activity [266].

Polymer based materials have been designed to take advantage of switchable properties for the above applications [25,272-275]. Polymers can be switched through a variety of external stimuli, as listed in Table 7-1, and there are important factors involved in the application of such stimulus (i.e. rate and magnitude of change, reversibility, stability).

Table 7-1: Examples of switchable stimuli

Stimulus	Type	Example	Mechanism	Control	Reference
Light	Energy	Methyl methacrylate with spirobenzopyran	Photoisomerization caused changes in wettability	Cell attachment	[272]
Electric fields	Energy	Polypyrrole	Switching surface polarity	Protein adsorption	[25]
Thermal	Energy	Poly(*N*-isopropyl acrylamide) (pNIPAM)	Change in hydration	Cellular detachment upon stimulus	[273-274]
pH	Chemical	Poly(acrylic acid) and poly(2-vinylpyridine)	Electrostatic interactions	Protein adsorption amount	[275]

Each of the stimuli listed above provides a single pathway to control the interfacial response between material and biomolecule. A developing area in the field of switchable materials is the use of multiple stimuli mechanisms. The ability to use dual or multiple switching triggers can give improved control over the interfacial response. For example, a dual mode material can be comprised of thermal and optically responsive materials. Thermoresponsive pNIPAM and photoresponsive

spirobenzopyran were merged to create a material which could control the spatial direction of cellular growth with UV light [269]. The cells could then be removed through low temperature washing. Furthermore, multiple triggers can be incorporated into a single material. The combination of light, temperature, and pH has been used to create volume tuneable microgels comprising a pNIPAM-allylamine copolymer microgel functionalized with spiropyran [276]. The optical properties of the copolymer changed the thermal threshold for volume changes of the microgel, as well as a photochromic change when switched. The amine groups in the microgel were pH sensitive and reduced swelling capability with an increase in pH [276].

The ability to use more than a single stimulus in a switchable material is promising in applications where both spatial and behavioural control over cells is desired. Optical switching in 'once-off' switching materials can be used to create a pattern [269], or to promote specific biomolecular adhesion to the surface [277]. Electrical switching is particularly applicable to OCP and can be used to manipulate cell growth and behaviour as already discussed (1.5.3, pg. 1-35). In Chapter 5 (5.4, pg. 5-181) we demonstrated a switchable change in protein interaction with electrical stimulus. The combination of both light and electrical stimulus for biological applications is an area that is not well understood and researched at this point in time.

7.1.1 *Optical Switching*

Light stimulus offers fast, non-invasive, and highly controllable switching, but has not been subject to the amount of study, in all types of analysis, as the other stimulus techniques. There are two main mechanisms through which control is achieved with

optical stimulus; the photosensitive molecule is cleaved from the surface, or the molecule undergoes isomerisation.

Photocleavable groups offer control over the chemistry of a surface and can be actively switched upon the stimulus of specific wavelengths of light. This has been demonstrated using a photocleavable group to switch a surface from preventing cell adhesion to promoting cell adhesion [277]. The molecule 2-nitrobenzyl cleaves from a silane coupling agent when stimulated with 365 nm light. Cell adhesion was prevented by adsorbing bovine serum albumin to a 2-nitrobenzyl functionalized surface prior to stimulation. The BSA was removed via cleavage from the surface when a light stimulus (365 nm) was applied, and subsequently FN was added and adsorbed to promote cell adhesion [277]. This type of switching only induces an irreversible change, but is useful for patterning of surfaces or for the release of molecules (i.e. drug delivery) [278].

The second common optical switching mechanism is photoisomerisation. Upon stimulus, the molecule undergoes heterolytic bond cleavage producing an isomer that will have a different polarity to the original molecule. Photoisomer molecules include a class of chemicals known as chromophores. Chromophores change colour upon photoisomerisation and have been studied in combination with polymers to produce photosensitive polymeric materials [269, 278-280]. These photosensitive polymers have been used in applications to control biomolecular and cellular adhesion to substrates. A photoresponsive polymer was demonstrated to have control over enzyme activity through conjugating the enzyme to the photosensitive molecule [278]. The enzyme, endoglucanase 12A, was controlled through the photoswitching of the azobenzene acrylamide polymer. The azobenzene underwent photoisomerisation in

UV light (350 nm), 'collapsing' the polymer and becoming hydrophobic, which in turn activated the enzyme. When the polymer expanded under visible light (520 nm), the enzyme became inactive. This occurs due to the steric blocking of the enzyme's active site from the polymer chains [278]. Another chromophore, spirobenzopyran (SP), is commonly used in photosensitive polymers. For example, a copolymer of pNIPAM and an SP derivative has demonstrated reversible photoswitching [279-280]. These chromophoric polymers are ideal for switchable surfaces as they are reversible compared to the non-reversible photocleavable molecules.

7.1.2 *Spirobenzopyran as a Switchable Molecule*

The structure of the SP, merocyanine-like and quinoidal-like MC is shown in Figure 7-1. The SP undergoes a heterolytic cleavage of the spiro carbon-oxygen bond to create an open ringed structure (MC) that has two resonance forms.

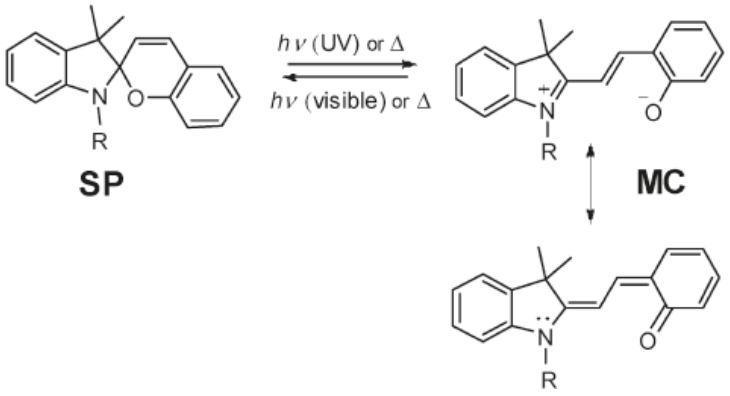

Figure 7-1: Benzospiropyran (SP) and the zwitter-ionic and quinoidal isomers in open form (MC).

The switchability of SP has been used previously to control cellular behaviour, via control of surface properties to induce cell detachment and pattern surfaces [269, 281]. SP has been incorporated in a copolymer with methyl methacrylate to produce a poly(spiropyran-co-methyl methacrylate) material that has a photosensitive surface [281]. Switching the SP to the MC caused the material to become more hydrophillic, as well as inducing detachment of platelets and mesenchymal stem cells [281]. A polymer, pNIPAM, was functionalized with SP in the configuration of side chains to produce a photosensitive culture surface and seeded with hamster ovary cells [269]. When the polymer was switched to the MC form, the cells adhered more strongly compared to cells seeded on non-irradiated polymer. The material was also patterned using a micrometer-scale light source to induce areas of cell adhesion (Figure 7-2). The cell adhesion was manipulated in the submillimeter range, as demonstrated by the immunofluorescence of live cells in a '?' pattern [269].

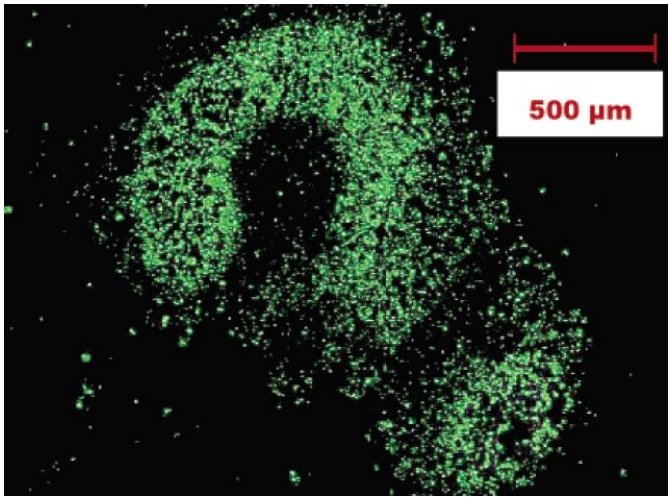

Figure 7-2: Micropatterned photosensitive surface where the cells are adhered on the UV irradiated area, and most cells detached on the nonirradiated background [269].

7.1.3 *Polyterthiophene Polymer*

To use the SP as a photosensitive surface the molecule must be immobilized on a surface in a manner that does not interfere with the light switching properties. Materials for such a surface have included self-assembled monolayers [282], bilayers [283] and polymers [284] have been used, and now recently OCPs [285-286]. By immobilizing the molecule on an electromaterial, such as an OCP, the spectrum of applications is broadened to areas including both optical and electrical stimulation which can add further control over electrode surfaces (i.e. cell patterning).

A novel polyterthiophene with SP incorporated into the polymer backbone has only recently been produced to produce a photosensitive conductive polymer [285]. Polyterthiophenes are desirable, as they are stable, easy to synthesis and functionalize.

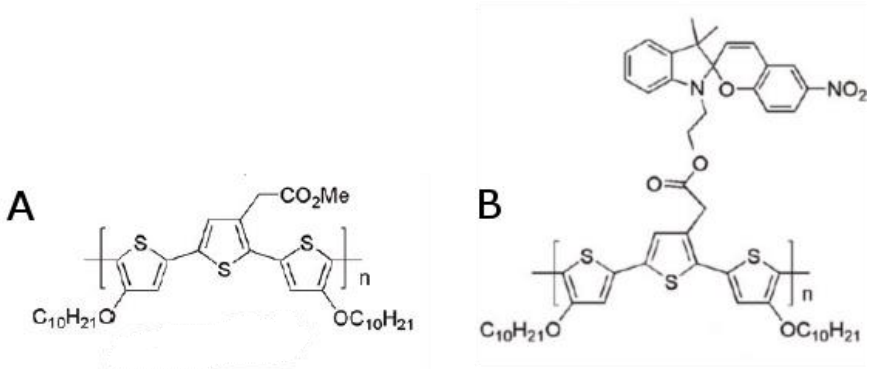

Figure 7-3: Structure of (A) pTThMA and (B) pTThSP1.

The 'blank' polymer (pTThMA), devoid of SP, is illustrated in Figure 7-3A. The SP was covalently bound to the alkoxyterthiophene monomer units to produce the polymer poly(2-(3,3"-dimethylindoline-6'-nitrobenzospiropyranyl)ethyl 4,4"-didecyloxy-2,2':5',2"-terthiophene-3-acetate) (pTThSP1) (Figure 7-3B). The electrical switching of

this compound has been demonstrated to have good reversibility and stability, and switching has also been confirmed using optical stimulus [285]. The visible light switched form is defined as pTih-SP and the UV light switched form as pTih-MC for this study.

7.2 Materials and Methods

7.2.1 Reagents

The functionalization chemicals 3-EDSPA, GAH, and human plasma FN were obtained from Sigma Aldrich. PBS was prepared at pH 7 in Milli-Q water (18.2MΩ).

7.2.2 Polymer Preparation

The polymers were prepared using the methods described in Wagner et al. [285]. The polymers were sonicated for 30 sec prior to experimentation to clean the films of any residue polymer particles on the surface.

7.2.3 AFM Topographical Imaging

The pTTh was imaged in air with AC mode AFM, using Nanoworld PNP-DB tips with a spring constant of 0.2 N/m. A scan was conducted over an area of 5 x 5 µm at a scan rate of 1 Hz. Roughness was calculated as root mean square (R_{RMS}) roughness using Asylum Research MFP3D software (CA). The pTThSP1 polymer was scanned initially in white ambient light, then switched using direct UV (254 nm) light and scanned again.

7.2.4 UV-vis Spectrometry

Absorbance spectra were recorded using a Shimadzu UV-1800 spectrophotometer. The pTThSP polymer was initially electrically stimulated at a constant -0.4 V after polymerisation in 0.1 M TBAP electrolyte (acetonitrile solvent) in order to guarantee the higher concentration possible of the SP isomer, and the absorbance spectra measured. The absorbance spectra was then measured for the pTThSP exposed to UV (254 nm) light for 5 min, and then once exposed to visible light (full spectrum) for 5

min. The pTThSP was then exposed to UV light for 15 min and the absorbance spectra measured.

7.2.5 *Contact Angle Measurements*

Four different freshly polymerised films were kept at -0.4 V. Each of them was subjected to 5 cycles of 15 minutes UV light (254 nm) and 5 cycles of 15 minutes of visible light (full spectrum) and after each exposition 3 contact angles were obtained for each film.

7.2.6 *Tip Functionalization*

The tip is functionalized using an aminosilzation method to covalently bind the FN to the tip. Silicon nitride Nanoworld PNP-DB tips are used for this method due to the availability of silicon oxide groups on the surface. The tips were initially cleaned with a plasma cleaner to remove any impurities or functionalized groups on the surface. Once cleaned the tips were immediately functionalized to minimise any contaminants on the surface. The tips were placed into the 3-EDSPA solution at room temperature for 1 h. The tips were then removed, washed consecutively with toluene, then PBS solution. The tips were then encapsulated with the GAH solution for 1 h, then rinsed with PBS solution. The tips were finally encapsulated in the FN solution for 1 h, then rinsed and refrigerated in PBS solution until use.

7.2.7 *Force Spectroscopy*

The force measurements were performed in PBS fluid using the experimental set-up described in (methodology chapter). The AFM parameters were set for 500 nm approach, 0.5 Hz scan rate, 1 sec dwell toward, and 1 nN trigger force. Single point

force spectroscopy measurements were performed with 5 consecutive measurements at one point, with a rest of 3 seconds, across 5 different points on the sample surface. 25 force curves were performed by 3 individual tips on 3 samples for measurements on pTThMA and pTThSP1 (total number of force curves 228 and 200 on pTThMA and pTThSP1 respectively).

The modified polymers were switched using optical stimulation to measure protein adhesion on the SP and MC form. The polymer was irradiated with UV light (wavelength 254 nm) for 10 minutes to switch it from pTTh-SP to pTTh-MC in PBS solution. The polymer was then exposed to room light for 10 minutes to switch from pTTh-MC to pTTh-SP. Force spectroscopy measurements were performed with 5 consecutive measurements at one point, with a rest of 3 seconds, across 5 different points on the sample surface. 25 force curves were performed on the polymer after the light stimulation was applied and 4 samples with 4 individual tips were used (total number of force curves 200 and 150 for SP and MC form respectively).

7.3 Results

7.3.1 AFM Topographical Imaging

Topographical scans in Figure 7-4 showed a change in the roughness of the polymer once it has been exposed to UV light. The RMS roughness of the polymer in SP form is 3.89 nm (an increase in surface area of 0.62%), while the MC form has a roughness of 1.56 nm (increased surface area of 0.07%).

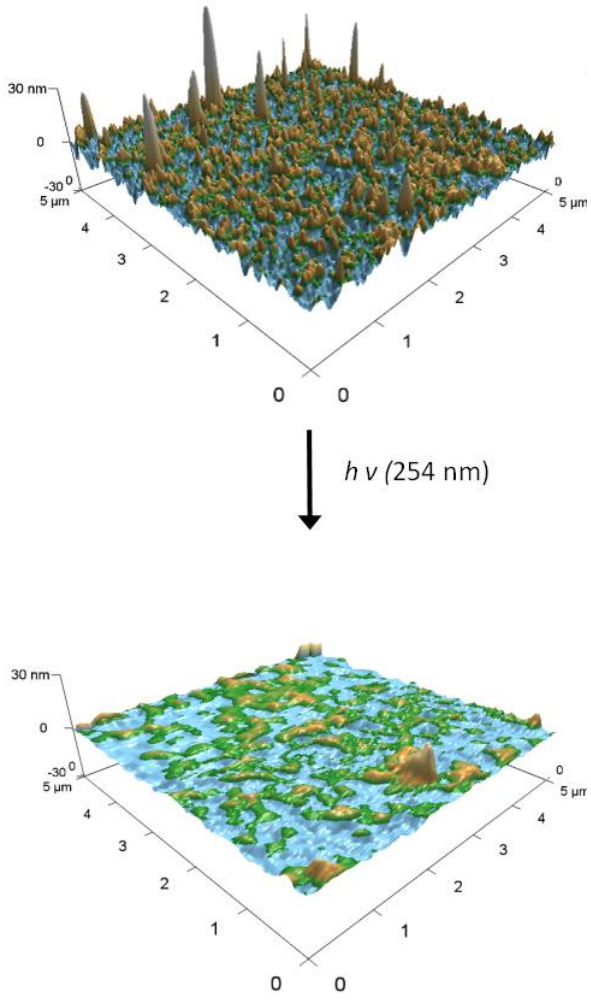

Figure 7-4: AFM topographical scan of pTTh polymer in the SP form, then switched to MC form via UV light.

7.3.2 *UV-Vis Spectral Analysis*

The UV-vis absorbance spectra for the switching pTThSP1 is shown in Figure 7-5A. The fully pTThSP1 switched polymer was initially measured (blue). The polymer was then switched to the MC form by exposure to UV light (red) and then switched back to the SP form again (green). The polymer was switched to MC a final time (purple). The absorbance spectra shows a shift with the optical stimulation, indicating that the polymer is undergoing photoisomerisation.

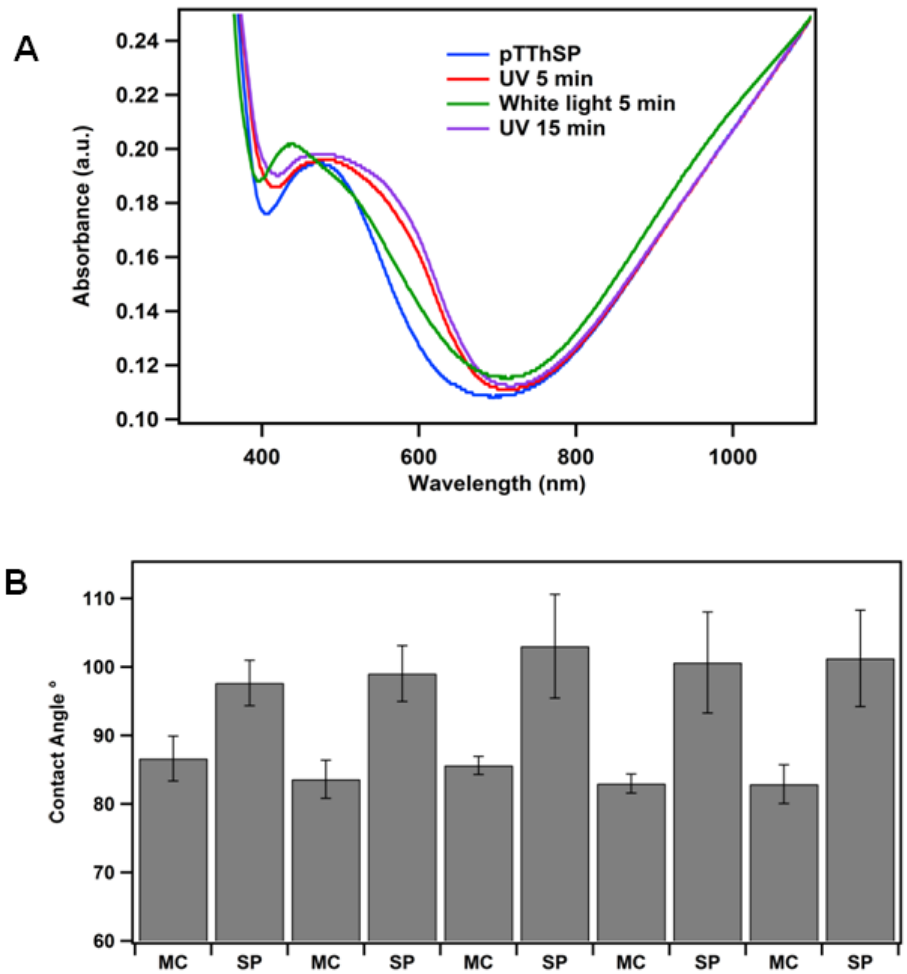

Figure 7-5: (A) UV-vis spectra of initial pTThSP (blue), UV stimulated 5 min (red), white light stimulated 5 min (green) and UV stimulated 15 min (purple). (B) Contact angle measurements on polymer as it is optically switched, measured on 4 individual films, cycled 5 times. Error bars are standard deviation.

7.3.3 *Contact Angle Measurements*

Figure 7-5B displays the average contact angle measurement as the polymer is optically switched from SP to MC form five times. The measurements show a stable, reversible change of the contact angle of the polymer. The SP form is the more hydrophobic form (an average contact angle of 100.0 ± 5.6°), and the MC form is more hydrophilic (an average contact angle of 84.3 ± 2.5°).

7.3.4 *Protein Adhesion*

The interaction of FN with the polymer was measured using functionalized force spectroscopy with FN functionalized probes. A typical force curve on the pTThMA polymer shows an adhesion force between the FN and polymer as the tip is retracted (Figure 7-6A). This adhesion force is the result of attractive forces between the protein and the polymer, which can be due to Coulombic, hydrophobic, or electrostatic interactions. The maximum adhesion force is measured as the maximum force applied to the tip as the protein is pulled off the surface. The extension length is measured as the distance the tip travels until the protein fully detaches from the surface, and is indicative of the length the protein can stretch before becoming detached.

The pTThMA showed a slightly higher average maximum adhesion (0.96 ± 0.14 nN) than the modified pTThSP1 surface (0.77 ± 0.08 nN), as displayed in Figure 7-6B. After exposure to UV, the total average maximum adhesion of the pTTh-MC was significantly smaller (0.49 ± 0.06 nN) than both the pTThMA and pTTh-SP.

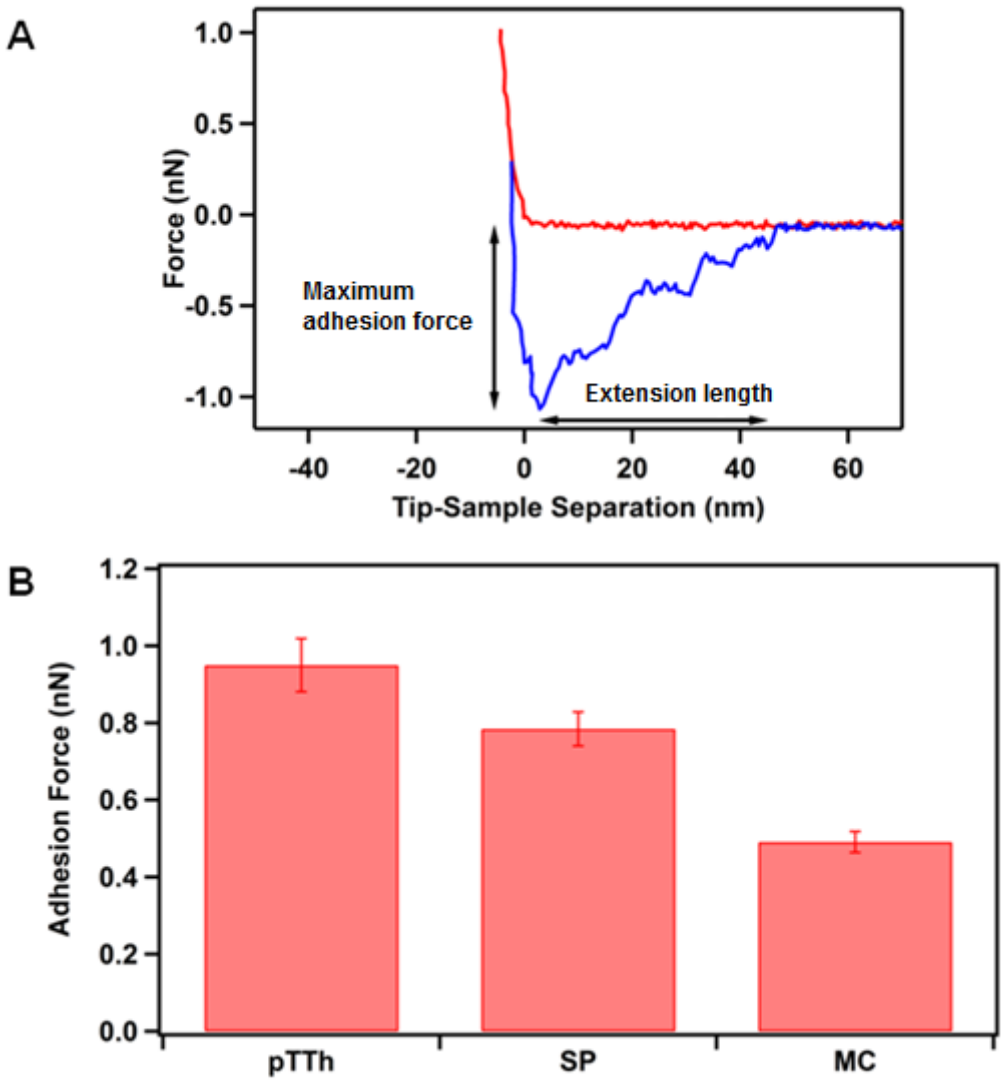

Figure 7-6: (A) Example force curve analysis, extension (red) and retraction (blue) curves. (B) Average adhesion forces for as-grown pTTh (n=228), SP (n=200) and MC form (n=150). Error bars are standard error.

Figure 7-7A displays the reversibility in protein adhesion as the polymer is switched between the SP and MC forms. Representative force curves on pTTh-SP demonstrate a much higher adhesion force (larger peaks) compared to pTTh-MC, clearly indicating a reversible effect of the optical stimulus on protein adhesion. Figure 7-7B shows the

mean maximum adhesion force of the SP and MC forms as they are reversibly switched over 2 cycles.

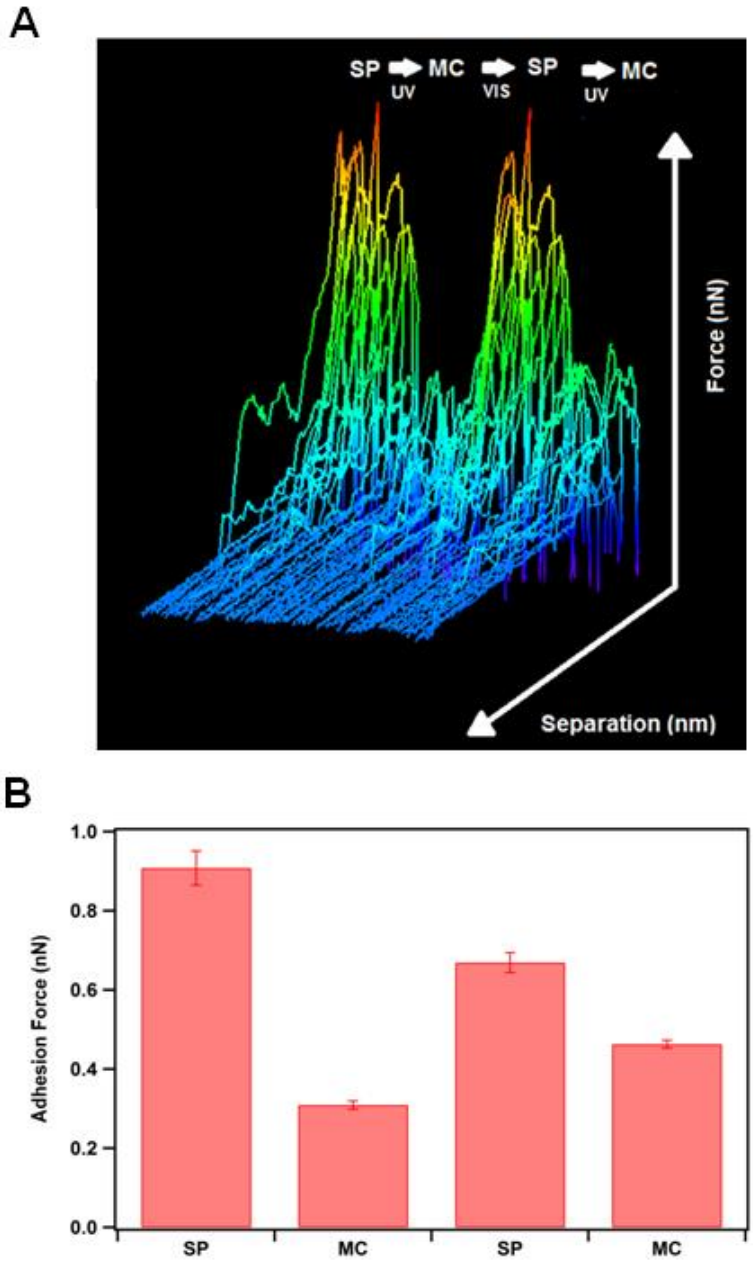

Figure 7-7: (A) Representative force curves during optical switching. Maximum force 2.4 nN, maximum tip-sample separation 100 nm. (B) Average adhesion forces during optical switching (n = 50, 75, 150, 75). Error bars are standard error.

The initial SP form (electrically stimulated to ensure complete conversion to the SP form) was measured to have a mean of 0.91 ± 0.04 nN (mean ± s.d., n=50). The first switch to pTTh-MC with UV light reduced the mean maximum adhesion to 0.31 ± 0.01 nN (mean ± s.d., n=75). The first switch back to pTTh-SP with visible light measured an increase in the mean maximum adhesion to 0.67 ± 0.03 (mean ± s.d., n=150) and the second switch to pTTh-MC with UV light decreased the mean again to 0.46 ± 0.01 (mean ± s.d., n=75).

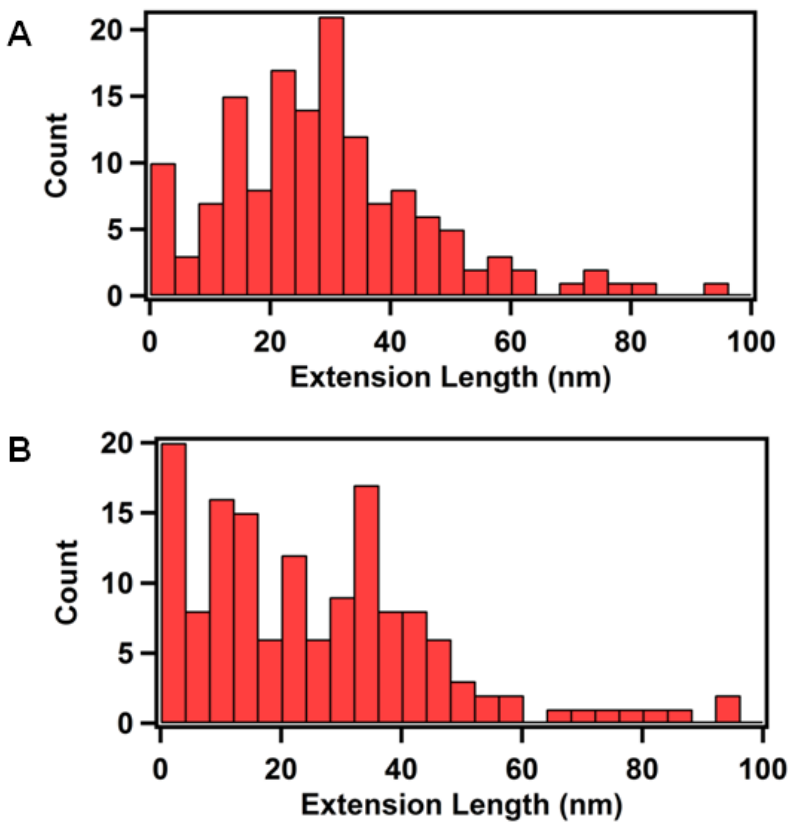

Figure 7-8: Distribution of extension length for SP (red) and MC (black), N=184 and N=171 respectively.

Force curves performed on both pTTh-SP and pTTh-MC had similar profiles, as represented by the force curve in Figure 7-6A. Histograms showing the distribution of the protein extension lengths did not show any significant difference between the two forms of the polymer (Figure 7-8). Mean peak distribution values for the pTTh-SP and pTTh-MC were 26.8 ± 1.3 nm and 22.5 ± 1.9 nm respectively. These extension lengths, which are significantly smaller than the known extended length of FN and those observed in the previous chapters for PPy doped with GAGs (Chapters 5 and 6; as demonstrated in 5.3.8 via calculation of individual domain lengths, pg. 5-176), indicate that the interaction (extension) of the protein is occurring over a distance more closely correlated to the dimensions of the compact conformation of FN.

7.4 Discussion

7.4.1 Switchable Control of pTTh-SP

The optical stimulation was shown to induce a change in the wettability of the pTTh-SP functionalized polymer, as demonstrated by the contact angle measurements. The SP form showed greater hydrophobicity than the MC form and this hydrophobic nature of SP has previously been related to its chemical structure [280, 287] and confirmed using contact angle measurements [281]. The weaker hydrophobicity of the MC form is attributed to its zwitterionic structure that forms due to cleavage of the spiro carbon-oxygen bond and results in the heterolysis of the nitrogen and oxygen (Figure 7-1) [287]. Furthermore, the contact angle measurements demonstrated that the change in wettability was reversible upon cycling of the optical switching. This confirms the previous study on the reversible optical switching properties of the OCP [288] and, in particular, demonstrates for the first time the effect on surface energy.

7.4.2 Protein Interaction with Switchable Polymer

The incorporation of SP into the pTThMA polymer is shown to decrease the maximum adhesion of the protein (Δ 0.17 ± 0.08 nN), indicating that the modification of the surface with the SP molecule changed the affinity between protein and polymer. The maximum adhesion decreases further once the polymer is switched from SP to MC form (0.29 ± 0.05 nN). When comparing the change in surface energy (contact angle) and adhesion, both parameters show a decrease in the order of pTThMA > SP > MC, suggesting that an increase in hydrophilicity (or conversely a decrease in hydrophobicity) correlates with a decrease in protein adhesion. Therefore, it appears

that hydrophobic interactions are likely to be the dominant forces involved in protein adhesion. The increased hydrophobicity of the pTThMA is due to its neutral backbone, in addition to the presence of polar decyloxy and acetate groups. This is in contrast to the pTThSP1 where the nitrate groups will introduce hydrophilicity. The reduction in hydrophobicity of the MC form is attributed to the zwitterionic nature of the MC molecule, as zwitterionic surfaces have been observed to reduce protein adhesion [289-290]. Zwitterionic surfaces are also believed to be resistant to non-specific protein adhesion due to hydration layer(s) bound through solvation of charged terminal groups, as well as hydrogen bonding around molecular chains [291]. Thus, this switch to the more hydrophilic MC form with zwitterionic species may either diminish the extent of hydrophobic interactions and/or play a role in actually deterring protein adhesion. Lastly, due to the observed change in roughness of the polymer between the SP and MC form, it is possible that topographic effect may also influence protein adhesion. For instance, the increased roughness of pTTh-SP, compared to the smoother pTTh-MC, may contribute to stronger adhesion due to an increase polymer surface area and associated increase in the interaction (contact) area of the AFM tip.

The reversibility of the protein adhesion exhibits a small amount of hysteresis as the switching is performed over multiple cycles. In particular, the average adhesion force of the SP does not return to its initial value (27% reduction in the average adhesion force) after switching back from the MC form, suggesting that not all of the MC isomers undergo switching back to the SP form. As the force measurements are not performed during the optical switching (i.e. the films are static in comparison to the electrical switching of PPy in Chapter 4) the measurements may be susceptible to 'lag'

time of the optical switch as the SP molecule converts form, however the duration of stimulation was kept constant to minimise any effect from this.

Previous work has suggested that the switching movement of the closed SP to the open MC can force protein fibrinogen to be removed from the surface [281], and that the hydrophobicity of the polymer does not directly contribute to the amount of fibrinogen adsorbed to the surface. In this study, however, we are measuring the protein interaction once the stimulus has been applied on a static surface.

7.4.3 *Protein Behaviour on Hydrophobic Materials*

The extension length of FN on the pTThSP1 polymer is short (~30 nm) in comparison to those observed on the PPy doped with GAGs in the previous chapter (corrected lengths of ~65 nm and much longer extended lengths of ~160 nm), indicating that the behaviour of the protein (e.g. extension) is different on the more hydrophobic pTTh-SP and -MC polymers. For example, the PPy/GAG is significantly more hydrophilic than pTThSP1, with contact angles of <50° [20]. The wettability of a surface has been shown to control the conformation of FN; on hydrophobic surfaces FN has a compact, 'pretzel' conformation as opposed to the elongated conformation on hydrophilic surfaces [97]. Hence, a hydrophobic surface like pTThSP1 is expected to promote a more compact conformation of the protein.

The intermolecular forces within the protein control its conformation, which in turn are influenced by the surrounding environment (i.e. pH, ionic environment)[255]. On a hydrophobic surface the interaction area between the protein and polymer will be reduced due to the geometry of the compact protein. Hence when the protein comes

into contact with the surface a shorter extension length is produced as only a small length of the protein is available to adsorb to the polymer. This is illustrated in Figure 7-9 where the hydrophobic surface encourages the compact conformation, resulting in a small extension length. The affinity of FN for the hydrophobic pTThSP1 polymer cannot overcome the intramolecular forces of the protein, and so the protein remains in a compact shape. The hydrophilic surface promotes the extended conformation, resulting in a greater length of the protein available to bind on the surface (as seen on the hydrophilic PPy/GAG polymers). As the protein force spectroscopy was performed under the same conditions for both the hydrophobic pTThSP1 and hydrophilic PPy (pH 7.4 PBS solution), the forces of attraction between the protein and polymer must dictate this conformation change.

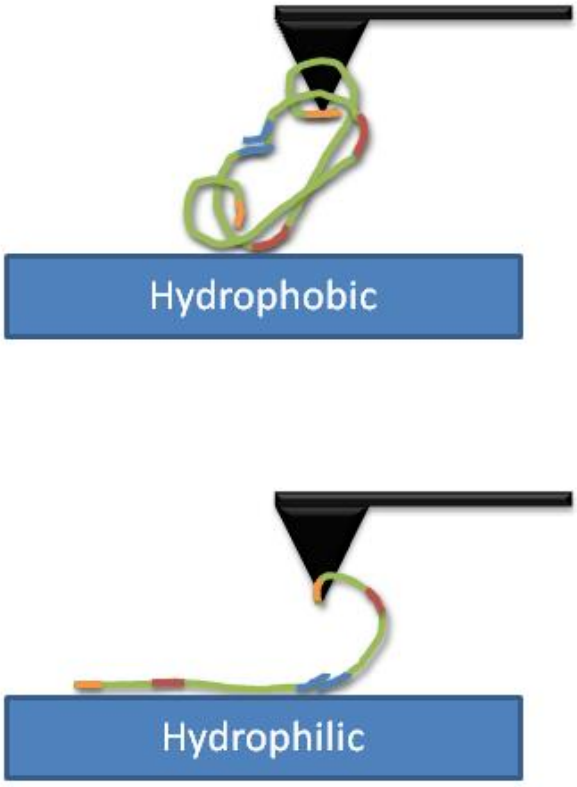

Figure 7-9: Illustration of FN functionalized tip interaction with a hydrophobic surface (top) and a hydrophilic surface (bottom). Orange represents the N terminal groups, red represents the RGD binding sites and blue represents the disulfide C-terminal bridge. Adapted from [97].

FN conformations are known to be associated with the bioactivity of the protein. The more bioactive form of FN, typically the extended conformation, exposes domains (i.e. the RGD region) that promote cellular interactions. When in the compact conformation, the RGD region is buried in the core of the compact protein and does not have access to integrin binding with cells [97]. Hence a material which promotes the elongated conformation may promote better cellular interactions, compared to a surface that promotes a compact conformation. Using this control it is possible to

engineer a material that can be anti-fouling (compact conformation) or adhesion-promoting (elongated conformation) with the applied stimulus.

7.4.4 *Implication for Control of Protein Adhesion*

Control of cellular adhesion is useful for several applications, including directed cell growth, flow cytometry, and self-cleaning biosensors [269, 272]. Through encouraging directed cell growth we open up possibilities in neural network patterning, or for prosthetic scaffolds in several types of tissues (neural, muscle, skeletal). Detaching cells for flow cytometry without the addition of degrading chemicals allows for better analysis of biological research [273], and discouraging the adhesion of proteins and unwanted cells to biosensors allows them to remain functioning for longer, and more accurately.

The adhesion of the protein fibrinogen (a glycoprotein), platelets, and mesenchymal stem cells (KUSA-A1) has been shown to reduce when SP is switched to the MC form in a single process [281]. Our results show a similar result, with the adhesion force and energy of FN reducing on the MC form of the pTTh polymer. The switchable nature of the polymers in this study and their effects on protein adhesion therefore suggest a potential use in priority-driven cellular adhesion to control cell growth, spatially and directionally. This has been demonstrated previously [269], but with the reversible nature of this experiment, finer control can be exercised over the cellular adhesion. As the pTThSP1 polymer is capable of responding to both optical and electrical stimulus we now have possible dual control over the material in biological applications.

7.5 Concluding Remarks

This study of an optically switchable polymer, opposed to an electroactive polymer explored in previous chapters, demonstrated the versatility of the single molecule AFM force spectroscopy technique.

The change in hydrophobicity of the pTTh-SP polymer directly correlated with a change in the adhesion force between FN and the polymer and was completely reversible.

The ability to create a dual-mode switchable material is highly desirable for biological applications; the pTThSp material can be switched both electrically and optically. Here we have shown that through optically switching the material we can manipulate protein adhesion which in turn has implications for the control of the bioactivity of FN.

Comparing the FN interaction with the hydrophilic PPy/GAG polymers with the hydrophobic pTThSP1 polymer we saw a clear conformation change as the protein adhered to the surface. This reinforces the sensitivity of the single molecule AFM force spectroscopy to detect changes in protein behaviour as it binds to different polymer surfaces.

8 Conclusions and Future Work

Conclusions

In summary, we have successfully observed nanoscale changes in the physicochemical properties of our PPy biomaterials. AFM characterisation, using numerous established and novel techniques, resolved lateral variations in the nanoscale surface properties and further elucidated of the effect of these dopants on these material properties of the polymer. We also conducted the first direct measurement of protein binding at the single molecular level for an OCP as a function of electrical stimulation.

8.1.1 *Laterally Resolved Nanoscale Properties*

The nature of the dopants used to synthesise the PPy biomaterials were demonstrated to modify the roughness, thickness, modulus, strain, conductivity and surface energy of the polymer. A correlation was observed between the physical properties of the films, with properties grouping with soft, smooth, and high actuation strain, or stiff, rough, and low actuation strain. The laterally resolved surface properties of the films were also found to vary depending on the dopant. Using AFM phase imaging, C-AFM, and KPFM a change in surface charge, conductivity, and potential due to variations in dopant distribution across the polymer was observed. The nodular features of the polymers were observed to have higher dopant loading compared to the peripheries, and this effect was particularly pronounced for PPy/HA. These findings are important

as they emphasize the importance of considering not just the biological activity of the dopant but also the effect it has on the material properties.

8.1.2 *Specific Protein Interaction with Bioactive Dopants*

The AFM measurements show that it is possible to deconvolute the complexity of interactions at these electrodes that are brought upon by their heterogeneous polymer structure coupled with dynamic redox properties. Using single molecule force spectroscopy, we were able to demonstrate the ability to resolve sub-molecular binding specificity between anionic or sulfate groups of biological dopants and the FNIII12-14 heparin binding domain of FN. The interaction exploits a form of biological 'charge complementarity' to enable specificity. When an electrical signal is applied to the polymer, the specific interaction is switched to a non-specific, high affinity binding state that can be reversibly controlled using electrochemical processes. Both the specific and non-specific interactions are integral for controlling protein conformation and dynamics – the details of which give new molecular insight into controlling cellular interactions at these polymer electrodes.

8.1.3 *Lateral Resolution of Protein Interactions at the Nanoscale*

The adhesion force-volume mapping using single molecule force spectroscopy demonstrated that the protein interaction varies across the surface of the polymer. The homogeneous distribution of the dopant for PPy/CS was found to support more multiple protein interactions, with a higher density of possible FN binding sites. In

contrast the heterogeneous distribution of the dopant for PPy/HA resulted in fewer binding sites available for the protein, culminating in lower surface adhesion and binding density. These surface influences with the protein interaction are known to be critical for cellular interactions, as FN density and the availability of RGD sites are factors which can control cellular responses.

8.2 Future Applications of the Atomic Force Spectroscopy Methods

AFM is a genuinely multifunctional analysis tool that will quantify these biomaterials in situ, measuring several important physical properties with the added control of direct electrical stimulation simultaneously. Significantly, the single molecule force spectroscopy allowed us to resolve changes in protein-polymer interactions both as a function of different dopants and electrical and optical stimulation. The ability to directly observe these interactions opens a gateway for understanding the underlying mechanisms of controlling cell interactions using OCP. Addressing these fundamental questions at the single molecule level is simplified compared to observing entire living cells and enables a direct controlled measurement of the interaction between protein and OCP. This technique was also effective for measuring the switching interaction between an optically dynamic polymer surface and the protein. Hence, the use of single molecule force spectroscopy can be used to analyse the cell- or protein-material interface as a function of different stimuli and with unprecedented sub-molecular resolution that will be beneficial for the design of OCP that exert control over living cells at the nanoscale and molecular level.

8.2.1 *The Significance of a Switchable Conductive Biomaterial*

Electrochemical switching of protein adhesion on OCPs holds much promise for future biomedical applications. For example, biomaterials that encourage or stop cell growth with an "on-demand" switch are highly desirable. Applications that require cell guidance such as neural and nerve tissue regeneration can benefit greatly from biomaterials that direct cell growth and differentiation with additional temporal control. Potential applications that would benefit include electronic Petri dishes and electronic 3-D gels, or implantable electrodes, for spatially and temporally controlling cell interactions.

8.2.2 *Electrochemical Tip Force Spectroscopy*

The ability of to control the conformation of a protein, such as FN, through an electrochemical surface offers another point of interest from the reverse end of the tip.

The change in FN conformation with electrical stimulation of the polymer has been used in initial studies for an electrochemical biosensing AFM tip. Control of the protein conformation can allow us to observe the interaction between differently conformations and specific substrate. The tips could be applied directly to living cells to observe how proteins in different conformation specifically bind to the cells.

This experiment involved covalently functionalizing FN to the electrochemical tips developed in collaboration with IABC (University of Ulm, Germany) and Dr. Christine Kranz, and with Dr Michael Higgins at IPRI (University of Wollongong, Australia). These tips are conductive and have a large PPy surface grown galvanostatically on the apex of the tip.

A constant potential was applied to the tip while performing the force curves onto a polymer substrate. Five curves per spot were performed, alternating positive and negative voltage cycled through three times each and graphed in Figure 8-1.

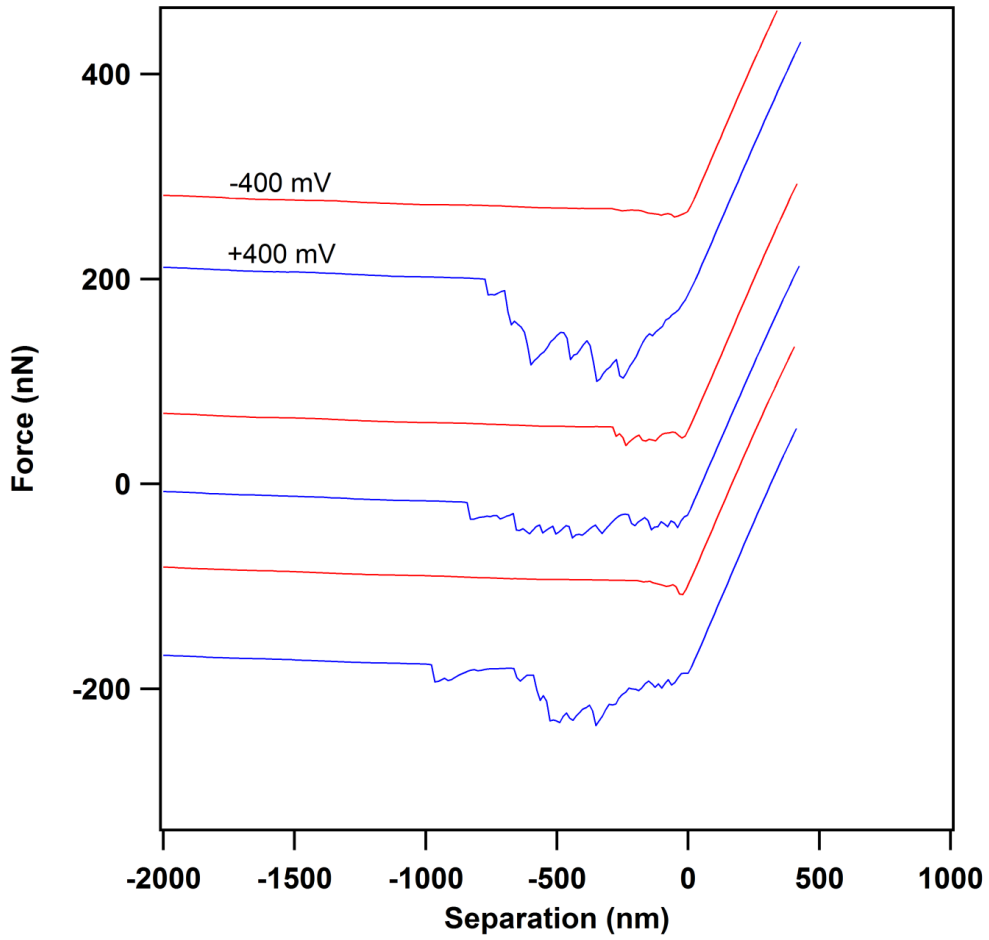

Figure 8-1: FN adhesion profiles while applying a constant potential to the tip, third point. Red is an applied voltage of -400mV, blue is an applied voltage of +400mV.

We see that when a negative potential is applied the protein adhesion is drastically reduced, and when a positive voltage is applied the adhesion is large with many binding events. This was fully cycled three times, and showed the same response for all potential applications. However, this effect was only observed once before the tip was degraded and no longer useable.

These results show promising possibilities for a switchable AFM biosensing tip, taking advantage of the molecular control over the protein conformation. This research is in an opposite direction to the control of a surface, but is an extremely useful technique in the study of single cell interactions with an electrochemical biomaterial.

9 Bibliography

1.Wallace, G.G., S.E. Moulton, R.M.I. Kapsa, and M.J. Higgins, *Medical Bionics*, in *Organic Bionics*. 2012, Wiley-VCH Verlag GmbH & Co. KGaA. p. 1-39.

2. Loizou, P.C., *Introduction to cochlear implants.* Engineering in Medicine and Biology Magazine, IEEE, 1999. **18**(1): p. 32-42.

3. Ong, J.M. and L. da Cruz, *The bionic eye: a review.* Clinical & Experimental Ophthalmology, 2012. **40**(1): p. 6-17.

4. Weiland, J.D., D.J. Anderson, and M.S. Humayun, *In vitro electrical properties for iridium oxide versus titanium nitride stimulating electrodes.* Biomedical Engineering, IEEE Transactions on, 2002. **49**(12): p. 1574-1579.

5. Geddes, L.A. and R. Roeder, *Criteria for the selection of materials for implanted electrodes.* Annals of Biomedical Engineering, 2003. **31**(7): p. 879-890.

6. Franks, W., W. Schenker, P. Schmutz, and A. Hierlemann, *Impedance characterization and modeling of electrodes for biomedical applications.* IEEE Transactions on Biomedical Engineering, 2005. **52**(7): p. 1295-1302.

7. Cogan, S.F., *Neural stimulation and recording electrodes*, in *Annual Review of Biomedical Engineering*. 2008, Annual Reviews. p. 275-309.

8. Merrill, D.R., M. Bikson, and J.G.R. Jefferys, *Electrical stimulation of excitable tissue : design of efficacious and safe protocols.* Journal of Neuroscience Methods, 2005. **141**(2): p. 171-198.

9. Polikov, V.S., P.A. Tresco, and W.M. Reichert, *Response of brain tissue to chronically implanted neural electrodes.* Journal of Neuroscience Methods, 2005. **148**(1): p. 1-18.

10. Green, R.A., N.H. Lovell, G.G. Wallace, and L.A. Poole-Warren, *Conducting polymers for neural interfaces: Challenges in developing an effective long-term implant.* Biomaterials, 2008. **29**(24-25): p. 3393-3399.

11. Wallace, G.G. and G.M. Spinks, *Conducting polymers: A bridge across the bionic interface.* Chemical Engineering Progress, 2007. **103**(12): p. S18-S24.

12. Hassler, C., T. Boretius, and T. Stieglitz, *Polymers for neural implants.* Journal of Polymer Science Part B: Polymer Physics, 2011. **49**(1): p. 18-33.

13. Wallace, G.G., S.E. Moulton, and G.M. Clark, *Electrode-cellular interface.* Science, 2009. **324**: p. 185-186.

14. Wallace, G.G., S.E. Moulton, R.M.I. Kapsa, and M.J. Higgins, *Organic Conducting Polymers*, in *Organic Bionics*. 2012, Wiley-VCH Verlag GmbH & Co. KGaA. p. 81-112.

15. Wallace, G. and G. Spinks, *Conducting polymers- bridging the bionic interface.* Soft Matter, 2007. **3**: p. 665-671.

16. Ludwig, K.A., J.D. Uram, J. Yang, D.C. Martin, and D.R. Kipke, *Chronic neural recordings using silicon microelectrode arrays electrochemically deposited with a poly(3,4-ethylenedioxythiophene) (PEDOT) film.* Journal of Neural Engineering, 2006. **3**(1): p. 59.

17. Khodagholy, D., et al., *Highly conformable conducting polymer electrodes for in vivo recordings.* Advanced Materials, 2011. **23**(36): p. H268-H272.

18. Guimard, N., N. Gomez, and C. Schmidt, *Conducting polymers in biomedical engineering.* Progress in Polymer Science, 2007. **32**(8-9): p. 876-921.

19. Cui, X., et al., *Surface modification of neural recording electrodes with conducting polymer / biomolecule blends.* Journal of Biomedical Material Research, 2001. **56**(2): p. 261-272.

20. Gilmore, K., et al., *Evaluation of primary muscle cell proliferation and differentiation on composite polypyrrole substrates.* Biomaterials, 2009. **30**(29): p. 5292-5304.

21. Hodgson, A.J., et al., *Reactive supramolecular assemblies of mucopolysaccharide, polypyrrole and protein as controllable biocomposites for a new generation of 'intelligent biomaterials'.* Supramolecular Science, 1994. **1**(2): p. 77-83.

22. Ateh, D.D., H.A. Navsaria, and P. Vadgama, *Polypyrrole-based conducting polymers and interactions with biological tissues.* Journal of the Royal Society Interface, 2006. **3**: p. 741-752.

23. Janata, J. and M. Josowicz, *Conducting polymers in electronic chemical sensors.* Nat Mater, 2003. **2**(1): p. 19-24.

24. Liu, X., K.J. Gilmore, S.E. Moulton, and G.G. Wallace, *Electrical stimulation promotes nerve cell differentiation on polypyrrole/poly (2-methoxy-5 aniline sulfonic acid) composites.* Journal of Neural Engineering, 2009. **6**(6): p. 065002.

25. Kotwal, A. and C.E. Schmidt, *Electrical stimulation alters protein adsorption and nerve cell interactions with electrically conducting biomaterials.* Biomaterials, 2001. **22**(10): p. 1055-1064.

26. Zhang, Z., et al., *Electrically conductive biodegradable polymer composite for nerve regeneration: Electricity-stimulated neurite outgrowth and axon regeneration.* Artificial Organs, 2007. **31**(1): p. 13-22.

27. Thompson, B.C., et al., *Conducting polymers, dual neurotrophins and pulsed electrical stimulation — Dramatic effects on neurite outgrowth.* Journal of Controlled Release, 2010. **141**(2): p. 161-167.

28. Schmidt, C.E., V.R. Shastri, J.P. Vacanti, and R. Langer, *Stimulation of neurite outgrowth using an electrically conducting polymer.* Proceeding of the National Academy of Sciences, 1997. **94**(17): p. 8948-8953.

29. Moreno, J.S., et al., *Polypyrrole-polysaccharide thin films characteristics: electrosynthesis and biological properties.* Journal of Biomedical Materials Research, 2009. **88A**(3): p. 832-840.

30. Garner, B., a. Georgevich, a.J. Hodgson, L. Liu, and G.G. Wallace, *Polypyrroleheparin composites as stimulus-responsive substrates for endothelial cell growth.* Journal of biomedical materials research, 1999. **44**(2): p. 121-129.

31. Gomez, N. and C.E. Schmidt, *Nerve growth factor-immobilized polypyrrole: Bioactive electrically conducting polymer for enhanced neurite extension.* Journal of Biomedical Materials Research Part A, 2007. **81A**(1): p. 135-149.

32. Richardson, R.T., et al., *The effect of polypyrrole with incorporated neurotrophin-3 on the promotion of neurite outgrowth from auditory neurons.* Biomaterials, 2007. **28**(3): p. 513-523.

33. Richardson, R.T., et al., *Polypyrrole-coated electrodes for the delivery of charge and neurotrophins to cochlear neurons.* Biomaterials, 2009. **30**(13): p. 2614-2624.

34. Thompson, B.C., S.E. Moulton, R.T. Richardson, and G.G. Wallace, *Effect of the dopant anion in polypyrrole on nerve growth and release of a neurotrophic protein.* Biomaterials, 2011. **32**(15): p. 3822-3831.

35. Terayama, Y., K. Kaneko, K. Tanaka, and K. Kawamoto, *Ultrastructural changes of the nerve elements following disruption of the organ of Corti. 2. Nerve elements outside the organ of Corti.* Acta Oto-Laryngologica, 1979. **88**(1-2): p. 27-36.

36. Thompson, B.C., et al., *Optimising the incorporation and release of a neurotrophic factor using conducting polypyrrole.* Journal of Controlled Release, 2006. **116**(3): p. 285-294.

37. Shirakawa, H., E.J. Louis, A.G. MacDiarmid, C.K. Chiang, and A.J. Heeger, *Synthesis of electrically conducting organic polymers: halogen derivatives of polyacetylene, (CH).* Journal of the Chemical Society, Chemical Communications, 1977(16): p. 578-580.

38. Bidez, P.R., et al., *Polyaniline, an electroactive polymer, supports adhesion and proliferation of cardiac myoblasts.* Journal of Biomaterials Science, Polymer Edition, 2006. **17**(1-2): p. 199-212.

39. Kim, J., D. Sohn, Y. Sung, and E.-R. Kim, *Fabrication and characterization of conductive polypyrrole thin film prepared by in situ vapor-phase polymerization.* Synthetic Metals, 2003. **132**(3): p. 309-313.

40. Wallace, G.G., G.M. Spinks, L.A.P. Kane-Maguire, and P.R. Teasdale, *Conductive Electroactive Polymers*. Third ed. 2009: CRC Press. 263.

41. Sadki, S., P. Schottland, N. Brodie, and G. Sabouraud, *The mechanisms of pyrrole electropolymerization.* Chemical Society Reviews, 2000. **29**(5).

42. Gao, M., et al., *Aligned coaxial nanowires of carbon nanotubes sheathed with conducting polymers.* Angewandte Chemie International Edition, 2000. **39**(20): p. 3664-3667.

43. Lee, J.Y., C.A. Bashur, A.S. Goldstein, and C.E. Schmidt, *Polypyrrole-coated electrospun PLGA nanofibers for neural tissue applications.* Biomaterials, 2009. **30**(26): p. 4325-4335.

44. Higgins, M.J., S.T. McGovern, and G.G. Wallace, *Visualizing dynamic actuation of ultrathin polypyrrole films.* Langmuir, 2009. **25**(6): p. 3627-3633.

45. Fonner, J.M., et al., *Biocompatibility implications of polypyrrole synthesis techniques.* Biomedical Materials, 2008. **3**(3): p. 1-12.

46. Inzelt, G., *Electron and proton conducting polymers: recent developments and prospects.* Electrochimica Acta, 2000. **45**(15-16): p. 2403-2421.

47. Davey, J.M., S.F. Ralph, C.O. Too, and G.G. Wallace, *Synthesis , characterization and ion transport studies on polypyrrole/polyvinylphosphate conducting polymer materials.* Synthetic Metals, 1999. **99**(3): p. 191-199.

48. Welzel, H.P., G. Kossmehl, H. Boettcher, G. Engelmann, and W.D. Hunnius, *Reactive groups on polymer-covered electrodes. 5. Synthesis and cyclovoltammetric analysis of 3-substituted thiophene derivatives.* Macromolecules, 1997. **30**(24): p. 7419-7426.

49. Kumar, D. and R.C. Sharma, *Advances in conductive polymers.* European Polymer Journal, 1998. **34**(8): p. 1053-1060.

50. Satoh, M., K. Kaneto, and K. Yoshino, *Dependences of electrical and mechanical properties of conducting polypyrrole films on conditions of electrochemical polymerization in an aqueous medium.* Synthetic Metals, 1986. **14**(4): p. 289-296.

51. Joo, J., et al., *Physical characterization of electrochemically and chemically synthesized polypyrroles.* Macromolecules, 2000. **33**(14): p. 5131-5136.

52. Fonner, J.M., C.E. Schmidt, and P. Ren, *A combined molecular dynamics and experimental study of doped polypyrrole.* Polymer, 2010. **51**(21): p. 4985-4993.

53. Vernitskaya, T.y.V. and O.N. Efimov, *Polypyrrole: a conducting polymer; its synthesis, properties and applications.* Russian Chemical Reviews, 1997. **66**(5): p. 443.

54. Mitchell, G.R., F.J. Davis, and C.H. Legge, *The effect of dopant molecules of the molecular order of electrically-conducting films of polypyrrole.* Synthetic Metals, 1988. **26**(3): p. 247 - 257.

55. Chen, S.A. and L.C. Lin, *Polyaniline doped by the new class of dopant, ionic saltstructure and properties.* Macromolecules, 1995. **28**(4): p. 1239-1245.

56. Tourillon, G. and F. Garnier, *Effect of dopant on the physicochemical and electrical properties of organic conducting polymers.* Journal of Physical Chemistry, 1983. **87**(13): p. 2289-2292.

57. Silk, T., Q. Hong, J. Tamm, and R.G. Compton, *AFM studies of polypyrrole film surface morphology II . Roughness characterization by the fractal dimension analysis.* Synthetic Metals, 1998. **93**: p. 65-71.

58. Jayakannan, M., S. Annu, and S. Ramalekshmi, *Structural effects of dopants and polymerization methodologies on the solid-state ordering and morphology of polyaniline.* Journal of Polymer Science Part B: Polymer Physics, 2005. **43**(11): p. 1321-1331.

59. Oh, K.W., H.J. Park, and S.H. Kim, *Electrical property and stability of electrochemically synthesized polypyrrole films.* Journal of Applied Polymer Science, 2004. **91**(6): p. 3659-3666.

60. Singh, P.R., S. Mahajan, S. Rajwade, and A.Q. Contractor, *EC-AFM investigation of reversible volume changes with electrode potential in polyaniline.* Journal of Electroanalytical Chemistry, 2009. **625**(1): p. 16-26.

61. Molino, P.J., M.J. Higgins, P.C. Innis, R.M.I. Kapsa, and G.G. Wallace, *Fibronectin and bovine serum albumin adsorption and conformational dynamics on inherently conducting polymers: A QCM-D study.* Langmuir, 2012. **28**(22): p. 8433-8445.

62. Silk, T., Q. Hong, J. Tamm, and R.G. Compton, *AFM studies of polypyrrole film surface morphology I. The influence of film thickness and dopant nature.* Synthetic Metals, 1998. **93**(1): p. 59-64.

63. Cassignol, C., P. Olivier, and A. Ricard, *Influence of the dopant on the polypyrrole moisture content: Effects on conductivity and thermal stability.* Journal of Applied Polymer Science, 1998. **70**(8): p. 1567-1577.

64. Han, D.-h., H.J. Lee, and S.-m. Park, *Electrochemistry of conductive polymers XXXV : Electrical and morphological characteristics of polypyrrole films prepared in aqueous media studied by current sensing Atomic Force Microscopy.* Electrochimica Acta, 2005. **50**(15): p. 3085-3092.

65. Li, D.F., et al., *Preparation of a hydrophobic polythiophene film to improve protein adsorption and proliferation of PC 12 cells.* Journal of Physical Chemistry B, 2008. **112**(51): p. 16290-16299.

66. Garner, B., A.J. Hodgson, G.G. Wallace, and P.A. Underwood, *Human endothelial cell attachment to and growth on polypyrrole-heparin is vitronectin dependent.* Journal of Materials Science: Materials in Medicine, 1999. **10**(1): p. 19-27.

67. Baughman, R.H., J.L. Bredas, R.R. Chance, R.L. Elsenbaumer, and L.W. Shacklette, *Structual basis for semiconducting and metallic polymer dopant systems.* Chemical Reviews, 1982. **82**(2): p. 209-222.

68. Suematsu, S., Y. Oura, H. Tsujimoto, H. Kanno, and K. Naoi, *Conducting polymer films of cross-linked structure and their QCM analysis.* Electrochimica Acta, 2000. **45**(22–23): p. 3813-3821.

69. Bay, L., et al., *Polypyrrole doped with alkyl benzenesulfonates.* Macromolecules, 2002. **35**(25): p. 9345-9351.

70. Spinks, G.M., D. Zhou, L. Liu, and G.G. Wallace, *The amounts per cycle of polypyrrole electromechanical actuators.* Smart Materials and Structures, 2003. **3**(3): p. 468.

71. Spinks, G.M., T.E. Campbell, and G.G. Wallace, *Force generation from polypyrrole actuators.* Smart Materials and Structures, 2005. **14**(2).

72. Zhu, B., et al., *Nanotopographical guidance of C6 glioma cell alignment and oriented growth.* Biomaterials, 2004. **25**(18): p. 4215-4223.

73. Park, J., S. Bauer, K.V.D. Mark, and P. Schmuki, *Nanosize and vitality : TiO_2 nanotube diameter directs cell fate.* Nano Letters, 2007. **7**(6): p. 1686-1691.

74. Chung, T.-w., D.-z. Liu, S.-y. Wang, and S.-s. Wang, *Enhancement of the growth of human endothelial cells by surface roughness at nanometer scale.* Biomaterials, 2003. **24**(25): p. 4655-4661.

75. Keiswetter, K., et al., *Surface roughness modulates the local production of growth factors and cytokines by osteoblast-like MG-63 cells.* Biomedical Materials, 1996. **32**(1): p. 55-63.

76. Martin, J.Y., et al., *Effect of titanium surface roughness on proliferation, differentiation, and protein synthesis of human osteoblast-like cells (MG63).* Journal of Biomedical Materials Research, 1995. **29**(3): p. 389-401.

77. Fan, Y.W., et al., *Culture of neural cells on silicon wafers with nano-scale surface topograph.* Journal of Neuroscience Methods, 2002. **120**(1): p. 17-23.

78. Wong, J.Y., J.B. Leach, and X.Q. Brown, *Balance of chemistry , topography , and mechanics at the cell – biomaterial interface : Issues and challenges for assessing the role of substrate mechanics on cell response.* Surface Science, 2004. **570**(1-2): p. 119-133.

79. Engler, A.J., et al., *Myotubes differentiate optimally on substrates with tissue like stiffness : pathological implications for soft or stiff microenvironments.* Cell Biology, 2004. **166**(6): p. 877-887.

80. Engler, A.J., S. Sen, H.L. Sweeney, and D.E. Discher, *Matrix elasticity directs stem cell lineage specification.* Cell, 2006. **126**(4): p. 677-689.

81. Williams, C.M., A.J. Engler, R.D. Slone, L.L. Galante, and J.E. Schwarzbauer, *Fibronectin expression modulates mammary epithelial cell proliferation during acinar differentiation.* Cancer Research, 2008. **68**(9): p. 3185-3192.

82. Pelham, R.J. and Y.-l. Wang, *Cell locomotion and focal adhesions are regulated by substrate flexibility.* Proceedings of the National Academy of Sciences, 1997. **94**(25): p. 13661-13665.

83. Wang, H.-B., M. Dembo, and Y.-L. Wang, *Substrate flexibility regulates growth and apoptosis of normal but not transformed cells.* American Journal of Physiology - Cell Physiology, 2000. **279**(5): p. C1345-C1350.

84. Lo, C.-M., H.-B. Wang, M. Dembo, and Y.-l. Wang, *Cell movement is guided by the rigidity of the substrate.* Biophysical Journal, 2000. **79**(1): p. 144-152.

85. Flanagan, L.A., Y.-E. Ju, B. Marg, M. Osterfield, and P.A. Janmey, *Neurite branching on deformable substrates.* NeuroReport, 2002. **13**(18): p. 2411-2415.

86. Deroanne, C.F., C.M. Lapiere, and B.V. Nusgens, *In vitro tubulogenesis of endothelial cells by relaxation of the coupling extracellular matrix-cytoskeleton.* Cardiovascular Research, 2001. **49**(3): p. 647-658.

87. Wong, J.Y., A. Velasco, P. Rajagopalan, and Q. Pham, *Directed movement of vascular smooth muscle cells on gradient-compliant hydrogels.* Langmuir, 2003. **19**(5): p. 1908-1913.

88. Thomas, T. and P. DiMilla, *Spreading and motility of human glioblastoma cells on sheets of silicone rubber depend on substratum compliance.* Medical and Biological Engineering and Computing, 2000. **38**(3): p. 360-370.

89. Gray, D.S., J. Tien, and C.S. Chen, *Repositioning of cells by mechanotaxis on surfaces with micropatterned Young's modulus.* Journal of Biomedical Materials Research Part A, 2003. **66A**(3): p. 605-614.

90. Genes, N.G., J.A. Rowley, D.J. Mooney, and L.J. Bonassar, *Effect of substrate mechanics on chondrocyte adhesion to modified alginate surfaces.* Archives of Biochemistry and Biophysics, 2004. **422**(2): p. 161-167.

91. Rowley, J.A. and D.J. Mooney, *Alginate type and RGD density control myoblast phenotype.* Journal of Biomedical Materials Research, 2002. **60**(2): p. 217-223.

92. Balgude, A.P., X. Yu, A. Szymanski, and R.V. Bellamkonda, *Agarose gel stiffness determines rate of DRG neurite extension in 3D cultures.* Biomaterials, 2001. **22**(10): p. 1077-1084.

93. Salloum, D.S., S.G. Olenych, T.C.S. Keller, and J.B. Schlenoff, *Vascular smooth muscle cells on polyelectrolyte multilayers: hydrophobicity-directed adhesion and growth.* Biomacromolecules, 2005. **6**(1): p. 161-7.

94. Wachem, P.B.V., et al., *Adhesion of cultured human endothelial cells onto methacrylate polymers with varying surface wettability and charge.* Biomaterials, 1987. **8**(5): p. 323-328.

95. Wachem, P.B.v., et al., *Interaction of cultured human endothelial cells with polymeric surfaces of different wettabilities.* Biomaterials, 1985. **6**(6): p. 403-408.

96. Meadows, P.Y. and G.C. Walker, *Force microscopy studies of fibronectin adsorption and subsequent cellular adhesion to substrates with well-defined surface chemistries.* Langmuir, 2005. **21**(9): p. 4096-4107.

97. Bergkvist, M., J. Carlsson, and S. Oscarsson, *Surface-dependent conformations of human plasma fibronectin adsorbed to silica, mica, and hydrophobic surfaces, studied with use of Atomic Force Microscopy.* Journal of Biomedical Materials Research, 2003. **64A**(2): p. 349-56.

98. García, a.J., M.D. Vega, and D. Boettiger, *Modulation of cell proliferation and differentiation through substrate-dependent changes in fibronectin conformation.* Molecular Biology of the Cell, 1999. **10**(3): p. 785-98.

99. Griesser, H.J., N.D. Spencer, and M. Textor, *Effects of ionic strength and surface charge on protein adsorption at PEGylated surfaces.* Society, 2005. **109**(37): p. 17545-17552.

100. Lee, M.H., P. Ducheyne, L. Lynch, D. Boettiger, and R.J. Composto, *Effect of biomaterial surface properties on fibronectin – a 5 b 1 integrin interaction and cellular attachment.* Biomaterials, 2006. **27**(9): p. 1907-1916.

101. Sigal, G.B., M. Mrksich, and G.M. Whitesides, *Effect of surface wettability on the adsorption of proteins and detergents.* Journal of the American Chemical Society, 1998. **120**(14): p. 3464-3473.

102. Gomez, N., J.Y. Lee, J.D. Nickels, and C.E. Schmidt, *Micropatterned polypyrrole: A combination of electrical and topographical characteristics for the stimulation of cells.* Advanced Functional Materials, 2007. **17**(10): p. 1645-1653.

103. Sanghvi, A.B., K.P.H. Miller, A.M. Belcher, and C.E. Schmidt, *Biomaterials functionalization using a novel peptide that selectively binds to a conducting polymer.* Nature Materials, 2005. **4**(6): p. 496-502.

104. Stauffer, W.R. and X.T. Cui, *Polypyrrole doped with 2 peptide sequences from laminin.* Biomaterials, 2006. **27**(11): p. 2405-2413.

105. Collier, J.H., J.P. Camp, T.W. Hudson, and C.E. Schmidt, *Synthesis and characterization of polypyrrole – hyaluronic acid composite biomaterials for tissue engineering applications.* Journal of Biomedical Material Research, 1999. **50**(4): p. 574-584.

106. Moreno, J.S., S. Panero, M. Artico, and P. Filippini, *Synthesis and characterization of new electroactive polypyrrole – chondroitin sulphate A substrates.* Bioelectrochemistry, 2008. **72**(1): p. 3-9.

107. Wong, J.Y., R. Langert, and D.E. Ingberi, *Electrically conducting polymers can noninvasively control the shape and growth of mammalian cells.* Science, 1994. **91**(8): p. 3201-3204.

108. Zhou, D., C.O. Too, and G.G. Wallace, *Synthesis and characterisation of polypyrrole / heparin composites.* Reactive and Functional Polymers, 1999. **39**: p. 19-26.

109. Sugahara, K., et al., *Recent advances in the structural biology of chondroitin sulfate and dermatan sulfate.* Current Opinion in Structural Biology, 2003. **13**(5): p. 612-620.

110. Hook, M., L. Kjellen, S. Johansson, and J. Robinson, *Cell-surface glycosaminoglycans.* Annual Review of Biochemistry, 1984. **53**(1): p. 847-869.

111. Johansson, S., G. Svineng, K. Wennerberg, A. Armulik, and L. Lohikangas, *Fibronectin-integrin interactions.* Frontiers in bioscience : a journal and virtual library, 1997. **2**: p. d126-46.

112. Ruoslahti, E., *Fibronectin and its Receptors.* Annual Review of Biochemistry, 1988. **57**(1): p. 375-413.

113. Laabs, T., D. Carulli, H.M. Geller, and J.W. Fawcett, *Chondroitin sulfate proteoglycans in neural development and regeneration.* Current Opinion in Neurobiology, 2005. **15**(1): p. 116-120.

114. Barkalow, F.J. and J.E. Schwarzbauer, *Interactions between fibronectin and chondroitin sulfate are modulated by molecular context.* Journal of Biological Chemistry, 1994. **269**(6): p. 3957-3962.

115. Fraser, J.R.E., T.C. Laurent, and U.B.G. Laurent, *Hyaluronan: its nature, distribution, functions and turnover.* Journal of Internal Medicine, 1997. **242**(1):p. 27-33.

116. West, D., I. Hampson, F. Arnold, and S. Kumar, *Angiogenesis induced by degradation products of hyaluronic acid.* Science, 1985. **228**(4705): p. 1324-1326.

117. Yuan, G.-L. and N. Kuramoto, *Water-processable chiral polyaniline derivatives doped and intertwined with dextran sulfate: Synthesis and chiroptical properties.* Macromolecules, 2002. **35**(26): p. 9773-9779.

118. Adeloju, S.B. and G.G. Wallace, *Conducting polymers and the bioanalytical sciences: new tools for biomolecular communications. A review.* Analyst, 1996. **121**(6): p. 699-703.

119. Stewart, E.M., X. Liu, G.M. Clark, R.M.I. Kapsa, and G.G. Wallace, *Inhibition of smooth muscle cell adhesion and proliferation on heparin-doped polypyrrole.* Acta Biomaterialia, 2012. **8**(1): p. 194-200.

120. Meng, S., M. Rouabhia, G. Shi, and Z. Zhang, *Heparin dopant increases the electrical stability, cell adhesion, and growth of conducting polypyrrole/poly(L,Llactide) composites.* Journal of Biomedical Materials Research Part A, 2008. **87A**(2): p. 332-344.

121. Lee, J.Y. and C.E. Schmidt, *Pyrrole – hyaluronic acid conjugates for decreasing cell binding to metals and conducting polymers.* Acta Biomaterialia, 2010. **6**(11): p. 4396-4404.

122. Morra, M. and C. Cassineli, *Non-fouling properties of polysaccharide-coated surfaces.* Journal of Biomaterials Science, Polymer Edition, 1999. **10**(10): p. 1107-1124.

123. Cen, L., K.G. Neoh, Y. Li, and E.T. Kang, *Assessment of in vitro bioactivity of hyaluronic acid and sulfated hyaluronic acid functionalized electroactive polymer.* Biomacromolecules, 2004. **5**(6): p. 2238-2246.

124. Hudson, T.W., G.R.D. Evans, and C.E. Schmidt, *Engineering strategies for peripheral nerve repair.* Orthopedic Clinics of North America, 2000. **31**(3): p. 485-+.

125. Bendrea, A.-D., L. Cianga, and I. Cianga, *Review paper: Progress in the field of conducting polymers for tissue engineering applications.* Journal of Biomaterials Applications, 2011. **26**(1): p. 3-84.

126. Ojingwa, J.C. and R.R. Isseroff, *Electrical stimulation of wound healing.* Journal of Investigative Dermatology, 2003. **121**(1): p. 1-12.

127. Rowlands, A.S. and J.J. Cooper-White, *Directing phenotype of vascular smooth muscle cells using electrically stimulated conducting polymer.* Biomaterials, 2008. **29**(34): p. 4510-4520.

128. Wadhwa, R., C.F. Lagenaur, and X.T. Cui, *Electrochemically controlled release of dexamethasone from conducting polymer polypyrrole coated electrode.* Journal of Controlled Release, 2006. **110**(3): p. 531-541.

129. Deister, C. and C.E. Schmidt, *Optimizing neurotrophic factor combinations for neurite outgrowth.* Journal of Neural Engineering, 2006. **3**(2): p. 172.

130. Valentini, R.F., T.G. Vargo, J.A. Gardella Jr, and P. Aebischer, *Electrically charged polymeric substrates enhance nerve fibre outgrowth In vitro.* Biomaterials, 1992. **13**(3): p. 183-190.

131. Patel, N. and M.M. Poo, *Orientation of neurite growth by extracellular electric fields.* The Journal of neuroscience : the official journal of the Society for Neuroscience, 1982. **2**(4): p. 483-96.

132. Sisken, B.F., M. Kanje, G. Lundborg, E. Herbst, and W. Kurtz, *Stimulation of rat sciatic nerve regeneration with pulsed electromagnetic fields.* Brain Research, 1989. **485**(2): p. 309-316.

133. Li, Y., K.G. Neoh, and E.T. Kang, *Controlled release of heparin from polypyrrolepoly(vinyl alcohol) assembly by electrical stimulation.* Journal of Biomedical Materials Research Part A, 2005. **73A**(2): p. 171-181.

134. Altschuler, R.A., et al., *Rescue and regrowth of sensory nerves following deafferentation by neurotrophic factors.* Annals of the New York Academy of Sciences, 1999. **884**(1): p. 305-311.

135. Du, J., L. Feng, F. Yang, and B. Lu, *Activity- and Ca2+-dependent modulation of surface expression of brain-derived neurotrophic factor receptors in hippocampal neurons.* The Journal of cell biology, 2000. **150**(6): p. 1423-1434.

136. Brown, T.D., *Techniques for mechanical stimulation of cells in vitro : a review.* Journal of Biomechanics, 2000. **33**: p. 3-14.

137. Mauney, J.R., et al., *Mechanical stimulation promotes osteogenic differentiation of human bone marrow stromal cells on 3-D partially demineralized bone scaffolds in vitro.* Calcified Tissue International, 2004. **74**(5): p. 458-468.

138. Altman, G.H., et al., *Cell differentiation by mechanical stress.* The Journal of the Federation of American Societies for Experimental Biology, 2001. **16**(2): p. 270-272.

139. Dartsch, P.C. and E. Betz, *Response of cultured endothelial cells to mechanical stimulation.* Basic Research in Cardiology, 1989. **84**(3): p. 268-281.

140. Svennersten, K., M. Berggren, A. Richter-Dahlfors, and E.W.H. Jager, *Mechanical stimulation of epithelial cells using polypyrrole microactuators.* Lab on a Chip, 2011. **11**(19): p. 3287-3293.

141. Lundin, V., A. Herland, M. Berggren, E.W.H. Jager, and A.I. Teixeira, *Control of neural stem cell survival by electroactive polymer substrates.* PLoS ONE, 2011. **6**(4): p. 1-8.

142. Smith, A.B. and C.J. Knowles, *Investigation of the relationship between conductivity and protein-binding properties of polypyrrole.* Journal of Applied Polymer Science, 1991. **43**: p. 399-403.

143. Svennersten, K., M.H. Bolin, E.W.H. Jager, M. Berggren, and A. Richter-Dahlfors, *Electrochemical modulation of epithelia formation using conducting polymers.* Biomaterials, 2009. **30**(31): p. 6257-6264.

144. Wan, A.M.D., D.J. Brooks, A. Gumus, C. Fischbach, and G.G. Malliaras, *Electrical control of cell density gradients on a conducting polymer surface.* Chemical Communications, 2009(35): p. 5278-5280.

145. Gumus, A., et al., *Control of cell migration using a conducting polymer device.* Soft Matter, 2010. **6**(20): p. 5138-5142.

146. Saltó, C., et al., *Control of neural stem cell adhesion and density by an electronic polymer surface switch.* Langmuir, 2008. **24**(24): p. 14133-14138.

147. Gao, M., et al., *Structure and functional significance of mechanically unfolded fibronectin type III1 intermediates.* Proceedings of the National Academy of Sciences of the United States of America, 2003. **100**: p. 14784-9.

148. Mao, Y. and J.E. Schwarzbauer, *Fibronectin fibrillogenesis, a cell-mediated matrix assembly process.* Matrix Biology, 2005. **24**(6): p. 389-399.

149. Katsumi, A., A.W. Orr, E. Tzima, and M.A. Schwartz, *Integrins in mechanotransduction.* Journal of Biological Chemistry, 2004. **279**(13): p. 12001-12004.

150. Wang, N., J.P. Butler, and D.E. Ingber, *Mechanotransduction across the cell surface and through the cytoskeleton.* Science, 1993. **260**(5111): p. 1124-1127.

151. Erickson, H.P., *Stretching fibronectin.* Journal of Muscle Research and Cell Motility, 2002. **23**(5-6): p. 575-580.

152. Erickson, H.P. and N.A. Carrell, *Fibronectin in extended and compact conformations- electron-microscopy and sedimentation analysis.* Journal of Biological Chemistry, 1983. **258**(23): p. 4539-4544.

153. Grinnell, F. and M.K. Feld, *Fibronectin adsorption on hydrophilic and hydrophobic surfaces detected by antibody binding and analyzed during cell adhesion in serum-containing medium.* The Journal of Biological Chemistry, 1982. **257**(9): p. 4888-93.

154. Keselowsky, B.G., D.M. Collard, and A.J. García, *Surface chemistry modulates fibronectin conformation and directs integrin binding and specificity to control cell adhesion.* Journal of Biomedical Materials Research, 2003. **66A**(2): p. 247-59.

155. Hull, J.R., G.S. Tamura, and D.G. Castner, *Structure and reactivity of adsorbed fibronectin films on mica.* Biophysical Journal, 2007. **93**(8): p. 2852-2860.

156. Binnig, G. and H. Rohrer, *Scanning Tunnelling Microscopy.* Physica B & C, 1984. **127**(1-3): p. 37-45.

157. Binnig, G., C.F. Quate, and C. Gerber, *Atomic Force Microscope.* Physical Review Letters, 1986. **56**(9): p. 930-933.

158. Abramovitch, D.Y., S.B. Andersson, L.Y. Pao, and G. Schitter, *A tutorial on the mechanisms, dynamics, and control of Atomic Force Microscopes.* Proceedings of the 2007 American Control Conference, 2007: p. 3488-3503.

159. O'Neil, K.D.O. and O.A. Semenikhin, *AFM phase imaging of electropolymerized polybithiophene films at different stages of their growth.* Physical Chemistry C, 2007. **111**(40): p. 14823-14832.

160. O'Neil, K.D., B. Shaw, and O.A. Semenikhin, *On the origin of mesoscopic inhomogeneity of conducting polymers.* Journal of Physical Chemistry B, 2007. **111**(31): p. 9253-9269.

161. Semenikhin, O.A., L. Jiang, T. Iyoda, K. Hasimoto, and A. Fujishima, *Atomic Force Microscopy and Kelvin Probe Force Microscopy evidence of local structural inhomogeneity and nonuniform dopant distribution in conducting polybithiophene.* Journal of Physical Chemistry, 1996. **100**(48): p. 9-11.

162. Cleveland, J.P., B. Anczykowski, A.E. Schmid, and V.B. Elings, *Energy dissipation in tapping-mode atomic force microscopy*. Vol. 72. 1998: AIP. 2613-2615.

163. James, P.J., et al., *Interpretation of contrast in tapping mode AFM and shear force microscopy . A study of Nafion.* Langmuir, 2001. **17**(2): p. 349-360.

164. Chen, X., et al., *Chemical and morphological analysis of surface enrichment in a biodegradable polymer blend by phase-detection imaging Atomic Force Microscopy.* Society, 1998. **31**(7): p. 2278-2283.

165. Scott, W.W. and B. Bhushan, *Use of phase imaging in atomic force microscopy for measurement of viscoelastic contrast in polymer nanocomposites and molecularly thick lubricant films.* Ultramicroscopy, 2003. **97**(1–4): p. 151-169.

166. Avila, A. and B. Bhushan, *Electrical measurement techniques in Atomic Force Microscopy.* Critical Reviews in Solid State and Materials Sciences, 2010. **35**(1): p. 38-51.

167. Barisci, J.N., R. Stella, G.M. Spinks, and G.G. Wallace, *Characterisation of the topography and surface potential of electrodeposited conducting polymer films using atomic force and electric force microscopies.* Electrochimica Acta, 2000. **46**(4): p. 519- 531.

168. Chaiṅ et, E. and M. Billon, *In situ STM study of the counterion effect on the doping stages of polypyrrole films.* Synthetic Metals, 1999. **99**(1): p. 21-26.

169. Nyffenegger, R., E. Ammann, H. Siegenthaler, R. Kötz, and O. Haas, *In-situ scanning probe microscopy for the measurement of thickness changes in an electroactive polymer.* Electrochimica Acta, 1995. **40**(10): p. 1411-1415.

170. Li, J., E. Wang, M. Green, and P.E. West, *In situ AFM study of the surface morphology of polypyrrole film.* Synthetic Metals, 1995. **74**(2): p. 127-131.

171. Ibanez, J.G., A. Alatorre-Ordaz, S. Gutierrez-Granados, and N. Batina, *Nanoscale degradation of polypyrrole films under oxidative stress: An atomic force microscopy study and review.* Polymer Degradation and Stability, 2008. **93**(4): p. 827-837.

172. Higgins, M., G.G. Wallace, A. Gelmi, and S.T. McGovern, *Electrochemical AFM.* Imaging & Microscopy, 2009. **11**(2): p. 40-43.

173. Heinz, W.F. and J.H. Hoh, *Spatially resolved force spectroscopy of biological surfaces using the atomic force microscope.* Trends in Biotechnology, 1999. **17**(4): p. 143-150.

174. Butt, H.-J., B. Cappella, and M. Kappl, *Force measurements with the atomic force microscope : Technique , interpretation and applications.* Surface Science Reports, 2005. **59**: p. 1-152.

175. Hutter, J.L. and J. Bechhoefer, *Calibration of atomic-force microscope tips.* Review of Scientific Instruments, 1993. **64**(7): p. 1868-1873.

176. Radmacher, M., *Studying the Mechanics of Cellular Processes by Atomic Force Microscopy*, in *Methods in Cell Biology*, W. Yu-Li and E.D. Dennis, Editors. 2007, Academic Press. p. 347-372.

177. Clifford, C.A. and M.P. Seah, *Modelling of nanomechanical nanoindentation measurements using an AFM or nanoindenter for compliant layers on stiffer substrates.* Nanotechnology, 2006. **17**(21): p. 5283.

178. Passeri, D., et al., *Quantitative measurement of indentation hardness and modulus of compliant materials by atomic force microscopy.* Review of Scientific Instruments, 2008. **79**(6): p. 066105.

179. Magonov, S.N. and D.H. Reneker, *Characterization of polymer surfaces with atomic force microscopy.* Annual Review Material Science, 1997. **27**: p. 175-222.

180. Haga, H., et al., *Elasticity mapping of living fibroblasts by AFM and immunofluorescence observation of the cytoskeleton.* Ultramicroscopy, 2000. **82**(1–4): p. 253-258.

181. Dupres, V., C. Verbelen, and Y.F. Dufrêne, *Probing molecular recognition sites on biosurfaces using AFM.* Biomaterials, 2007. **28**(15): p. 2393-2402.

182. Smith, D.A., S.D. Connell, C. Robinson, and J. Kirkham, *Chemical force microscopy: applications in surface characterisation of natural hydroxyapatite.* Analytica Chimica Acta, 2003. **479**(1): p. 39-57.

183. Noy, A., D.V. Vezenov, and C.M. Lieber, *Chemical force microscopy.* Annual Review of Materials Science, 1997. **27**: p. 381-421.

184. Leite, F.L. and P.S.P. Herrmann, *Application of atomic force spectroscopy (AFS) to studies of adhesion phenomena: a review.* Journal of Adhesion Science and Technology, 2005. **19**(3-5): p. 365-405.

185. Hinterdorfer, P. and Y.F. Dufrene, *Detection and localization of single molecular recognition events using atomic force microscopy.* Nature Methods, 2006. **3**(5): p. 347-355.

186. Tsapikouni, T.S. and Y.F. Missirlis, *Measuring the force of single protein molecule detachment from surfaces with AFM.* Colloids and Surfaces B: Biointerfaces, 2010. **75**(1): p. 252-259.

187. Li, F., S.D. Redick, H.P. Erickson, and V.T. Moy, *Force measurements of the $\alpha_5\beta_1$ integrin–fibronectin interaction.* Biophysical Journal, 2003. **84**(2): p. 1252-1262.

188. Hinterdorfer, P., W. Baumgartner, H.J. Gruber, K. Schilcher, and H. Schindler, *Detection and localization of individual antibody-antigen recognition events by atomic force microscopy.* Proceedings of the National Academy of Sciences, 1996. **93**(8): p. 3477-3481.

189. Touhami, A., B. Hoffmann, A. Vasella, F.A. Denis, and Y.F. Dufrêne, *Probing specific lectin-carbohydrate interactions using Atomic Force Microscopy imaging and force measurements.* Langmuir, 2002. **19**(5): p. 1745-1751.

190. Meadows, P.Y., J.E. Bemis, and G.C. Walker, *Single-molecule force spectroscopy of isolated and aggregated fibronectin proteins on negatively charged surfaces in aqueous liquids.* Spectroscopy, 2003. **19**(23): p. 9566-9572.

191. Zlatanova, J., S.M. Lindsay, and S.H. Leuba, *Single molecule force spectroscopy in biology using the atomic force microscope.* Progress in Biophysics and Molecular Biology, 2000. **74**(1–2): p. 37-61.

192. Mitsui, K., M. Hara, and A. Ikai, *Mechanical unfolding of a2-macroglobulin molecules with atomic force microscope.* FEBS Letters, 1996. **385**(1–2): p. 29-33.

193. Rief, M., M. Gautel, F. Oesterhelt, J.M. Fernandez, and H.E. Gaub, *Reversible unfolding of individual titin immunoglobulin domains by AFM.* Science, 1997. **276**(5315): p. 1109-1112.

194. Carrion-Vazquez, M., et al., *Mechanical design of proteins studied by single molecule force spectroscopy and protein engineering.* Progress in Biophysics and Molecular Biology, 2000. **74**(1–2): p. 63-91.

195. Oberhauser, A.F., P.E. Marszalek, H.P. Erickson, and J.M. Fernandez, *The molecular elasticity of the extracellular matrix protein tenascin.* Nature, 1998. **393**(6681): p. 181-185.

196. Rief, M., J. Pascual, M. Saraste, and H.E. Gaub, *Single molecule force spectroscopy of spectrin repeats: low unfolding forces in helix bundles.* Journal of Molecular Biology, 1999. **286**(2): p. 553-561.

197. Oberhauser, A.F., C. Badilla-fernandez, M. Carrion-vazquez, and J.M. Fernandez, *The mechanical hierarchies of fibronectin observed with single molecule AFM.* Journal of Molecular Biology, 2002. **319**(2): p. 433-447.

198. Li, M., et al., *Detecting CD20-Rituximab interaction forces using AFM single molecule force spectroscopy.* Chinese Science Bulletin, 2011. **56**(35): p. 3829-3835.

199. Conti, M., G. Donati, G. Cianciolo, S. Stefoni, and B. Samorì, *Force spectroscopy study of the adhesion of plasma proteins to the surface of a dialysis membrane: Role of the nanoscale surface hydrophobicity and topography.* Journal of Biomedical Materials Research, 2002. **61**(3): p. 370-379.

200. Grandbois, M., W. Dettmann, M. Benoit, and H.E. Gaub, *Affinity imaging of red blood cells using an Atomic Force Microscope.* Journal of Histochemistry & Cytochemistry, 2000. **48**(5): p. 719-724.

201. Lhoest, J.B., E. Detrait, P. van den Bosch de Aguilar, and P. Bertrand, *Fibronectin adsorption, conformation, and orientation on polystyrene substrates studied by*

radiolabeling, XPS, and ToF SIMS. Journal of Biomedical Materials Research, 1998. **41**(1): p. 95-103.

202. Lai, C.S., N.M. Tooney, and E.G. Ankel, *Structure and flexibility of plasma fibronectin in solution: electron spin resonance spin-label, circular dichroism and sedimentation studies.* Biochemistry, 1984. **23**(26): p. 6393-6397.

203. Patel, S., A.F. Chaffotte, F. Goubard, and E. Pauthe, *Urea-Induced Sequential Unfolding of Fibronectin: A Fluorescence Spectroscopy and Circular Dichroism Study.* Biochemistry, 2004. **43**(6): p. 1724-1735.

204. Castano, H., E.A. O'Rear, P.S. McFetridge, and V.I. Sikavitsas, *Polypyrrole thin films formed by admicellar polymerization support the osteogenic differentiation of mesenchymal stem cells.* Macromolecular Bioscience, 2004. **4**(8): p. 785-794.

205. Clark, P., P. Connolly, and G.R. Moores, *Cell guidance by micropatterned adhesiveness in vitro.* J Cell Sci, 1992. **103**(1): p. 287-292.

206. Curtis, A. and C. Wilkinson, *Topographical control of cells.* Biomaterials, 1997. **18**(24): p. 1573-1583.

207. De Rossi, D., A. Della Santa, and A. Mazzoldi, *Performance and work capacity of a polppyrrole conducting polymer linear actuator.* Synthetic Metals, 1997. **90**(2): p. 93-100.

208. Gandhi, M.R., P. Murray, G.M. Spinks, and G.G. Wallace, *Mechanism of electromechanical actuation in polypyrrole.* Synthetic Metals, 1995. **73**(3): p. 247-256.

209. Sisken, B.F., J. Walker, and M. Orgel, *Prospects on clinical applications of electrical stimulation for nerve regeneration.* J Cell Biochem, 1993. **51**(4): p. 404-409.

210. Chen, S.J., et al., *Template sythesis of the polypyrrole tube and its bridging in vivo sciatic nerve regeneration.* Materials Science Letters, 2000. **19**(23): p. 2157-2159.

211. Xinyan, C., et al., *Surface modification of neural recording electrodes with conducting polymer/biomolecule blends.* Journal of Biomedical Materials Research, 2001. **56**(2): p. 261-272.

212. Schmidt, C., T. Rivers, T. Hudson, and J. Collier, *Modification of electroactive biomaterials for neural engineering applications.* Conducting Polymers and Polymer Electrolytes: from Biology to Photovoltaics, 2003. **832**: p. 154-165.

213. Froeck, C., A. Bartl, and L. Dunsch, *STM- and AFM-investigations of one- and two-dimensional polypyrrole structures on electrodes.* Electrochimica Acta, 1995. **40**(10): p. 1421-1425.

214. Hallab, N.J., K.J. Bundy, K. O'Connor, R.L. Moses, and J.J. Jacobs, *Evaluation of metallic and polymeric biomaterial surface energy and surface roughness characteristics for directed cell adhesion.* Tissue Engineering, 2001. **7**(1): p. 55-71.

215. Goa, K.L. and P. Benfield, *Hyaluronic acid. A review of its pharmacology and use as a surgical aid in opthalmology, and its therapeutic potential in joint disease and wound healing.* Pub. Med., 1994. **47**(3): p. 536-566.

216. Zhao, H. and G.G. Wallace, *Polypyrrole/poly(2-methoxyaniline-5-sulfonic acid) polymer composite.* Polymer Gels and Networks, 1998. **6**(3-4): p. 233-245.

217. Otero, T.F., J.J.L. Cascales, and G.V. Arenas, *Mechanical characterization of freestanding polypyrrole film.* Materials Science and Engineering C, 2007. **27**(1): p. 18-22.

218. Chiarelli, P., A.D. Santa, D. de Rossi, and A. Mazzoldi, *Actuation properties of electrochemically driven polypyrrole free-standing films.* Journal of Intelligent Material Systems and Structures, 1995. **6**(1): p. 32-37.

219. Lang, U., N. Naujoks, and J. Dual, *Mechanical characterization of PEDOT:PSS thin films.* Synthetic Metals, 2009. **159**(5-6): p. 473-479.

220. Lang, U. and J. Dual. *Mechanical properties of the intrinsically conductive polymer poly(3,4-ethylenedioxythiophene) poly(styrenesulfonate) (PEDOT/PSS)*. *10th International Conference on Mechanical Behavior of Materials*. 2007: Trans Tech Publications Ltd.

221. Spinks, G.M., L. Liu, G.G. Wallace, and D. Zhou, *Strain response from polypyrrole actuators under load.* Advanced Functional Materials, 2002. **12**(6-7): p. 437-440.

222. Passeri, D., et al., *Indentation modulus and hardness of viscoelastic thin films by atomic force microscopy: A case study.* Ultramicroscopy, 2009. **109**(12).

223. Wang, X.-S. and X.-Q. Feng, *Effects of thickness on mechanical properties of conducting polythiophene films.* Journal of Materials Science Letters, 2002. **21**(9): p. 715-717.

224. Spinks, G.M., G. Alici, S.T. McGovern, B. Xi, and G.G. Wallace, *Conjugated Polymer Actuators: Fundamentals*, in *Biomedical Applications of Electroactive Polymer Actuators*, F. Carpi and E. Smela, Editors. 2009, John Wiley and Sons. p. 496.

225. Levy-mishali, M., J. Zoldan, and S. Levenberg, *Effect of scaffold stiffness on myoblast differentiation.* Tissue Engineering: Part A, 2008. **14**: p. 23-27.

226. Barrias, C.C., M.C.L. Martins, G. Almeida-porada, M.A. Barbosa, and P.L. Granja, *The correlation between the adsorption of adhesive proteins and cell behavior on hydroxyl-methyl mixed self-assembled monolayers.* Biomaterials, 2009. **30**(3): p. 307-316.

227. Magonov, S.N., V. Elings, and M.-H. Whangbo, *Phase imaging and stiffness in tapping-mode atomic force microscopy.* Surface Science, 1997. **375**(2-3): p. 385-391.

228. Schmitz, I., M. Schreiner, G. Friedbacher, and M. Grasserbauer, *Phase imaging as an extension to tapping mode AFM for the identification of material properties on humidity-sensitive surfaces.* Applied Surface Science, 1997. **115**(2): p. 190-198.

229. Planes, J., Y. Samson, and Y. Cheguettine, *Atomic force microscopy phase imaging of conductive polymer blends with ultralow percolation threshold.* Applied Physics Letters, 1999. **75**(10): p. 1395-1397.

230. Semenikhin, O., *Kelvin probe force microscopic study of anodically and cathodically doped poly-3-methylthiophene.* Synthetic Metals, 2000. **110**(2): p. 115-122.

231. Magonov, S.N., V. Elings, D. Denley, and M.-H. Whangbo, *Tapping-mode atomic force microscopy study of the near-surface composition of a styrene butadienestyrene triblock copolymer film (a) (b).* Surface Science, 1997. **389**(1-3): p. 201-211.

232. Bar, G., Y. Thomann, R. Brandsch, H. Cantow, and M.H. Whangbo, *Factors affecting the height and phase images in Tapping Mode Atomic Force Microscopy. Study of phase-separated polymer blends of poly(ethene-costyrene) and poly(2,6dimethyl-1,4-phenylene oxide).* Langmuir, 1997. **13**(14): p. 3807-3812.

233. Gilmore, K.J., et al., *Biomaterials skeletal muscle cell proliferation and differentiation on polypyrrole substrates doped with extracellular matrix components.* Biomaterials, 2009. **30**(29): p. 5292-5304.

234. Moreno, J.S., et al., *Polypyrrole-polysaccharide thin films characteristics: electrosynthesis and biological properties.* Journal of Biomedical Materials Research. Part A, 2009. **88A**(3): p. 832-840.

235. Leclere, P., et al., *Microdomain morphology analysis of block copolymers by Atomic Force Microscopy with phase detection imaging.* Langmuir, 1996. **12**(18): p. 4317-4320.

236. Liu, Y.-c., *Characteristics of vibration modes of polypyrrole on surface-enhanced Raman scattering spectra.* Electroanalytical Chemistry, 2004. **571**(1): p. 255-264.

237. Zuo, F., M. Angelopoulos, A.G. Macdiarmid, and A.J. Epstein, *Transport studies of protonated emeraldine polymer: A granular polymeric metal system.* Physical Review B, 1987. **36**(6): p. 3475-3478.

238. Prigodin, V. and A.J. Epstein, *Nature of insulator–metal transition and novel mechanism of charge transport in the metallic state of highly doped electronic polymers.* Synthetic Metals, 2002. **125**(1): p. 43-53.

239. Laarz, E., A. Meurk, J.A. Yanez, and L. Bergstro, *Silicon nitride colloidal probe measurements: Interparticle forces and the role of surface-segment interactions in poly(acrylic acid) adsorption from aqueous solution.* Journal of the American Ceramic Society, 2001. **84**(8): p. 1675-1682.

240. Lamour, G., et al., *Influence of surface energy distribution on neuritogenesis.* Colloids and surfaces. B, Biointerfaces, 2009. **72**(2): p. 208-18.

241. Cheung, J.W.C. and G.C. Walker, *Immuno-atomic force microscopy characterization of adsorbed fibronectin.* Langmuir, 2008. **24**(24): p. 13842-13849.

242. Hileman, R.E., J.R. Fromm, J.M. Weiler, and R.J. Linhardt, *Glycosaminoglycanprotein interactions: definition of consensus sites in glycosaminoglycan binding proteins.* BioEssays, 1998. **20**(2): p. 156-167.

243. Turnbull, J., A. Powell, and S. Guimond, *Heparan sulfate: decoding a dynamic multifunctional cell regulator.* Trends in Cell Biology, 2001. **11**(2): p. 75-82.

244. Kowalczyńska, H.M., et al., *Adsorption characteristics of human plasma fibronectin in relationship to cell adhesion.* Journal of Biomedical Materials Research, 2002. **61**(2): p. 260-269.

245. Wan, A.M.D., et al., *Electrical control of protein conformation.* Advanced Materials, 2012. **24**(18): p. 2501-2505.

246. Sekar, R.B. and A. Periasamy, *Fluorescence resonance energy transfer (FRET) microscopy imaging of live cell protein localizations.* The Journal of cell biology, 2003. **160**(5): p. 629-633.

247. Allen, S., et al., *Detection of Antigen–An□body Binding Events with the Atomic Force Microscope†.* Biochemistry, 1997. **36**(24): p. 7457-7463.

248. Vinckier, A., et al., *Immobilizing and imaging microtubules by atomic force microscopy.* Ultramicroscopy, 1995. **57**(4): p. 337-343.

249. Rief, M., M. Gautel, and H.E. Gaub, *Unfolding forces of titin and fibronectin domains directly measured by AFM.* 2000(0065-2598 (Print)).

250. Hugel, T., et al., *Elasticity of single polyelectrolyte chains and their desorption from solid supports studied by AFM based single molecule force spectroscopy.* Macromolecules, 2001. **34**(4): p. 1039-1047.

251. Minko, S. and Y. Roiter, *AFM single molecule studies of adsorbed polyelectrolytes.* Current Opinion in Colloid & Interface Science, 2005. **10**(1-2): p. 9-15.

252. Erickson, H.P., N. Carrell, and J. McDonagh, *Fibronectin molecule visualized in electron microscopy: a long, thin, flexible strand.* Journal of Cell Biology, 1981. **91**: p. 673-678.

253. Erickson, H.P., *Reversible unfolding of fibronectin type III and immunoglobulin domains provides the structural basis for stretch and elasticity of titin and fibronectin.* 1994. **91**: p. 10114-10118.

254. Smith, M., et al., *Force-induced unfolding of fibronectin in the extracellular matrix of living cells.* PLOS Biol, 2007. **5**: p. 2243-2254.

255. Johnson, K.J., H. Sage, G. Briscoe, and H.P. Erickson, *The compact conformation of fibronectin is determined by intramolecular ionic interactions.* Journal of Biological Chemistry, 1999. **274**(22): p. 15473-15479.

256. Rabenstein, D.L., *Heparin and heparan sulfate: structure and function.* Natural Product Reports, 2002. **19**(3): p. 312-331.

257. Busby, T.F., et al., *Heparin binding by fibronectin module III-13 involves six discontinuous basic residues brought together to form a cationic cradle.* The Journal of biological chemistry, 1995. **270**(31): p. 18558-18562.

258. Ruoslahti, E., A. Pekkala, and E. Engvall, *Effect of dextran sulfate on fibronectincollagen interaction.* FEBS Letters, 1979. **107**: p. 51-54.

259. Yamagata, M., K.M. Yamada, M. Yoneda, S. Suzuki, and K. Kimata, *Chondroitin sulfate proteoglycan (PG-M-like Proteoglycan) is involved in binding of*

hyaluronic acid to cellular fibronectin. Journal of Biological Chemistry, 1986. **261**: p. 13526-13535.

260. Pernodet, N., et al., *Fibronectin fibrillogenesis on sulfonated polystyrene surfaces.* Journal of Biomedical Materials Research, 2003. **64A**(4): p. 684-692.

261. Grinnell, F. and M.K. Feld, *Adsorption characteristics of plasma fi- bronectin in relationship to biological activity.* Journal of Biomedical Materials Research, 2004. **15**: p. 363-381.

262. Hynes, R.O. and K.M. Yamada, *Fibronectins: multifunctional modular glycoproteins.* The Journal of cell biology, 1982. **95**(2 Pt 1): p. 369-77.

263. Cavalcanti-Adam, E.A., et al., *Lateral spacing of integrin ligands influences cell spreading and focal adhesion assembly.* European Journal of Cell Biology, 2006. **85**(3–4): p. 219-224.

264. Maheshwari, G., G. Brown, D.A. Lauffenburger, A. Wells, and L.G. Griffith, *Cell adhesion and motility depend on nanoscale RGD clustering.* Journal of Cell Science, 2000. **113**(10): p. 1677-1686.

265. Palecek, S.P., J.C. Loftus, M.H. Ginsberg, D.A. Lauffenburger, and A.F. Horwitz, *Integrin-ligand binding properties govern cell migration speed through cellsubstratum adhesiveness.* Nature, 1997. **385**(6616): p. 537-540.

266. Cole, M.A., N.H. Voelcker, H. Thissen, and H.J. Griesser, *Stimuli-responsive interfaces and systems for the control of protein–surface and cell–surface interactions.* Biomaterials, 2009. **30**(9): p. 1827-1850.

267. Haimovich, B., et al., *A new method for membrane construction on ePTFE vascular grafts: Effect on surface morphology and platelet adhesion.* Journal of Applied Polymer Science, 1997. **63**(11): p. 1393-1400.

268. Sung, W.J. and Y.H. Bae, *A glucose oxidase electrode based on polypyrrole with polyanion/PEG/enzyme conjugate dopant.* Biosensors and Bioelectronics, 2003. **18**(10): p. 1231-1239.

269. Edahiro, J.-i., et al., *In situ control of cell adhesion using photoresponsive culture surface.* Biomacromolecules, 2005. **6**(2): p. 970-974.

270. Jagur-Grodzinski, J., *Polymers for tissue engineering, medical devices, and regenerative medicine. Concise general review of recent studies.* Polymers for Advanced Technologies, 2006. **17**(6): p. 395-418.

271. Yasuda, A., et al., *In vitro culture of chondrocytes in a novel thermoreversible gelation polymer scaffold containing growth factors.* Tissue Engineering, 2006. **12**(5): p. 1237-1245.

272. Auernheimer, J., C. Dahmen, U. Hersel, A. Bausch, and H. Kessler, *Photoswitched cell adhesion on surfaces with RGD peptides.* Journal of the American Chemical Society, 2005. **127**(46): p. 16107-16110.

273. Kwon, O.H., A. Kikuchi, M. Yamato, Y. Sakurai, and T. Okano, *Rapid cell sheet detachment from Poly(N-isopropylacrylamide)-grafted porous cell culture membranes.* Journal of Biomedical Materials Research, 2000. **50**(1): p. 82-89.

274. Hyeong Kwon, O., A. Kikuchi, M. Yamato, and T. Okano, *Accelerated cell sheet recovery by co-grafting of PEG with PIPAAm onto porous cell culture membranes.* Biomaterials, 2003. **24**(7): p. 1223-1232.

275. Uhlmann, P., et al., *In-Situ Investigation of the Adsorption of Globular Model Proteins on Stimuli-Responsive Binary Polyelectrolyte Brushes†.* Langmuir, 2006. **23**(1): p. 57-64.

276. Garcia, A., et al., *Photo-, thermally, and pH-responsive microgels.* Langmuir, 2006. **23**(1): p. 224-229.

277. Nakanishi, J., et al., *Photoactivation of a substrate for cell adhesion under standard fluorescence microscopes.* Journal of the American Chemical Society, 2004. **126**(50): p. 16314-16315.

278. Shimoboji, T., et al., *Photoresponsive polymer-enzyme switches*. 2002, National Academy of Sciences. p. 16592-16596.

279. Ivanov, A.E., N.L. Eremeev, P.O. Wahlund, I.Y. Galaev, and B. Mattiasson, *Photosensitive copolymer of N-isopropylacrylamide and methacryloyl derivative of spyrobenzopyran.* Polymer, 2002. **43**(13): p. 3819-3823.

280. Sumaru, K., M. Kameda, T. Kanamori, and T. Shinbo, *Characteristic phase transition of aqueous solution of poly(N-isopropylacrylamide) functionalized with spirobenzopyran.* Macromolecules, 2004. **37**(13): p. 4949-4955.

281. Higuchi, A., et al., *Photon-modulated changes of cell attachments on poly(spiropyran-co-methyl methacrylate) membranes.* Biomacromolecules, 2004. **5**(5): p. 1770-1774.

282. Katsonis, N., M. Lubomska, M.M. Pollard, B.L. Feringa, and P. Rudolf, *Synthetic light-activated molecular switches and motors on surfaces.* Progress in Surface Science, 2007. **82**(7-8): p. 407-434.

283. Seki, T. and K. Ichimura, *Thermal-isomerization behaviors of a spiropyran in bilayers immobilized with a linear polymer and a smectitic clay.* Macromolecules, 1990. **23**(1): p. 31-35.

284. Stitzel, S., R. Byrne, and D. Diamond, *LED switching of spiropyran-doped polymer films.* Journal of Materials Science, 2006. **41**(18): p. 5841-5844.

285. Wagner, K., et al., *A multiswitchable poly(terthiophene) bearing a spiropyran functionality: Understanding photo- and electrochemical control.* Journal of the American Chemical Society, 2011. **133**(14): p. 5453-5462.

286. Bardavid, Y., I. Goykhman, D. Nozaki, G. Cuniberti, and S. Yitzchaik, *Dipole assisted photogated switch in spiropyran grafted polyaniline nanowires.* Journal of Physical Chemistry C, 2011. **115**(7): p. 3123-3128.

287. Irie, M., K. Hayashi, and A. Menju, *Photoresponsive polymers IV. Photocontrol of viscosity and pH-value in aqueous systems using poly(methacrylic acid) having spirobenzopyran side groups.* Polymer Photochemistry, 1981. **1**(3): p. 233-242.

288. Joseph, G., J. Pichardo, and G. Chen, *Reversible photo-/thermoresponsive structured polymer surfaces modified with a spirobenzopyran-containing copolymer for tunable wettability.* Analyst, 2010. **135**(9): p. 2303-2308.

289. Olenych, S.G., M.D. Moussallem, D.S. Salloum, J.B. Schlenoff, and T.C.S. Keller, *Fibronectin and cell attachment to cell and protein resistant polyelectrolyte surfaces.* Biomacromolecules, 2005. **6**(6): p. 3252-3258.

290. Chen, S., J. Zheng, L. Li, and S. Jiang, *Strong resistance of phosphorylcholine selfassembled monolayers to protein adsorption: Insights into nonfouling properties of zwitterionic materials.* Journal of the American Chemical Society, 2005. **127**(41): p. 14473-14478.

291. Ladd, J., Z. Zhang, S. Chen, J.C. Hower, and S. Jiang, *Zwitterionic polymers exhibiting high resistance tononspecificprotein adsorption from human serum and plasma.* Biomacromolecules, 2008. **9**(5): p. 1357-1361.

Appendix 1

In order to determine that the voltage being reported from the pseudo-reference electrode is correct, the e-cell needs to be characterised with a standard electrochemical red-ox reaction and Ag/AgCl reference electrode. The red-ox potentials of ferri-ferrocyanide are well defined and have been used to characterise this e-cell. Working electrodes of plain gold mylar were used in these experiments.

The characterisation of the e-cell was carried out through cyclic voltammetry and the voltammogram displayed in Figure 0-1. A potential window of -600 mV to 600 mV was applied with a scan rate of 50 mV/s.

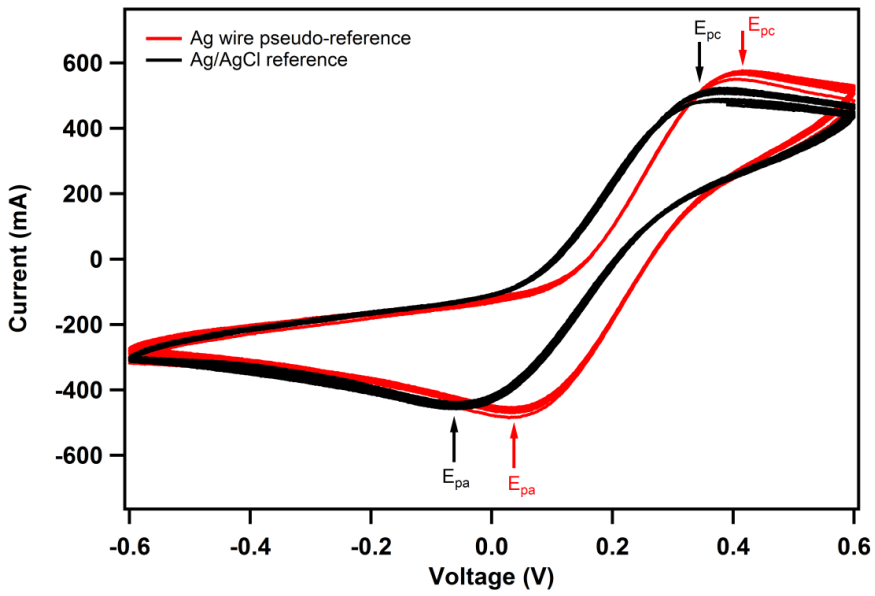

Figure 0-1: Cyclic voltammogram of ferri-ferrocyanide. Peak separation of Ag wire

The peak separation for the red-ox reaction was measured in order to observe any shift when using the Ag wire reference as compared to the Ag/AgCl reference. The peak separation for the Ag wire pseudo-reference and Ag/AgCl reference was 0.43 V and 0.38V respectively. The peak separations for the two different reference electrodes are similar, and so far this e-cell the Ag wire pseudo-reference is an acceptable reference electrode.